UNIVERSITÀ DEGLI STUDI DI PADOVA

DIPARTIMENTO DI FISICA E ASTRONOMIA "G. GALILEI"

CORSO DI DOTTORATO DI RICERCA IN ASTRONOMIA

CICLO XXXI

MASS DETERMINATION OF SUPERMASSIVE BLACK HOLES IN NEARBY GALAXIES

Tesi redatta con il contributo finanziario della
Fondazione Cassa di Risparmio di Padova e Rovigo (Cariparo)

Coordinatore: Ch.mo Prof. Giampaolo Piotto
Supervisore: Prof. Enrico Maria Corsini
Co-supervisore: Dott. Elena Dalla Bontà

Dottoranda: Ilaria Pagotto

Valutatori / External referees:
Prof. Stephen John Magorrian
Prof. Bradley M. Peterson

Contents

List of Figures

List of Tables

Riassunto

Questo lavoro di tesi è dedicato alla misura della massa $M_\bullet$ dei buchi neri supermassicci (SBH) che si celano al centro delle galassie quiescenti vicine. Aumentare il campione di SBH di massa nota permette di studiarne le relazioni con le altre proprietà delle galassie per poterne investigare l'evoluzione congiunta. Grandi campioni di $M_\bullet$ ottenuti per i diversi tipi morfologici sono necessari per comprendere i processi fisici che sono alla base delle relazioni osservate e che possono esprimersi non solo nella pendenza di queste relazioni, ma anche nella dispersione delle $M_\bullet$ misurate e nella distribuzione di quelle che scartano dalle relazioni stesse.

Nuovi limiti stringenti sulla massa $M_\bullet$ di 7 galassie sono stati fissati dalla misura della larghezza delle righe nebulari del gas ionizzato in spettri presi con l'Hubble Space Telescope (HST) entro aperture di dimensioni inferiori al secondo d'arco. La dispersione di velocità delle stelle è stata misurata con spettri a fenditura lunga presi da terra, il raggio efficace è stato ricavato dalla decomposizione fotometrica di immagini in banda i della Sloan Digital Sky Survey oppure dalla letteratura, ed infine è stata calcolata la dispersione di velocità delle stelle $\sigma_{\rm c}$ entro 1/8 il raggio efficace. Questi limiti di $M_\bullet$ si dispongono parallelamente e al di sopra della relazione $M_\bullet - \sigma_{\rm c}$ e non dipendono dalla morfologia o dalla distanza delle galassie. Questo suggerisce che il potenziale gravitazionale nei nuclei galattici è ben tracciato dalla larghezza delle righe di emissione se il gas si concentra verso il centro. Il numero delle galassie con un limite sulla massa $M_\bullet$ dalla larghezza delle righe di emissione sale così a 114 oggetti.

Queste galassie sono state poi analizzate includendo nel modello dinamico il contributo della massa stellare per ottenere limiti ancora più stringenti sulla massa $M_\bullet$. A questo scopo la brillanza superficiale misurata da immagini HST e il rapporto massa-luminosità tipico di una popolazione stellare vecchia e ricca in metalli sono stati usati per 100 galassie vicine ($D < 103$ Mpc) e con un'ampia varietà di morfologie (E-Sc) e dispersioni di velocità (54-404 km s^{-1}). La forma dei profili delle righe di emissione e dell'andamento radiale del loro flusso sono stati studiati per escludere che le forze non gravitazionali giocassero un ruolo rilevante nella stima di $M_\bullet$. Il contributo stellare è maggiore per galassie con bassa dispersione di velocità efficace $\sigma_{\rm e}$ anche per la presenza di un ammasso/disco stellare nucleare, e trascurabile per le ellittiche. Esso dipende dalle dimensioni dell'apertura ma non dalla distanza della galassia. I nuovi limiti di massa si dispongono parallelamente alla relazione $M_\bullet - \sigma_{\rm e}$ ed eccedono il valore predetto dalla medesima solo di un fattore 1.7. Questo è un risultato notevole visto che il modello dinamico si basa su una distribuzione e cinematica del gas non spazialmente risolte.

Infine, sono state ottenute nuove misure di dispersione di velocità stellare nel nucleo di

28 galassie. Gli spettri HST ottenuti con il reticolo G750M sono stati interpolati grazie a una serie di modelli di popolazioni stellari e varie righe di emissione gaussiane, vincolando la popolazione stellare nel nucleo delle galassie grazie a spettri presi con il reticolo G430L. Queste misure permettono di porre dei forti vincoli su $M_\bullet$ come mostrano i casi di NGC 4435 e NGC 4459. Si tratta di due galassie lenticolari caratterizzate da valori simili di $\sigma_{\rm e}$ ma con $M_\bullet$ molto diverse. In particolare, quella di NGC 4435 è molto più bassa rispetto a quanto predetto dalla relazione tra $M_\bullet - \sigma_{\rm e}$ secondo quanto ottenuto dalla dinamica del gas ionizzato. Grazie a modelli dinamici stellari assisimmetrici è stata riprodotta la cinematica da spettroscopia a campo integrale usando immagini ad alta risoluzione prese con la Advanced Camera for Surveys e adottando come $M_\bullet$ quella predetta dalla relazione con la dispersione di velocità. Questi modelli permettono di predire il valore centrale di dispersione di velocità e di confrontarlo con il valore osservato. Mentre per NGC 4459 il valore teorico e quello osservato sono in accordo, il valore misurato per NGC 4435 è molto più basso rispetto che a quello del modello dinamico indicando che la galassia effettivamente ospita un SBH meno massiccio del normale.

Stando ai modelli teorici di evoluzione delle galassie, definire la frazione di SBH meno massicci del normale nelle galassie vicine sarebbe cruciale per caratterizzare i processi che guidano la crescita di massa dei SBH e fanno sì che essi si insedino al centro delle galassie. Gli oggetti più peculiari del campione potranno essere oggetto di future osservazioni per misurarne e modellare la cinematica risolta di gas e stelle.

Abstract

This thesis focuses on the measurement of the mass $M_\bullet$ of supermassive black holes (SBH) lurking in the center of nearby quiescent galaxies. Increasing the demography of SBHs allows study of the correlations between their mass and the properties of their host to get insights about the joint evolution of SBHs and galaxies. Large $M_\bullet$ samples across different morphological types are needed to fully understand the underlying processes that cause correlations. Indeed, clues may be present not only in the slope of these correlations but also in their scatter and secondary trends related, for instance, to galaxy morphology, or in the behavior of outliers.

New stringent limits on $M_\bullet$ for 7 nearby galaxies are obtained by modeling the central width of the nebular emission lines measured over subarcsecond apertures with the Hubble Space Telescope (HST). The central stellar velocity dispersion of each galaxy is obtained from new long-slit spectra from ground-based observations, the bulge effective radius is derived either from a two-dimensional photometric decomposition of the i-band images of the Sloan Digital Sky Survey or from literature, and the stellar velocity dispersion $\sigma_{\rm c}$ within 1/8 the effective radius is calculated. The $M_\bullet$ limits run parallel to but above the $M_\bullet - \sigma_{\rm c}$ relation with no systematic trend depending on the galaxy distance or morphology. This gives further support to previous findings suggesting that the nuclear gravitational potential is remarkably well traced by the nebular-line width when the gas is centrally peaked. With this investigation, the number of galaxies with $M_\bullet$ stringent limits obtained from nebular-line width increases to 114.

These galaxies are further analyzed to more tightly constrain $M_\bullet$ by taking into account the stellar mass contribution in the galaxy nucleus. To this aim, the surface brightness distribution is measured from HST images and the mass-to-light ratio of an old and metal-rich stellar population is adopted for 100 nearby galaxies ($D < 103$ Mpc) spanning a wide range of Hubble types (E-Sc) and effective velocity dispersions (54-404 km s^{-1}). The shape of the profile of the emission lines and of the radial profile of emission-line flux are analysed to verify that nongravitational forces have a minor impact on the $M_\bullet$ estimate. On average, the stellar mass contribution is larger for galaxies with low effective velocity dispersion $\sigma_{\rm e}$ partly due to the presence of a nuclear stellar cluster or disk. Moreover, the stellar mass contribution is negligible in ellipticals and depends on the aperture size rather than on galaxy distance. These new $M_\bullet$ limits run parallel to the relation between the SBH mass and the stellar velocity dispersion and they exceed the expected values by a median factor of 1.7. This is a striking result, since the dynamical analysis does not rely on spatially-resolved gas

distribution and kinematics.

Finally, new stellar velocity dispersions within subarcsecond apertures are obtained for the nuclei of a sample of 28 nearby galaxies. HST spectra obtained with the G750M grating are fitted using a library of single stellar population models and Gaussian emission lines, while constraining in most cases the stellar population content from an initial fit to HST G430L spectra. These measurements are useful for constraining $M_\bullet$ as illustrated by the cases of the lenticular galaxies NGC 4435 and NGC 4459. These are characterized by similar ground-based $\sigma_{\rm e}$ but remarkably different $M_\bullet$, where in particular NGC 4435 appears to host a significantly undermassive SBH compared to what expected from the $M_\bullet - \sigma_{\rm e}$ relation as found from ionized-gas dynamics. Jeans axisymmetric dynamical models are built to match the ground-based stellar kinematics obtained with integral-field spectroscopy assuming a $M_\bullet$ as predicted from the relation with $\sigma_{\rm e}$ and using high-resolution images obtained with the Advanced Camera for Surveys as a base for constructing the stellar-mass model. Such reference models are used to make a prediction for the nuclear velocity dispersion. Whereas it agrees with the nuclear measurement for NGC 4459, for NGC 4435 the observed velocity dispersion is remarkably smaller than predicted, which further suggests that this galaxy hosts an undermassive SBH.

Theoretical work on galaxy evolution indicates that assessing the fraction of undermassive SBHs in nearby galaxies would be quite important to constrain the processes driving the mass growth of SBHs and how they settled in galactic nuclei. Outlier galaxies in the SBH correlations are priority targets for a future follow up to measure and model the spatially-resolved kinematics of gas and stars.

Chapter 1

Introduction

1.1 Supermassive black holes

The first clue that galactic nuclei could harbor black holes more massive than the stellar ones came from the discovery of the quasi-stellar radio source 3C 273 (Schmidt, 1963). This object was characterized for the first time by a very large redshift ($z = 0.158$) and luminosity and it was later identified as a quasar. In those years, active galactic nuclei (AGN) were already classified as astonishingly energetic phenomena (Baade & Minkowski, 1954; Woltjer, 1959; Burbidge et al., 1963; Lynds & Sandage, 1963), since they emit a large amount of energy from a very small region. The compact object that is supposed to reside in the galactic nucleus progressively accretes material and from a theoretical point of view the primary source powering AGNs should be constituted by the gravitational potential energy released during the accretion (Salpeter, 1964; Lynden-Bell, 1969).

The nature of the central compact object remained a long-debated issue. Sargent et al. (1978) by using spherical isotropic stellar models of ground based observations claimed that the kinematic data collected within the core radius of M 87 were consistent with a central mass concentration with a mass of 5×10^9 $M_\odot$, which was identified as a putative supermassive black hole (SBH). Strong evidence was also provided from the Milky Way (Genzel & Townes, 1987) based on the kinematic analysis of individual stars or on integrated K-band spectra of molecular gas absorption bands. Rees (1984) pointed out that all the scenarios that had been proposed to explain the observed AGN phenomena resulted in the final formation of a SBH. From an observational point of view, the energetic AGN events are easily detectable even from large distances, whereas in the case of quiescent galaxies there was only weaker evidence and the inactive-galaxy community remained doubtful about the assumption that a SBH could reside in the center of all the galaxies.

Strong evidence came from the observation of the highly-broadened gravitationally redshifted ionized iron $K\alpha$ line (6.4 keV) in the galaxy MCG-6-30-15 (Tanaka et al., 1995) which arises from a region very close to the event horizon. Other important evidence was provided by the observation of water maser emission in the Seyfert galaxy NGC 4258 (Miyoshi et al., 1995) from a central gas disk characterized by a Keplerian rotation curve which requires a

mass of 3.6×10^7 $M_\odot$ within a very small volume. However, the most important step towards the evidence of the presence of SBHs at the center of quiescent galaxies was accomplished with the Hubble Space Telescope (HST). Indeed, its superb spatial resolution allowed to analyze the orbiting stars and gas within the sphere of influence of the SBH, where it dominates the gravitational potential of the galaxy, and so to obtain a measure for its mass $M_\bullet$. A more recent confirmation came from the high spatial resolution measurements of the stellar orbits in the very center of the Milky Way from which the presence of a SBH was definitely proved (Schödel et al., 2002; Ghez et al., 2005, 2008; Gillessen et al., 2009). Moreover, in this case it was possible to place extremely tight constraints on the radius within which the dynamically inferred $M_\bullet$ must be contained.

These findings pointed out that a SBH is lurking in the nuclei of all the quiescent galaxies. Thus the only difference between them and active galaxies consists in the degree of activity of the central engine. While the AGNs are more common in the distant Universe with a maximum of volume density at $2 < z < 3$, the quiescent SBHs are harbored by galaxies mainly located in the nearby Universe. A key finding to understand the evolution of galaxies was the discovery that $M_\bullet$ correlates with several properties of the host galaxy. This suggested a joint evolution between SBHs and their host galaxies. Some hints of this coevolution were already provided by the AGN accretion and feedback activity, through which the SBH interacts with its host galaxy. So by looking at these two classes of galaxies from an evolutionary point of view, the SBHs of quiescent galaxies can be considered as the remnants of the past AGN activity.

SBHs have been found in about 230 galaxies by dynamical modeling of the spatially resolved and unresolved kinematics (van den Bosch, 2016). They were mainly found within ellipticals or in the bulges of lenticulars and spirals with $M_\bullet$ between 10^6 and 10^{10} $M_\odot$, but also in bulgeless galaxies with $M_\bullet$ between 10^5 and 10^6 $M_\odot$ (Kormendy & Ho, 2013). Even if in the last three decades the number of $M_\bullet$ measurements led to a collection composed by hundreds of objects, currently there are important biases in the analyzed samples. Shankar et al. (2016) compared a sample of local galaxies with $M_\bullet$ measurements to a sample of Sloan Digital Sky Survey (SDSS) local galaxies and pointed out that the SBH-host galaxies are characterized by higher stellar velocity dispersions with respect to SDSS objects of similar stellar mass. Moreover, van den Bosch et al. (2015) found that the SBH-host galaxies of their sample are biased towards densest galaxies whereas those with a large disk and low velocity dispersion are under-represented.

1.2 Measurements of the supermassive black holes mass

$M_\bullet$ is strongly related to other properties of the host galaxy and so it is crucial to measure it in a proper way to understand the formation and evolution of galaxies. In order to obtain an accurate $M_\bullet$ determination, it is necessary to resolve the sphere of influence of the SBH that is the nuclear region within

$$R = \frac{GM_\bullet}{\sigma_\star^2} \tag{1.1}$$

where σ_* is the central stellar velocity dispersion and G is the gravitational constant. Otherwise, the $M_\bullet$ estimate should be considered only as an upper limit to the actual value. For many years HST was the only facility that could reach such spatial resolution. At a later time, the installation of adaptive optics (AO) modules on the instruments mounted at the largest telescopes, like the Very Large Telescope (VLT) of the European Southern Observatory (ESO), allowed accurate measurement of $M_\bullet$ in nearby galaxies also from the ground.

Considering AGNs, the main measurement techniques employ the reverberation mapping and single-epoch spectroscopy of AGN broad emission lines (see Peterson 2014). These two techniques are only mentioned here but not described in the following since they were not employed in this work. On the other hand, the stellar and gaseous kinematics modeling are mostly used for quiescent or low-activity galaxies. Finally, the study of maser dynamics of molecular gas is noteworthy (see Kormendy & Ho 2013).

It is possible to follow the innermost orbits of single stars and map their proper motions by exploiting near infrared images and AO only in the case of our own Galaxy (see Genzel et al. 2010). A lower limit of the mass density inside the pericenters of these orbits can be derived from the motion of each one of these stars. These measurements imply that a SBH should be present beyond any reasonable doubt. The most reliable results have been obtained by analyzing the motion of the star S2, characterized by an orbital period of 15.8 yr. Parsa et al. (2017) estimated the mass and distance of Sgr A* by targeting the three stars with the shortest period and using VLT to perform AO-assisted K_s-band imaging data of the Galactic Center from 2002 to 2015.

A very powerful method to measure $M_\bullet$ relies on the analysis of the maser emission of molecular gas. This technique was first exploited by Miyoshi et al. (1995) who modeled the Keplerian rotation curve in the center of NGC 4258 by carrying out radio interferometry on the water maser emission coming from its nuclear molecular gas disk. More recently, this method was applied also by Kuo et al. (2011) who provided accurate $M_\bullet$ for a sample of seven active galaxies by analyzing their water maser emission with Very Long Baseline Interferometry images and kinematics. Superb angular resolution of the order of few milliarcseconds can be reached and this technique is useful also in gas-rich galaxies whose nucleus is optically obscured.

Currently, the modeling of the stellar resolved kinematics is the most widely used technique to provide $M_\bullet$ estimates (Kormendy & Ho, 2013; van den Bosch, 2016) and this is due also to the fact that stars can be always adopted as dynamical tracer since they are present in all the galaxy nuclei. Both the measurements and models of stellar kinematics in galaxies have been improved dramatically in the last 30 years. Early stellar-dynamical $M_\bullet$ measurements were suspect because of the mass-anisotropy degeneracy (Binney & Mamon, 1982). With higher-order moments of the line-of-sight velocity distribution, it became possible to break this degeneracy for the nearest galaxies. Considering ground-based facilities, the sphere of influence can now be resolved with the advantage of using the integral-field spectroscopy with 8-m class telescopes provided with AO facilities (e.g. Nowak et al. 2008; Saglia et al. 2016). Nowadays, the three-integral dynamical models based on the orbit superposition method designed by Schwarzschild (1979, 1993) are mostly employed whereas the Jeans modeling

method was used more in the past (van der Marel, 1994). Schwarzschild models provide not only the $M_\bullet$ estimate, but also the information about the orbits within the galaxy nucleus (Saglia et al., 2016). Nevertheless this technique is quite demanding because small-scale high-resolution and large-scale lower-resolution integral-field spectroscopic data are required for successfully modeling the kinematics of the central and outer regions, respectively. In addition, both HST and ground-based images are needed to determine the inner and outer spatial distribution of stars beyond the spatial extent of the spectroscopic data, respectively.

Finally, since the gas dynamics was employed repeatedly in this work, it is described here with more details with respect to other techniques. Firstly, the $M_\bullet$ measurements available in the literature based on this method can be divided between those derived from spatially resolved kinematics and those based on unresolved kinematics. The main difference is that in the first case they are actual estimates, whereas in the second one they represent only upper limits.

These two methods both rely on gas kinematic measurements in the nuclear region. The spectral lines commonly employed are Hα and [NII] 6583 Å in the optical range, Brγ 2.16 μm, [FeII] 1.64 μm, [SiVI] 1.96 μm and molecular hydrogen H_2 2.12 μm line in the infrared domain. The gas from which the optical nebular emission lines arise is commonly found in the center of spirals and it is also detected in more than 50% of ellipticals and lenticulars (Ho et al., 1997). An advantage is constituted by the fact that it is less challenging to analyze the emission lines compared to the absorption lines so that the signal-to-noise requirements are more easily fulfilled.

For both spatially resolved and unresolved ionized-gas kinematic techniques, HST images are required to model both the luminosity density and ionized gas distribution of the nuclear region, whereas spectra (obtained with HST or AO ground-based facilities) are needed to extract the kinematics (e.g., Dalla Bontà et al., 2009). If narrow-band images are not available, the gas distribution can be retrieved by measuring the emission line flux from the spectra along the slit direction. In the case of spatially resolved ionized gas kinematics, two or more slits are required, to constrain the inclination of the gaseous disk. As commonly found in literature, usually one slit is placed along the major axis of the gas disk crossing the center, while other two slits are positioned parallel to the first one, but displaced in the two opposite perpendicular directions by a small amount (see Fig. 1.1). In the case of spatially unresolved ionized-gas kinematic technique, spectra obtained with only one slit crossing the nucleus are needed and the kinematics is extracted within an aperture centered on the galaxy nucleus.

The basic assumptions of the dynamical model are the same in both cases. The gas is assumed to be settled in a thin disk in rotation around the central SBH on circular orbits. The gravitational potential acting on the gas is due to both the stars and SBH. The stellar contribution to the potential is taken into account by deprojecting the stellar surface-brightness distribution and assuming a mass-to-light ratio for the stellar component. Then a model for the velocity field is computed that has to match the observed flux distribution, velocity, and velocity dispersion of the gas by taking into account the point spread function (PSF), the size of the spectroscopic aperture and the intrinsic spatial distribution of the gas emission. These models are cheap from a computational point of view and not much prone to degeneracy

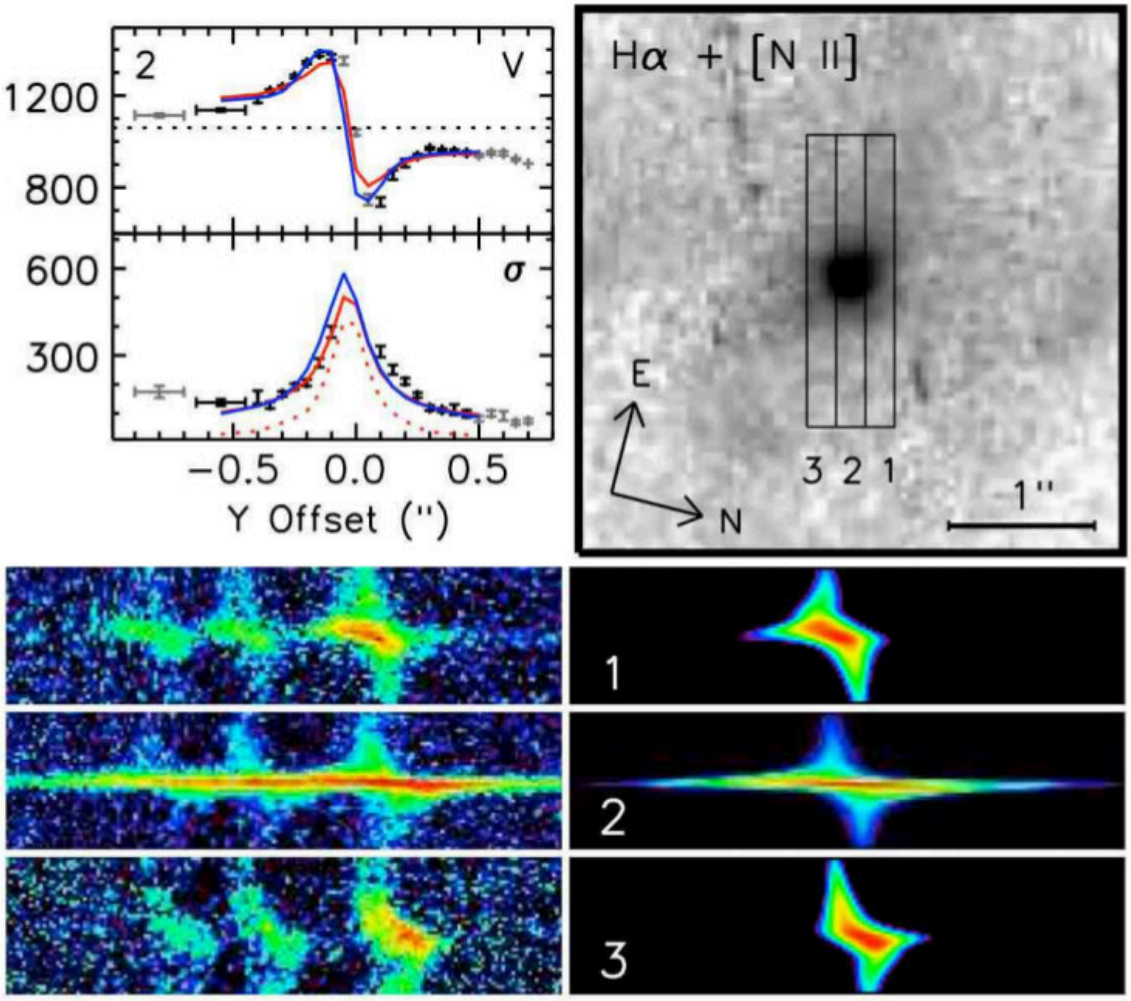

Figure 1.1: Analysis of the ionized-gas kinematics of NGC 4374 performed by Walsh et al. (2010) from HST observations of Bower et al. (1998). *Top left panel*: radial profile of mean velocity and velocity dispersion of the [NII]λ6583 line with overlaid the best SBH model with (blue line) and without (red solid curve) the asymmetric drift correction and the contribution from rotational line broadening (red dotted line). *Top right panel*: WFPC2 continuum-subtracted Hα+ [NII]$\lambda\lambda$6548, 6583 image from which the ionized disk is visible with the three superimposed slits. *Bottom left panel*: two-dimensional STIS spectra of the Hα+ [NII]$\lambda\lambda$6548, 6583 region where the continuum has been subtracted. *Bottom right panel*: synthetic spectra of [NII]λ6583 line. The spatial direction is along the vertical axis and the wavelength along the horizontal one. The three panels correspond to the three slits. The figure is from Kormendy & Ho (2013).

among parameters. A dust disk with nearly the same position and inclination of the gaseous one is frequently observed. The presence of dust obscures the surface brightness distribution and affects the estimation of the stellar mass and gas emission. Nevertheless, a regular morphology of the dust lanes is indicative of regular gas kinematics (Ho et al., 2002). In some cases the dust lanes allow us to constrain the gaseous disk orientation and inclination. This

can be useful when modeling the unresolved gas kinematics, through which it is impossible to obtain the inclination of the gas disk since only one slit crossing the nucleus and a central aperture are considered in the analysis. As a consequence, the $M_\bullet$ values are calculated for reference inclinations. Since randomly oriented disks have uniformly distributed $\cos i$, considering the two reference inclinations of 33° and 81° is equivalent to bracketing the 68% of randomly inclined disks (Sarzi et al. 2002; Beifiori et al. 2009). Furthermore, even though with this method no information is retrievable also for the position angle of the gaseous disk, this is not so relevant for the final result since the kinematics is measured in a nearly square aperture. Sarzi et al. (2002) tested the $M_\bullet$ results with respect to the kinematic behavior of the ionized gas by considering the extreme case of pure hydrostatic support. They obtained $M_\bullet$ values corresponding to those that would be found for a rotating disk model with inclinations between 45° and 49°. Thus the $M_\bullet$ value obtained from these different physical conditions is encompassed between the ones obtained at inclinations of 33° and 81°.

The most critical issue of both spatially resolved and unresolved kinematic techniques is the strong assumption that the gas rotates around the SBH in a thin and dynamically cold disk. In some cases this disk could be warped and not coplanar, as usually assumed in the models. In order to have an accurate $M_\bullet$ determination, the gas should be well-distributed within the sphere of influence and not influenced by nongravitational forces, like radiation pressure, magnetic fields, and shocks. In some cases, the contribution of turbulent pressure support was included in the dynamical model (Barth et al., 2001; Neumayer et al., 2007), but a suitable way to properly describe the gas behavior has still to be developed. The result is that the derived $M_\bullet$ could be overestimated by a large amount.

Measuring the $M_\bullet$ with different techniques could be useful in order to evaluate the reliability of each method. The values of $M_\bullet$ obtained from gas and stellar kinematics are consistent with each other for some galaxies (NGC 3031, gas: Devereux et al. 2003, stars: Bower et al. 2000; NGC 4258, gas: Pastorini et al. 2007, stars: Siopis et al. 2009; NGC 5128, gas: Neumayer et al. 2007, stars: Cappellari et al. 2009). In other cases the value obtained from the gas kinematics is unexpectedly lower than that from the stellar kinematics (M 87, gas: Macchetto et al. 1997, stars: Gebhardt et al. 2011; NGC 3998, gas: de Francesco et al. 2006, stars: Walsh et al. 2012). This is true also for IC 1459 (gas: Cappellari et al. 2002, stars: Cappellari et al. 2002), NGC 3379 (gas: Shapiro et al. 2006, stars: van den Bosch & de Zeeuw 2010), and NGC 4335 (gas: Verdoes Kleijn et al. 2002, stars: Verdoes Kleijn et al. 2002). Unfortunately so far there is not a sufficient overlap between $M_\bullet$ samples measured with different techniques so that an extended and unbiased comparison has not been performed yet.

1.3 Correlations between the mass of supermassive black holes and properties of their host galaxies

$M_\bullet$ is tightly related to the host galaxy properties, i.e. to those of the whole galaxy in the case of ellipticals and to those of the bulge in the case of lenticulars and spirals. These correlations represent the clear signature of past or still ongoing coevolution between SBHs

and galaxies, so their analysis is ultimately aimed at improving the current understanding of galaxy evolution. In this context another puzzling ingredient is represented by the possible presence of a nuclear star cluster (NSC) which, along with the SBH, form the class of central compact massive objects (CMOs). Unlike the scenario that was initially proposed by Ferrarese et al. (2006b), NSCs and SBHs can coexist in the galaxy nucleus and this was observed in a meaningful number of galaxies (e.g., Seth et al., 2008; Graham & Spitler, 2009). Scott & Graham (2013) claimed that they do not constitute a single family of CMOs, since the relations between their mass and central σ_* are characterized by different slopes. Recently, Graham (2016a) obtained a correlation between $M_\bullet$ and the mass of NSCs which could be useful to estimate the evolutionary growth of SBHs within NSCs.

Focusing now only on SBHs, over the past twenty years a multitude of scaling relations have been proposed. Some of them have been dismissed by considering different samples or simply by enlarging them (e.g., the one with the dark matter halo mass, see Kormendy & Ho 2013). On the other hand, the first correlations that have been observed and that are still confirmed are those with the stellar velocity dispersion σ_* (Ferrarese & Merritt 2000, Gebhardt et al. 2000), luminosity L_k (Kormendy & Richstone 1995; Marconi & Hunt 2003), stellar mass $M_\star$ (Magorrian et al. 1998; Häring & Rix 2004), and stellar light and mass deficit associated with the core ellipticals (Lauer et al., 2007; Rusli et al., 2013b; Thomas et al., 2016). The correlation with the Sérsic index n is still debated (Savorgnan, 2016; Shankar et al., 2017).

A distinction has to be made between classical and pseudobulges (see Fisher & Drory 2016). The first tightest correlations (e.g., those with σ_* and L_k) were obtained for classical bulges, which resemble small elliptical galaxies. At first glance, by adding few pseudobulges to the samples of ellipticals and classical bulges, it seemed that their $M_\bullet$ followed the same scaling relations (Gültekin et al., 2009). On the contrary, Kormendy et al. (2011) and Kormendy & Ho (2013) concluded that $M_\bullet$ does not correlate with pseudobulge properties of disk galaxies. This issue is still under discussion and in the majority of cases the problem still resides in how different authors distinguish between bulges and pseudobulges (Graham, 2016b).

The $M_\bullet - \sigma_\star$ relation is described here with more details, since it is employed and investigated in the rest of the thesis. Among all the relations listed above, it is the most widely studied and analyzed in literature and interestingly it is still the tightest one also by considering the currently most comprehensive samples. It was firstly presented independently by Gebhardt et al. (2000) and Ferrarese & Merritt (2000) who considered the stellar velocity dispersions $\sigma_{\rm e}$ and $\sigma_{\rm c}$ within the effective radius and within a radius equal to 1/8 of the effective radius, respectively. They pointed out that the scatter of this relation was only due to measurement errors. Gültekin et al. (2009), who derived again this relation for a larger sample of 49 $M_\bullet$ estimates and 19 $M_\bullet$ upper limits, claimed that there is not another parameter that could provide a tighter correlation with $M_\bullet$. They obtained the smallest scatter when fitting the $M_\bullet - \sigma_{\rm e}$ relation by considering only ellipticals. Moreover, they pointed out that selecting objects for which the sphere of influence was resolved could introduce a bias, which results in an overestimation of the intercept and slope of the relation and a wrong estimation of the intrinsic scatter. McConnell & Ma (2013) considered a larger sample of 72 objects and found

a significantly steeper $M_\bullet - \sigma_e$ power law with respect to the one of Gültekin et al. (2009).

Considering more comprehensive samples produced a variety of slopes and intercepts. According to Graham (2016b), this was mainly due to the fact that authors employed different methods to fit the $M_\bullet - \sigma_e$ relation, even if the fact that each author considered a different sample could also have played a role. On the other hand, including very different galaxy in the same sample yielded to a larger scatter in the $M_\bullet - \sigma_e$ relation. As a consequence, the authors tried to split galaxies in subsamples in order to obtain a $M_\bullet - \sigma_e$ relation with a smaller scatter for each galaxies type. McConnell & Ma (2013) divided the samples in early and late-type galaxies and obtained similar slopes (5.20 ± 0.36 versus 5.06 ± 1.16, respectively) but significantly different intercepts (8.39 ± 0.06 versus 8.07 ± 0.21, respectively). They concluded that it is not safe to employ in theoretical evolutionary models the $M_\bullet - \sigma_e$ relation derived from a sample which includes both early and late-type galaxies and suggested to consider them separately. In addition, they further divided the early-types in core and power-law galaxies and found that the intercept for the core galaxies is larger than that for the power-law ones. This indicates that the core galaxies have larger $M_\bullet$ than power-law ones. Saglia et al. (2016) carried out a complete work in this sense by deriving the $M_\bullet - \sigma_e$ relation for their entire sample of 96 galaxies and for numerous subsamples by distinguishing also between core and power-law ellipticals, classical and pseudobulges, barred and unbarred galaxies. Overall, they found that the $M_\bullet - \sigma_e$ relations are those with the lowest measured and intrinsic scatter and their slopes are in agreement within errors with literature. By regarding the main results obtained for the above mentioned subsamples, the power-law early-type galaxies and classical bulges follow a similar $M_\bullet - \sigma_e$ relation. Pseudobulges harbor smaller SBHs with respect to all the other galaxies, at a given σ_e. Moreover, the smallest scatter for the $M_\bullet - \sigma_e$ was obtained by using the core ellipticals, which were also characterized by larger $M_\bullet$ with respect to classical bulges and noncore galaxies, at a given σ_e.

Currently, the more debated issues about the $M_\bullet - \sigma_e$ relation regard the high and low-$M_\bullet$ ends. Concerning the high-σ_e end, it is noteworthy the so called "saturation effect". Basically, at $\sigma_e \gtrsim 270$ km s^{-1}, the core ellipticals and/or brightest cluster galaxies (BCGs) harbor SBH with $M_\bullet$ that are almost independent of σ_e, whereas, by considering the $M_\bullet - L_k$ relation, they remain dependent on the luminosity of the spheroidal component even at high luminosities (Kormendy & Ho, 2013). An explanation for this was already provided by Lauer et al. (2007), who suggested that the saturation of the Faber-Jackson relation for core galaxies was the reason for the $M_\bullet - \sigma_e$ saturation. Recently, Krajnović et al. (2018a) observed that the variations of $M_\bullet$ in the plane defined by galaxy stellar mass and the effective radius are closely related to those of the σ_e by considering systems with stellar mass $\lesssim 2 \times 10^{11}$ M$_\odot$. On the other hand, the $M_\bullet$ is progressively less correlated with the σ_e by considering more massive objects. These latter galaxies probably grew with a sequence of dissipationless mergers, whereas the former grew through star formation. Mezcua et al. (2018) further inspected the high-$M_\bullet$ end with a sample of 72 local ($z \leq 0.3$) BCGs and found that their $M_\bullet$ were higher than predicted by the scaling relations, as suggested by Dalla Bontà et al. (2009). A unified evolutionary scenario which could explain this behavior is still not clear.

Concerning the low-$M_\bullet$ end, which is mostly populated by pseudobulges, small bulges or

dwarf galaxies, the situation is quite puzzling. From an observational point of view, it is quite challenging to properly measure low value of both $M_\bullet$ and σ_e. Xiao et al. (2011) collected a sample of 93 galaxies which includes 76 Seyfert 1 galaxies having $M_\bullet \lesssim 10^6$ $M_\odot$ taken from the catalogue of Greene & Ho (2007), who estimated the $M_\bullet$ using the line width-luminosity mass scaling relation established for broad-line AGNs. They derived an $M_\bullet - \sigma_e$ relation that almost follows the extrapolation at low $M_\bullet$ of the one of quiescent galaxies. Moreover, they found no differences between the slope for barred and unbarred galaxies. Woo et al. (2015) used a sample of 93 narrow-line Seyfert 1 galaxies to study the low-end of the $M_\bullet - \sigma_e$ relation by measuring $M_\bullet$ from the size-luminosity relation. They found that these $M_\bullet$ follow the $M_\bullet - \sigma_e$ relation derived with quiescent galaxies and reverberation-mapped AGNs. Martín-Navarro & Mezcua (2018) analyzed a sample of 127 low-mass galaxies with $M_\bullet$ from Xiao et al. (2011) and Woo et al. (2015) by restricting to galaxies with $45 < \sigma_e < 100$ km s^{-1}and $10^5 < M_\bullet < 10^7$ $M_\odot$. They pointed out that the $M_\bullet - \sigma_e$ relation flattens for low-mass galaxies so that their $M_\bullet$ tend asymptotically to the value of 10^5 $M_\odot$, as already observed by Mezcua (2017). These SBHs could be relics of high-z galaxy seeds for which the SN feedback does not allow to accrete gas and this could explain why these hosts are so weakly coupled to the central SBHs.

Even if the $M_\bullet - \sigma_e$ relation was demonstrated to be a very tight scaling relation, several authors investigated if a combination of more than two parameters leads to a reduction of the scatter. Marconi & Hunt (2003) already verified that $M_\bullet$ is separately correlated both with σ_e and the effective radius r_e and by combining them ($\propto r_e\ {\sigma_e}^2$) they found a tight correlation. Hopkins et al. (2007) proposed the idea of the existence of a SBH Fundamental Plane (BHFP), which involves $M_\bullet$, σ_e and the effective surface brightness, similar to the one of elliptical galaxies (FP). This further suggested a coevolution between the SBH and the host galaxy. Beifiori et al. (2012), with a considerably larger sample of $M_\bullet$, found that there was only a slight improvement in the scatter compared to $M_\bullet - \sigma_e$. By collecting a heterogeneous sample of 230 $M_\bullet$, van den Bosch (2016) found the SBH-size-luminosity relation (quite expected from the combination of the $M_\bullet - \sigma_e$ relation and the FP) to have the same scatter as $M_\bullet - \sigma_e$ and to be aligned with the galaxy FP. Such a relation can be used to derive σ_e in faint galaxies, in objects with σ_e below the instrumental resolution, and in bulgeless galaxies. Since the sample contained all morphological types, it was verified that these relations are valid for all existing galaxies. In the case of bulgeless galaxies, only the $M_\bullet - \sigma_e$ is suitable since they lack the bulge and its properties can not be used as $M_\bullet$ proxy, further underlining the universality of this relation.

All these scaling relations should be used with caution and not assumed as reliable a priori. Indeed, Shankar et al. (2016) verified that the scaling relations currently provided in literature are biased, as previously claimed by Bernardi et al. (2007). The SBHs for which $M_\bullet$ estimates are present in literature are hosted by galaxies characterized by large σ_e with respect to the bulk of the galaxy population at a given stellar mass. This does not depend on morphological type or on the aperture considered for the σ_e measurement. But, it is mainly due to the fact that the sphere of influence has to be resolved in order to obtain reliable $M_\bullet$ estimates. Another aspect is that it is more difficult to detect SBHs harbored in pseudobulges

with respect to those in classical bulges or in ellipticals. Thus, it is not possible to know if the measured $M_\bullet$ distribution in scaling relations is the actual one or only an upper envelope, as already found by Barth et al. (2005). The scaling relation which involves σ_e suffers from a smaller bias with respect to the one with the stellar mass for which the apparent tightness is actually a selection effect. From these findings, it follows that the relations have to be corrected for these biases in order to properly identify some outliers or to better characterize the coevolution models. Anyway, the stellar velocity dispersion remains the most fundamental parameter as a proxy for the SBH mass.

1.4 Aim and outline of the thesis

This thesis is focused on the $M_\bullet$ determination. On one hand, larger samples are required to better constrain the scaling relations, in particular in the low and high-$M_\bullet$ ranges. On the other hand, the outliers from these relations are equally interesting for the purpose of understanding the formation and evolution of their host galaxies and also track down some limits or biases in scaling relations obtained so far.

Firstly, the sample of $M_\bullet$ constraints was increased by measuring 7 $M_\bullet$ stringent limits exploiting the unresolved ionized-gas kinematics for a sample of mostly late type galaxies which are always under-represented even in the larger samples. Secondly, an additional 100 $M_\bullet$ stringent limits were obtained including in the dynamical model the stellar mass contribution, which was disregarded in previous works, in order to study the impact of the stellar contribution on the final $M_\bullet$ value. Finally, a catalogue of nuclear σ_* was obtained with HST spectra on sub-arcsecond apertures. It was shown how by combining these measurements with HST photometry and spectroscopic integral-field SAURON data can lead to $M_\bullet$ constraints.

Chapter 2: We present new $M_\bullet$ stringent limits on for a sample of 7 nearby galaxies. Our $M_\bullet$ estimates are based on the dynamical modeling of the central width of the nebular emission lines measured over subarcsecond apertures with the HST. The central stellar velocity dispersion of each galaxy was obtained from new long-slit spectra from ground-based observations, the bulge effective radius was derived either from a two-dimensional photometric decomposition of the i-band images of the SDSS or from literature, and the stellar velocity dispersion σ_c within 1/8 the effective radius was calculated. The derived $M_\bullet$ stringent limits run parallel to and above the $M_\bullet - \sigma_c$ relation with no systematic trend depending on the galaxy distance or morphology. This gives further support to previous findings suggesting that the nuclear gravitational potential is remarkably well traced by the width of the nebular lines when the gas is centrally peaked. With our investigation, the number of galaxies with $M_\bullet$ stringent limits obtained from nebular-line width increased to 114 and can be used for studying the scaling relations between $M_\bullet$ and the properties of their host galaxies.

Chapter 3: Based on the dynamical modeling of the central width of nebular emission lines measured over subarcsecond apertures with HST, we presented stringent limits on $M_\bullet$ for a sample of 100 nearby galaxies ($D < 103$ Mpc) spanning a wide range of Hubble types (E-Sc) and values of σ_e (54-404 km s^{-1}). In constraining $M_\bullet$, we took into account the stellar mass contribution to the gravitational potential in the galaxy nucleus. To this aim,

we modeled the surface brightness distribution measured from HST images and adopted the mass-to-light ratio of an old and metal-rich stellar population. The shape of the profile of the emission lines and of the radial profile of emission-line flux were analysed to verify that nongravitational forces have a minor impact on the $M_\bullet$ estimate. We found that on average the stellar mass contribution is larger for galaxies with $\sigma_{\rm e}<$ 90 km s^{-1} mostly due to the presence of a nuclear stellar cluster/disk. Moreover, the stellar mass contribution is negligible in ellipticals but it is not in lenticulars and spirals. It depends on the aperture size rather than on the galaxy distance. Our $M_\bullet$ stringent limits run parallel to the $M_\bullet - \sigma_{\rm e}$ relation and exceed the expected $M_\bullet$ values by a median factor of 1.7. This is a striking result if we consider that our dynamical analysis does not rely on spatially-resolved distribution and kinematics of the gaseous tracer and it makes $M_\bullet$ stringent limits particularly suitable for the analysis of the scaling relations between $M_\bullet$ and the properties of their host galaxies.

Chapter 4: We present new measurements for the nuclear σ_* within sub-arcsecond apertures for a sample of 28 nearby galaxies. Our data consisted of Space Telescope Imaging Spectrograph (STIS) long-slit spectra obtained with the G750M grating centered on the Hα spectral range. We fitted the spectra using an extensive library of single stellar population models and Gaussian emission lines, while constraining in most cases the stellar-population content from an initial fit to G430L STIS spectra equally present in the HST archive. We illustrated how these sub-arcsecond σ_* measurements can be useful for constraining the mass of SBHs by concentrating specifically on the cases of the lenticular galaxies NGC 4435 and NGC 4459. These are characterized by similar ground-based $\sigma_{\rm e}$ values but remarkably different $M_\bullet$ as obtained from modeling their central ionized-gas kinematics. In particular NGC 4435 appears to host a significantly undermassive SBH compared to what expected from the well-known $M_\bullet - \sigma_{\rm e}$ relation. For both galaxies, we built Jeans axisymmetric dynamical models to match the ground-based stellar kinematics obtained with SAURON integral-field spectrograph, including a SBH with $M_\bullet$ values as predicted by the $M_\bullet - \sigma_{\rm e}$ relation and using high-resolution HST images taken with the Advanced Camera for Surveys as a base for constructing the stellar-mass model. By mimicking the HST observing conditions we then used such reference models to make a prediction for the nuclear σ_* value. Whereas this was found to agree with our nuclear σ_* measurement for NGC 4459, for NGC 4435 the observed σ_* was remarkably smaller than predicted, which further suggests that this galaxy could host an undermassive SBH.

Chapter 5: In this chapter we report some conclusions and future perspectives.

Chapter 2

Stringent limits on the masses of the supermassive black holes in seven nearby galaxies

Abstract. We present new stringent limits on the mass $M_\bullet$ of the central supermassive black hole for a sample of 7 nearby galaxies. Our $M_\bullet$ estimates are based on dynamical modeling of the central width of the nebular emission lines measured over subarcsecond apertures with the Hubble Space Telescope. The central stellar velocity dispersion of each galaxy is obtained from new long-slit spectra from ground-based observations, the bulge effective radius is derived either from a two-dimensional photometric decomposition of the i-band images of the Sloan Digital Sky Survey or from literature, and the stellar velocity dispersion σ_c within 1/8 the effective radius is calculated. The derived $M_\bullet$ stringent limits run parallel to and above the $M_\bullet - \sigma_c$ relation with no systematic trend depending on the galaxy distance or morphology. This gives further support to previous findings suggesting that the nuclear gravitational potential is remarkably well traced by the width of the nebular lines when the gas is centrally peaked. With our investigation, the number of galaxies with $M_\bullet$ stringent limits obtained from nebular-line width increases to 114 and can be used for studying the scaling relations between $M_\bullet$ and properties of their host galaxies.

2.1 Introduction

Over nearly three decades of measurements of the mass $M_\bullet$ of central supermassive black holes (SBHs) have led to the conclusion that such objects should be nearly always present at the center of elliptical galaxies and bulges of disk galaxies (see Kormendy & Ho, 2013, for a review). Furthermore, the finding that $M_\bullet$ correlates with several properties of their host galaxies, and in particular with the velocity dispersion σ_* of their spheroidal component (Gebhardt et al. 2000; Ferrarese & Merritt 2000), suggests that somehow SBHs and spheroids grew together (see Saglia et al. 2016). These mutual relationships between the black holes

Table 2.1: Properties of the galaxy sample.

Galaxy	Mor. T.	Bar	Sp. Cl.	D [Mpc]	M_B^0 [mag]	σ_c [km s^{-1}]	σ_e [km s^{-1}]	$M_\bullet$ [33°] [M$_\odot$]	$M_\bullet$ [81°] [M$_\odot$]
(1)	(2)	(3)	(4)	(5)	(6)	(7)	(8)	(9)	(10)
NGC 2654	SBab: sp	yes	-	19.4	−19.77	150 ± 3	162 ± 3	1.9e7	4.2e6
NGC 3003	Sbc?	no	H	23.2	−20.56	22 ± 8	23 ± 8	4.3e7	3.9e7
NGC 3049	SB(rs)ab	yes	H	23.9	−19.12	84 ± 9	86 ± 10	4.3e6	1.2e6
NGC 3259	SAB(rs)bc:	no	S1	24.0	−19.40	76 ± 7	63 ± 6	3.6e6	1.0e6
NGC 4343	SA(rs)b:	no	-	18.1	−18.92	110 ± 4	154 ± 5	6.4e7	5.1e7
NGC 4420	SB(r)bc:	no	H-L	27.1	−19.88	62 ± 7	68 ± 8	1.2e7	4.6e6
NGC 5141	S0	-	-	72.4	−20.59	248 ± 7	222 ± 6	6.3e8	2.0e8
NGC 5635	S pec	no	-	60.1	−20.96	238 ± 6	216 ± 5	1.1e9	2.9e8
NGC 5713	SAB(rs)bc pec	yes	H	28.3	−20.68	71 ± 5	78 ± 6	3.4e7	1.4e7

Notes. Col.(1): galaxy name. Col.(2): morphological type from de Vaucouleurs et al. (1991, RC3). Col.(3): presence of the bar according to the photometric decomposition. We inferred the presence of a bar in the edge-on galaxy NGC 2654 from its boxy/peanut bulge. NGC 5141 turned out to be an elliptical galaxy. Col.(4): nuclear spectral class from NASA/IPAC Extragalactic Database (NED), where H = HII nucleus, L = LINER, S1 = Seyfert of type 1. The spectral class for NGC 3003 is from Ho et al. (1997). Col.(5): distance. The distances were obtained as $D = V_{3K}/H_0$, where V_{3K} is the weighted mean recessional velocity corrected to the reference frame of the microwave background radiation given in RC3 and adopting $H_0 = 75$ km s^{-1} Mpc^{-1}. Col.(6): absolute total corrected B magnitude obtained from B_T^0 (RC3) and adopted distance. Col.(7): stellar velocity dispersion within $r_e/8$ from this work. Col.(8): stellar effective velocity dispersion within circularized r_e from the aperture correction from Falcón-Barroso et al. (2017). Col.(9): $M_\bullet$ stringent limit assuming $i = 33°$ for the gas disk from this work. Col.(10): $M_\bullet$ stringent limit assuming $i = 81°$ for the gas disk from this work.

and their host galaxies could come from feedback mechanisms (see Silk & Rees 1998; Fabian 1999). Large $M_\bullet$ samples across different morphological types are needed to fully understand the underlying process behind the $M_\bullet - \sigma_\star$ relation, as clues may be present not only in the slope of this relation but also in its scatter, the behavior of outliers, and secondary trends related, for instance, to galaxy morphology (Beifiori et al. 2012; McConnell & Ma 2013; Shankar et al. 2016).

For this purpose Beifiori et al. (2009, 2012) used archival Hubble Space Telescope (HST) spectroscopic data obtained with the Space Telescope Imaging Spectrograph (STIS) to estimate stringent limits on $M_\bullet$ for 107 galaxies of various Hubble types, following the approach of Sarzi et al. (2002) to model the velocity dispersion of ionized-gas emission observed at subarcsecond scales. The sample of Beifiori et al. (2009) included an additional 21 objects with STIS data, but those were excluded since they lacked a ground-based σ_* measurement and thus could not be placed on the $M_\bullet - \sigma_\star$ relation. In this work, we aim at increasing the sample of galaxies with $M_\bullet$ stringent limits, by selecting 9 northern galaxies (Dec (J2000.0) $> -10°$) with detected emission lines in STIS spectra from the objects excluded by Beifiori et al. (2009) and observing them with the Asiago Astrophysical Observatory in order to derive their central

σ_*.

The chapter is organized as follows. We derive the bulge effective radius r_e from the analysis of broad-band imaging in Sect. 2.2. We measure the central stellar velocity dispersion from ground-based spectroscopy and apply the aperture correction to $r_e/8$ in Sect. 2.3. We obtain the distribution and central velocity dispersion of the ionized gas from HST spectroscopy in Sect. 2.4. We estimate the $M_\bullet$ stringent limit from gas dynamics in Sect. 2.5. Finally, we discuss our results in the framework of the $M_\bullet - \sigma_\star$ relation in Sect. 2.6. In this chapter we adopt $H_0 = 75$ km s^{-1} Mpc^{-1}, $\Omega_M = 0.3$, and $\Omega_\Lambda = 0.7$ as cosmological parameters.

2.2 Surface brightness distribution

2.2.1 Sloan Digital Sky Survey imaging

We retrieved the flux-calibrated i-band images of the sample galaxies from Data Release 12 of the Sloan Digital Sky Survey (SDSS-DR12, Alam et al., 2015).

We measured the sky level to be subtracted from the image of each sample galaxy, as done by Morelli et al. (2016). We masked the stars, galaxies, and spurious sources in the galaxy neighborhoods and measured its surface brightness radial profile with the `ellipse` task in IRAF[1]. First, we fitted the galaxy isophotes with ellipses having the center, ellipticity, and position angle free to vary. Then, we repeated the isophotal fit fixing the center we previously obtained for the inner ellipses and the ellipticity and position angle of the outer ones. We calculated the sky level by averaging the surface brightness measured at large radii, where there is no light contribution from the galaxy. We used the IRAF task `imexamine` to measure the standard deviation of the background in the sky-subtracted images and to fit the stars of the field of view with a circular Moffat profile (Moffat, 1969), which we adopted to model the point spread function (PSF). Finally, we trimmed the sky-subtracted images to reduce the computing time required to perform a reliable photometric decomposition and we ran `ellipse` on the trimmed images to derive the radial profiles of surface brightness, ellipticity, and position angle. They were used as an input to get the initial guesses of the galaxy structural parameters for the two-dimensional photometric decomposition.

2.2.2 Photometric decomposition

To measure the effective radius of the bulge, we performed two-dimensional photometric decomposition of the SDSS images of the sample galaxies by using the Galaxy Surface Photometry 2-Dimensional Decomposition IDL[2] algorithm (GASP2D, Méndez-Abreu et al., 2008, 2014).

GASP2D performs a two-dimensional parametric photometric decomposition assuming that the observed surface brightness of the galaxy in each image pixel is expressed as the sum

[1]Image Reduction and Analysis Facility is distributed by the National Optical Astronomy Observatory (NOAO), which is operated by the AURA, Inc., under cooperative agreement with the National Science Foundation.

[2]Interactive Data Language is distributed by Harris Geospatial Solutions.

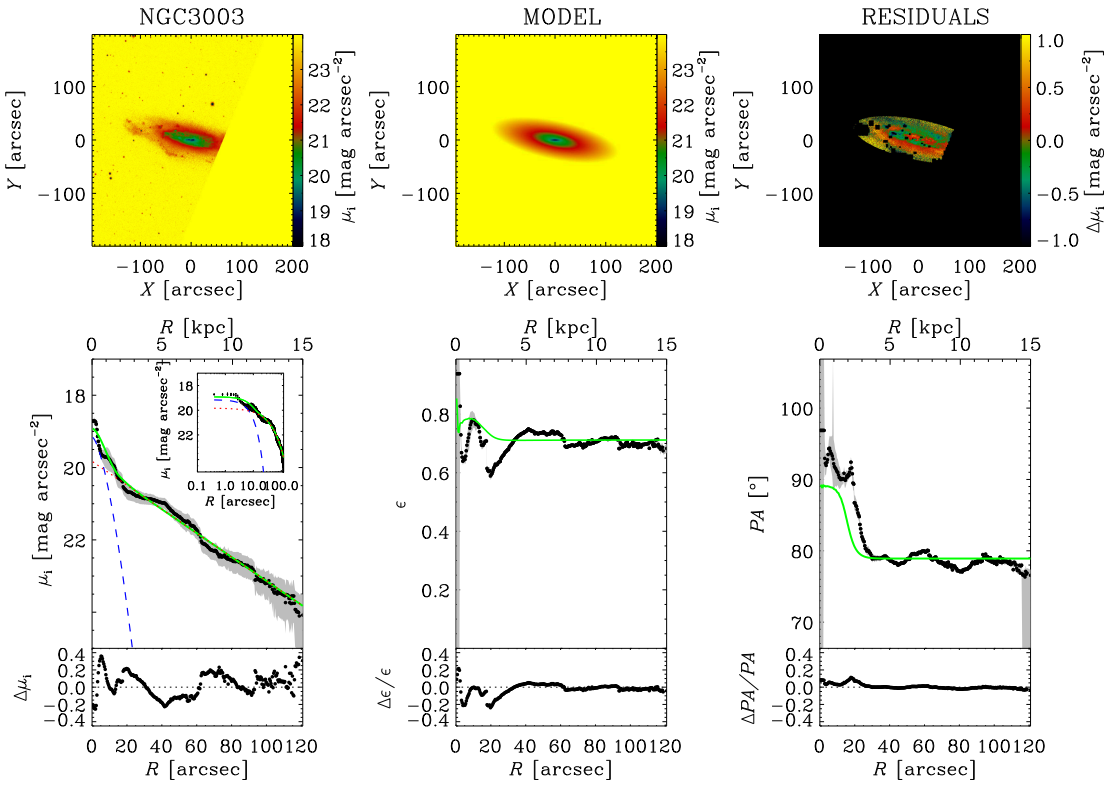

Figure 2.1: Two-dimensional photometric decomposition of the i-band SDSS image of NGC 3003. The images in the upper panels are oriented with the North up and the East left. *Top left panel*: map of the observed surface-brightness distribution. *Top middle panel*: map of the modeled surface-brightness distribution. *Top right panel*: map of the residuals obtained by subtracting the modeled from the observed surface-brightness distribution. The black areas are not considered in the fit. *Bottom left panel*: ellipse-averaged radial profile of the surface brightness extracted from the observed (black dots with gray error bars) and modeled image (green solid line) . The intrinsic profiles of the bulge (blue dashed line) and disk (red dotted line) are shown in linear and logarithmic radial scale (*upper inset*). *Bottom middle panel*: ellipse-averaged radial profile of the ellipticity extracted from the observed (black dots with gray error bars) and modeled image (green solid line). *Bottom right panel*: ellipse-averaged radial profile of the position angle extracted from the observed (black dots with gray error bars) and modeled image (green solid line). The comparison between the ellipse-averaged profiles of the observed and model images shows the quality of the decomposition.

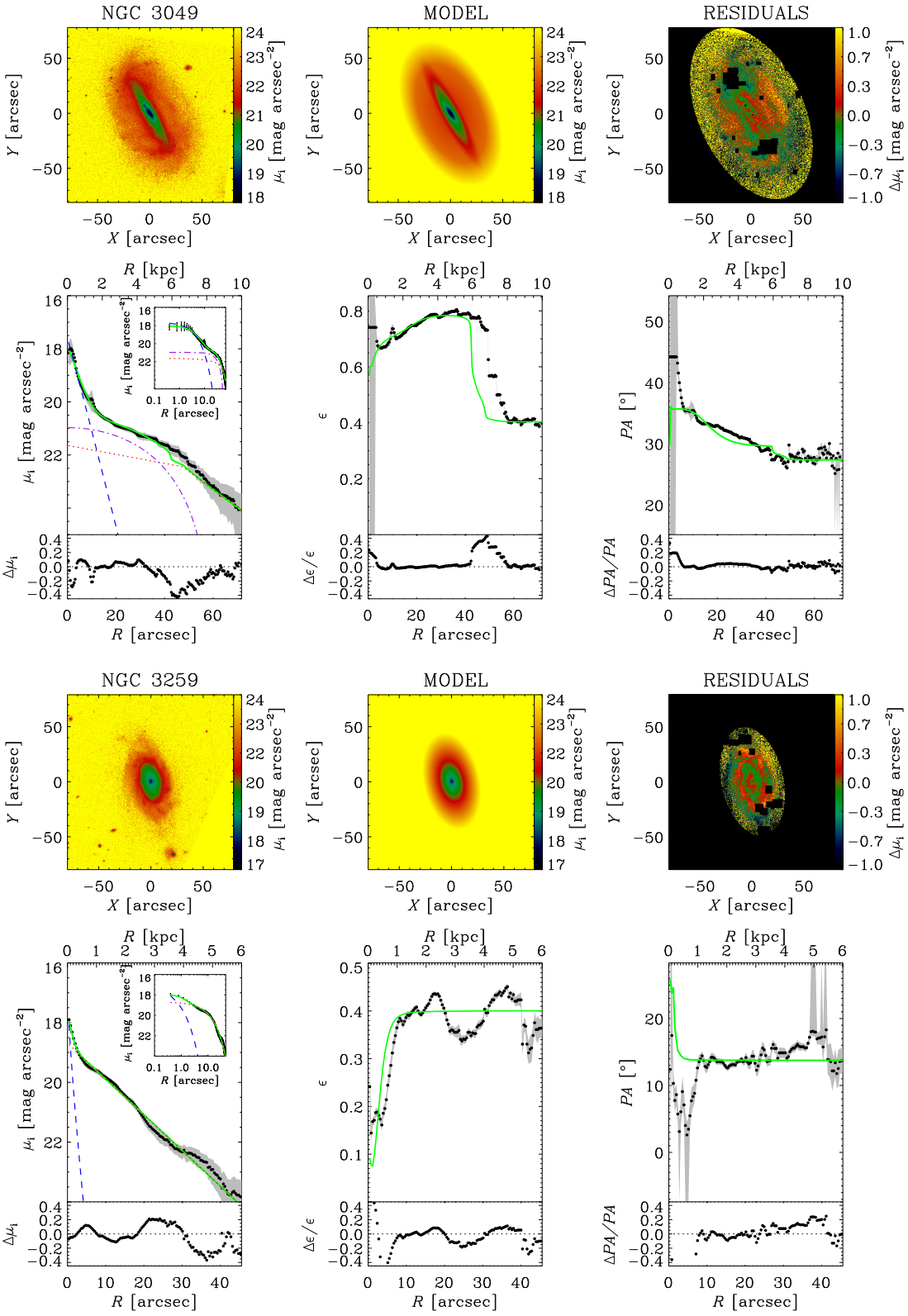

Figure 2.1: Continued. The same but for NGC 3049 and NGC 3259.

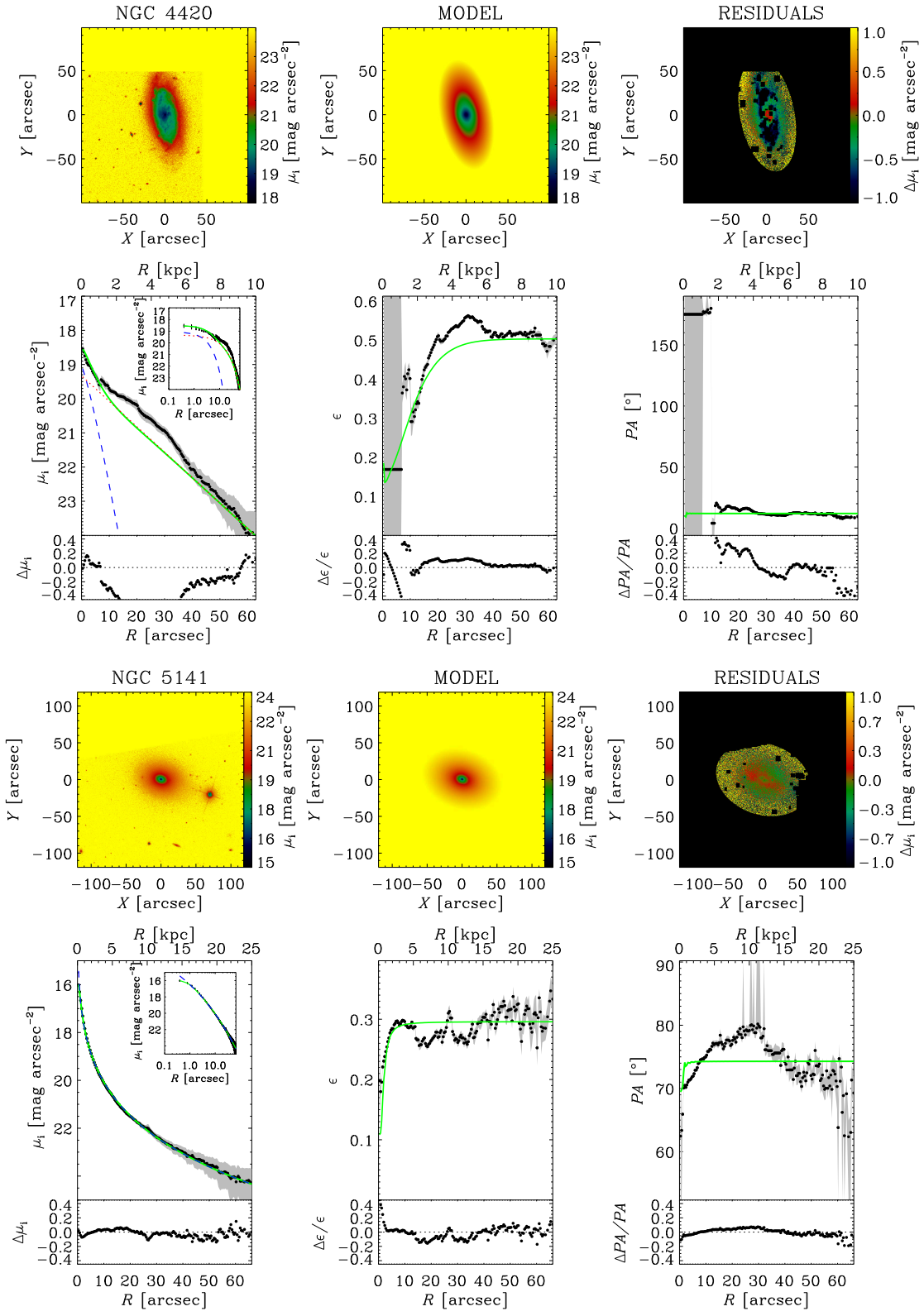

Figure 2.1: Continued. The same but for NGC 4420 and NGC 5141.

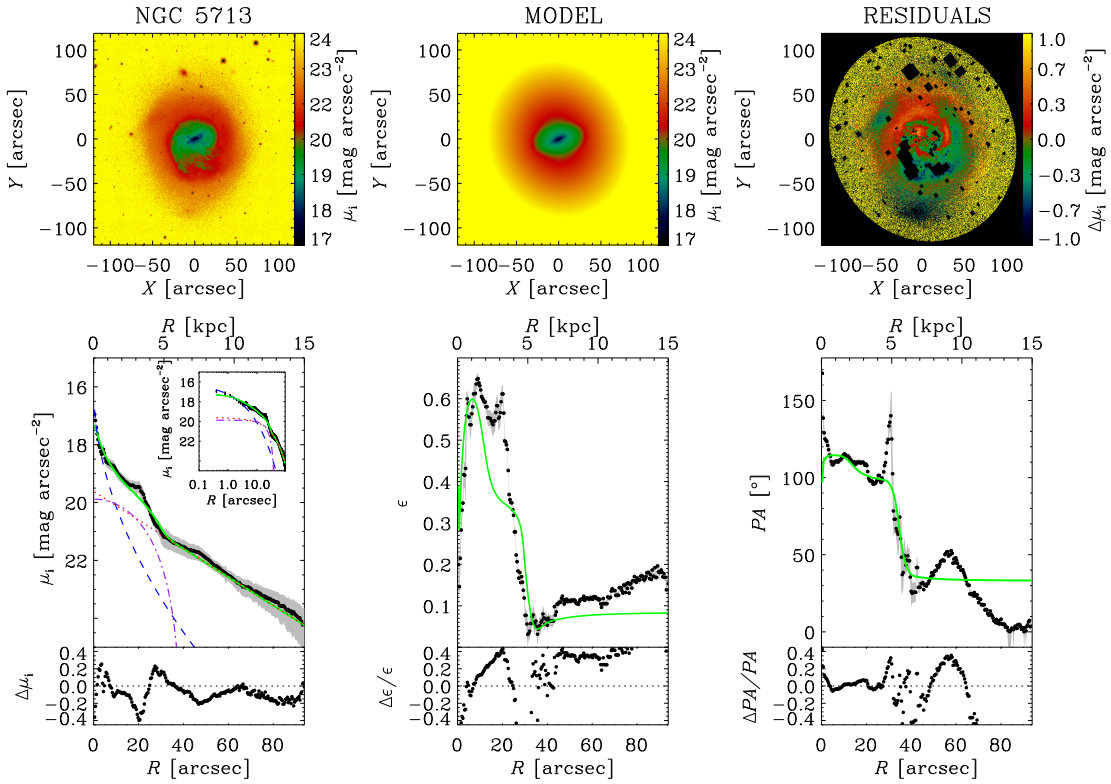

Figure 2.1: Continued. The same but for NGC 5713.

of analytical functions describing the light contribution of the structural components. We modeled (1) the surface brightness of the bulge with a Sérsic law (Sérsic, 1968)

$$I_{\rm bulge}(r) = I_{\rm e} 10^{-b_n[(r/r_{\rm e})^{1/n}-1]}, \tag{2.1}$$

where $r_{\rm e}$ is the effective radius, $I_{\rm e}$ is the surface brightness at $r_{\rm e}$, n is the shape parameter of the surface brightness profile, and $b_n = 0.868n - 0.142$ (Caon et al., 1993) is a normalization coefficient; (2) the surface brightness of the disk either with a single exponential law (Freeman, 1970)

$$I_{\rm disk}(r) = I_0 e^{-r/h}, \tag{2.2}$$

where I_0 is the central surface brightness and h is the scale length, or with a broken exponential law (van der Kruit, 1979)

$$I_{\rm disk}(r) = I_0 e^{-r_{\rm break}(h_{\rm out}-h)/(h_{\rm out}h)} e^{-r/h}, \tag{2.3}$$

where I_0 is the central surface brightness, $r_{\rm break}$ is the break radius at which the slope change occurs, h and $h_{\rm out}$ are the scale lengths of the inner and outer exponential profiles, respectively; (3) the surface brightness of the bar with a Ferrers law (Ferrers 1877; Aguerri & González-

García 2009)

$$I_{\rm bar}(r) = \begin{cases} I_{0,\rm bar}\left[1-\left(r/a_{\rm bar}\right)^2\right]^{2.5} & \text{if } r \le a_{\rm bar} \\ 0 & \text{if } r > a_{\rm bar}, \end{cases} \tag{2.4}$$

where $I_{0,\rm bar}$ is the central surface brightness and $a_{\rm bar}$ is the bar length. We assumed the isophotes of the bulge, disk, and bar to be elliptical, centered onto the galaxy center, and with constant position angle $PA_{\rm bulge}$, $PA_{\rm disk}$, and $PA_{\rm bar}$ and constant axial ratio $q_{\rm bulge}$, $q_{\rm disk}$, and $q_{\rm bar}$, respectively. We did not consider other components, such as rings, lenses, ovals, or spiral arms.

GASP2D returns the best-fitting values of the structural parameters of the bulge ($I_{\rm e}$, $r_{\rm e}$, n, $PA_{\rm bulge}$, $q_{\rm bulge}$), disk (I_0, h, $h_{\rm out}$, $r_{\rm b}$, $PA_{\rm disk}$, $q_{\rm disk}$), and bar ($I_{0,\rm bar}$, $a_{\rm bar}$, $PA_{\rm bar}$, $q_{\rm bar}$) with a χ^2 minimization by weighting the surface brightness of the image pixels according to the variance of the total observed photon counts due to the contribution of both galaxy and sky. It accounts as well for photon noise, CCD gain and read-out noise, and image PSF. We derived the errors on the structural parameters by analyzing a sample of mock galaxies generated with Monte Carlo simulations, as done by Costantin et al. (2017).

We successfully performed the photometric decomposition of all the sample galaxies, except for NGC 2654, NGC 4343, and NGC 5635.

The surface brightness distribution of NGC 3003 does not show any peculiar features and we fitted it with a Sérsic bulge and an exponential disk. For the barred galaxy NGC 3049, we adopted the double-exponential disk to fit the slope change measured in the surface brightness distribution at about 50 arcsec. We fitted NGC 3259 with a Sérsic bulge and an exponential disk, although it is classified as a weakly barred galaxy. Indeed, an accurate inspection of the image shows that what it looks like a bar is actually an artifact resulting from the tightly wound spiral arms. We did not include a bar component in fitting NGC 4420, despite its barred classification. The light excess observed between about 8 arcsec and 40 arcsec is due to the tightly wound spiral pattern rather to a bar, as it resulted from a careful inspection of the image. A full masking of the spiral arms was not possible, therefore we resorted to extrapolating inward the slope of the disk fitted in the outer regions. NGC 5141 is classified as a lenticular galaxy, but we successfully fitted its surface brightness with a single Sérsic component. The best-fitting model was chosen by applying the Bayesian information criterion (Schwarz, 1978) as done in Méndez-Abreu et al. (2017, 2018) to discriminate between ellipticals and lenticulars. Therefore, the best-fitting value of $r_{\rm e}$ refers to the entire galaxy. The prominent spiral arms of NGC 5713 produce the abrupt changes in surface brightness, ellipticity, and position angles measured at about 30 arcsec. We included the bar component in the fit in order to not overestimate the bulge contribution. We show in Fig. 2.1 the photometric decompositions and report the results for the sample galaxies we analyzed in Table 2.2.

The GASP2D photometric decomposition of the i-band SDSS image of NGC 5635 was performed by Méndez-Abreu et al. (2017) and we took for the bulge their best-fitting value of $r_{\rm e} = 8.0 \pm 0.9$ arcsec.

NGC 2654 and NGC 4343 are two nearly edge-on galaxies. This prevented us from

Table 2.2: Structural parameters of the sample galaxies from the photometric decomposition of the i-band SDSS images.

Parameter	NGC 3003	NGC 3049	NGC 3259	NGC 4420	NGC 5141	NGC 5713
(1)	(2)	(3)	(4)	(5)	(6)	(7)
$\mu_{\rm e}$ [mag arcsec^{-2}]	20.2 ± 0.3	19.4 ± 0.8	19.4 ± 0.6	20.5 ± 0.1	21.25 ± 0.07	19.8 ± 0.4
$r_{\rm e}$ [arcsec]	7.6 ± 0.1	5.2 ± 0.1	1.06 ± 0.02	4.85 ± 0.06	18.0 ± 0.2	8.7 ± 0.2
n	0.646 ± 0.007	0.97 ± 0.02	1.28 ± 0.01	0.841 ± 0.005	5.58 ± 0.03	1.93 ± 0.02
$q_{\rm bulge}$	0.154 ± 0.003	0.270 ± 0.006	1.000 ± 0.003	1.000 ± 0.002	0.704 ± 0.001	0.311 ± 0.005
$PA_{\rm bulge}$ [°]	89.9 ± 0.5	35.8 ± 0.9	13.8 ± 0.5	180.0 ± 0.3	74.3 ± 0.1	115.1 ± 0.5
μ_0 [mag arcsec^{-2}]	19.8 ± 0.2	21.64 ± 0.03	18.7 ± 0.6	19.3 ± 0.2	-	19.6 ± 0.1
h [arcsec]	32.8 ± 0.4	64.1 ± 0.6	9.1 ± 0.1	14.58 ± 0.07	-	22.0 ± 0.1
$h_{\rm out}$ [arcsec]	-	16.0 ± 0.3	-	-	-	-
$r_{\rm break}$ [arcsec]	-	47.4 ± 0.7	-	-	-	-
$q_{\rm disk}$	0.288 ± 0.002	0.596 ± 0.002	0.599 ± 0.002	0.497 ± 0.001	-	0.916 ± 0.001
$PA_{\rm disk}$ [°]	78.9 ± 0.2	27.36 ± 0.09	13.7 ± 0.2	12.01 ± 0.09	-	33.15 ± 0.05
$\mu_{0,\rm bar}$ [mag arcsec^{-2}]	-	20.97 ± 0.03	-	-	-	19.91 ± 0.04
$a_{\rm bar}$ [arcsec]	-	60.8 ± 0.2	-	-	-	40.05 ± 0.07
$q_{\rm bar}$	-	0.182 ± 0.001	-	-	-	0.549 ± 0.001
$PA_{\rm bar}$ [°]	-	29.74 ± 0.06	-	-	-	98.73 ± 0.03
$L_{\rm bulge}/L_{\rm T}$	0.03	0.11	0.03	0.12	1.00	0.08
$L_{\rm disk}/L_{\rm T}$	0.97	0.71	0.97	0.88	-	0.76
$L_{\rm bar}/L_{\rm T}$	-	0.18	-		-	0.16

Notes. $L_{\rm bulge}/L_{\rm T}$, $L_{\rm disk}/L_{\rm T}$, and $L_{\rm bar}/L_{\rm T}$ are the bulge-to-total, disk-to-total, and bar-to-total luminosity ratio, respectively.

Table 2.3: Details of the T122/B&C observations and central stellar velocity dispersion of the sample galaxies.

Galaxy	*PA*	Exp. T.	Apert.		σ_*
	[°]	[h]	[arcsec]	[pc]	[km s^{-1}]
(1)	(2)	(3)	(4)	(5)	(6)
NGC 2654	63	3.0	3×2	282×188	144 ± 3
NGC 3003	79	4.0	7×2	787×225	21 ± 8
NGC 3049	25	5.0	5×2	579×232	81 ± 9
NGC 3259	20	3.5	5×2	581×233	68 ± 6
NGC 4343	133	3.0	3×2	263×175	112 ± 4
NGC 4420	8	5.0	5×2	657×263	59 ± 7
NGC 5141	80	3.0	3×2	1053×702	253 ± 7
NGC 5635	65	3.5	3×2	874×583	235 ± 6
NGC 5713	10	3.0	3×2	412×274	70 ± 5

Notes. Col.(1): galaxy name. Col.(2): position angle of the slit along the galaxy major axis as given by RC3. Col.(3): total exposure time. Col.(4): size of the central aperture where we measured the stellar velocity dispersion. Col.(5): physical size of the central aperture where we measured the stellar velocity dispersion. Col.(6): central stellar velocity dispersion.

performing the photometric decomposition with GASP2D, which is best designed for galaxies with low-to-intermediate inclination (see Méndez-Abreu et al., 2008, for a discussion). We adopted the bulge r_e obtained by Salo et al. (2015, NGC 2654: $r_\mathrm{e} = 3.9$ arcsec, NGC 4343: $r_\mathrm{e} = 18.7$ arcsec) from the analysis of the infrared images of the Spitzer Survey of Stellar Structure in Galaxies (S^{4}G, Sheth et al., 2010).

2.3 Stellar kinematics

2.3.1 Ground-based spectroscopy

We performed the spectroscopic observations of the sample galaxies from 2016 January 4 to May 5 with the 1.22-m Galileo telescope (T122) at the Asiago Astrophysical Observatory (Italy). We used the Boller & Chivens spectrograph (B&C) and the grating with 1200 grooves mm^{-1} in combination with a 2 arcsec $\times$ 7.75 arcmin slit and the Andor iDus DU440 CCD comprised of 2048×512 pixels of 26 μm $\times$ 26 μm each. The CCD gain and readout noise rms were 0.97 e^- ADU^{-1} and 3.4 e^-, respectively. The spectra were characterized by a wavelength range between about 4500 – 5700 Å with a reciprocal dispersion of 0.60 Å pixel^{-1} and a spatial scale of 1.0 arcsec pixel^{-1}. We estimated the instrumental resolution as the mean of the Gaussian FWHMs measured for the unblended emission lines of a wavelength-calibrated comparison spectrum. We found $FWHM_\mathrm{inst} = 1.578 \pm 0.002$ Å corresponding to $\sigma_\mathrm{inst} \simeq 40$ km s^{-1} at 5100 Å. During the observing nights, we measured a seeing $FWHM_\mathrm{PSF} = 3$–5 arcsec by fitting the guiding star with a circular Gaussian function.

We observed all the sample galaxies by centering their nuclei in the slit which we aligned along the galaxy major axis according to the position angle tabulated in Table 2.3. We split

the total integration time into single exposures of 1800 s each for better rejection of cosmic ray events. At the beginning of each exposure, we moved the slit of 10 arcsec along the galaxy major axis in order to avoid bad pixels in the same CCD position. Each night, we observed some spectrophotometric standard stars from the list of Hamuy et al. (1992, 1994) to perform the flux calibration. Finally, we obtained a comparison spectrum of the available HeFeAr arc lamp before and after each object exposure to ensure an accurate wavelength calibration. The total exposure time of the T122 spectra is reported in Table 2.3. For NGC 3003, we binned the T122 spectrum over a rather large aperture in order to meet the target S/N but we measured a σ_* quite close to the instrumental resolution.

We reduced the T122 spectra using standard tasks in IRAF, as done by Corsini et al. (2017). The reduction steps included the bias subtraction, correction for internal and sky flat-field, trimming of the spectra, removal of bad pixels and cosmic rays, correction for CCD misalignment, subtraction of the sky contribution, wavelength and flux calibration, alignment, and combination of the spectra obtained for the same galaxy. The combined T122 spectra of the sample galaxies are given in Fig. 2.2.

2.3.2 Absorption line fitting

To measure the central stellar velocity dispersion, we analyzed the absorption lines in the combined T122 spectra of the sample galaxies with the Penalized Pixel Fitting (pPXF, Cappellari & Emsellem, 2004) and Gas and Absorption Line Fitting (GANDALF, Sarzi et al., 2006) algorithms.

For each galaxy, we rebinned the combined spectrum along the dispersion direction to a logarithmic scale and deredshifted it to the rest frame. We then averaged the rebinned spectrum along the spatial direction either to cover a nearly square aperture (Table 2.3) or to have a signal-to-noise ratio $S/N \geq 10$ per resolution element. We convolved a linear combination of stellar spectra from the ELODIE library at medium resolution ($\sigma_{\rm inst} = 13$ km s^{-1}, Prugniel & Soubiran, 2001) with a Gauss-Hermite line-of-sight velocity distribution (LOSVD, Gerhard, 1993; van der Marel & Franx, 1993) to fit the summed spectrum by a χ^2 minimization in pixel space. We selected 229 stellar spectra to fully cover the ELODIE parameter space of the effective temperature, surface gravity, and metallicity. They were broadened to match the T122 instrumental resolution, logarithmically rebinned, and cropped along the dispersion direction in order to match the wavelength range of each galaxy spectrum.

In addition, we simultaneously fitted all the ionized-gas emission lines in the wavelength range covered. We also added a fourth-order multiplicative Legendre polynomial to correct for reddening and large-scale residuals of flat-fielding. We excluded from the fitting procedure the wavelength ranges with a spurious signals due to imperfect subtraction of cosmic rays and sky emission lines.

First, we obtained the best-fitting values of the LOS velocity $v_\star$, velocity dispersion σ_*, and Gauss-Hermite coefficients h_3 and h_4 of the stellar component. The fitting procedure returned the value of σ_* corrected for instrumental resolution. After checking that $h_3 = h_4 = 0$ within the errors, we fitted again the galaxy spectra adopting a Gaussian LOSVD to measure σ_* (Table 2.3). We assumed its error to be the formal error of the best fit after evaluating χ^2

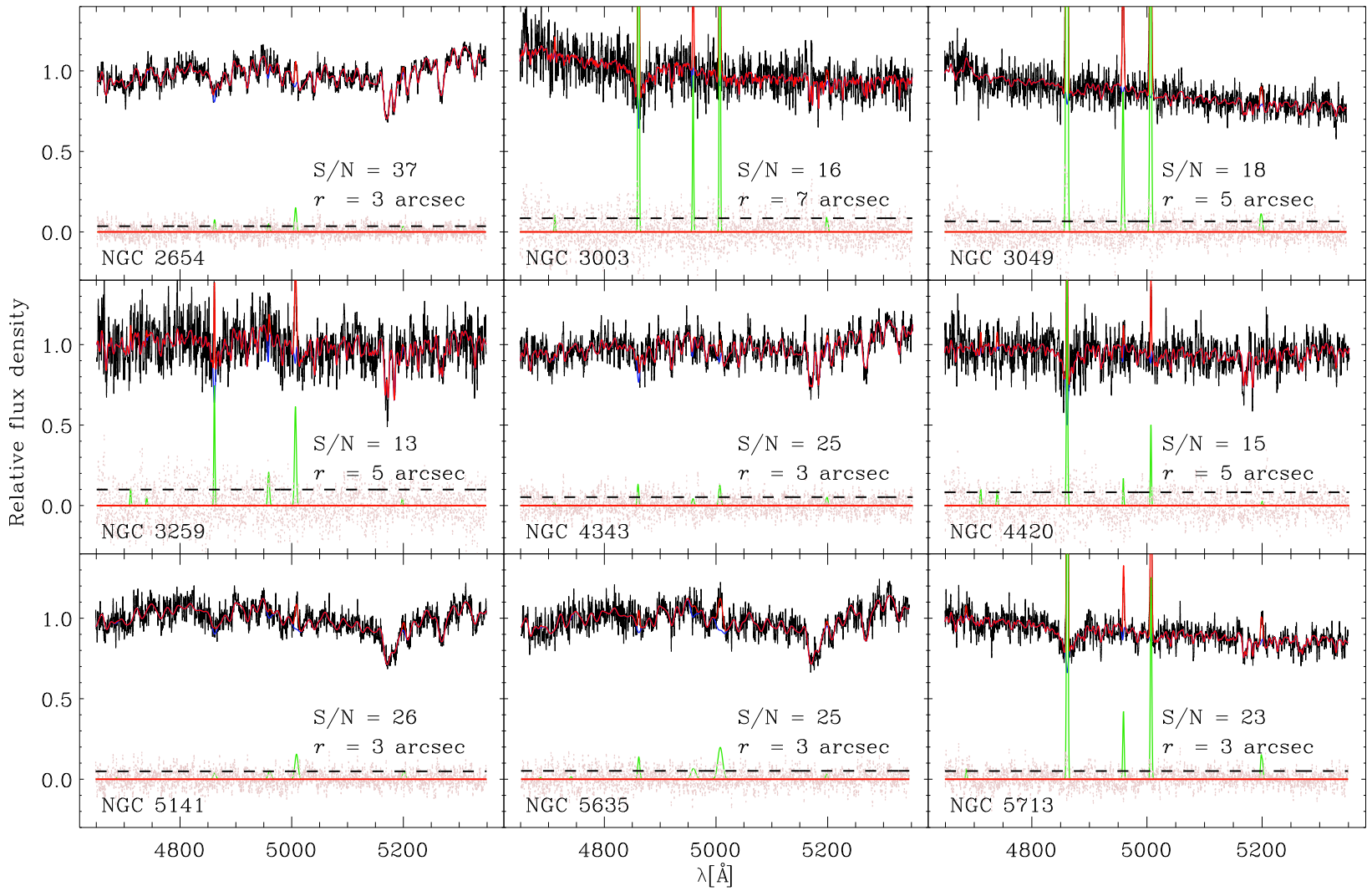

Figure 2.2: Rest-frame T122/B&C spectra (black solid line) with the best-fitting model (red solid line) that is calculated as the sum of the spectra of the ionized-gas (green solid line) and stellar (blue solid line) components. The residuals (pink points) are defined as the difference between the observed and model spectrum. The S/N is provided per resolution element and r gives the size of the central aperture where we extracted the spectrum and measured σ_*.

Table 2.4: Details of the HST/STIS observations and central gas velocity dispersion of the sample galaxies.

Galaxy	Prop. Id.	*PA*	Exp. T.	Sp. Range	Slit	Bin.	Apert.		$\sigma_{\rm gas}$
		[°]	[h]	[Å]	[arcsec]		[arcsec]	[pc]	[km s^{-1}]
(1)	(2)	(3)	(4)	(5)	(6)	(7)	(8)	(9)	(10)
NGC 2654	9046	62.0	1.25	6480 – 7060	0.1	1×1	0.1×0.15	9×14	71 ± 13
NGC 3003	8228	79.1	0.23	6480-7060	0.2	2×2	0.2×0.30	22×34	56 ± 4
NGC 3049	7513	42.1	0.27	6300 – 6870	0.1	1×1	0.1×0.15	12×17	31 ± 2
NGC 3259	8228	20.1	0.24	6480 – 7060	0.2	1×1	0.2×0.25	23×29	23 ± 3
NGC 4343	9068	144.1	0.81	6300 – 6870	0.2	1×1	0.2×0.25	18×22	79 ± 15
NGC 4420	8228	18.1	0.20	6480-7060	0.2	2×2	0.2×0.30	26×39	31 ± 29
NGC 5141	8236	72.3	0.36	6480 – 7060	0.2	2×2	0.2×0.30	70×105	142 ± 6
NGC 5635	7354	63.6	0.13	6480 – 7060	0.1	2×1	0.1×0.15	29×44	333 ± 25
NGC 5713	8228	10.1	0.20	6480 – 7060	0.2	2×2	0.2×0.30	27×41	49 ± 6

Notes. Col.(1): galaxy name. Col.(2): HST proposal number. Col.(3): position angle of the slit. Col.(4): total exposure time. Col.(5): spectral range. Col.(6): size of the slit. Col.(7): pixel binning. Col.(8): size of the central aperture where the gas velocity dispersion was measured. Col.(9): physical size of the central aperture where the gas velocity dispersion was measured. Col.(10): central gas velocity dispersion.

to achieve $\chi^2 = N_{\rm dof} = N_{\rm d} - N_{\rm fp}$, where $N_{\rm dof}$, $N_{\rm d}$, and $N_{\rm fp}$ are the number of the degrees of freedom, data points, and fitting parameters, respectively (Press et al., 1992). The best-fitting models of the T122 spectra of the sample galaxies are displayed in Fig. 2.2. Finally, for full consistency with Beifiori et al. (2009, 2012) we applied the aperture correction of Jørgensen et al. (1995) to obtain the stellar velocity dispersion $\sigma_{\rm c}$, that would have been measured within a circular aperture of radius $r_{\rm e}/8$ (Table 2.1).

2.4 Ionized-gas distribution and kinematics

2.4.1 Hubble Space Telescope spectroscopy

From the Mikulski Archive for Space Telescopes (MAST), we retrieved the STIS spectra of the sample galaxies obtained with the G750M grating through either the 0.1×52 arcsec^2 or the 0.2×52 arcsec^2 slit placed across the galaxy nucleus at position angle close to the galaxy major axis. The detector is a SITe CCD with 1024×1024 pixel of 21×21 μm^2. The spectra cover a wavelength range of either 6480 – 7060 or 6300 – 6870 Å depending on the tilt angle of the grating. The reciprocal dispersion was 0.554 and 1.108 Å pixel^{-1} for the 1-pixel and 2-pixel binning read-out mode along the dispersion direction, respectively. This setup yielded an instrumental FWHM of 0.87 Å ($\sigma_{\rm inst} = 17$ km s^{-1}) in the case of a 0.1 arcsec-wide slit and 1.6 Å ($\sigma_{\rm inst} = 32$ km s^{-1}) for the 0.2 arcsec-wide slit (Sarzi et al. 2002; Beifiori et al. 2009). The spatial scale was 0.0507 arcsec and 0.101 arcsec pixel^{-1} for the 1-pixel and 2-pixel binning read-out mode along the spatial direction, respectively. The HST proposal number, slit width and position angle, pixel binning, wavelength range, and total exposure times of

the HST spectra of the sample galaxies are reported in Table 2.4.

We reduced the HST spectra using IRAF tasks, as done by Beifiori et al. (2009). The reduction steps included subtraction of the overscan, bias and dark contributions, correction for internal flat-field, trimming of the spectra, removal of bad pixels and cosmic rays, wavelength and flux calibration, correction for geometrical distortion, alignment and combination of the spectra obtained for the same galaxy. The combined HST spectra of the sample galaxies are shown in Fig. 2.3.

2.4.2 Emission line fitting

To measure the distribution and kinematics of the ionized gas, we decided to analyze the [NII]$\lambda\lambda$6548, 6583, Hα, and [SII]$\lambda\lambda$6716, 6731 emission lines in the combined HST spectra of the sample galaxies, following the prescriptions by Beifiori et al. (2009) and using their IDL algorithm based on MPFIT package (Markwardt, 2009).

We fitted the stellar continuum with a low-order polynomial and the narrow and broad components of the observed emission lines with a sum of Gaussian functions. For all the objects the ionized-gas emission was always much stronger compared to the stellar continuum. The best-fitting parameters and their errors were derived by a χ^2 minimization in pixel space and evaluating $\chi^2 = N_{\rm dof}$. We adopted both a narrow and broad component for the emission lines of NGC 3259 and NGC 5141, two narrow components for NGC 3049, and a single narrow component for all the other sample galaxies, including NGC 5635 for which the presence of two distinct components was not clear. For NGC 2654 and NGC 3049 the Hα line was not accurately fitted due to the low S/N and presence of an asymmetric broad component, respectively. This does not influence our results since we considered only the [NII]λ6583 line for the dynamical modeling.

We focused on the [NII]λ6583 line because it was always the brightest nebular line in our spectra. The nebular lines actually probe the nuclear kinematics better than the Hα line, which could be affected by both the absorption from the stellar component and emission from circumnuclear starforming regions (e.g., Coccato et al., 2006).

We measured the radial profile of the [NII]λ6583 flux along the spatial direction to constrain the distribution of the ionized gas. All the galaxies show a Gaussian flux profile, except for NGC 3003 which has a rather asymmetric profile with a central minimum (Fig. 2.4). So, as a first attempt, we symmetrized the flux profile of NGC 3003 with respect to its left side (Fig. 2.5) so that it could be fitted with a Gaussian, even if it appears quite clear right away that probably it is not a good approximation overall. We assumed the gas to be distributed into a infinitesimally thin disk centered on the galaxy nucleus with an intrinsically Gaussian flux profile. We derived the intrinsic flux profile for two inclinations of the gaseous disk ($i = 33°, 81°$) by a χ^2 minimization to match the observed flux, while accounting for the STIS PSF, which we generated with the TINY TIM package by Krist et al. (2011). The results for the sample galaxies are plotted in Fig. 2.5. We measured the [NII]λ6583 line width within a nearly square aperture centered on the continuum peak to estimate the central gas velocity dispersion $\sigma_{\rm gas}$. In the case of the 1-pixel spatial binning, we used an aperture of 0.15 arcsec (3 pixels) or 0.25 arcsec (5 pixels) along the spatial direction when the spectrum was obtained

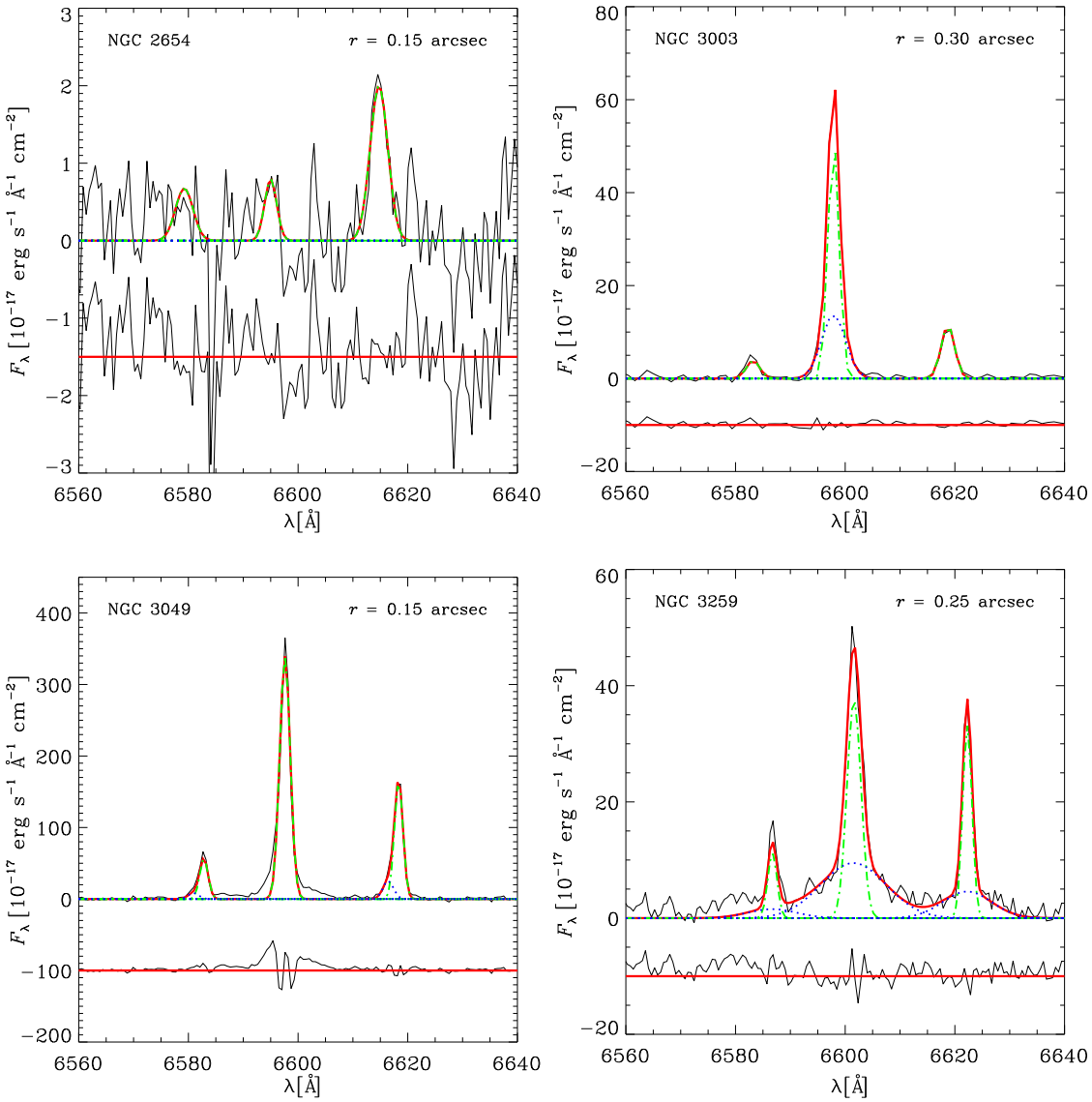

Figure 2.3: HST/STIS spectra of the sample galaxies (black solid line) with best-fitting model (red solid line) obtained adopting broad (blue dotted lines) and narrow (green dashed lines) components for the [NII]$\lambda\lambda$6548, 6583 and Hα lines. r gives the size of the central aperture where we extracted the spectrum and measured $\sigma_{\rm gas}$. The residuals are defined as the difference between the observed and model spectrum. They are shifted to have an arbitrary zero point for viewing convenience.

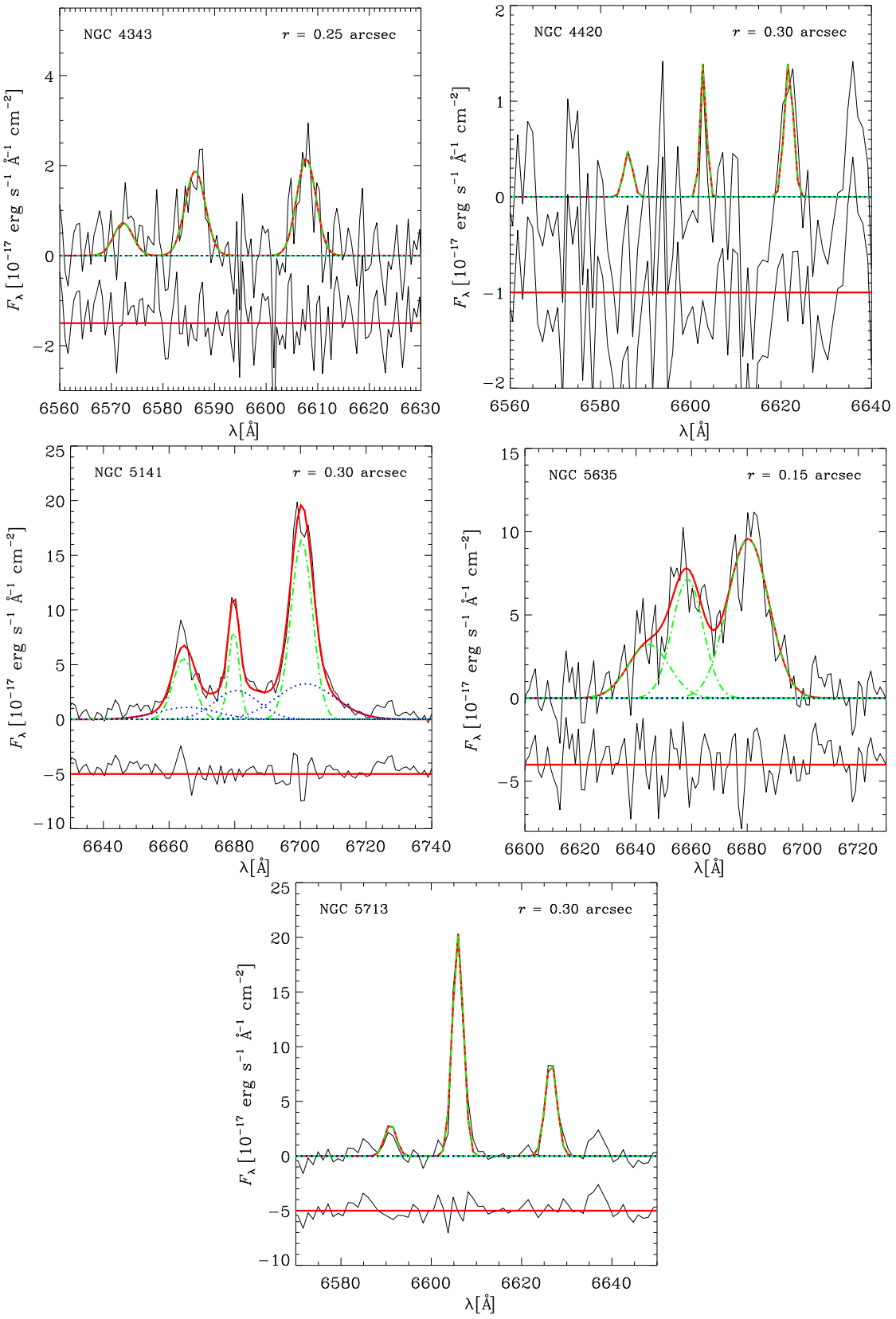

Figure 2.3: Continued.

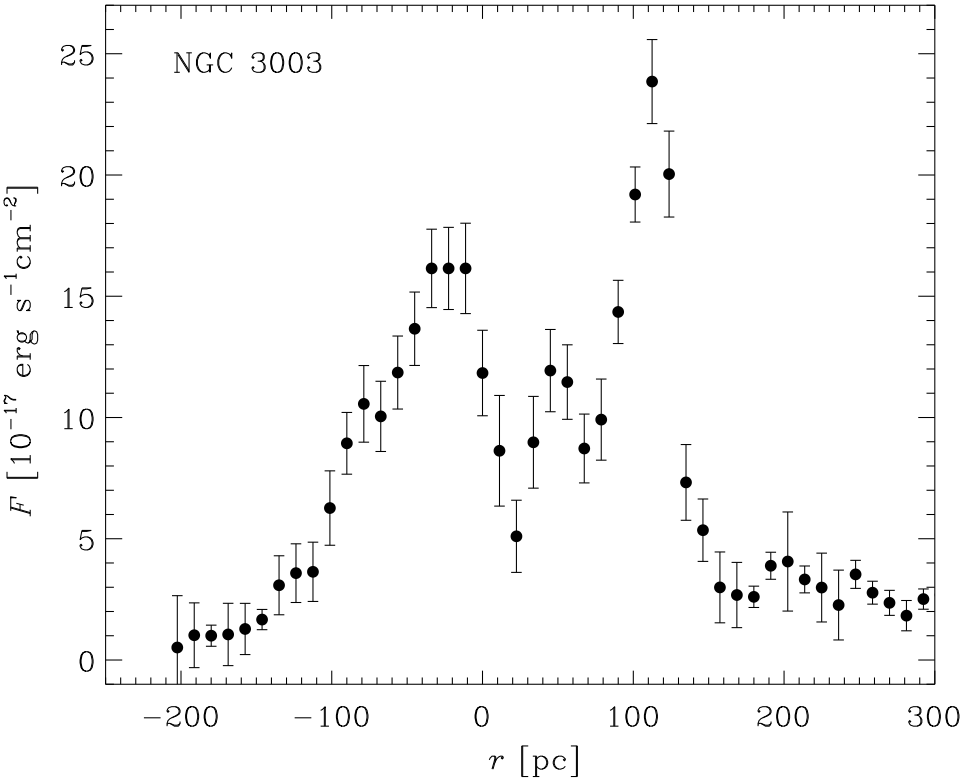

Figure 2.4: Flux radial profile of the [NII]λ6583 emission line measured in the HST/STIS spectrum of NGC 3003.

with a 0.1 arcsec or a 0.2 arcsec-wide slit, respectively. In the case of a 2-pixel spatial binning, we used an aperture of 0.30 arcsec (3 pixels). The aperture sizes are listed in Table 2.4. We corrected the measured line width for instrumental resolution to obtain $\sigma_{\rm gas}$ (Table 2.4).

2.5 Dynamical modeling

To derive $M_\bullet$ stringent limits for our sample galaxies we followed the approach of Sarzi et al. (2002). This is based on the assumption that the nuclear gravitational potential is traced by the line width of the nebular emission originating from ionized gas in Keplerian rotation around the SBH. We assumed the gas moving onto coplanar circular orbits in a infinitesimally thin disk with the intrinsic distribution we derived from the measured flux radial profile. The kinematics was measured along only one direction across the galaxy nucleus, which does not provide constraints on the orientation of the gas disk. We disregarded the effect of the unknown position angle of the gas disk, since we extracted our spectrum in a nearly square aperture. Thus, we could assume that the STIS slit was placed along the major axis of the gas disk and we estimated $M_\bullet$ at two inclinations of 33° and 81°, which bracket the 68% of randomly inclined disks (see Sarzi et al., 2002). Our choice of parametrization for the intrinsic flux of the gas is conservative, a cuspier function would lead to a more concentrated

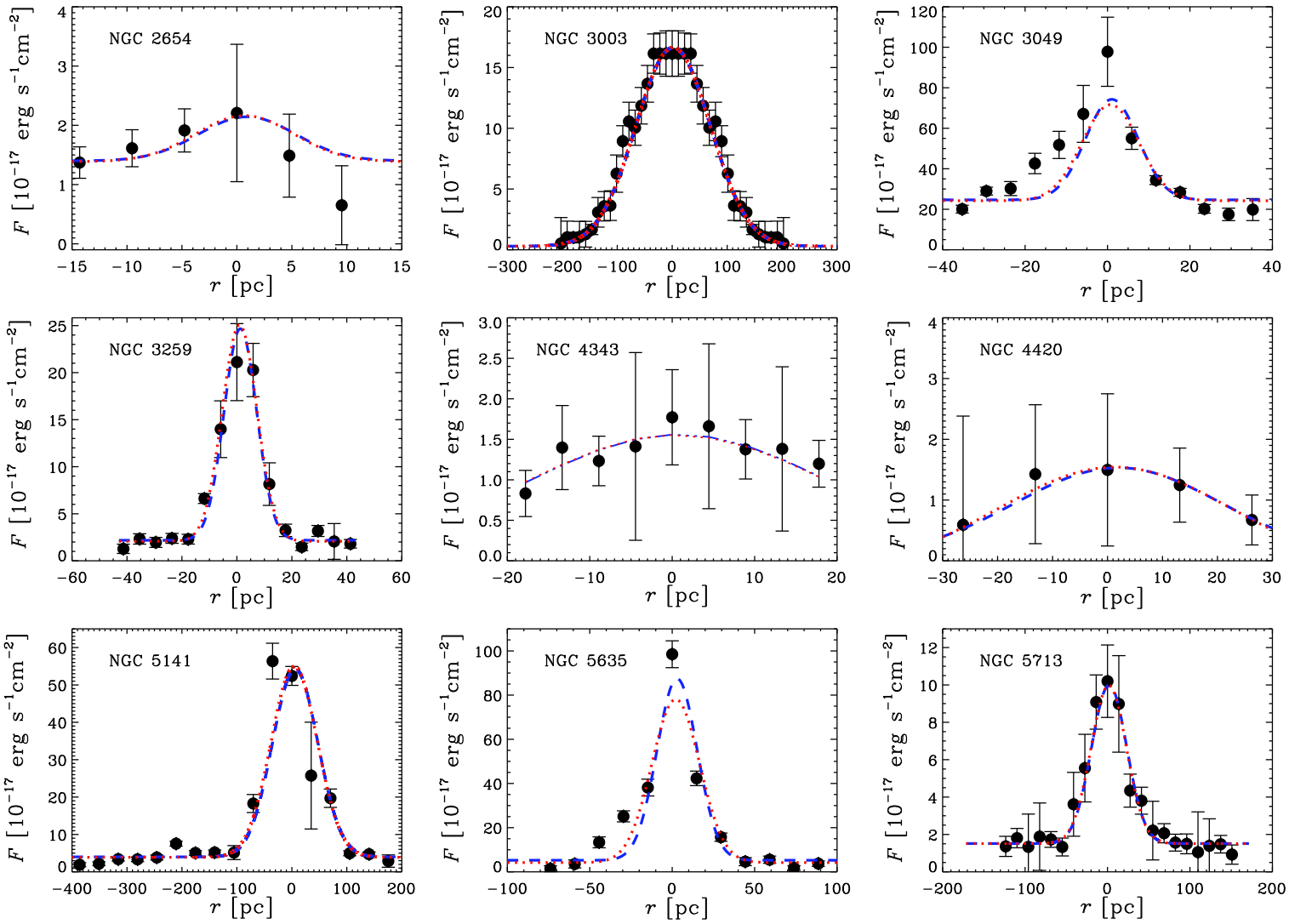

Figure 2.5: Flux radial profile of the [NII]λ6583 emission line measured in the HST/STIS spectra of the sample galaxies. The best-fitting radial profiles of intrinsic flux for a gas disk with $i = 33°$ (blue dashed line) and 81° (red dotted line) are shown after being convolved with STIS PSF.

gas distribution and, therefore, to a smaller value of $M_\bullet$ (see Sarzi et al., 2002). We also expect to find a smaller value of $M_\bullet$ when taking into account the contributions of the stellar potential and nongravitational forces (due for instance to the activity of the central SBH). These last factors imply that our $M_\bullet$ estimates based on the assumption of a rotating gaseous disk should be strictly speaking regarded only as upper limits, although in practice it is unlikely that the gas motions are entirely driven by nongravitational forces. In particular, the finding that the narrow-line ionized-gas emission is always rather concentrated around the nucleus contrasts with the idea that such gas would not respond to the central gravitational pull of the SBH. In fact, that nongravitational forces are generally unimportant is also supported by the finding that the $M_\bullet$ estimates derived from the central ionized-gas flux profile and line-width always agree with actual $M_\bullet$ measurements based on resolved stellar and ionized-gas kinematics (Beifiori et al., 2012). Nonetheless, in some instances there are indications that $M_\bullet$ estimates based on our method could be biased either due to the presence of nongravitational forces or to the stellar potential (Beifiori et al., 2009).

2.6 Discussion and conclusions

We decided to remove NGC 3003 and NGC 4420 from the final sample. NGC 3003 has an asymmetric [NII]λ6583 flux profile that was artificially symmetrized in order to perform the Gaussian fit. This makes the estimate of the $M_\bullet$ upper limit rather unreliable and demanding for a better constrained dynamical modeling based on resolved ionized-gas kinematics. Concerning NGC 4420, we evaluated the STIS fit as uncertain because we were not fully confident about the presence of the gas at the center of this galaxy. NGC 4420 was actually the only sample galaxy for which we identified the [NII]λ6583 emission line using the galaxy redshift. Moreover, it was very difficult to fit the bulge component in the photometric decomposition because of the presence of dust.

In Fig. 2.6, we compare our final sample of $M_\bullet$ stringent limits to that of Beifiori et al. (2009, 2012) who considered the $M_\bullet - \sigma_c$ relation by Ferrarese & Ford (2005).

The $M_\bullet$ limits of NGC 2654, NGC 3049, NGC 3259, NGC 4343, NGC 5141, and NGC 5635 are within the 3σ scatter of the $M_\bullet - \sigma_c$ relation. The $M_\bullet$ of NGC 5635 is displaced towards higher values because we probably overestimated the σ_{gas} value from the HST/STIS spectrum, where it was not possible to distinguish the broad and narrow components of the [NII]λ6583 line.

The $M_\bullet$ value for NGC 5713 exceeds more than three times the scatter of the $M_\bullet - \sigma_c$ relation. For this galaxy the contribution of the stellar mass that we disregarded in our analysis could play a significant role, as already pointed out by Beifiori et al. (2009) for a number of other galaxies with a $M_\bullet$ stringent limit in the lower end of the $M_\bullet - \sigma_c$ relation. On the top of this, the center NGC 5713 is poorly constrained because its nuclear surface brightness distribution are characterized by several bright knots rather than a well-defined peak (see also Scarlata et al., 2004).

Our galaxies cover different morphological types (1 elliptical, 3 unbarred and 3 barred spirals according to the photometric decomposition) and span a wide range of central stellar

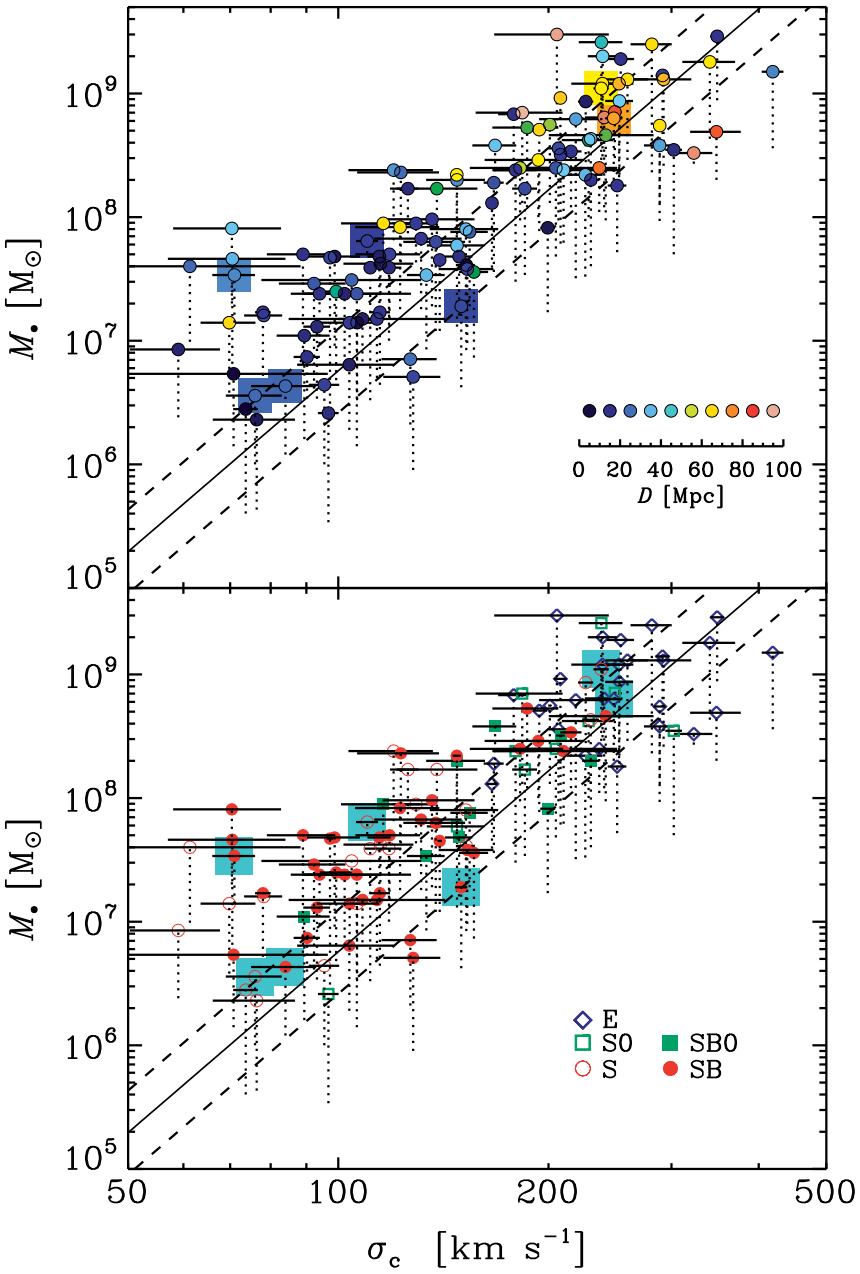

Figure 2.6: Comparison between the $M_\bullet$ stringent limits of our (symbols with large squares) and Beifiori et al. (2009, 2012) sample of galaxies as a function of galaxy distance (*top panel*) and morphological type (*bottom panel*). The upper and lower edges of the dotted lines correspond to $M_\bullet$ values estimated assuming an inclination of $i = 33°$ and 81° for the gas disk, respectively. In both panels the solid line is $M_\bullet - \sigma_c$ relation by Ferrarese & Ford (2005) with the dashed lines showing the 1σ (0.34 dex) scatter in $M_\bullet$.

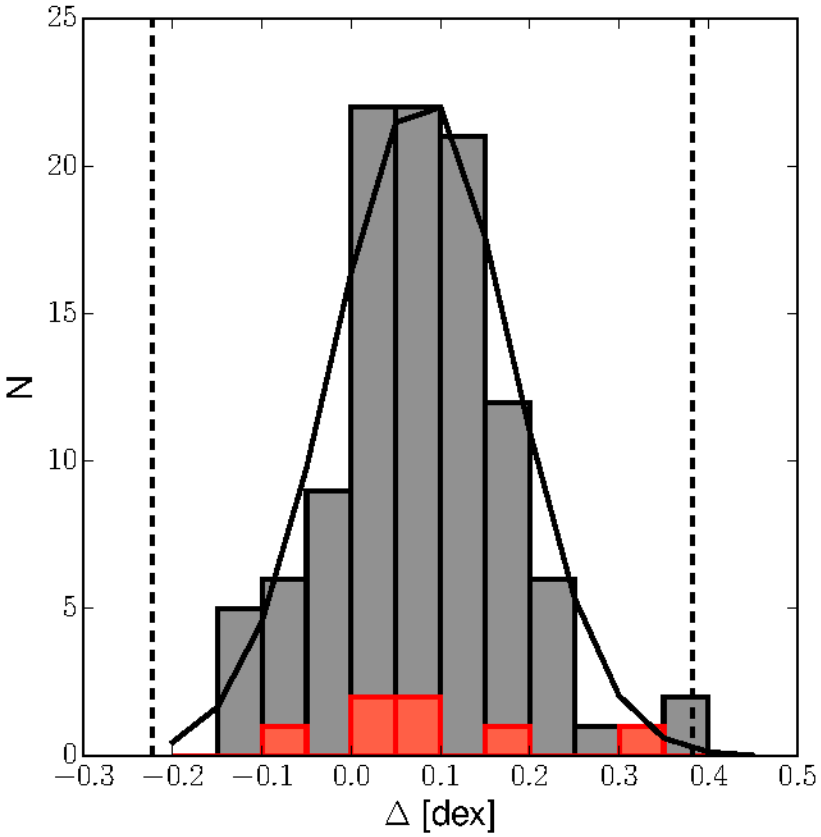

Figure 2.7: Distribution of the distance of the $(\sigma_c, M_\bullet)$ values measured for our (red histogram) and Beifiori et al. (2009, 2012) (black histogram) sample of galaxies from the $M_\bullet - \sigma_c$ relation by Ferrarese & Ford (2005). The black solid line is the Gaussian fit to Beifiori et al. (2009) distribution, which is centered at $\Delta = 0.08$ dex with the black dotted lines marking its $\pm 3\sigma$ range ($\sigma = 0.10$ dex).

velocity dispersion ($71 < \sigma_c < 248$ km s^{-1}) and $M_\bullet$ ($3.6 \cdot 10^6 < M_\bullet < 1.1 \cdot 10^9$ M$_\odot$ for $i = 33°$ and $1.0 \cdot 10^6 < M_\bullet < 2.9 \cdot 10^8$ M$_\odot$ for $i = 81°$). The $M_\bullet$ stringent limits we measured are fully consistent with those of Beifiori et al. (2009, 2012). This is confirmed by the distribution of the distances of the two $(\sigma_c, M_\bullet)$ datasets from the $M_\bullet - \sigma_c$ relation by Ferrarese & Ford (2005), which we show in Fig. 2.7 for $i = 33°$. On average, our $M_\bullet$ run parallel to and above the $M_\bullet - \sigma_c$ relation with no systematic trend depending on distance or presence of a bar.

With our investigation, the number of galaxies with $M_\bullet$ stringent limits obtained from nebular-line width increases to 114 and can be used for studying the scaling relations between $M_\bullet$ and properties of their host galaxies. Most of our $M_\bullet$ limits actually populate the low-σ end of the $M_\bullet - \sigma_c$ relation. They could be used to prove the claim by Beifiori et al. (2009) that the contribution of the stellar component to the gravitational potential is particularly significant in the low-σ regime and biases the measured $M_\bullet$ towards exceedingly large values, as we investigate in Chap. 3.

Chapter 3

Stringent limits on the masses of the supermassive black holes of 100 nearby galaxies by accounting for the stellar mass contribution in the galactic nucleus

Abstract. Based on dynamical modeling of the central width of nebular emission lines measured over subarcsecond apertures with the Hubble Space Telescope, we present stringent limits on the mass $M_\bullet$ of the central supermassive black hole for a sample of 100 nearby galaxies ($D < 103$ Mpc) spanning a wide range of Hubble types (E-Sc) and values of the central velocity dispersion (54-404 km s^{-1}). In constraining $M_\bullet$ we took into account the stellar mass contribution to the gravitational potential in the galaxy nucleus. To this aim, we model the surface brightness distribution measured from Hubble Space Telescope images and adopt the mass-to-light ratio of an old and metal-rich stellar population. The shape of the profile of the emission lines and of the radial profile of emission-line flux are analysed to verify that nongravitational forces have a minor impact on the $M_\bullet$ estimate. We find that on average the stellar mass contribution is larger for galaxies with effective velocity dispersion $\sigma_{\rm e}< 90$ km s^{-1} mostly due to the presence of a nuclear stellar cluster/disk. Moreover, the stellar mass contribution is negligible in ellipticals, but it is not in lenticulars and spirals. It depends on the aperture size rather than on galaxy distance. Our stringent limits run parallel to the $M_\bullet - \sigma_{\rm e}$ relation and exceed the expected $M_\bullet$ values by a median factor of 1.7. This is a striking result if we consider that our dynamical analysis does not rely on spatially-resolved distribution and kinematics of the gaseous tracer. This makes $M_\bullet$ stringent limits particularly suitable for the analysis of correlations between the mass of supermassive black holes and properties of their host galaxies.

3.1 Introduction

Observational evidence for central mass concentration measured from nuclear kinematics and not due only to the stellar content show that a supermassive black hole (SBH) is present in most nearby galaxies. In the last several years, SBHs have been extensively studied in all morphological types and have been invoked to interpret both the energetic phenomena observed in the active galactic nuclei (AGN) and the motions of stars and gas clouds in the very central regions of quiescent galaxies.

An important requirement that has to be fulfilled to obtain reliable measurements of the SBH mass ($M_\bullet$) is with observations characterized by enough spatial resolution to resolve the kinematics in the region where the gravitational potential is dictated by the SBH. Not considering the Milky Way for which orbits of single stars can be observed (Genzel et al., 2010), NGC 4258 (Miyoshi et al., 1995) and a few megamaser disk galaxies (Kuo et al., 2011) for which the maser dynamics of molecular gas can be exploited, about ~ 90 $M_\bullet$ are available in the literature. These were obtained from spatially-resolved stellar or gas kinematics. Important steps in this sense have been accomplished thanks to the Hubble Space Telescope (HST) or to the ground-based telescopes assisted with adaptive optics. $M_\bullet$ values between 10^6 and 10^{10} $M_\odot$ have been obtained and SBHs of smaller $M_\bullet$ have also been unveiled in several bulgeless galaxies (see Kormendy & Ho, 2013, for a review).

Nowadays, the stellar dynamical models are the most widely employed due to the advent of integral-field spectroscopy which provides better constraints on the stellar orbital structure and as a consequence on $M_\bullet$ measurements (e.g., Gebhardt et al., 2003; Thomas et al., 2004; Saglia et al., 2016). On the other hand, this technique is quite challenging and time-consuming from both an observational and modeling point of view. On the contrary, ionized-gas dynamical models are simpler and require lesser observational efforts, but they can not be used in all the cases. Indeed, nuclear gaseous disks are not present in the center of all the galaxies and their kinematics could be affected by the presence of nongravitational forces (Ho et al., 2002; Walsh et al., 2008). In some cases, the contribution of turbulent pressure support is included in the dynamical model (Barth et al., 2001; Neumayer et al., 2007), but a suitable way to properly describe the gas behaviors has still to be developed. The tightest $M_\bullet$ measurements from resolved gas kinematics available in the literature are based on HST observations carried out by using parallel slits to determine the inclination of the gaseous disk (e.g., Coccato et al., 2006; Dalla Bontà et al., 2009). Despite the intrinsic advantages of this method, there are not many secure $M_\bullet$ estimates based on gas dynamics compared to those obtained with stellar dynamical models. On the contrary, the unresolved gas kinematics led to a large sample of $M_\bullet$ determinations. Indeed, Beifiori et al. (2009, hereinafter B09), Beifiori et al. (2012, hereinafter B12) and Pagotto et al. (2017) provided stringent limits of $M_\bullet$ in 114 nearby galaxies. These $M_\bullet$ are actually upper limits on SBH masses because they were obtained from unresolved kinematics, the stellar mass contribution was not included in the dynamical model, and the contribution of nongravitational forces, if present, was not taken into account. Nevertheless, this technique is observationally cheaper with respect to the gas resolved kinematics since it requires only long-slit spectra centered on the galaxy nucleus.

The mass of SBHs is related to several properties of their host galaxies, like the stellar mass (Häring & Rix, 2004), luminosity (Marconi & Hunt, 2003) and central stellar velocity dispersion (Ferrarese & Merritt 2000; Gebhardt et al. 2000) of the spheroid in the case of lenticulars and spirals or of the whole galaxy in the case of ellipticals. These correlations reveal that the SBH and the stars of the spheroidal component interacted and grew together. Larger galaxy samples including all morphological types and luminosities in order better constrain such correlations are needed. This is strictly required to improve the understanding of SBH-galaxy formation and coevolution. One significant contribution in this direction was indeed given by the previously mentioned $M_\bullet$ stringent limits. In fact, even if they are not accurate estimates, they provide useful constraints to these correlations (Beifiori et al., 2012; van den Bosch, 2016).

In this chapter we consider the sample of 114 $M_\bullet$ stringent limits collected by B09, B12, and Pagotto et al. (2017). The main purpose is to account for the stellar contribution in the dynamical model in order to provide tighter $M_\bullet$ limits. Only for 21 sample galaxies a $M_\bullet$ estimate from resolved kinematics is provided so far in the literature, so this analysis enriches the existing $M_\bullet$ catalogues. The chapter is organized as follows. We describe the sample selection in Sect. 3.2. We perform the surface brightness analysis by using HST images in Sect. 3.3. We present the gas dynamical model in Sect. 3.4 and we describe the analysis of results in Sect. 3.5. Finally, we draw conclusions in Sect. 3.6. In this chapter, $H_0 = 70$ km s^{-1} Mpc^{-1}, $\Omega_{\rm M} = 0.3$, and $\Omega_\Lambda = 0.7$ were adopted as cosmological parameters.

3.2 Sample selection

We considered the galaxy sample compiled by B09, B12 and Pagotto et al. (2017). It comprises relatively nearby galaxies ($D < 103$ Mpc) with Hubble types spanning from ellipticals to late-type spirals (E-Sc) and covering a large range of central stellar velocity dispersions ($54 < \sigma < 404$ km s^{-1}).

We aimed at deriving the stellar mass content in the nucleus of these galaxies by analyzing their surface brightness distribution from the images available in the Hubble Space Telescope Legacy Archive (HLA[1]). This allowed us to take advantage of the superb spatial resolution of HST in characterizing the light distribution of galaxy nuclei. Moreover, we considered only broad-band images in the wavelength range from about 4800 to about 7200 Å to properly trace the light of the stellar component and to accurately recover its mass distribution. We made an effort to collect a set of images which was as homogeneous as possible, and as a consequence we gathered a final galaxy sample which mostly depended on which images were actually available in the HLA.

We analyzed Wide-Field Planetary Camera 2 (WFPC2), Advanced Camera for Surveys (ACS) or Wide Field Camera 3 (WFC3) images. We started by selecting the WFPC2 images with the galaxy nucleus targeted by the PC detector and after that we considered the WFPC2 images having the galaxy nucleus within one of WF detectors. For each galaxy, we looked for multiple exposures to get a final reduced image already cleaned of cosmic rays. For this reason,

[1] `http://hla.stsci.edu/`

we retrieved all the multiple WFPC2/F814W images available for the sample galaxies and then we considered the multiple WFPC2/F606W, or WFPC2/F702W, or WFPC2/F791W images. For the sample galaxies without multiple exposures, we retrieved the available single WFPC2/F814W or WFPC2/F606W images. As last choice, we considered the ACS/F814W or WFC3/F814W images.

We lost 14 galaxies from the initial sample of 114 galaxies: 4 galaxies did not have WFPC2 or ACS or WFC3 images at all, 4 galaxies did not have broad-band images, 4 galaxies had saturated images of their nuclei, 2 galaxies did not have images targeting their nuclei. Therefore, our final sample is composed of 100 galaxies, 56 of which have WFPC2/F814W images, 26 have WFPC2/F606W images, 6 have WFPC2/F702W images, 7 have WFPC2/F791W images, 2 have ACS/F814W images, and 3 have WFC3/F814W images. Their names, morphological type, and setup of the images we analysed are reported in Table 3.1. The discarded galaxies and the reason for their rejection are given in Table 3.2.

3.3 Surface brightness distribution analysis

3.3.1 Data retrieval and reduction

We retrieved from the HLA the reduced and drizzled images of the 84 galaxies for which multiple exposures were available (Table 3.1). In this case the cosmic rays were removed during the automatic data reduction. The WFPC2 images were reduced with `multidrizzle` Pyraf[2] package, while the ACS and WFC3 images were reduced with the `astrodrizzle` Pyraf package.

As far as the WFPC2 images, the PC images have a spatial scale of 0.0455 arcsec pixel^{-1}, while the WF1, WF2, and WF3 images have a spatial scale of 0.1 arcsec pixel^{-1}. We decided to use the mosaic WFPC2 images with a spatial scale of 0.1 arcsec pixel^{-1} all over the field of view for homogeneity. The most common WFPC2 configuration targeted the galaxy nucleus within the PC field, but for many objects the galaxy center was too close to the image edge. In this case, the PC image only was not useful to properly derive the light distribution of the nuclear regions. Moreover, since `multidrizzle` estimates the sky level from the outer portions of the image, the sky value of PC images was over-estimated since the galaxy filled the field of view. Finally, we needed the mosaic WFPC2 image covering most if not all the galaxy to build an accurate photometric model in some cases.

Only a single exposure was available in the HLA for the remaining 16 galaxies (Table 3.1), so their reduced and drizzled images still had cosmic rays. To address this issue, we retrieved the reduced but not drizzled images of these objects. We successfully cleaned the cosmic rays with the IRAF[3] task `lacos_im` (van Dokkum, 2001). We could not apply it to the drizzled images because the cosmic rays were grossly spread out during the resampling carried out by `multidrizzle`. We processed the cleaned images with `astrodrizzle` to deal with the

[2]Pyraf is a product of the Space Telescope Science Institute, which is operated by AURA for NASA.

[3]Image Reduction and Analysis Facility is distributed by the National Optical Astronomy Observatory (NOAO), which is operated by the AURA, Inc., under cooperative agreement with the National Science Foundation.

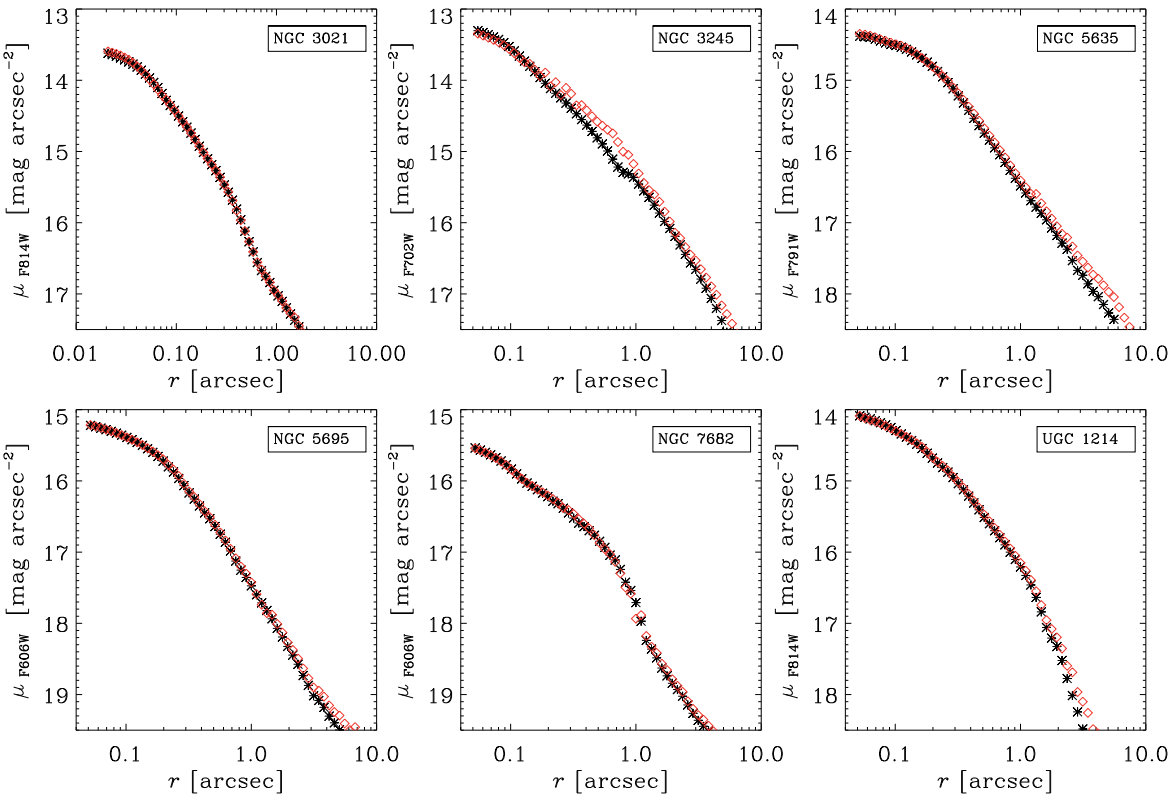

Figure 3.1: Comparison between the azimuthally-averaged surface-brightness radial profiles extracted from the original drizzled (black asterisks) and reprocessed (red open diamonds) HLA images of some sample galaxies. NGC 3021 was imaged with WFC3/F814W, NGC 3245 with WFPC2/F702W, NGC 5635 with WFPC2/F791W, NGC 5695 with WFPC2/F606W, NGC 7682 with WFPC2/F606W, and UGC 1214 with WFPC2/F814W.

format of the archival images, to correct for geometric distortions, to resample the images to a spatial scale of 0.1 arcsec pixel^{-1}, and to rotate them to be oriented with north at at the top and east to the left. We used the `DrizzlePac v2.0` package (Gonzaga et al., 2012) running through `astroconda`[4]. Finally, we subtracted from the drizzled images the sky value given by McMaster et al. (2008).

To verify that we reduced and resampled the images in a proper way, we compared the azimuthally-averaged surface-brightness radial profiles extracted from our images to those obtained from the reduced and drizzled images available in the HLA. To this aim, we fitted the galaxy isophotes with ellipses using the IRAF task `ellipse`. We performed a first fit by allowing the center of the ellipses free to vary. Then, we repeated the fit by fixing the center to the value which we previously obtained for the inner ellipses. We show the result for some galaxies in Fig. 3.1. We calibrated the surface brightnesses in Vegamag magnitudes and plotted at least one example for each adopted combination of camera and filter. For all the 6 galaxies shown in Fig. 3.1, the agreement between the two surface brightness profiles in

[4] `https://astroconda.readthedocs.io/en/latest/`

the nuclear regions is good with a maximum discrepancy of about 0.05 mag arcsec^{-2}. Larger discrepancies are found in the outer regions and they could be caused by spiral arms or dust affecting the isophotal fitting.

This consistency check also confirmed us that the HLA images of the other 84 sample galaxies, which were reduced and drizzled with an older pipeline, are fully reliable for the purposes of our analysis.

3.3.2 Dust masking

As a first step, we carefully inspected the images of all the sample galaxies to analyze the distribution of the dust as reported in Table 3.1. Its presence could severely affect the measurement of both the surface brightness distribution of the stars and flux distribution of the ionized gas. This effect is particularly important when considering the nuclear regions (i.e., within $\simeq 1$ arcsec from the galaxy center) because it could prevent the correct determination of the stellar and total mass, and consequently of $M_\bullet$. We decided to mask the dust lanes/filaments in the galaxy images rather than performing a color-based dust correction of the measured surface brightness distribution. Such a correction was indeed not feasible for all the objects, because it requires at least two images obtained with different broad-band filters, which are not available in the HLA for all the sample galaxies. Moreover, several authors pointed out that the color-based dust correction is a challenging and unfinished task because it is not always possible to deal with the dust filaments (e.g., Ferrarese et al., 2006a; Coccato et al., 2006, but see also Sect. 4 for a discussion).

Galaxies with a nucleus free of dust

The nucleus of 53 sample galaxies is free of dust (Table 3.1). In some cases, we masked the dust lanes/filaments in the outer regions of the galaxy by means of the IRAF task `ellipse`. This was necessary when the model of the surface brightness distribution at small radii was affected by the presence of dust at large radii.

Galaxies hosting a dust disk

The dust shows a symmetric and regular pattern in 15 sample galaxies (Table 3.1).

For these objects, we adopted a mask with the shape of an elliptical annulus with ellipticity $\epsilon = 1 - \cos i_{\rm dust}$ given by the inclination of the dust disk. The mask is circular if the galaxy nucleus hosts a face-on dust disk, otherwise it has an elliptical shape except for the edge-on dust disks when it is just a strip crossing the galaxy center. We obtained a first guess of the center coordinates with the IRAF task `imexamine` and we constrained their final values by fitting galaxy isophotes with ellipses with the IRAF task `ellipse`. We found $30^\circ < i_{\rm dust} < 78^\circ$ and we always aligned the mask with the major axis of the dust disk. To define the location and size of the masked region and verify whether the galaxy center was obscured, we compared the surface brightness measured in each pixel of the central portion of the image as a function of the distance from the galaxy center. We expected that the unmasked pixels

on the unobscured side of the galaxy had a systematically brighter surface brightness than those on the dusty side.

We show the elliptical mask and surface-brightness radial profiles of NGC 4335 and NGC 6861 in Fig. 3.2 as an example. NGC 6861 has a more extended dust disk compared to NGC 4335. These two galaxies are representative of the behavior of the dust in NGC 3245, NGC 4435, NGC 4459, NGC 7052, and UGC 12064 where the obscured regions can be easily identified and masked and did not extend inward to the galaxy center.

NGC 315, NGC 383, and NGC 4335 have a nuclear disk of dust too, but only the dust disk of NGC 315 is nearly edge on. In this last case, we built a mask by adopting a lower disk inclination than the actual one in order to not mask the galaxy center. Due to residual presence of dust there could be a partial light dimming and the stellar contribution could have been underestimated.

We successfully masked the dust disk of NGC 4526, which was very extended ($r \simeq 15$ arcsec) and highly inclined ($i = 78°$). On the contrary, NGC 2110 is characterized by a dusty structure that is more similar to wounded spiral arms rather than to a disk and the galaxy center is presumably affected by obscuration. The main stellar disks of NGC 4343, NGC 4429, and NGC 5005 are characterized by prominent dust lanes. Since these galaxies are very inclined, the dust severely obscures their central regions and it was impossible to effectively mask it all.

Galaxies with an irregular dust pattern

In the remaining 34 galaxies, the dust was characterized by an irregular pattern (Table 3.1). For these objects, it was pointless to use the elliptical mask and we used the IRAF task `ellipse` to mask the dust-affected pixels of their images. We constrained the center coordinates of these galaxies by using first the IRAF task `imexamine` and then `ellipse`, except for the galaxies with an obscured nucleus. In these cases, we adopted as galaxy center the center of the ellipses we fitted to the bulge isophotes.

The center of 11 of these galaxies was free of dust and there was a little amount of it within $r < 1$ arcsec from the center. It was easily masked out and consequently it did not affect the surface brightness model of the galaxy.

For another 13 galaxies, the galaxy center was not obscured but the region within $r < 1$ arcsec from the center contained a remarkable amount of dust and we were forced to mask large portions of the image. It was a challenging task to build a reliable model of the surface brightness distribution of the galaxy.

NGC 4150, NGC 4212, NGC 4261, and NGC 5127 are characterized by dust filaments crossing exactly the galaxy center which made it impossible to obtain a reliable surface brightness model. We decided to mask the filaments, since no useful information could be retrieved from those regions and we extrapolated the photometric model inward. The central regions of NGC 4150 and NGC 5127 are shown in Fig. 3.3 as an example.

There are 6 galaxies characterized by dust distributed in patchy regions or in filaments within $r < 1$ arcsec from the center that in some cases were partially masked (NGC 0613, NGC 2748, NGC 3801, NGC 4374) and in others were not masked at all (NGC 3351,

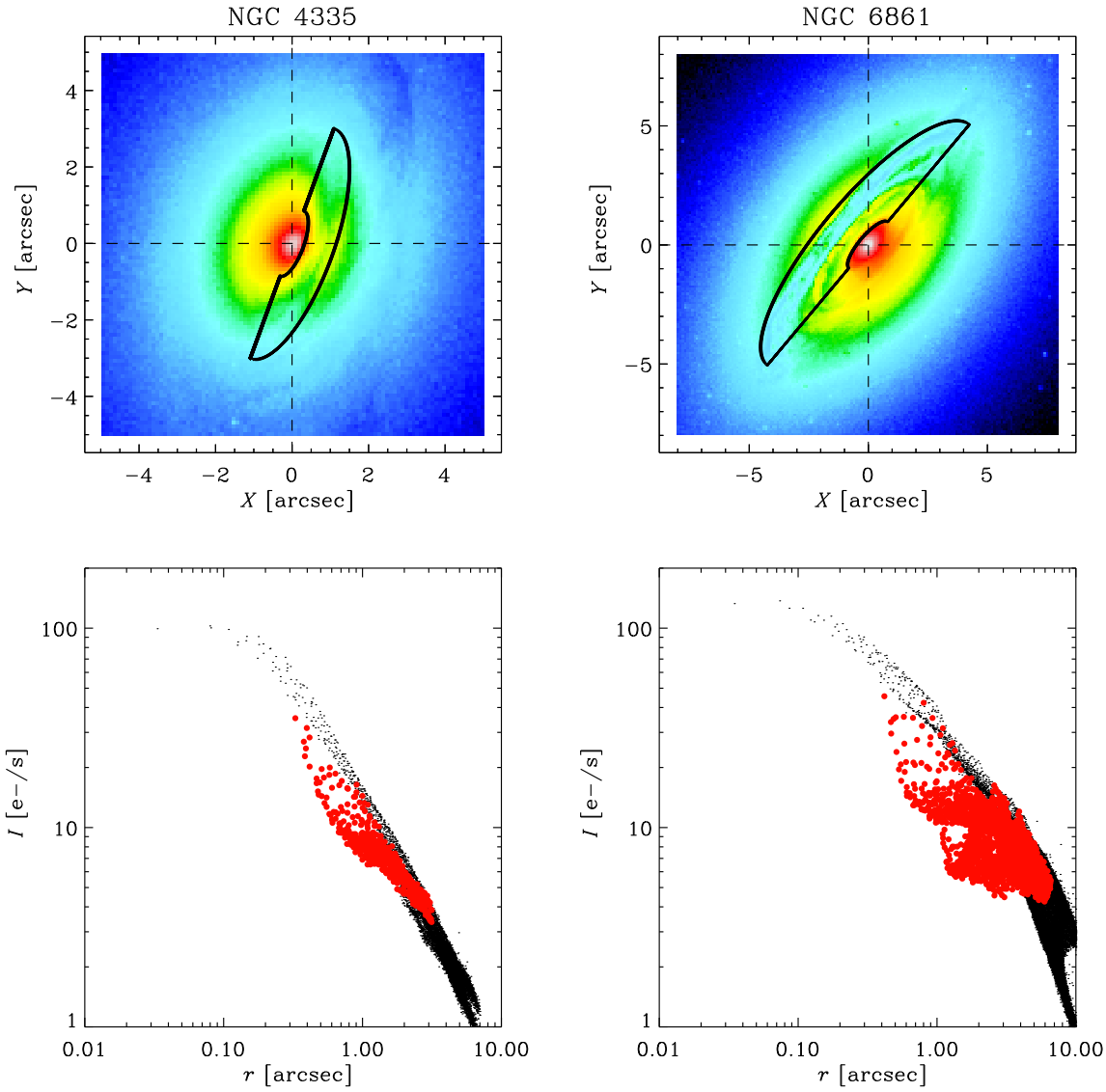

Figure 3.2: *Left-hand panels*: Central portion of the WFPC2/F814W image of NGC 4335 with the contour (black thick line) of the adopted mask (*upper panel*) and surface brightness of the masked (red filled circles) and unmasked pixels (black dots) as a function of their distance from the galaxy center (*lower panel*). The image is oriented with north at the top and east to the left and the size of the field of view is given. The dashed lines mark the galaxy center. *Right-hand panels*: Same as above, but for the WFPC2/F814W image of NGC 6861.

NGC 5194). For these objects can not be excluded the presence of a certain amount of dust on the very center. As a consequence, there could be partial dimming and the stellar contribution could have been underestimated.

We decided not to discard those galaxies for which the dust was not masked in the nuclear

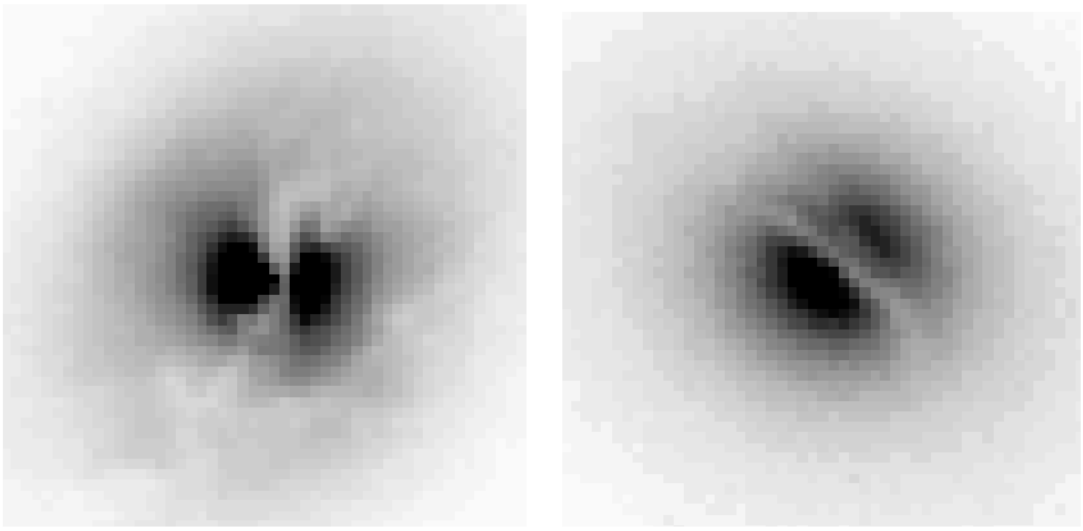

Figure 3.3: Central portion of the WFPC2/F814W images of NGC 4150 (*left-hand panel*) and NGC 5127 (*right-hand panel*). Both images are oriented with the north at the top and the east to the left and have a field of view of 5×5 arcsec^2.

region, noting that in those cases the central stellar mass could have been underestimated. By considering only the dust free objects, our sample should have been composed by only 53 galaxies, whereas here we aimed at having the largest possible sample. This point will be further addressed in future work.

3.3.3 Multi-Gaussian expansion analysis

We modeled the surface brightness distribution of the sample galaxies as a sum of a set of Gaussian components by using the axisymmetric Multi Gaussian Expansion (MGE) IDL[5] algorithm by (Cappellari, 2002). The main advantages of the MGE method are that it leads to a simple model of the intrinsic surface brightness distribution and to a direct deprojection of the intrinsic surface brightness into the luminosity volume density expressed as a sum of a set of Gaussian components too. We built a PSF image with the `TINY TIM` package (Krist et al., 2011) for each combination of camera and filter and we parametrized it as a sum of a set of Gaussians to be used in the MGE fitting process. This is particularly important because we aimed at obtaining the best photometric model of the galaxy nucleus since in the dynamical model we considered only the stellar mass contribution within the central aperture. As a consequence, we carefully set up our MGE models only for the inner regions of the sample galaxies and their extension outwards depend mostly on the morphology of the galaxies (Table 3.1). In fact, we realized that sometimes including the outer galaxy regions in the MGE model led to a less accurate model of the inner regions because of morphological peculiarities, like the presence of dust lanes, an edge-on disk, or prominent spiral arms.

We calculated the center, average ellipticity, and position angle of the galaxy inner

[5]Interactive Data Language is distributed by Harris Geospatial Solutions.

isophotes by fitting them with ellipses with the IRAF task `ellipse`. We gave these values as input for the `sector_photometry` procedure that performed the photometric analysis of the galaxy image along sectors. In this process, we excluded from the analysis the dust-affected pixels masked in Sect. 3.3.2.

We subtracted the sky level from the images in order to obtain sky-subtracted MGE models. We estimated the sky level of the WFC3 and ACS images as the mean value of the surface brightness level measured with the IRAF task `imexamine` in a large number of 5×5-pixel areas free of sources and far from the galaxy to avoid contamination. We then subtracted it from the galaxy image as constant value. The sky level was already subtracted by the automatic `multidrizzle` procedure from the HLA WFPC2 images and its value was stored in the image header. We found that often such a sky level was over-estimated since it was measured in the outer parts of the image and most of the sample galaxies extended beyond the WFPC2 field of view. So we added the sky value from the header to the galaxy image and we subtracted the sky value tabulated by McMaster et al. (2008) by taking into account for the different instrumental configurations. We also subtracted these tabulated sky values from the single WFPC2 images we drizzled.

For most sample galaxies, we ran the `mge_fit_sectors_regularized` procedure which calls repeatedly the `mge_fit_sectors` procedure to restrict the range of the resulting observed axial ratios of the Gaussian components and keep the fit acceptable. When this was not required, especially for ellipticals or old bulges with regular light distribution and no dust (see the MGE model of UGC 7115 in Fig. 3.4 as an example), we employed only the `mge_fit_sectors` procedure.

A few MGE models are plotted in Fig. 3.4 as example. We show one example for each adopted combination of camera and filter to point out different peculiarities. NGC 1497 is crossed by a dust lane although it does not obscure the galaxy center. NGC 1358 shows the correction of cosmic rays that we performed by running the `lacos_im` procedure on single WFPC2 images. NGC 3245 needed an elliptical dust mask where only the innermost pixels were not rejected. NGC 3259 is an example of a late-type spiral for which we modeled only the central regions because of the bright spiral arms present in the disk. NGC 3368 has several dust filaments which we masked out to the very center of the galaxy. NGC 3393 shows some dust filaments which are near to the galaxy center but do not obscure it. Finally, NGC 4143 and UGC 7115 exemplify two cases of perfect central MGE models.

For each galaxy image, we obtained with MGE the total luminosity $C_{\rm tot}$ in electrons $\rm s^{-1}$, the dispersion σ in pixels, and the observed axial ratio $q_{\rm obs}$ of all the Gaussians fitting the surface brightness distribution of the galaxy.

Firstly, we derived the central surface brightness C_0 in electrons $\rm s^{-1}$ $\rm pixel^{-1}$ as

$$C_0 = \frac{C_{\rm tot}}{2\pi\sigma^2 q_{\rm obs}} \tag{3.1}$$

and we converted it in mag $\rm arcsec^{-2}$ in the I band as

$$\mu_{0,I} = -2.5 \log\left(\frac{C_0}{G \cdot s^2}\right) + z_{\rm cal} - A_I + CC_{\rm syn} \tag{3.2}$$

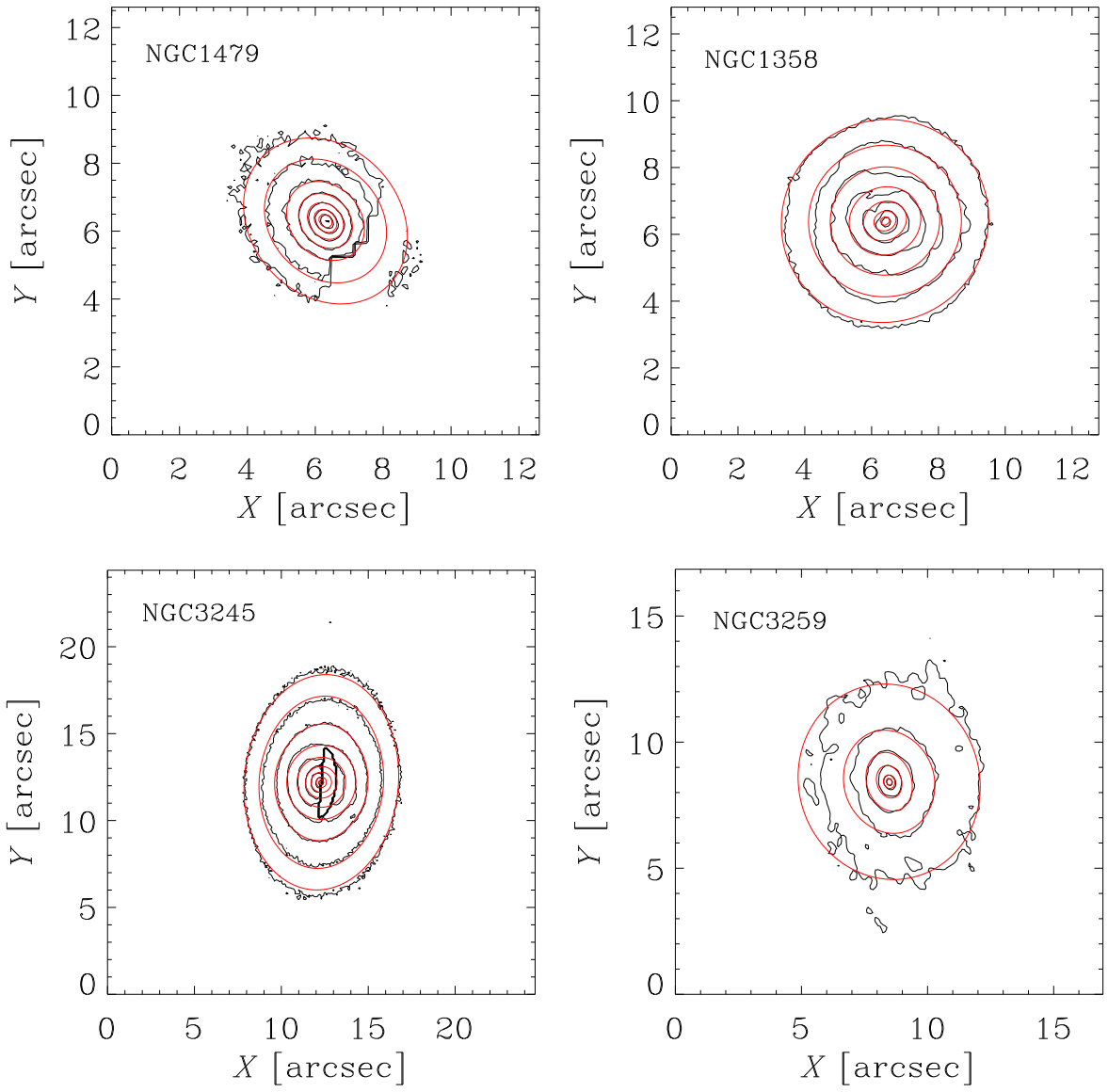

Figure 3.4: Few reference isophotes in the central portion of the images (black lines) and MGE models (red lines) of some sample galaxies. The images are oriented with north at the top and east to the left and the size of their field of view is given. Flux levels are normalized to the central surface brightness of the image and the contours are spaced by 0.5 mag arcsec^{-2}. While the MGE models were constrained using the original images, the images shown here are binned to reduce the noise for the comparison purposes only. The missing portions of the galaxy isophotes correspond to masked regions. NGC 1497 was imaged with WFPC2/F791W, NGC 1358 with WFPC2/F606W, NGC 3245 with WFPC2/F702W, and NGC 3259 with ACS/F814W.

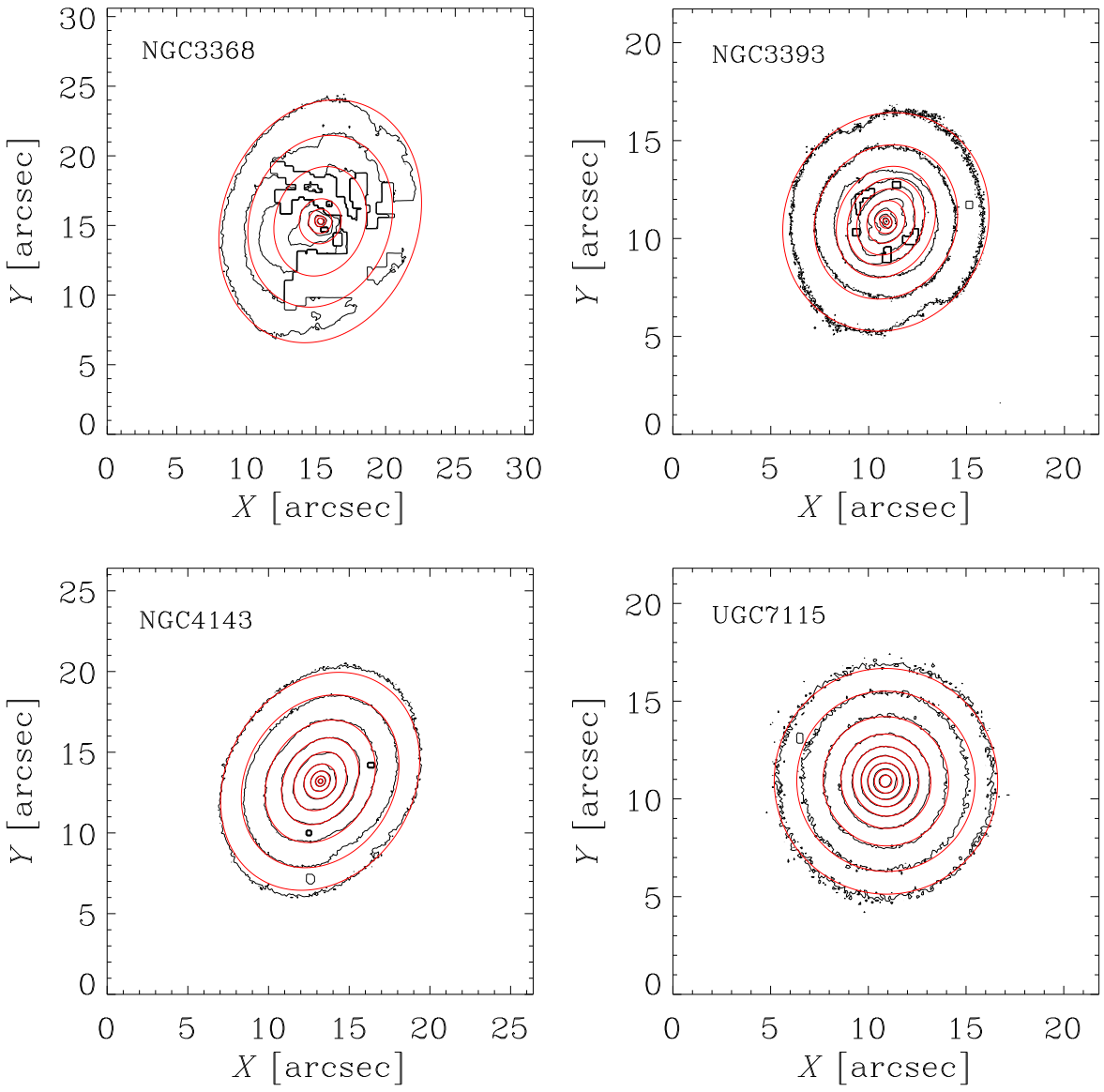

Figure 3.4: Continued. NGC 3368 was imaged with WFPC2/F814W, NGC 3393 with WFC3/F814W, NGC 4143 with WFPC2/F606W, and UGC 7115 with WFPC2/F814W.

where G is the gain in electron ADU^{-1} from the image header, s is the plate scale in arcsec pixel^{-1} from the image header, $z_{\rm cal}$ is the calibration constant in the Vegamag photometric system from the image header, A_I is the Johnson-Cousins I-band extinction term retrieved from Schlafly & Finkbeiner (2011) and $CC_{\rm syn}$ is the color correction needed to convert magnitudes from the Vegamag to Johnson-Cousins photometric system which we calculated with `synphot` IRAF package. In particular, the adopted values of G and s depends on the camera, $z_{\rm cal}$ on the camera and filter, A_I on the filter and galaxy coordinates, and $CC_{\rm syn}$ on the the filter and galaxy morphological type. For $CC_{\rm syn}$ we used the Kinney-Calzetti Spectral Atlas of Galaxies (Calzetti et al., 1994; Kinney et al., 1996).

We converted the central surface brightness from mag arcsec^{-2} to L$_\odot$ pc^{-2} as

$$I_0 = \left(\frac{64800}{\pi}\right)^2 \cdot 10^{-0.4(\mu_I - M_{\odot,I})} \tag{3.3}$$

where $M_{\odot,I} = 4.08$ mag is the absolute magnitude for the Sun in the I band.

We circularized the MGE models:

$$\sigma_{\rm circ} = \sigma\sqrt{q_{\rm obs}} \tag{3.4}$$

as this was a good approximation for the nuclear regions. We modeled only the central part of all the sample galaxies in order to make this correction shallower. Finally, we converted the $\sigma_{\rm circ}$ to parsecs by using the distance of each galaxy. The values of I_0 (L$_\odot$ pc^{-2}) and $\sigma_{\rm circ}$(pc) of each Gaussian were provided as inputs to the dynamical model.

Table 3.1: Results from the MGE and flux profile analysis.

Galaxy	Mor. T.	Camera/Detector	Filter	Dust	σ [pc]	MGE Fit	[NII]λ6583 Flux
(1)	(2)	(3)	(4)	(5)	(6)	(7)	(8)
IC 0342	SABcd(rs)	WFPC2/PC	F814W	-	132.236	uf	g
IC 3639	SBbc(rs):	WFPC2/PC	F606W	-	713.587	rc	c
NGC 0193	SAB0$^-$(s):	WFPC2/PC	F814W	sm	754.090	-	n
NGC 0289	SBbc(rs)	WFPC2/PC	F606W	sm	728.344	-	n
NGC 0315	E$^+$:	WFPC2/PC	F814W	nm, em	1162.19	-	g
NGC 0383	SA0$^-$:	WFPC2/PC	F814W	em	1099.51	-	g
NGC 0541	S0$^-$:	WFPC2/PC	F814W	dm	27852.8	-	g
NGC 0613	SBbc(rs)	WFPC2/WF3	F814W	nm, dm	653.014	-	c
NGC 0741	E0:	WFPC2/PC	F814W	-	1405.50	ng	g
NGC 0788	SA0/a(s)	WFPC2/PC	F606W	-	3529.04	rc	a
NGC 1358	SAB0/a(r)	WFPC2/PC	F606W	-	1047.03	rc	g
NGC 1497	S0	WFPC2/PC	F791W	-	699.058	rc	g
NGC 1667	SAB(r)c	WFPC2/PC	F606W	sm	987.574	rc	a
NGC 1961	SABc(rs)	WFPC2/PC	F606W	dm	1029.06	-	g
NGC 2110	SAB0$^-$	WFPC2/PC	F791W	em	498.967	-	a
NGC 2179	SA0/a(s)	WFPC2/PC	F606W	sm	607.634	-	a
NGC 2273	SBa(r):	WFPC2/PC	F791W	sm	1324.50	-	g
NGC 2329	S0$^-$:	WFPC2/PC	F814W	dm	3956.34	-	g
NGC 2654	SBab:sp	WFPC2/PC	F814W	-	202.186	-	g
NGC 2685	(R)SB0$^+$pec	WFPC2/PC	F814W	-	319.750	-	g
NGC 2748	SAbc	WFPC2/WF3	F814W	nm, sm	544.482	-	g
NGC 2787	SB0$^+$(r)	WFPC2/PC	F814W	-	238.993	-	g
NGC 2892	E$^+$pec:	WFPC2/PC	F814W	-	1319.95	-	g
NGC 2903	SABbc(rs)	WFPC2/PC	F814W	dm	132.016	uf	g
NGC 2964	SABbc(r):	WFPC2/WF3	F814W	sm	515.249	-	a
NGC 3021	SAbc(rs)	WFC3/UVIS	F814W	-	224.485	rc	g
NGC 3078	E2-3	WFPC2/PC	F702W	dm	990.831	-	g

Table 3.1 – Continued

Galaxy	Mor. T.	Camera/Detector	Filter	Dust	σ [pc]	MGE Fit	[NII]λ6583 Flux
(1)	(2)	(3)	(4)	(5)	(6)	(7)	(8)
NGC 3081	(R)SAB0/a(r)	WFPC2/WF3	F814W	-	429.957	-	g
NGC 3245	SA0^0(r):?	WFPC2/PC	F702W	em	354.886	rc	i
NGC 3259	SABbc(rs)	ACS/WFC	F814W	-	428.998	-	g
NGC 3310	SABbc(r) pec	WFPC2/PC	F814W	-	146.662	-	g
NGC 3351	SBb(r)	WFPC2/PC	F606W	nm	873.401	-	g
NGC 3368	SABab(rs)	WFPC2/WF3	F814W	sm	392.968	-	g
NGC 3393	(R′)SBa(rs):	WFC3/UVIS	F814W	-	1157.24	-	a
NGC 3627	SABb(s)	WFPC2/WF4	F814W	sm	337.774	-	n
NGC 3642	SAbc(r):	ACS/WFC	F814W	-	495.649	mc	g
NGC 3675	SAb(s)	WFPC2/PC	F606W	dm	374.984	-	g
NGC 3801	S0?	WFPC2/PC	F814W	nm, sm	2134.73	uf	a
NGC 3862	E	WFPC2/PC	F791W	sm	2112.50	-	g
NGC 3982	SABb(r):	WFPC2/WF3	F814W	-	423.695	-	n
NGC 3998	SA0^0(r)?	WFPC2/PC	F791W	-	447.349	-	g
NGC 4036	S0^-	WFPC2/WF4	F814W	-	430.501	-	g
NGC 4041	SAbc(rs):	WFPC2/WF3	F814W	-	262.202	-	c
NGC 4143	SAB0^0(s)	WFPC2/PC	F606W	-	336.058	-	g
NGC 4150	SA0^0(r)?	WFPC2/PC	F814W	cm	466.010	-	i
NGC 4203	SAB0^-:	WFPC2/PC	F814W	-	355.395	-	n
NGC 4212	SAc:	WFPC2/PC	F606W	cm, sm	52.4606	uf	f
NGC 4245	SB0/a(r):	WFPC2/PC	F606W	sm	282.017	-	f
NGC 4258	SABbc(s)	WFPC2/PC	F606W	-	177.667	-	g
NGC 4261	E2-3	WFPC2/WF3	F814W	cm	2390.92	uf	c
NGC 4278	E1-2	WFPC2/PC	F814W	-	930.689	-	c
NGC 4314	SBa(rs)	WFPC2/PC	F814W	-	251.971	-	i
NGC 4321	SABbc(s)	WFPC2/PC	F702W	dm	216.657	-	g
NGC 4335	E	WFPC2/PC	F814W	em	806.469	-	g
NGC 4343	SAb(rs):	WFPC2/PC	F814W	em	464.718	-	g

Table 3.1 – Continued

Galaxy	Mor. T.	Camera/Detector	Filter	Dust	σ [pc]	MGE Fit	[NII]λ6583 Flux
(1)	(2)	(3)	(4)	(5)	(6)	(7)	(8)
NGC 4374	E1	WFPC2/PC	F814W	nm, sm	1181.96	-	n
NGC 4429	SA0$^+$(r)	WFPC2/PC	F606W	em	460.463	-	g
NGC 4435	SB0^0(s)	WFPC2/PC	F814W	em	392.030	-	g
NGC 4450	SAab(s)	WFPC2/PC	F814W	-	390.371	-	g
NGC 4459	SA0$^+$(r)	WFPC2/PC	F814W	em	615.754	-	g
NGC 4477	SB0(s):?	WFPC2/PC	F606W	-	364.496	-	g
NGC 4486	E$^+$0-1 pec	WFPC2/PC	F814W	-	639.163	-	c
NGC 4501	SAb(rs)	WFPC2/PC	F606W	-	408.296	-	c
NGC 4507	(R′)SABb(rs)	WFPC2/PC	F814W	em	488.301	-	g
NGC 4526	SAB0(s):	WFPC2/PC	F814W	em	844.366	-	g
NGC 4552	E0-1	WFPC2/PC	F814W	-	550.821	-	n
NGC 4579	SABb(rs)	WFPC2/PC	F791W	dm	1129.00	-	g
NGC 4594	SAa(s) sp	WFPC2/PC	F814W	-	136.068	-	g
NGC 4596	SB0$^+$(r)	WFPC2/PC	F606W	-	563.599	-	g
NGC 4636	E0-1	WFPC2/PC	F814W	-	749.339	-	g
NGC 4698	SAab(s)	WFPC2/WF3	F814W	-	543.798	-	c
NGC 4800	SAb(rs)	WFPC2/PC	F606W	-	193.527	-	n
NGC 5005	SABbc(rs)	WFPC2/PC	F606W	em	722.482	uf	c
NGC 5077	E3-4	WFPC2/PC	F702W	-	2016.28	ng	g
NGC 5127	E pec	WFPC2/PC	F814W	cm	2191.41	-	g
NGC 5141	S0	WFPC2/PC	F814W	-	1905.92	-	g
NGC 5194	SAbc(s) pec	WFPC2/WF3	F814W	nm	410.273	-	f
NGC 5248	SABbc(rs)	WFPC2/PC	F814W	-	443.089	-	g
NGC 5252	S0	WFPC2/PC	F606W	-	997.768	rc	a
NGC 5283	S0?	WFPC2/PC	F702W	-	943.160	-	g
NGC 5347	(R′)SBab(rs)	WFPC2/PC	F606W	-	581.422	rc	g
NGC 5427	SAc(s)pec	WFPC2/PC	F606W	-	351.315	rc	g
NGC 5490	E	WFPC2/PC	F814W	-	5666.15	-	g

Table 3.1 – Continued

Galaxy	Mor. T.	Camera/Detector	Filter	Dust	σ [pc]	MGE Fit	[NII]λ6583 Flux
(1)	(2)	(3)	(4)	(5)	(6)	(7)	(8)
NGC 5635	S pec	WFPC2/WF2	F791W	-	553.502	rc	g
NGC 5643	SABc(rs)	WFPC2/PC	F606W	-	203.454	-	a
NGC 5695	S?	WFPC2/PC	F606W	-	836.661	rc	g
NGC 5728	SABa(r):	WFC3/UVIS	F814W	sm	573.918	-	f
NGC 5879	SAbc(rs):?	WFPC2/PC	F814W	dm	124.104	-	g
NGC 6300	SBb(rs)	WFPC2/WF3	F814W	dm	251.413	-	a
NGC 6861	SA0$^-$(s):	WFPC2/PC	F814W	em	992.468	-	g
NGC 6951	SABbc(rs)	WFPC2/WF4	F814W	-	258.310	-	c
NGC 7052	E	WFPC2/PC	F814W	em	4289.17	-	a
NGC 7331	SAb(s)	WFPC2/PC	F814W	-	453.129	-	i
NGC 7626	E pec:	WFPC2/PC	F814W	-	1024.63	-	g
NGC 7682	SBab(r)	WFPC2/PC	F606W	dm	773.189	rc	i
UGC 1214	(R$'$)SAB0$^+$(rs):	WFPC2/PC	F814W	-	1556.61	rc	g
UGC 1395	SAb(rs)	WFPC2/PC	F606W	-	598.707	rc	g
UGC 1841	E	WFPC2/PC	F814W	-	1275.45	-	g
UGC 7115	E	WFPC2/PC	F814W	-	1770.18	-	g
UGC 12064	S0$^-$:	WFPC2/PC	F702W	em	1805.67	-	g

Notes: Col.(1): galaxy name. Col.(2): morphological type from de Vaucouleurs et al. (1991, RC3). Col.(3): Camera and detector which targeted the galaxy center. Col.(4): broad-band filter mounted during the observation. Col.(5): dust distribution and properties of the dust mask in the central region of the galaxy: dm = the dust mask extends inwards and the region within 1 arcsec from the galaxy center has been slightly masked; sm = the region within 1 arcsec from the galaxy center has been severely masked; em = the dust mask has the shape of an half-elliptical annulus and extends inwards in the region within 1 arcsec from the galaxy center; nm = some dust lane/filaments within 1 arcsec from the galaxy center were not masked; cm = some dust lane/filaments crossing the galaxy center were masked and the MGE photometric model was extrapolated inward. Col.(6): circularized σ of the outermost Gaussian used in the MGE photometric model and adopting the galaxy distance given in Table 3.3. Col.(7): notes about the MGE fit: rc = the cosmic rays were removed with `lacos_im` from the single exposure image; mc = the residual cosmic rays were successfully masked; ng = a nearby galaxy was masked; uf = uncertain MGE fit in the central region because of the presence of star clumps

rather than a well-defined galaxy nucleus and/or a complicated dust pattern. Col.(8): notes about the shape of the radial profile of [NII]λ6583 flux: g = Gaussian profile; n = irregular Gaussian profile; c = only the central points were considered for the Gaussian fit; f = only a few points were considered for the Gaussian fit; a = asymmetric Gaussian profile; i = very irregular profile (i.e., the galaxy was removed from the sample).

Table 3.2: Properties of the galaxies rejected from the sample.

Galaxy (1)	Comment (2)
NGC 1052	only ACS/F250W, ACS/F330W, and WFPC2/F658N available images
NGC 2911	only WFPC2/F547M and WPFC2/FR680N available images
NGC 3031	saturated ACS/F606W images
NGC 3049	no images
NGC 3227	saturated WFPC2/F606W images
NGC 3953	no nucleus
NGC 3992	only WFPC2/F218W and WFPC2/F547M available images
NGC 4088	no images
NGC 4548	no nucleus
NGC 4736	saturated WFPC2/F814W images
NGC 4826	saturated WFPC2/F814W images
NGC 5713	no images
NGC 5921	no images
NGC 6500	only ACS/F250W, ACS/F330W, WFPC2/F218W, WFPC2/F547M, and WFPC2/FR680N available images

Notes: Col.(1): galaxy name. Col.(2): reason for rejection: no images = no image of the galaxy is available in the HLA; no nucleus = the nucleus is not within the field of view of the HLA broad-band images of the galaxy; saturated images = the nucleus is saturated in the HLA broad-band images of the galaxy; only available images = only narrow-band and/or ultraviolet broad-band images of the galaxy obtained with WFPC2, WFC3, and ACS are available in the HLA.

Table 3.3: Galaxy properties and results for $M_\bullet$.

Galaxy	D [Mpc]	σ_e [km s^{-1}]	Apert. [arcsec]	$M_\bullet$ [33°] [$M_\odot$]	$M_\bullet$ [81°] [$M_\odot$]	$M_{\bullet,\star}$ [33°] [$M_\odot$]	$M_{\bullet,\star}$ [81°] [$M_\odot$]	$M_{\bullet,\mathrm{reskin}}$ [$M_\odot$]	Ref.
(1)	(2)	(3)	(4)	(5)	(6)	(7)	(8)	(9)	(10)
IC 0342	4.3	65 ± 24	0.1×0.15	4.1E6	1.4E6	1.5E6	1.0E5	$<$ 1E6	CO, 3
IC 3639	51.4	91 ± 5	0.2×0.25	2.8E7	5.2E6	2.7E7	5.0E6	-	-
NGC 0193	57.0	185 ± 17	0.2×0.30	9.0E8	2.9E8	8.8E8	2.7E8	-	-
NGC 0289	19.6	109 ± 12	0.2×0.25	5.8E7	1.4E7	5.1E7	9.1E6	-	-
NGC 0315	66.2	313 ± 27	0.1×0.15	1.3E9	2.3E8	1.3E9	2.2E8	-	-
NGC 0383	67.9	239 ± 17	0.1×0.15	1.0E9	2.9E8	1.0E9	2.8E8	-	-
NGC 0541	73.1	191 ± 4	0.2×0.30	1.3E9	3.8E8	1.3E9	3.5E8	-	-
NGC 0613	17.7	125 ± 19	0.2×0.25	1.2E8	2.6E7	1.2E8	2.6E7	-	-
NGC 0741	75.4	232 ± 11	0.2×0.30	1.3E9	2.4E8	1.3E9	2.4E8	-	-
NGC 0788	55.0	127 ± 18	0.2×0.25	3.2E8	6.4E7	2.9E8	4.3E7	-	-
NGC 1358	55.3	172 ± 19	0.2×0.25	5.8E8	1.3E8	5.1E8	8.4E7	-	-
NGC 1497	86.4	246 ± 23	0.1×0.15	7.3E8	3.0E8	7.2E8	2.9E8	-	-
NGC 1667	64.4	178 ± 29	0.2×0.25	2.9E8	1.1E8	2.5E8	6.6E7	-	-
NGC 1961	55.8	222 ± 38	0.2×0.30	6.5E8	1.8E8	6.5E8	1.7E8	-	-
NGC 2110	33.4	201 ± 23	0.2×0.25	7.4E8	1.9E8	7.4E8	1.9E8	-	-
NGC 2179	41.1	154 ± 11	0.2×0.25	3.7E8	1.3E8	3.5E8	1.2E8	-	-
NGC 2273	26.8	117 ± 11	0.2×0.25	7.3E6	2.2E6	1.0E5	1.0E5	7.82($\pm$0.42)E6	m, 18
NGC 2329	83.0	218 ± 13	0.2×0.30	4.5E8	2.7E8	4.4E8	2.0E8	-	-
NGC 2654	20.8	162 ± 3	0.1×0.15	2.0E7	4.5E6	2.0E7	4.0E6	-	-
NGC 2685	14.4	82 ± 7	0.2×0.30	1.6E7	3.3E6	1.4E7	1.5E6	-	-
NGC 2748	21.3	115 ± 5	0.2×0.25	1.6E7	5.0E6	1.6E7	4.4E6	4.04(-1.66;+1.60)E7	g, 8
NGC 2787	8.0	189 ± 9	0.2×0.25	1.0E8	2.4E7	1.0E8	2.1E7	4.37(-0.56;+0.43)E7	g, 5
NGC 2892	99.0	297 ± 19	0.2×0.30	5.8E8	5.7E8	5.8E8	5.4E8	-	-
NGC 2903	12.0	94 ± 12	0.2×0.30	3.4E7	1.4E7	2.5E7	4.9E6	-	-
NGC 2964	22.6	95 ± 19	0.2×0.25	2.7E7	4.8E6	2.6E7	4.2E6	-	-
NGC 3021	25.7	56 ± 25	0.2×0.25	4.3E7	1.1E7	1.2E7	1.0E5	-	-
NGC 3078	37.7	208 ± 12	0.2×0.30	4.3E8	8.5E7	4.0E8	6.9E7	-	-

Table 3.3 – Continued

Galaxy	D	σ_e	Apert.	$M_\bullet$ [33°]	$M_\bullet$ [81°]	$M_{\bullet,\star}$ [33°]	$M_{\bullet,\star}$ [81°]	$M_{\bullet,\mathrm{reskin}}$	Ref.
	[Mpc]	[km s^{-1}]	[arcsec]	[$M_\odot$]	[$M_\odot$]	[$M_\odot$]	[$M_\odot$]	[$M_\odot$]	
(1)	(2)	(3)	(4)	(5)	(6)	(7)	(8)	(9)	(10)
NGC 3081	38.5	123 ± 8	0.2×0.25	3.6E7	9.0E6	2.3E7	1.0E5	-	-
NGC 3245	22.4	205 ± 10	0.2×0.25	2.2E8	9.3E7	1.4E8	1.1E7	2.50(-0.80;+0.28)E8	g, 4
NGC 3259	25.7	63 ± 6	0.2×0.25	3.9E6	1.3E6	1.1E6	1.0E5	-	-
NGC 3310	16.7	83 ± 4	0.2×0.30	1.9E7	1.0E7	1.0E5	1.0E5	$<$ 4.0E7	g, 12
NGC 3351	10.7	95 ± 15	0.2×0.25	9.0E6	2.8E6	7.6E6	1.4E6	-	-
NGC 3368	11.1	105 ± 4	0.2×0.25	4.6E7	1.4E7	4.1E7	9.6E6	8.00($\pm$1.13)E6	s, 23
NGC 3393	58.1	168 ± 26	0.2×0.25	2.4E8	9.9E7	1.6E8	1.2E7	1.85(-1.17;+1.16)E7	g, 16
NGC 3627	10.8	97 ± 8	0.2×0.30	2.7E7	1.5E7	2.6E7	1.2E7	9.12($\pm$1.20)E6	s, 23
NGC 3642	24.9	96 ± 25	0.2×0.25	3.0E7	2.6E7	3.0E7	2.2E7	-	-
NGC 3675	14.2	105 ± 4	0.2×0.30	4.6E7	1.8E7	3.4E7	3.9E6	-	-
NGC 3801	53.1	210 ± 18	0.2×0.30	7.1E8	2.4E8	7.0E8	2.4E8	-	-
NGC 3862	97.1	210 ± 13	0.2×0.30	1.2E9	3.1E8	8.9E8	3.9E7	-	-
NGC 3982	18.2	78 ± 2	0.2×0.25	1.8E7	5.5E6	8.3E6	1.0E5	-	-
NGC 3998	15.1	305 ± 15	0.1×0.15	3.6E8	4.3E7	3.5E8	4.1E7	8.92(-0.70;-0.74)E8	s, 19
NGC 4036	21.9	164 ± 5	0.2×0.25	2.0E8	3.9E7	2.0E8	3.8E7	-	-
NGC 4041	19.5	88 ± 4	0.2×0.25	3.5E6	7.9E5	3.1E6	3.9E5	$<$ 2.0E7	g, 7
NGC 4143	17.0	201 ± 6	0.2×0.25	2.2E8	4.3E7	2.1E8	3.7E7	-	-
NGC 4150	14.7	86 ± 3	0.2×0.30	2.3E7	4.4E6	2.3E7	4.3E6	-	-
NGC 4203	16.2	157 ± 3	0.2×0.25	1.4E8	4.2E7	1.1E8	1.7E7	$<$ 8.7E7	g, 5
NGC 4212	3.6	68 ± 3	0.2×0.25	2.2E6	3.4E5	2.2E6	3.4E5	-	-
NGC 4245	16.7	83 ± 3	0.2×0.25	3.7E7	5.1E6	3.7E7	5.0E6	-	-
NGC 4258	7.8	115 ± 10	0.2×0.25	5.2E7	9.8E6	5.1E7	9.4E6	4.09($\pm$0.04)E7	m, 10
NGC 4261	33.9	315 ± 15	0.1×0.15	3.1E8	9.4E7	3.1E8	9.4E7	5.54(-1.13;+1.12)E8	g, 1
NGC 4278	17.2	233 ± 7	0.2×0.25	1.9E8	5.5E7	1.9E8	5.5E7	-	-
NGC 4314	17.8	107 ± 4	0.2×0.25	1.9E7	4.8E6	1.2E7	1.0E5	-	-
NGC 4321	16.3	83 ± 4	0.2×0.25	1.8E7	3.6E6	1.4E7	1.1E6	-	-
NGC 4335	67.8	259 ± 5	0.2×0.30	9.2E8	2.9E8	7.7E8	1.4E8	$<$ 6.0E7	g, 6
NGC 4343	19.4	154 ± 5	0.2×0.25	6.9E7	5.5E7	6.1E7	2.9E7	-	-

Table 3.3 – Continued

Galaxy	D	σ_e	Apert.	$M_\bullet$ [33°]	$M_\bullet$ [81°]	$M_{\bullet,\star}$ [33°]	$M_{\bullet,\star}$ [81°]	$M_{\bullet,\mathrm{reskin}}$	Ref.
	[Mpc]	[km s^{-1}]	[arcsec]	[$M_\odot$]	[$M_\odot$]	[$M_\odot$]	[$M_\odot$]	[$M_\odot$]	
(1)	(2)	(3)	(4)	(5)	(6)	(7)	(8)	(9)	(10)
NGC 4374	19.7	296 ± 14	0.2×0.25	1.4E9	5.0E8	1.4E9	4.9E8	9.84(-0.93;+1.04)E8	g, 15
NGC 4429	20.9	170 ± 7	0.2×0.30	1.4E8	3.8E7	6.2E7	1.0E5	-	-
NGC 4435	15.9	150 ± 7	0.2×0.25	3.4E7	6.2E6	3.3E7	5.8E6	< 7.5E6	g, 11
NGC 4450	32.5	108 ± 15	0.2×0.25	2.5E8	7.0E7	1.4E8	1.0E5	-	-
NGC 4459	17.2	167 ± 8	0.2×0.25	2.8E8	3.2E7	2.5E8	2.7E7	7.48(-1.44;+1.43)E7	g, 5
NGC 4477	23.9	145 ± 9	0.2×0.25	1.1E8	2.9E7	1.0E8	2.2E7	-	-
NGC 4486	17.0	375 ± 18	0.2×0.25	3.0E9	9.4E8	3.0E9	9.0E8	3.32(-0.66;+0.85)E9	g, 22
NGC 4501	37.1	140 ± 16	0.2×0.25	8.7E7	6.8E7	1.7E7	6.2E6	4.50($\pm$2.70)E7	s, 23
NGC 4507	54.0	144 ± 7	0.2×0.25	3.9E7	8.0E6	1.0E5	1.0E5	-	-
NGC 4526	18.1	195 ± 3	0.2×0.25	3.5E8	6.6E7	3.5E8	6.5E7	4.97(-1.13;+1.54)E8	CO, 20
NGC 4552	16.5	234 ± 11	0.2×0.25	1.8E9	6.2E8	1.8E9	6.1E8	5.19($\pm$0.52)	s, 14
NGC 4579	26.4	110 ± 15	0.2×0.25	2.4E8	4.5E7	2.3E8	3.7E7	-	-
NGC 4594	10.5	240 ± 12	0.1×0.15	6.8E8	2.4E8	6.8E8	2.4E8	7.07(-0.44;+0.43)E8	s, 17
NGC 4596	31.4	136 ± 6	0.2×0.25	2.2E8	4.4E7	1.9E8	2.5E7	1.46(-0.62;+0.71)E8	g, 5
NGC 4636	15.7	174 ± 9	0.2×0.25	5.0E8	2.0E8	5.0E8	2.0E8	-	-
NGC 4698	18.9	124 ± 8	0.2×0.25	8.5E7	4.6E7	6.6E7	2.2E7	-	-
NGC 4800	14.4	102 ± 2	0.2×0.25	4.2E7	3.6E6	4.2E7	3.5E6	-	-
NGC 5005	16.8	198 ± 7	0.2×0.25	3.1E8	6.5E7	3.1E8	6.3E7	-	-
NGC 5077	44.9	222 ± 11	0.1×0.15	1.7E9	4.6E8	1.7E9	4.6E8	9.92(-5.20;+5.08)E8	g, 13
NGC 5127	71.8	199 ± 49	0.2×0.30	5.8E8	1.4E8	5.8E8	1.4E8	-	-
NGC 5141	77.6	154 ± 5	0.2×0.30	6.7E8	2.1E8	5.9E8	1.3E8	-	-
NGC 5194	9.1	70 ± 9	0.2×0.25	2.4E6	4.6E5	2.4E6	4.6E5	-	-
NGC 5248	20.6	127 ± 11	0.2×0.25	7.1E6	1.3E6	6.3E6	8.3E5	-	-
NGC 5252	102.5	169 ± 24	0.2×0.25	7.7E8	1.4E8	6.4E8	6.3E7	1.06(-5.01;+16.15)E9	g, 9
NGC 5283	39.6	136 ± 13	0.2×0.25	4.9E7	1.1E7	1.0E5	1.0E5	-	-
NGC 5347	37.1	65 ± 12	0.2×0.25	3.8E7	5.4E6	1.0E5	1.0E5	-	-
NGC 5427	41.7	65 ± 11	0.2×0.25	8.7E7	2.2E7	6.7E7	6.4E6	-	-
NGC 5490	75.0	261 ± 25	0.2×0.30	2.4E9	6.2E8	2.3E9	5.9E8	-	-

Table 3.3 – Continued

Galaxy	D	σ_e	Apert.	$M_\bullet$ [33°]	$M_\bullet$ [81°]	$M_{\bullet,\star}$ [33°]	$M_{\bullet,\star}$ [81°]	$M_{\bullet,\mathrm{reskin}}$	Ref.
	[Mpc]	[km s^{-1}]	[arcsec]	[M$_\odot$]	[M$_\odot$]	[M$_\odot$]	[M$_\odot$]	[M$_\odot$]	
(1)	(2)	(3)	(4)	(5)	(6)	(7)	(8)	(9)	(10)
NGC 5635	64.4	216 ± 5	0.1×0.15	1.2E9	3.1E8	1.2E9	3.0E8	-	-
NGC 5643	19.9	90 ± 1	0.2×0.25	5.0E7	3.3E6	4.8E7	3.2E6	-	-
NGC 5695	62.7	143 ± 2	0.2×0.25	9.5E7	2.1E7	1.0E5	1.0E5	-	-
NGC 5728	43.2	193 ± 40	0.1×0.15	1.8E8	6.0E7	1.7E8	5.5E7	-	-
NGC 5879	12.2	54 ± 8	0.2×0.30	1.4E7	5.0E6	1.4E7	4.9E6	-	-
NGC 6300	16.3	87 ± 5	0.2×0.25	2.6E7	1.0E7	2.5E7	8.3E6	-	-
NGC 6861	30.1	404 ± 36	0.2×0.30	2.9E9	8.8E8	2.9E9	8.7E8	2.20(-0.10;+0.66)E9	s, 21
NGC 6951	18.3	96 ± 10.0	0.2×0.25	1.5E7	6.1E6	1.4E7	2.7E6	-	-
NGC 7052	66.1	266 ± 13	0.1×0.15	9.6E8	3.2E8	9.6E8	3.2E8	3.72(-1.46;+2.59)E8	g, 2
NGC 7331	14.0	116 ± 4	0.2×0.25	3.1E8	1.5E8	2.4E8	7.5E7	-	-
NGC 7626	43.7	233 ± 11	0.2×0.30	1.5E9	4.5E8	1.5E9	4.3E8	-	-
NGC 7682	68.0	113 ± 16	0.2×0.25	3.8E8	8.6E7	2.3E8	1.0E5	-	-
UGC 1214	68.8	107 ± 14	0.2×0.25	1.5E8	4.1E7	4.5E7	1.0E5	-	-
UGC 1395	69.9	64 ± 6	0.2×0.25	1.4E7	3.9E6	1.0E5	1.0E5	-	-
UGC 1841	86.0	295 ± 25	0.2×0.30	7.1E8	5.2E8	7.1E8	4.9E8	-	-
UGC 7115	101.2	183 ± 34	0.2×0.30	4.9E9	9.7E8	4.8E9	9.3E8	-	-
UGC 12064	69.0	259 ± 18	0.1×0.15	2.6E9	2.8E8	2.6E9	2.7E8	-	-

Notes: Col.(1): galaxy name. Col.(2): distance from B09 and B12, rescaled to $H_0 = 70$ km s^{-1} Mpc^{-1}. Col.(3): stellar effective velocity dispersion from B12. Col.(4): size of the central aperture. Col.(5): $M_\bullet$ stringent limit measured by disregarding the stellar mass in the dynamical model and assuming $i = 33°$ for the unresolved gaseous disk. Col.(6): $M_\bullet$ stringent limit measured by disregarding the stellar mass in the dynamical model and assuming $i = 81°$ for the unresolved gaseous disk. Col.(7): $M_\bullet$ stringent limit measured by including the stellar mass contribution in the dynamical model and assuming $i = 33°$ for the unresolved gaseous disk. Col.(8): $M_\bullet$ stringent limit measured by including the stellar mass contribution in the dynamical model and assuming $i = 33°$ for the unresolved gaseous disk. Col.(9): mass estimates and their 1σ errors derived from dynamical models based on resolved kinematics models. Col.(10): dynamical tracer (CO = molecular gas, g = ionized gas, s = stars, m = masers) and corresponding reference for Col.(8): (1) Ferrarese et al. (1996), (2) van der Marel & van den Bosch (1998), (3) Böker et al. (1999), (4) Barth et al. (2001), (5) Sarzi et al. (2001), (6) Verdoes Kleijn et al. (2002), (7) Marconi et al. (2003), (8) Atkinson et al. (2005), (9) Capetti

et al. (2005), (10) Herrnstein et al. (2005), (11) Coccato et al. (2006), (12) Pastorini et al. (2007), (13) de Francesco et al. (2008), (14) Hu (2008), (15) Walsh et al. (2010), (16) Huré et al. (2011), (17) Jardel et al. (2011), (18) Kuo et al. (2011), (19) Walsh et al. (2012), (20) Davis et al. (2013), (21) Rusli et al. (2013a), (22) Walsh et al. (2013), (23) Saglia et al. (2016).

3.3.4 Stellar mass-to-light ratio

We needed to constrain the mass-to-light ratio $(M/L)_\star$ of the stellar component to convert the light distribution derived from the MGE analysis into a mass distribution.

To this aim we investigated the library of synthetic spectral energy distributions for single-age, single-metallicity stellar populations provided by Vazdekis et al. (2010, 2012) and based on the Medium Resolution Isaac Newton Telescope Library of Empirical Spectra (MILES, Sánchez-Blázquez et al. 2006). In first approximation the value of $(M/L)_\star$ increases with the age and metallicity of the stellar population and depends on the initial mass function (IMF) and content of stellar remnants. We considered the model prediction of $(M/L)_{\star,I} = 4.32$ $M_\odot/L_\odot$ obtained with the Padova isochrones (Girardi et al., 2000) and a Kroupa revised IMF (Kroupa, 2001) for an old ($t = 14.13$ Gyr) and metal-rich ($Z = 0.22$ dex) stellar population. We adopted an I-band $(M/L)_\star$ since the MGE models were calibrated in Johnson-Cousins I band.

In some cases, the adopted $(M/L)_\star$ could overestimate the actual value if a younger and/or metal-poorer population is present in the galaxy nucleus. This results from a number of dynamical processes, like the capture of external gas from the environment or the bar driven gas from the outer galaxy regions that form the stars of nuclear star cluster (NSC) or nuclear stellar disk (NSD). The NSCs are known to contain a mix of stellar populations (e.g., Seth et al. 2006; Rossa et al. 2006). Walcher et al. (2005) found that the stellar nuclei of bulgeless galaxies are massive and dense NSCs that are recurrently forming stars until the present day. Moreover, Georgiev & Böker (2014) showed that recent star formation is ubiquitous in the NSCs of late-type spiral galaxies and one third of them was consistent with luminosity-weighted ages younger than 1-2 Gyr assuming solar metallicity. NSDs are flattened structures rotating around the centers of about 20% of elliptical (Ledo et al., 2010) and spiral galaxies (Pizzella et al., 2002), which could be much younger than the host spheroid (Sarzi et al., 2015; Corsini et al., 2016).

Determining the actual $(M/L)_\star$ for each sample galaxy would require at least two broad-band images or a low-resolution spectrum at HST resolution to constrain the stellar population properties of the galaxy nucleus. Unfortunately, such images and spectra are not available to us for all the sample galaxies. We therefore decided to adopt the same value of $(M/L)_\star$ for all the sample galaxies and we chose the $(M/L)_\star$ of a very old and metal-rich stellar population for the purpose of including the highest amount of stellar mass in the dynamical model to obtain the lowest $M_\bullet$ value.

3.4 Dynamical model

We adopted the dynamical model developed by Sarzi et al. (2002), which makes use of the line broadening of the nuclear emission arising from ionized gas to trace the depth of the gravitational potential well.

We assumed the ionized gas to be dynamically cold and moving in circular orbits in a coplanar thin disk around the central SBH. We considered the gas motion to be dictated only by the gravitational potential of the SBH and stars and we neglected the contribution

of nongravitational forces (but see also Sect. 3.5.2). In this case, the central width of the emission lines depends only on the gravitational potential and we assumed that the spatial flux Σ of the ionized gas is intrinsically axisymmetric, has a Gaussian radial profile and is centered on the galaxy nucleus. We convolved the ionized-gas intrinsic flux with the STIS PSF generated with the TINY TIM package (Krist et al., 2011) to match the radial profile of the [NII]λ6583 flux along the slit taking into account for the inclination of the gaseous disk. As a matter of facts, this is unknown since the gaseous disk is spatially unresolved and we have kinematic measurements only along one direction. Therefore, we computed the dynamical models for two configurations corresponding to a nearly edge-on ($i = 81°$, $\cos i = 0.16$) and to an almost face-on ($i = 33°$, $\cos i = 0.84$) disk, respectively. This range of inclinations brackets the 68% upper and lower confidence limits of the $M_\bullet$ values that can explain a given line width for randomly oriented gaseous disks, which have uniformly distributed $\cos i$. The position angle of the gaseous disk was unknown too. But we extracted the nuclear spectra from nearly square apertures (Table 3.3), which actually corresponds to assume that the slit was placed along the disk major axis.

Considering both the SBH and stellar contributions to the gravitational potential, the shape of the circular velocity curve depends on the relative importance of the $M_\bullet$ and $(M/L)_\star$ values. The circular velocity v_c at the radius r is traced by the ionized-gas rotation curve and it is given by

$$v_c(r) = \left[\frac{GM(r)}{r}\right] = \left[\frac{GM_\bullet}{r} + \left(\frac{M}{L}\right)_\star v_\star^2(r)\right]^{1/2} \tag{3.5}$$

where M is the total galaxy mass enclosed by the circular orbit of radius r, $(M/L)_\star$ is the constant mass-to-light ratio of the stellar component and $v_\star$ is the circular velocity of a stellar component with $(M/L)_\star = 1$. We derived the radial profile of $v_\star$ from the surface brightness distribution I measured from HST images, which we deprojected to obtain the stellar luminosity density ν following Cappellari (2002) and assuming spherical symmetry, as explained in Sect. 3.3.3. We derived the $(M/L)_\star$ ratio following Vazdekis et al. (2010, 2012), as discussed in Sect. 3.3.4. For a constant $(M/L)_\star$, the stellar mass density $\rho(r) = (M/L)_\star \nu(r)$ can be described as a sum of a set of Gaussians as the stellar luminosity density and the surface brightness distribution.

Considering all the assumptions done so far and to make a prediction for the ionized-gas velocity dispersion within the central aperture, we built the two-dimensional maps of the moments of the line-of-sight velocity distribution (LOSVD) at any position (x, y) on the sky as

$$\overline{\Sigma v^k}(x, y) = \int \mathrm{LOSVD}\,(x, y, v_z) v_z^k dv_z \;\; (k = 0, 1, 2), \tag{3.6}$$

and we convolved them for STIS PSF. Then we sampled these maps over the desired aperture to retrieve the PSF-convolved, aperture-averaged LOSVD velocity moments. The final step consisted of comparing the computed velocity dispersion within the aperture with the observed one, thus obtaining the $M_\bullet$ value.

We estimated the $M_\bullet$ values for $i = 33°$ and $i = 81°$ for the all the galaxies in the finale sample by first disregarding and then including the stellar potential contribution (Table 3.3).

The first set of values was already obtained by B09, B12, and Pagotto et al. (2017). We decided to redo the calculation of the $M_\bullet$ stringent limits of B09 and B12 for consistency. Unfortunately, all the input values they adopted to build their dynamical models were not available to us. To address this issue, we refitted the radial profile of the [NII]λ6583 flux for all the sample galaxies. Unlike B09 and B12, we took into account for measurement errors and in some cases we excluded some of the external points to better fit the central portion of the [NII]λ6583 flux profile. Since the aim of this work is to estimate the stellar contribution on the gravitational potential in galaxy nuclei and to understand how much $M_\bullet$ depends on it, rederiving the $M_\bullet$ values of B09 and B12 ensured us to proper comparison of the values of $M_\bullet$ obtained with and without the stellar mass in the dynamical model.

3.5 Results

Hereinafter, we refer to Sample A when considering all the $M_\bullet$ values derived disregarding the stellar mass contribution and to Sample B when examining the $M_\bullet$ values obtained from the dynamical model which accounts for the stellar mass contribution.

In Sect. 3.5.1 we compare the $M_\bullet$ of Sample A to those obtained by B09 and B12. In Sect. 3.5.2 we qualitatively discuss the contribution of nongravitational forces by analyzing the shape of the emission lines and of their flux radial profiles. In Sect. 3.5.3 we investigate the stellar mass contribution on the $M_\bullet$ values by comparing the stringent limits of Sample A and Sample B. Finally, in Sect. 3.5.4 we study the $M_\bullet$ of Sample B in the framework of the $M_\bullet - \sigma_{\rm e}$ relation by Kormendy & Ho (2013).

3.5.1 Comparison with B09 and B12 sample

We compared the $M_\bullet$ values of Sample A with those by B09 and B12 at the two different inclinations of the unresolved gaseous disk.

For $i = 33°$, there are 13 $M_\bullet$ stringent limits equal to those of B09 and B12 rescaled to $H_0 = 70$ km s^{-1} Mpc^{-1}. Concerning the cumulative distribution for the other $M_\bullet$ values, we found that 26 of them have a relative differences smaller than 5% , 48 smaller than 14%, 65 smaller than 30%, 76 smaller than 40%. The remaining 19 $M_\bullet$ have a relative differences larger than 40%. Fig. 3.5 shows that 44 $M_\bullet$ stringent limits of Sample A are larger and 38 are smaller than the corresponding B09 and B12 $M_\bullet$ values.

For $i = 81°$ there are 20 $M_\bullet$ stringent limits equal to those of B09 and B12 rescaled to $H_0 = 70$ km s^{-1} Mpc^{-1}. Concerning the cumulative distribution for the other $M_\bullet$ values, we found that 27 of them have a relative differences smaller than 5% , 48 smaller than 14%, 58 smaller than 30%, 61 smaller than 40%. The remaining 34 $M_\bullet$ have a relative differences larger than 40%. Fig. 3.5 shows that 43 $M_\bullet$ stringent limits of Sample A are larger and 32 are smaller than the corresponding B09 and B12 $M_\bullet$ values.

It can be noticed that the $M_\bullet$ stringent limits of Sample A are on average larger than those of B09 and B12. This is particularly true for $i = 81°$ with no dependence on $M_\bullet$ and for the $M_\bullet$ stringent limits of Sample A that differ by more than 70% from those of B09 and

B12. In this sense, our $M_\bullet$ stringent limits are on average more conservative than those of B09 and B12.

3.5.2 Influence of nongravitational forces

We based our dynamical analysis on the hypothesis that the ionized gas in the galaxy nucleus is highly concentrated toward the center and its motion is driven only by the gravitational forces of the central SBH and of stars residing within the nuclear regions. But unlike stars, the gas could be influenced by nongravitational forces, like radiation pressure, shock waves, turbulence, and magnetic fields (Kormendy & Ho, 2013).

We examined the regularity of the morphology of the dust lanes/filaments to have an *a priori* guess about the behavior of the ionized gas, as proposed by Ho et al. (2002) and Sarzi et al. (2002). However, the presence of nearly symmetric and well ordered dust features does not ensure that the ionized gas is characterized by a symmetric and regular velocity field (e.g., Dalla Bontà et al., 2009).

We analyzed the shape of the emission lines and of their flux radial profiles as an *a posteriori* check to test the presence of nongravitational forces altering the gas orbital motion. We limited this qualitative analysis to the aperture and direction of the slit. The shape of the emission lines can also reveal the presence of kinematically-distinct gaseous components. The emission lines of the nuclear spectra of the galaxy sample were fitted with a sum of Gaussian components (B09, B12, Pagotto et al. 2017). The shape of the flux profile traces the gas distribution in the galaxy nucleus and it can unveil the presence of more gas on one side of the galaxy with respect to the other, ionizing sources like star-forming regions, or shock waves. In principle, in this way it is not possible to disentangle the nongravitational from gravitational forces nor to quantitatively derive their respective contributions. However, the presence of well-defined single narrow-line components and symmetric and very regular shapes of the flux radial profiles can rule out strong nongravitational perturbations. We fitted the flux radial profile arising from the analysis of the [NII]λ6583 emission line with a Gaussian. We found that this solution was appropriate for all the different flux profiles of the sample galaxies. Moreover, using an exponential would have led to lower $M_\bullet$ values (Sarzi et al. 2002, B09). Therefore, we considered the Gaussian as a more conservative choice for the $M_\bullet$ estimates.

Shape of the [NII]λ6583 emission line

In some cases the analysis of the shape of the [NII]λ6583 emission line revealed the presence of multiple gas components with a different kinematics in terms of line-of-sight velocity and velocity dispersion.

The nuclear spectra of NGC 1667, NGC 2273, NGC 3081, NGC 3393, NGC 3982, NGC 4321, NGC 5194, NGC 5283, NGC 5347, NGC 5643, NGC 5695, and NGC 6300 present double-peaked narrow-line components which could be caused by gas outflows.

Some nongravitational forces could be also present in NGC 3998, NGC 4203, NGC 4450, NGC 4579, and UGC 1395 since their nuclear spectra are characterized by a strong broad-line

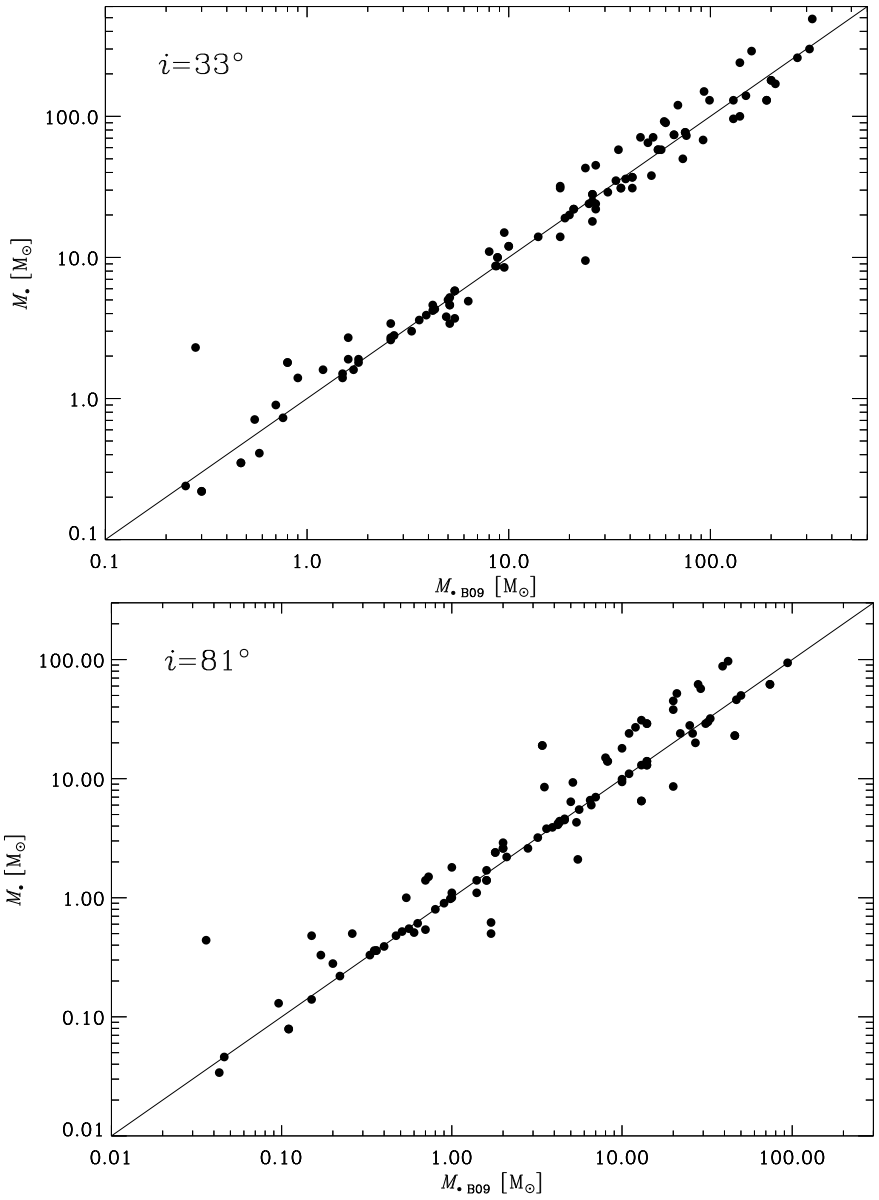

Figure 3.5: Comparison between the $M_\bullet$ stringent limits we estimated assuming an inclination of $i = 33°$ (*upper panel*) and 81° (*lower panel*) for the unresolved gaseous disk and those by B09 and B12 rescaled to $H_0 = 70$ km s^{-1} Mpc^{-1}.

component arising from the AGN. This effect is less strong in the other 48 sample galaxies with [NII]λ6583 emission lines characterized by both broad and narrow components.

Shape of the [NII]λ6583 flux radial profile

We analyzed and classified the radial profiles of the flux of the [NII]λ6583 emission line of all the sample galaxies as reported in Table 3.1.

The [NII]λ6583 flux radial profile of 62 galaxies has a symmetric and regular shape well fitted by a Gaussian. This means that the ionized gas is presumably organized in a disk spinning around the galaxy center with a well-behaved velocity field. In these conditions, the ionized gas constitutes a good tracer of the gravitational potential and the $M_\bullet$ values we obtained are the most strongly reliable estimates of our sample. The [NII]λ6583 flux profiles of NGC 2787 and NGC 3368 are shown in Fig. 3.6 as an example for this class of objects, which are marked with a "g" in Table 3.1.

The [NII]λ6583 flux radial profile of the 11 galaxies, which are marked with an "a" in Table 3.1, is asymmetric with a small excess/lack of flux on one side of the galaxy. These flux asymmetries are probably due to shock waves, higher/lower gas concentration, or ionizing star-forming regions. We disregarded these deviations in the fit since they are far from the galaxy center and we regularly fitted the central peak of the [NII]λ6583 flux profile with a Gaussian. The [NII]λ6583 flux profile of NGC 5252 is shown in Fig. 3.6 as an example.

The [NII]λ6583 flux profile of the 8 galaxies, which are marked with a "n" in Table 3.1, was successfully fitted in spite of its not so regular shape. The nuclear spectra of NGC 193, NGC 4203, NGC 4374, and NGC 4552 are indeed characterized by strong broad emission-line components, which could have affected the flux estimate of the [NII]λ6583 narrow component. As a consequence, the [NII]λ6583 flux profile displays a few points in the central region that do not follow a Gaussian function. In a similar way, the fit of the [NII]λ6583 narrow component of NGC 3982 could have been influenced by the presence of a second narrow component with a slightly different velocity and that of NGC 289 and NGC 3627, and NGC 4800 could be affected by the presence of fair amount of dust in their nuclei. The [NII]λ6583 flux profile of NGC 289 is shown in Fig. 3.6 as an example.

We fitted only the central points of the [NII]λ6583 flux profile of the 10 galaxies marked with a "c" in Table 3.1. The flux profile of NGC 4278, NGC 4501, NGC 4698, NGC 5005, and NGC 6951 is characterized by the presence of secondary flux peaks close to the central one, which we did not consider in the fit. The flux profile of IC 3639, NGC 613, NGC 4041, NGC 4261, and NGC 4486 shows a central peak with a symmetric and regular shape in contrast to the irregular trend measured in outer regions, which we excluded from the fit. The nuclei of all the above galaxies are free of dust, except for those of NGC 613 and NGC 4261. In particular, NGC 4261 hosts a nuclear dust disk, which obscures the galaxy center and strongly dims the emission lines of the nuclear spectrum. The [NII]λ6583 flux profile of NGC 613 is shown in Fig. 3.6 as an example for these galaxies.

The [NII]λ6583 flux profiles of NGC 4212, NGC 4245, NGC 5194, and NGC 5728 show a few central points, which follow a Gaussian trend, with many outer points characterized by strongly irregular behavior. In such circumstances, the nongravitational forces may play a

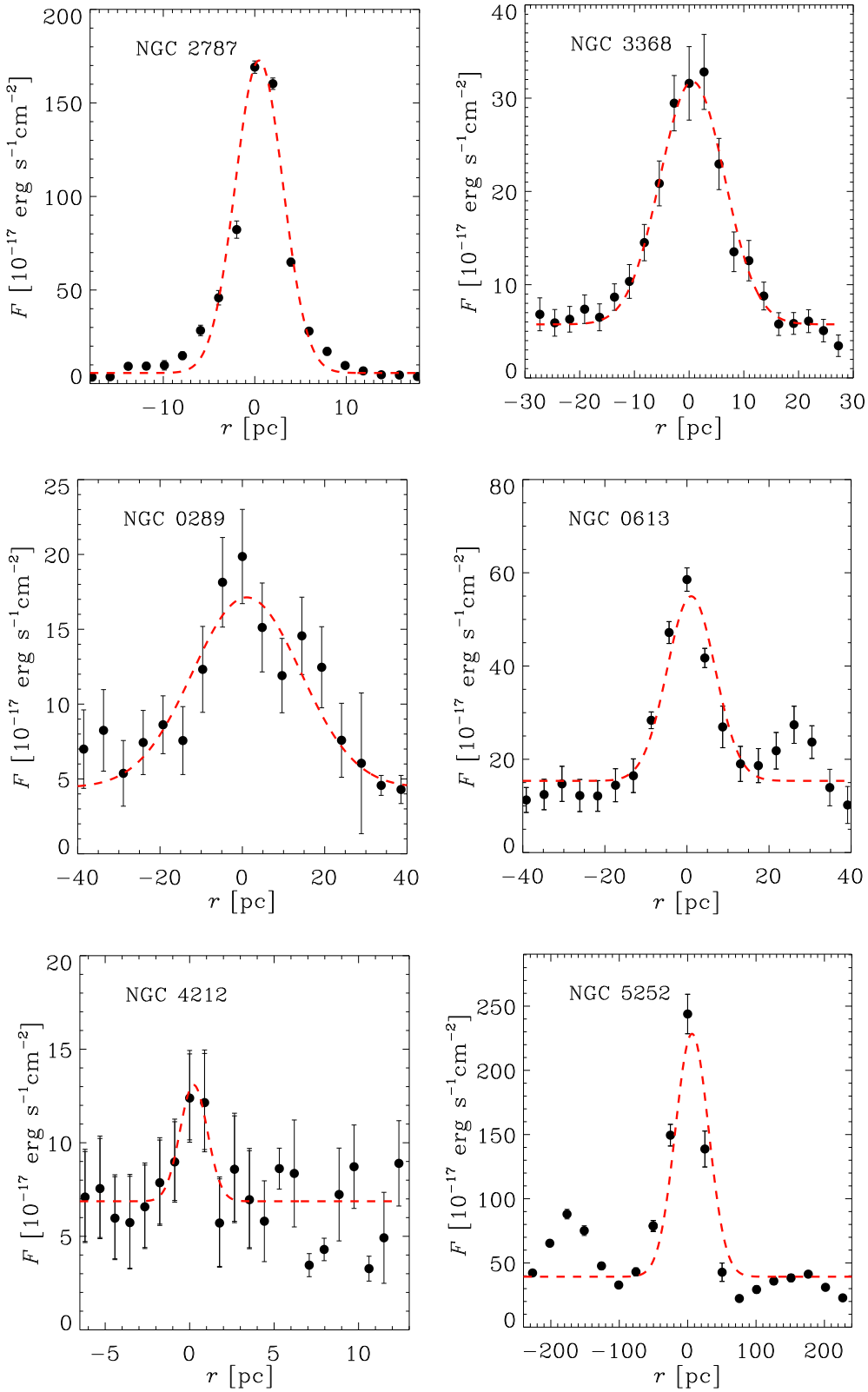

Figure 3.6: Examples of sample galaxies with a regular radial profile of the [NII]λ6583 flux. The Gaussian fit (red dashed line) to the flux measurements (black filled circles) is also shown in each panel.

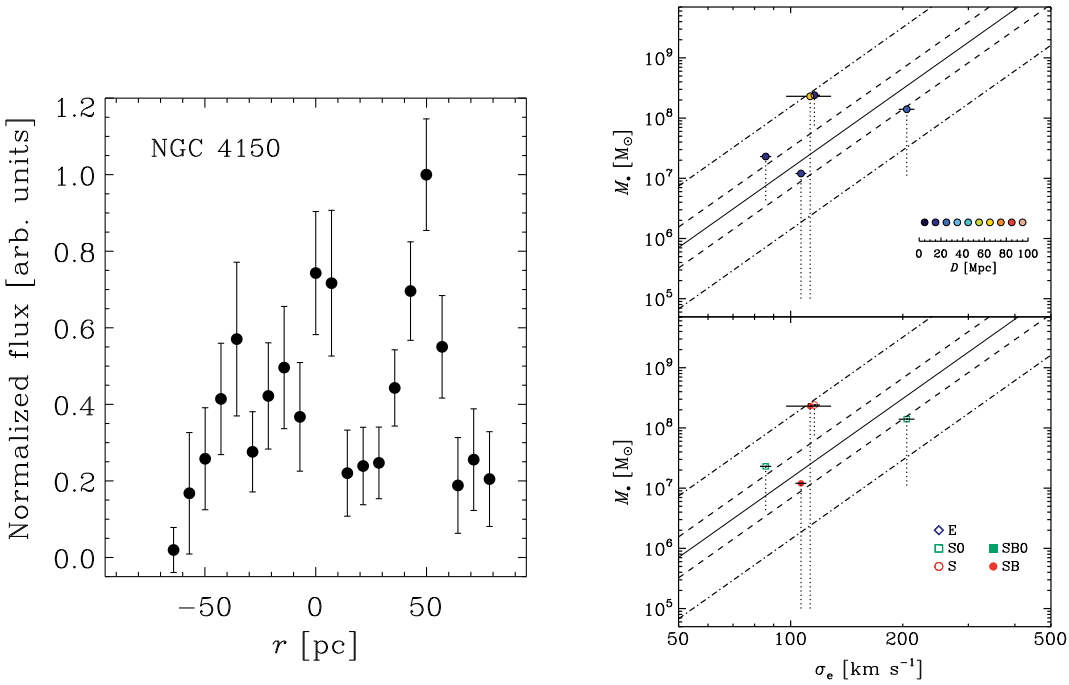

Figure 3.7: *Left panel:* Irregular radial profile of the [NII]λ6583 flux of NGC 4150, as an example. *Right panel*: Comparison between the $M_\bullet$ stringent limits of the sample galaxies with an irregular [NII]λ6583 flux radial profile and the $M_\bullet - \sigma_e$ relation by Kormendy & Ho (2013) as a function of galaxy distance (*upper panel*) and morphological type (*lower panel*). The dashed and dotted-dashed lines show the $\pm1\sigma$ and $\pm3\sigma$ scatter in $M_\bullet$, respectively. The plotted galaxies are NGC 4150, NGC 4314, NGC 7682, NGC 7331, and NGC 3245 (from small to large σ_e values).

role. But, it has also to be kept in mind that the central regions of these galaxies are heavily contaminated by dust (see Table 3.1). Moreover, the spectra of NGC 4212, NGC 4245, and NGC 5728 are characterized by [NII]λ6583 emission lines with a low S/N. The [NII]λ6583 flux profile of NGC 4212 is shown in Fig. 3.6 as an example for this class of objects, which are marked with a "f" in Table 3.1.

The [NII]λ6583 flux profiles of NGC 3245, NGC 4150, NGC 4314, NGC 7331 and NGC 7682 are irregular even in their central portion. The nuclear regions of these galaxies are free of dust, except for NGC 4150. Its [NII]λ6583 flux profile is shown in Fig. 3.7 as an example. The nongravitational perturbations may have an important role, even if the irregular flux profile could be also a consequence of the low S/N of the [NII]λ6583 emission line. This is particularly true for NGC 4150 and NGC 7331, but also for NGC 3245 and NGC 4314. On the contrary, the [NII]λ6583 emission line of the nuclear spectrum of NGC 7682 has a good S/N but the galaxy is slightly dust affected. The $M_\bullet$ values of these galaxies, which are marked with a "i" in Table 3.1, are shown in Fig. 3.7 to identify their location with respect to the $M_\bullet - \sigma_e$ relation of Kormendy & Ho (2013). We noted that all of them are within the 3σ scatter of the relation. However, we decided to exclude these galaxies from the following analysis because the motion of their gas is not regular and undermines our dynamical model.

We concluded that the [NII]λ6583 flux profile has to be characterized by a symmetric and regular shape (at least in the central regions of the galaxy) to be reasonably sure that the ionized gas is a good tracer of the gravitational potential and its kinematics allows to obtain a reliable $M_\bullet$ value. We refrain from fitting a regular function to [NII]λ6583 flux profiles with a high degree of irregularity (particularly in the central regions of the galaxy), because the resulting $M_\bullet$ could be plausible but not physically motivated as shown in Fig. 3.7.

3.5.3 Stellar mass contribution

In order to investigate the impact of the stellar mass contribution on the $M_\bullet$ values, we compared the $M_\bullet$ stringent limits of Sample B to those of Sample A. We further curbed Sample A and B in the following analysis by discarding NGC 3245, NGC 4150, NGC 4314, NGC 7331, and NGC 7682 because of their irregular [NII]λ6583 flux profiles as explained in Sect. 3.5.2. Moreover, we rejected all the galaxies of Sample B with $M_\bullet = 10^5$ $M_\odot$ (Table 3.3) because we were not able to match the low gas velocity dispersion measured for these objects with the one predicted by our dynamical model. The value of $M_\bullet = 10^5$ $M_\odot$ is indeed the lowest one we considered for our models and it constitutes an upper limit. We removed the galaxies with $M_\bullet = 10^5$ $M_\odot$ also from Sample A when we compared the two samples and we separately analyzed them in Sect. 3.5.3.

In this way, we arrived at 88 $M_\bullet$ values for an inclination of the unresolved gaseous disk of $i = 33°$ and 80 $M_\bullet$ values for $i = 81°$ for both Sample A and B. We separately carried out the analysis of the stellar mass contribution for $i = 33°$ and $i = 81°$ since the two samples are not composed of the same galaxies. This choice allowed us to not discard 8 more galaxies in the low/intermediate-$\sigma_e$range at $i = 33°$. This is important for the statistics since this σ_e range is characterized by fewer galaxies with respect to other ones.

We estimated the percentage of decrease γ of the $M_\bullet$ value due to the stellar mass contribution as

$$\gamma = \frac{M_\bullet - M_{\bullet,\star}}{M_\bullet} \cdot 100 \tag{3.7}$$

where $M_\bullet$ and $M_{\bullet,\star}$ are the $M_\bullet$ values ignoring (Sample A) or accounting for (Sample B) the stellar mass contribution. $M_{\bullet,\star}$ is expected to be always equal or smaller than $M_\bullet$.

Analysis of the black hole masses obtained for $i = 33°$

We divided the sample of 88 galaxies with $M_\bullet$ obtained for $i = 33°$ in three subsamples to separately investigate the stellar mass contribution in the low ($\sigma_e < 90$ km s^{-1}), intermediate ($90 < \sigma_e < 220$ km s^{-1}), and high ($\sigma_e > 220$ km s^{-1}) ranges of effective stellar velocity dispersion. We calculated the mean value of γ for each supsample and report them in Table 3.4. It can be noticed that the stellar mass contribution is larger in the low-σ_e range (24%) than in the intermediate one (11%), and it is negligible (2%) for high σ_e. In the case of a large $M_\bullet$, the SBH dominates the gravitational potential of the galaxy within the nuclear aperture. On the contrary, the stellar component could be a significant contributor to the nuclear gravitational potential of galaxies with low $M_\bullet$. Disregarding the stellar mass could lead to

Table 3.4: Amount of decrease of the $M_\bullet$ stringent limits by including the stellar mass contribution in the dynamical model and assuming $i = 33°$ for the unresolved gaseous disk as a function of σ_e.

	All	σ_e< 90 km s^{-1}	90 < σ_e< 220 km s^{-1}	σ_e> 220 km s^{-1}
N	88	14	52	22
γ	10.9%	23.8%	11.3%	1.7%

Notes: The mean decrease and number of galaxies are reported for each sample.

Table 3.5: As in Table 3.4 but as a function of the morphological type.

	All	E	SA0+SB0	SA0	SB0	SA+SB	SA	SB
N	88	29	16	6	10	43	17	26
γ	10.9%	3.2%	15.2%	14.8%	15.4%	14.4%	16.8%	12.9%

Notes: The mean decrease and number of galaxies are reported for each sample.

a large overestimate of $M_\bullet$. This confirms the early results obtained by Sarzi et al. (2002) who analysed of a small sample of 16 galaxies spread over a wide σ_e range (71 < σ_e < 271 km s^{-1}). The distributions of γ for the entire galaxy sample and for the different σ_e ranges are given in Figs. 3.8 and 3.9, respectively.

We then divided the galaxies as function of their morphological type into ellipticals, lenticulars, and spirals taking also into account the presence of a bar. We calculated the mean value of γ for the above subsamples and report our findings in Table 3.5. In the case of ellipticals, the stellar mass contribution is quite small (3%). On the contrary, it is larger and similar for lenticulars (15%) and spirals (14%). It should be noted that the 29 ellipticals are characterized by $M_\bullet > 10^8$ M$_\odot$ at $i = 33°$ and that the stellar contribution is small in this $M_\bullet$ range. The presence of a bar does not make a difference in lenticulars, whereas we found a weak correlation for spirals in the sense that the stellar mass contribution is larger for unbarred spirals. The distribution of γ for the different morphological types is given in Fig. 3.10.

Finally, we studied the influence of the aperture size and galaxy distance on the stellar mass contribution. Indeed, in principle a wider aperture could include a larger amount of stellar mass and this amount could be even larger if the object is more distant. It has to be kept in mind that the galaxy sample was originally limited in distance (D < 103 Mpc at $H_0 = 70$ km s^{-1} Mpc^{-1}) by B09 for the purpose of minimizing the impact of the stellar contribution to the galaxy potential.

First, we separately estimated the stellar mass contribution as a function of the aperture size and galaxy distance. In particular, we defined the distance ranges in order to have samples with at least three galaxies (Tables 3.6 and 3.7). We give the mean values and distributions of γ for the all subsamples in Table 3.6 and Fig. 3.11 as function of the aperture size and in Table 3.7 and Fig. 3.12 as a function of galaxy distance, respectively. Overall, we noticed that the stellar mass contribution is smaller for the 0.1×0.15 arcsec^2 aperture compared to

Table 3.6: As in Table 3.4 but as a function of the size of the central aperture.

	All	0.1×0.15 arcsec^2	0.2×0.25 arcsec^2	0.2×0.30 arcsec^2
N	88	13	52	23
γ	10.9%	5.6%	13.2%	8.6%
	E	0.1×0.15 arcsec^2	0.2×0.25 arcsec^2	0.2×0.30 arcsec^2
N	29	6	8	15
γ	3.2%	0.0%	2.7%	4.8%
	S0	0.1×0.15 arcsec^2	0.2×0.25 arcsec^2	0.2×0.30 arcsec^2
N	16	2	11	3
γ	14.8%	2.1%	15.4%	23.2%
	S	0.1×0.15 arcsec^2	0.2×0.25 arcsec^2	0.2×0.30 arcsec^2
N	43	5	33	5
γ	14.4%	13.8%	15.0%	11.3%

Notes: The mean decrease and number of galaxies are reported for each sample.

Table 3.7: As in Table 3.4 but as a function of the galaxy distance.

	All	$D < 25$ Mpc	$25 < D < 50$ Mpc	$D > 50$ Mpc
N	88	45	16	27
γ	10.9%	9.6%	18.7%	8.4%
	E	$D < 25$ Mpc	$25 < D < 50$ Mpc	$D > 50$ Mpc
N	29	7	6	16
γ	3.2%	3.1%	1.2%	4.0%
	S0	$D < 25$ Mpc	$25 < D < 50$ Mpc	$D > 50$ Mpc
N	16	9	3	4
γ	14.8%	10.9%	18.4%	22.4%
	S	$D < 25$ Mpc	$25 < D < 50$ Mpc	$D > 50$ Mpc
N	43	29	7	7
γ	14.4%	10.7%	33.9%	10.3%

Notes: The mean decrease and number of galaxies are reported for each sample.

Table 3.8: As in Table 3.4 but as a function of the size of central aperture and galaxy distance.

	0.1×0.15 arcsec^2	0.2×0.25 arcsec^2	0.2×0.30 arcsec^2
$D < 25$ Mpc	16.5%	6.9%	20.7%
$25 < D < 50$ Mpc	1.9%	28.7%	2.3%
$D > 50$ Mpc	0.2%	22.7%	4.7%

Notes: The mean decrease is reported for each sample.

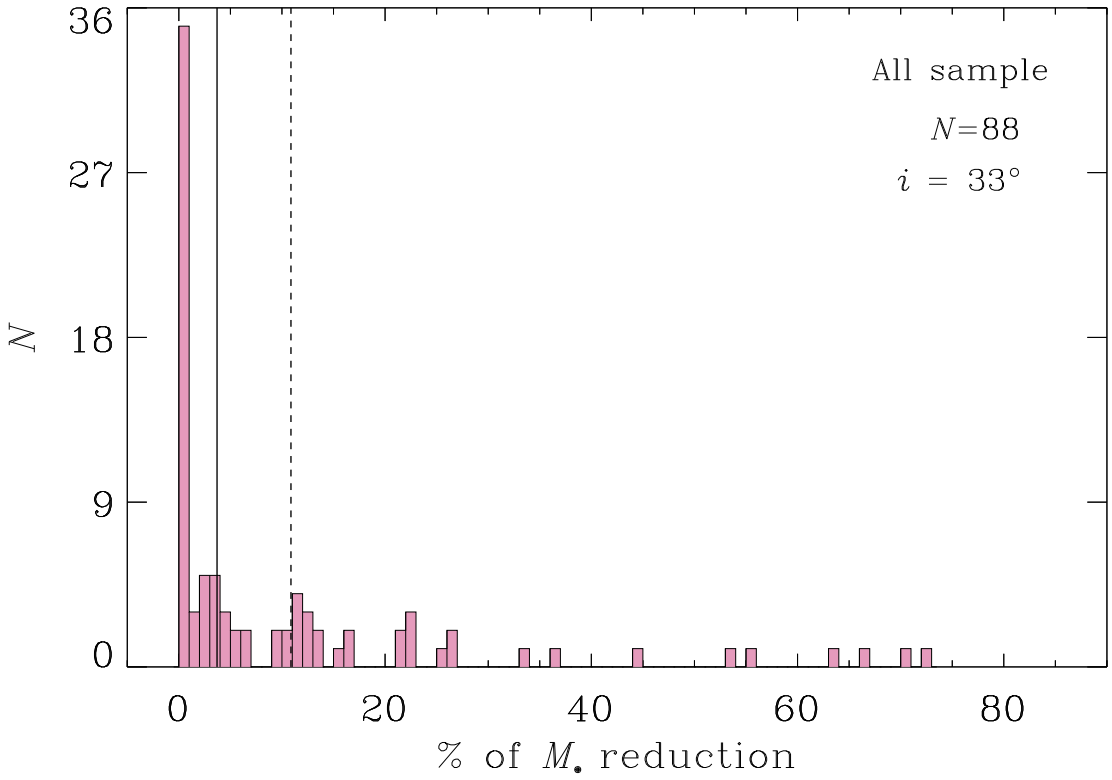

Figure 3.8: Distribution of the relative decrease of the $M_\bullet$ value derived by taking into account the contribution of the stellar mass for an inclination of $i = 33°$ of the unresolved gaseous disk. The total number of galaxies is $N = 88$. The solid and dashed vertical lines mark the median and mean values of the distribution, respectively.

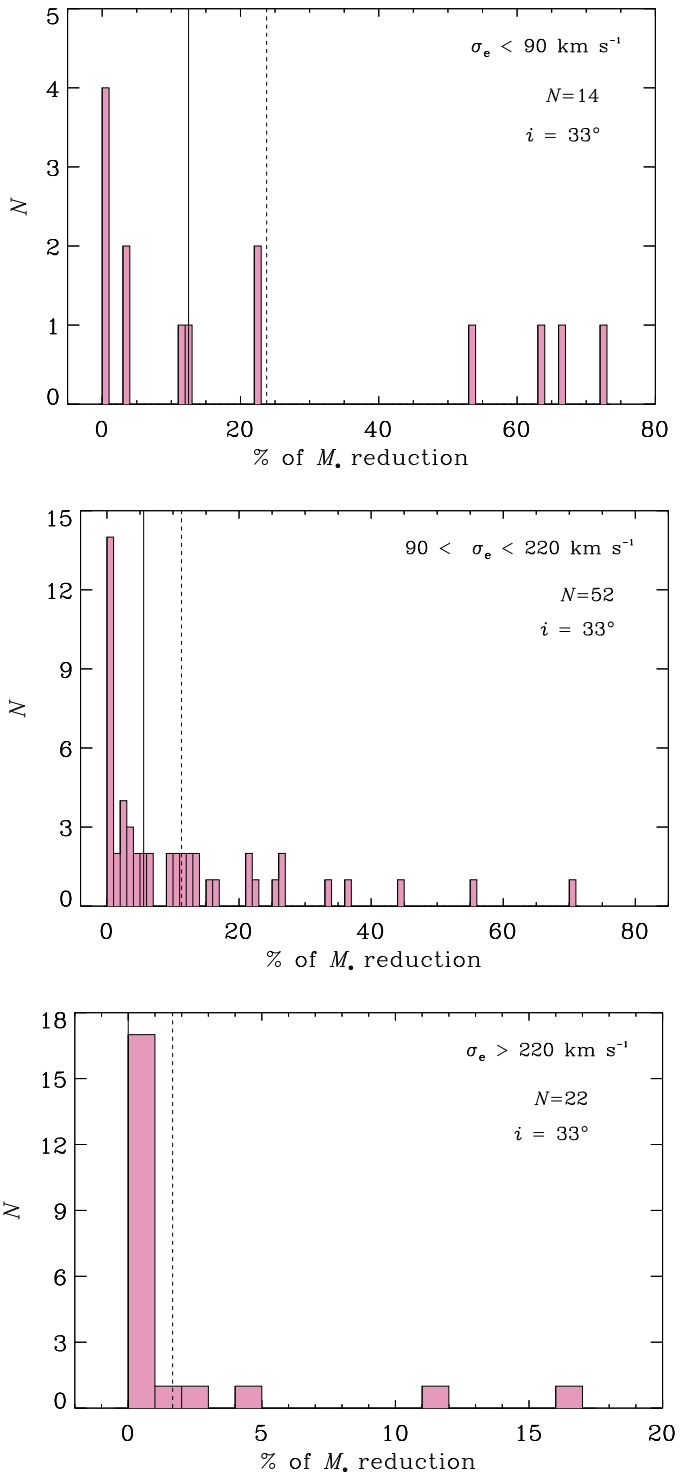

Figure 3.9: Same as in Fig. 3.8, but for galaxies with $\sigma_{\rm e} < 90$ km s^{-1} (*top panel*), $90 < \sigma_{\rm e} < 220$ km s^{-1} (*middle panel*), and $\sigma_{\rm e} > 220$ km s^{-1} (*bottom panel*). The number N of galaxies in each subsample is given.

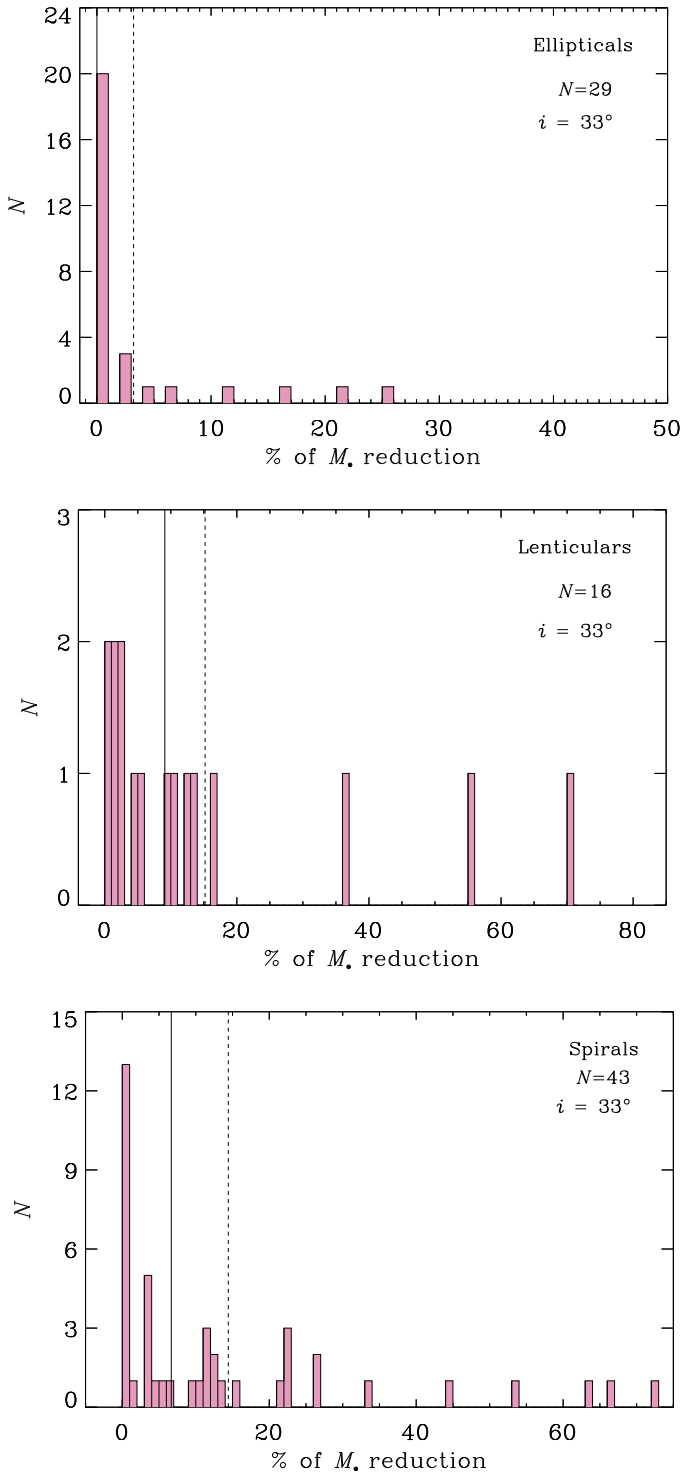

Figure 3.10: Same as in Fig. 3.8, but for elliptical (*top panel*), lenticular (*middle panel*), and spiral galaxies (*bottom panel*). The number N of the galaxies in each subsample is given.

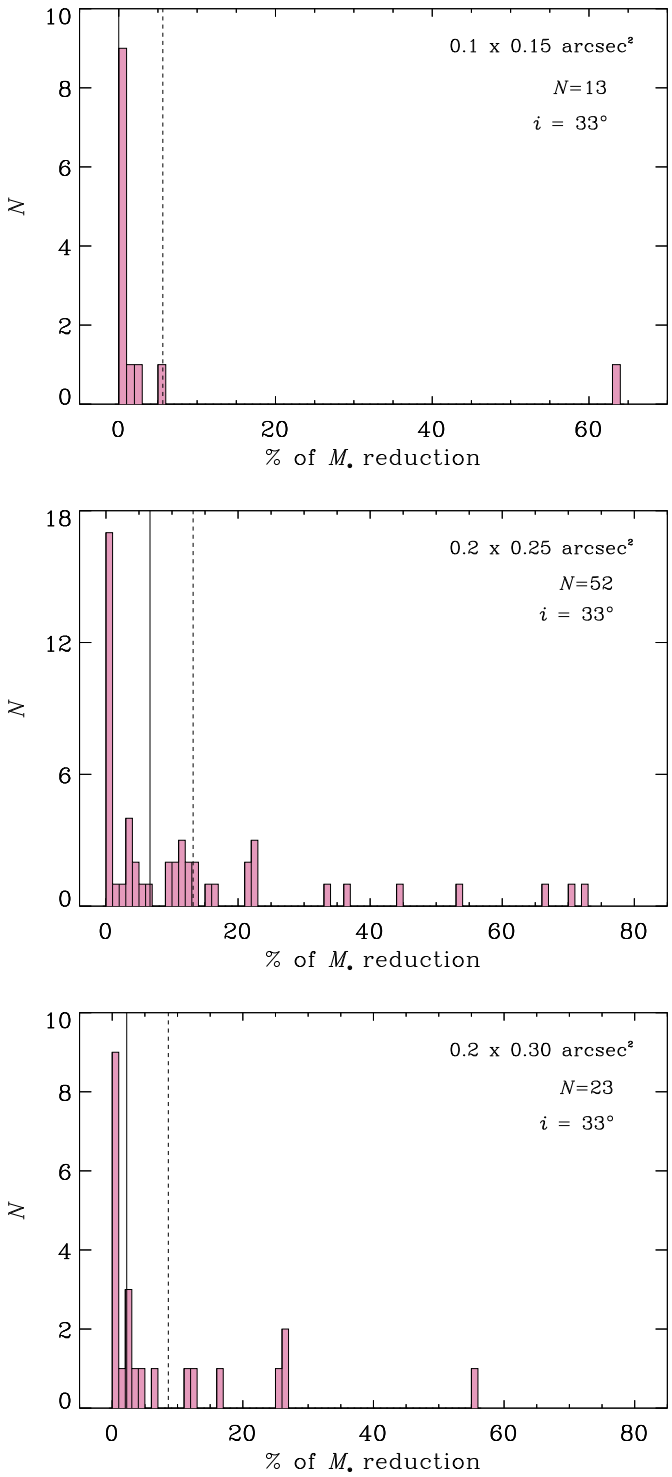

Figure 3.11: Same as in Fig. 3.8, but for galaxies with a nuclear spectrum obtained within a 0.1×0.15 arcsec^2 (*top panel*), 0.2×0.25 arcsec^2 (*middle panel*), and 0.2×0.30 arcsec^2 aperture (*bottom panel*). The number N of galaxies in each subsample is given.

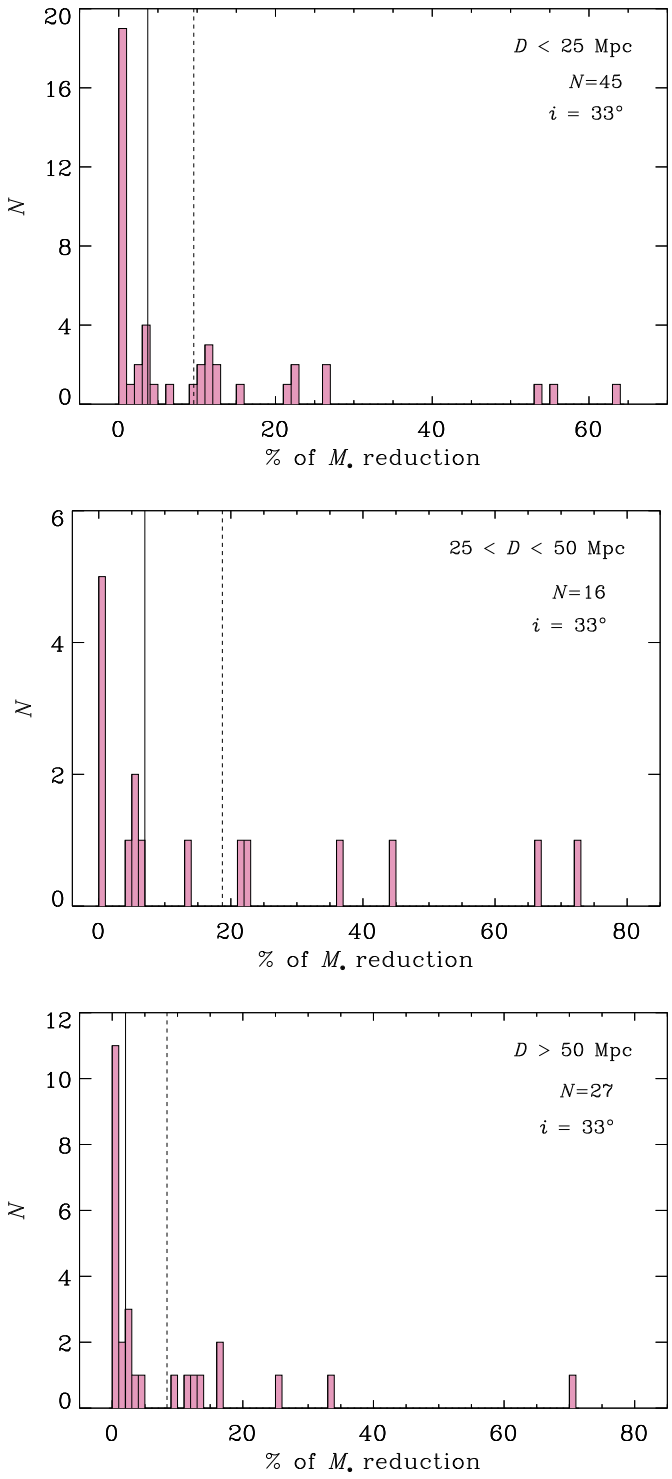

Figure 3.12: Same as in Fig. 3.8, but for galaxies with $D < 25$ Mpc (*top panel*), $25 < D < 50$ Mpc (*middle panel*), and $D > 50$ Mpc (*bottom panel*). The number N of galaxies in each subsample is given.

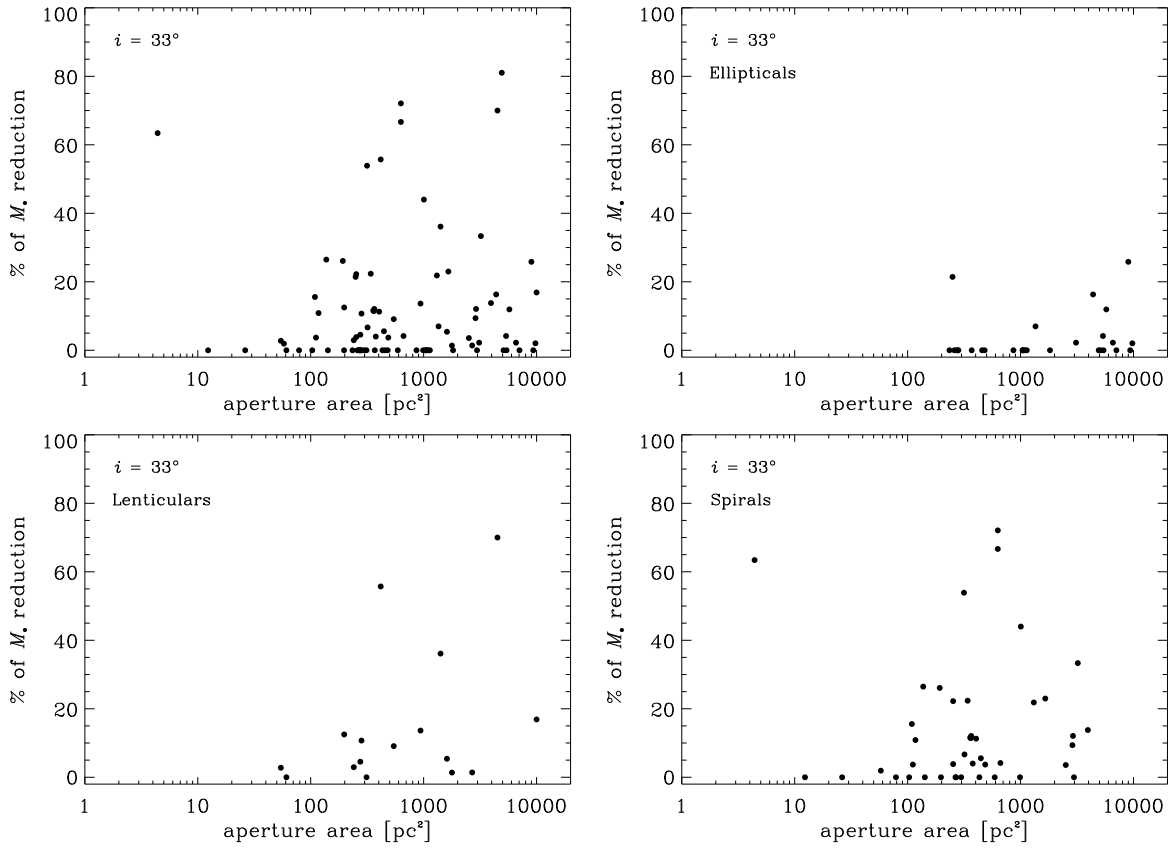

Figure 3.13: *Upper left-hand panel*: Distribution of the relative decrease of the $M_\bullet$ value derived by taking into account the contribution of the stellar mass for an inclination of $i = 33°$ for the unresolved gaseous disk as a function of the aperture area of the nuclear spectrum. The total number of galaxies is $N = 88$. *Upper right-hand panel*: Elliptical galaxies. *Lower left-hand panel*: Lenticular galaxies. *Lower right-hand panel*: Spiral galaxies. The number N of galaxies in each subsample is given.

0.2×0.25 arcsec^2 (13%) and 0.2×0.30 arcsec^2 (9%). On the contrary, there is not a clear dependency of the stellar mass contribution from the distance. With the aim of verifying if this behavior was due to the fact that all the morphological types were mixed up together, we calculated the mean values of γ for them all by further splitting the galaxies into ellipticals, lenticulars, and spirals. We did not consider the presence of the bar in order to have enough objects for each morphological bin. We found that in ellipticals the stellar mass contribution increases with the aperture size. This is true also for lenticulars, whereas there is not evidence of such a correlation for spirals. There is no correlation with distance independently from the morphological type. We conclude that for such a nearby galaxies, at first approximation the impact of the stellar mass on $M_\bullet$ does not depend on the galaxy distance.

Then, we jointly estimated the stellar mass contribution as a function of the aperture size and galaxy distance. We did not find any clear-cut correlation from the mean values of γ obtained for the all subsamples and given in Table 3.8. As a last attempt, we looked for a possible correlation between the stellar mass contribution and the physical size of the aperture in parsecs. As shown in Fig. 3.13, there is no trend even splitting the sample galaxies according to their morphological types.

Analysis of the black hole masses obtained for $i = 81°$

We repeated the analysis for the sample of 80 galaxies with $M_\bullet$ obtained for $i = 81°$. Even if this sample is not directly comparable with the one at $i = 33°$ due to the different number of objects, we inspected it to see if similar results were found during the analysis. At $i = 81°$, the stellar mass contribution is larger. Overall the $M_\bullet$ decreases by 20% and the distribution of γ for the entire sample is given in Fig. 3.14.

The stellar mass contribution decreases when considering the low (27%), intermediate (25%), and high-σ_e (7%) range (Table 3.9) similarly for the sample of $M_\bullet$ obtained for $i = 33°$ (Table 3.4). It increases from ellipticals (12%), to lenticulars (19%), and to spirals (28%) and it is larger for barred galaxies with respect to unbarred galaxies (Table 3.10). We found a slightly different behavior for the sample at $i = 33°$, for which the stellar mass contribution was similar for lenticulars and spirals and there was no dependence on the bar presence for lenticulars. The distributions of γ for all the σ_e and morphological subsamples are given in Figs. 3.15 and 3.16, respectively.

It can be noticed that the stellar mass contribution increases with the aperture size for all morphological types (Table 3.11), whereas this was not true for spirals in the sample at $i = 33°$ (Table 3.6). On the contrary, there is no correlation with the distance of the galaxy (Table 3.12) as found at $i = 33°$. The distributions of γ for all the aperture size and galaxy distance subsamples are given in Figs. 3.17 and 3.18, respectively.

Finally, we jointly estimated the stellar mass contribution as a function of the aperture size and galaxy distance (Table 3.13). Considering each distance bin, the stellar mass contribution in the 0.1×0.15 arcsec^2 aperture is smaller compared to 0.2×0.25 arcsec^2 and 0.2×0.30 arcsec^2 (Table 3.13). This dependence was not obtained in the sample at $i = 33°$. On the other hand we found no trend with the physical area of the aperture in parsec as shown in Fig. 3.19 and this was true also in the sample at $i = 33°$.

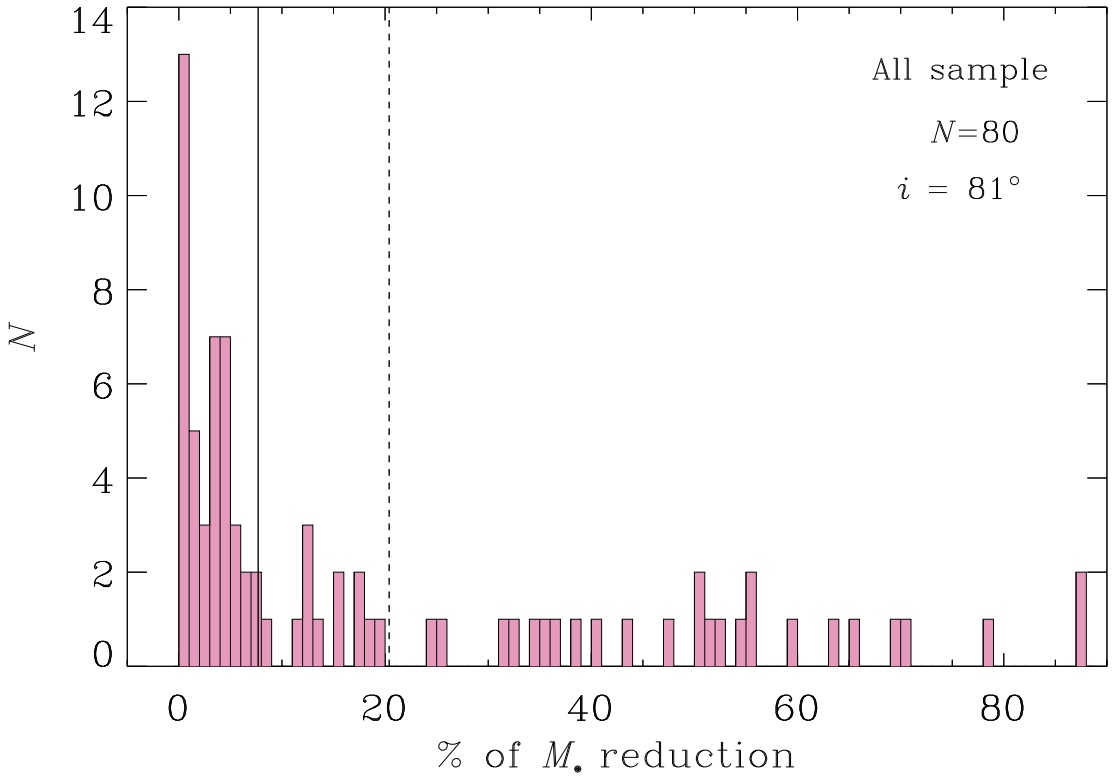

Figure 3.14: Distribution of the relative decrease of the $M_\bullet$ value derived by taking into account the contribution of the stellar mass for an inclination of $i = 81°$ of the unresolved gaseous disk. The total number of galaxies is $N = 80$. The solid and dashed vertical lines mark the median and mean values of the distribution, respectively.

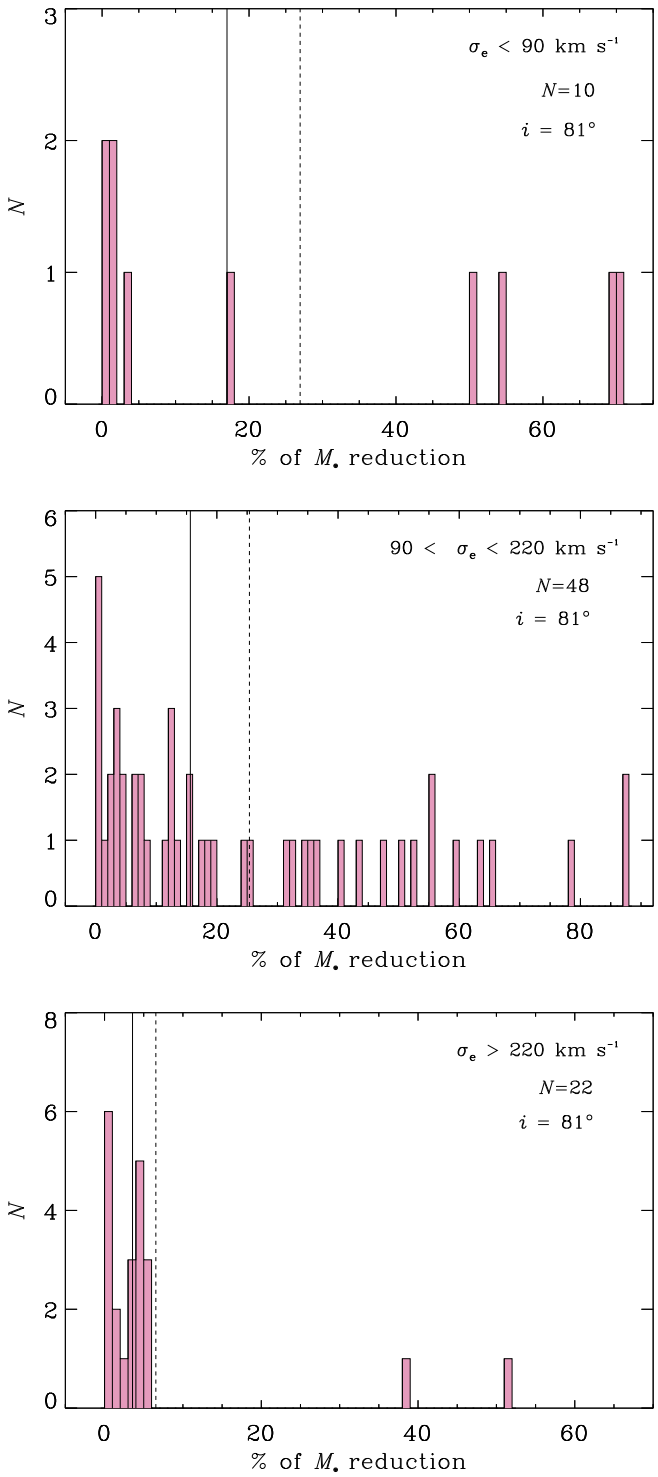

Figure 3.15: Same as in Fig. 3.14, but for galaxies with $\sigma_{\rm e} < 90$ km s^{-1} (*top panel*), $90 < \sigma_{\rm e} < 220$ km s^{-1} (*middle panel*), and $\sigma_{\rm e} > 220$ km s^{-1} (*bottom panel*). The number N of galaxies in each subsample is given.

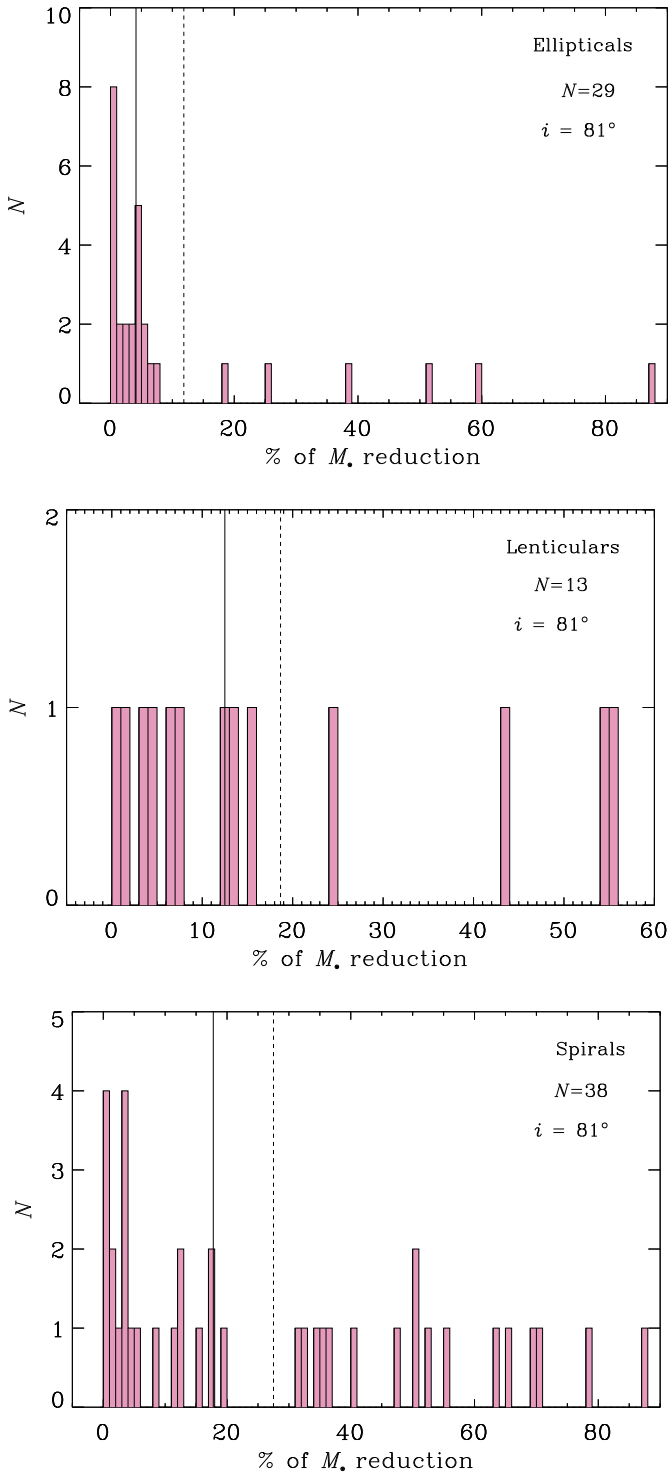

Figure 3.16: Same as in Fig. 3.14, but for elliptical (*top panel*), lenticular (*middle panel*), and spiral galaxies (*bottom panel*). The number N of galaxies in each subsample is given.

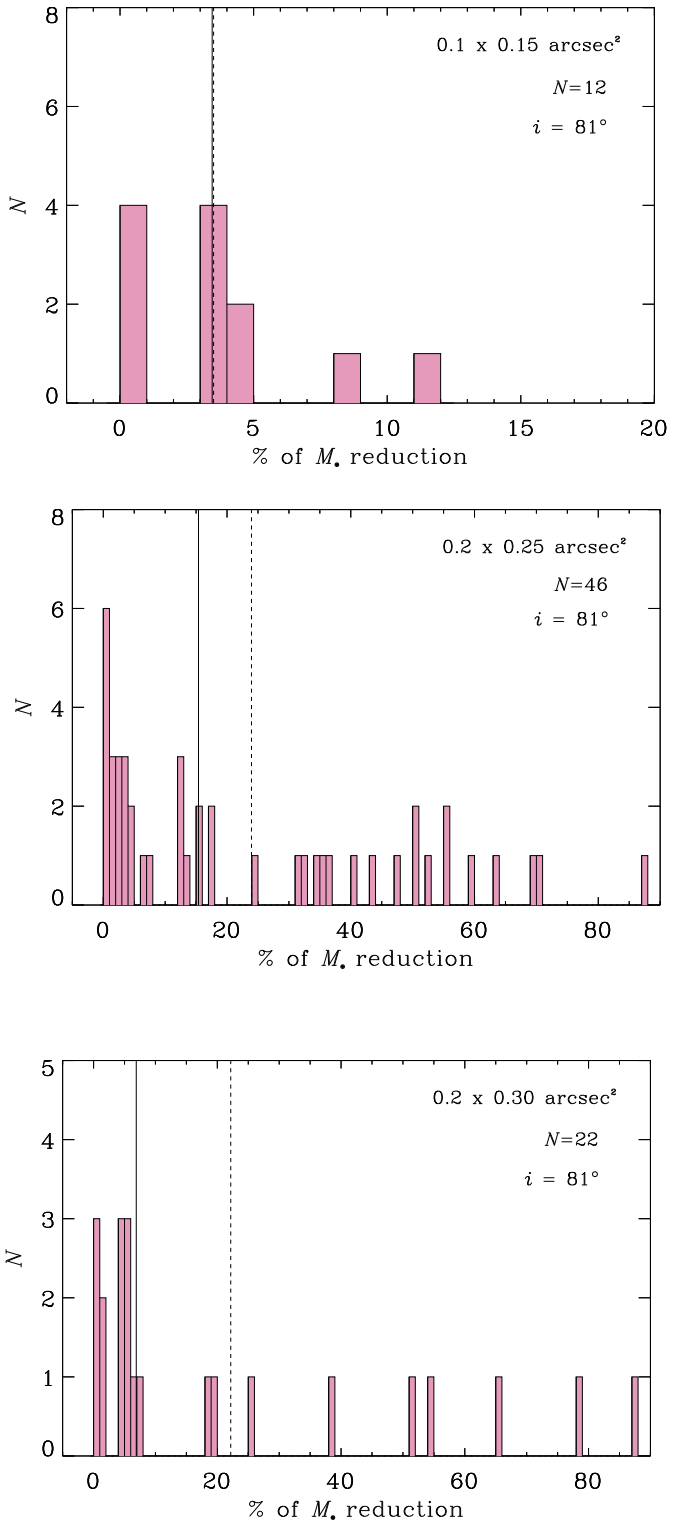

Figure 3.17: Same as in Fig. 3.14, but for galaxies with a nuclear spectrum obtained within a 0.1×0.15 arcsec^2 (*top panel*), 0.2×0.25 arcsec^2 (*middle panel*), and 0.2×0.30 arcsec^2 aperture (*bottom panel*). The number N of galaxies in each subsample is given.

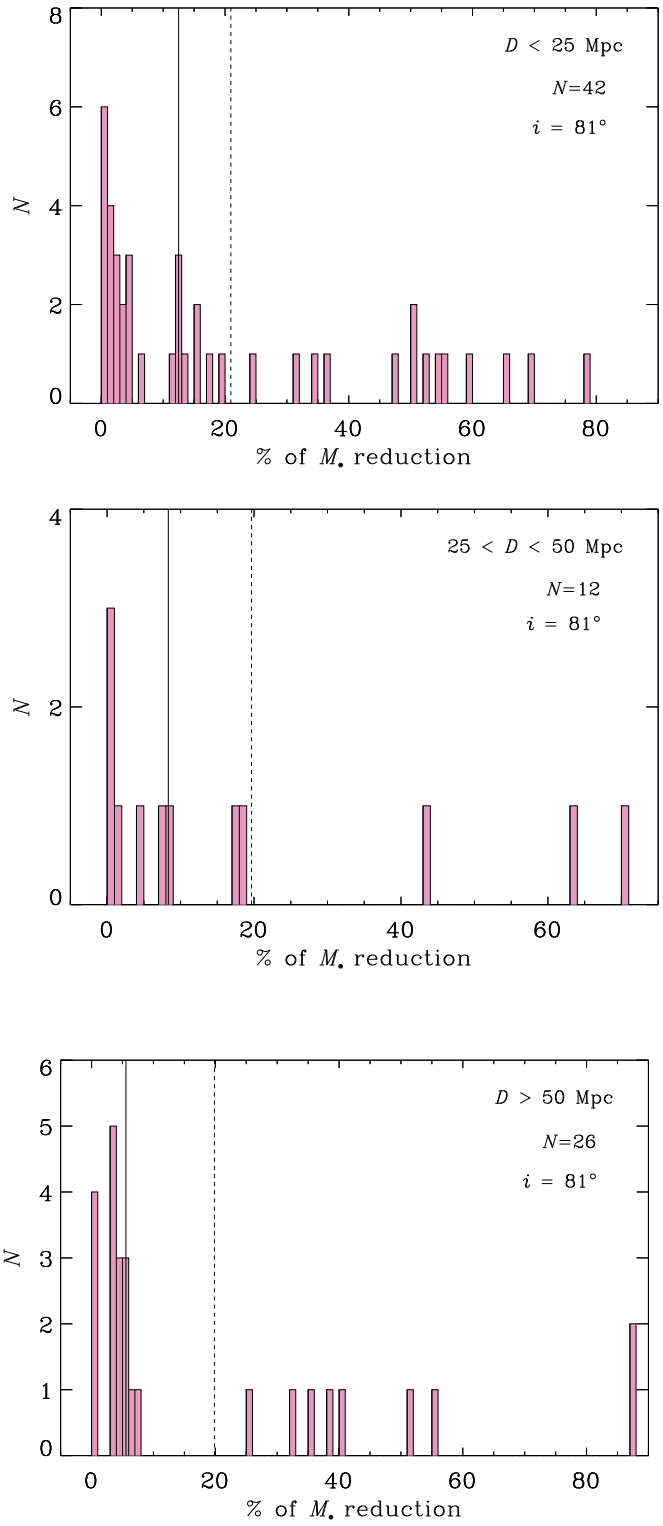

Figure 3.18: Same as in Fig. 3.14, but for galaxies with $D < 25$ Mpc (*top panel*), $25 < D < 50$ Mpc (*middle panel*), and $D > 50$ Mpc (*bottom panel*). The number N of galaxies in each subsample is given.

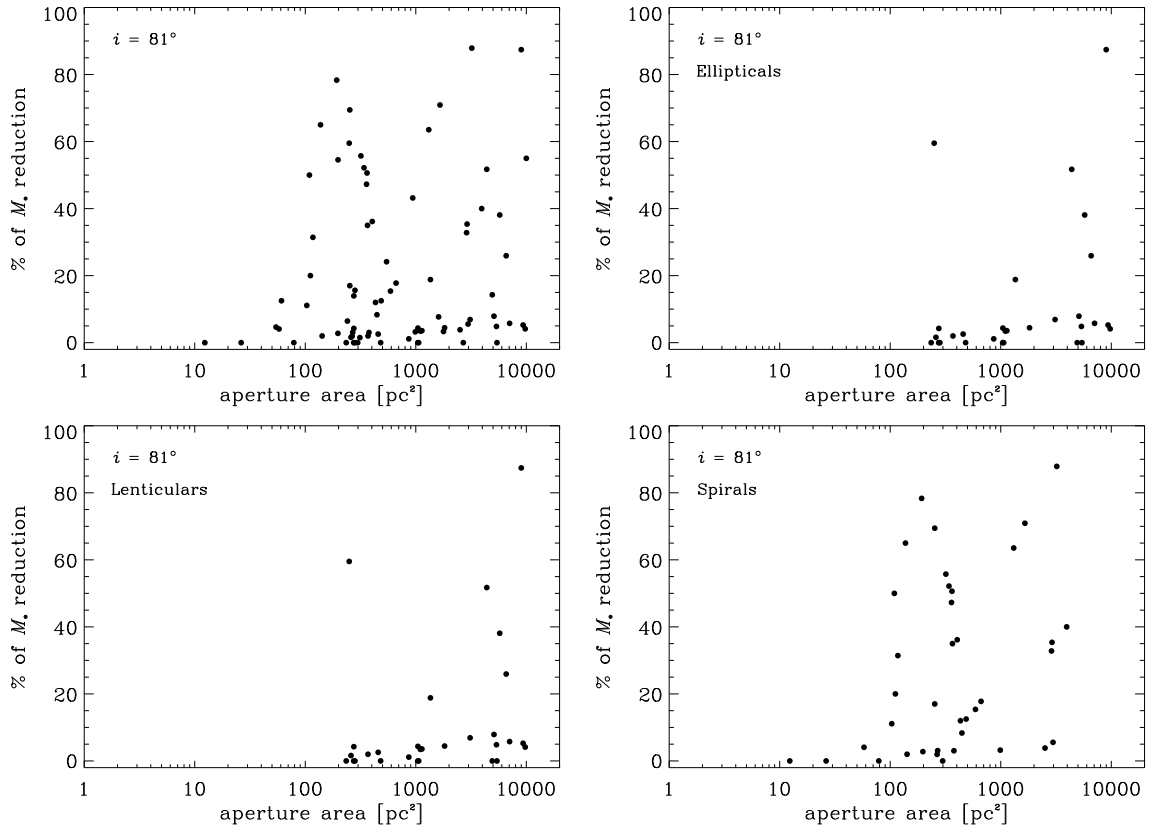

Figure 3.19: *Upper left-hand panel*: Distribution of the relative decrease of the $M_\bullet$ value derived by taking into account the contribution of the stellar mass for an inclination of $i = 81°$ of the unresolved gaseous disk as a function of the aperture area of the nuclear spectrum. The total number of galaxies is $N = 80$. *Upper right-hand panel*: Elliptical galaxies. *Lower left-hand panel*: Lenticular galaxies. *Lower right-hand panel*: Spiral galaxies. The number N of galaxies in each subsample is given.

Table 3.9: Amount of decrease of the $M_\bullet$ stringent limits including the stellar mass contribution in the dynamical model and assuming $i = 81°$ for the unresolved gaseous disk as a function of σ_e.

	All	σ_e< 90 km s^{-1}	90 < σ_e< 220 km s^{-1}	σ_e> 220 km s^{-1}
N	80	10	48	22
γ	20.4%	27.0%	25.4%	6.5%

Notes: The mean decrease and number of galaxies are reported for each sample.

Table 3.10: As in Table 3.9 but as a function of the morphological type.

	All	E	SA0+SB0	SA0	SB0	SA+SB	SA	SB
N	80	29	13	5	8	38	14	24
γ	20.4%	11.9%	18.7%	15.7%	20.5%	27.5%	25.7%	28.5%

Notes: The mean decrease and number of galaxies are reported for each sample.

Nuclear star clusters in the low-σ_e range

In principle, the presence of a NSC could partially explain the cases with the larger stellar mass contribution. Such a stellar mass is even larger if the galaxy is characterized by a large distance and it was observed through a wide aperture. These effects could play an important role for the galaxies with a small $M_\bullet$ as pointed out by Beifiori et al. (2009) and deserve to be investigated. For this reason we focused on the galaxies in the low-σ_e range and considered their $M_\bullet$ values at $i = 33°$.

We discarded NGC 3310, NGC 5347, and UGC 1395 from the low-σ_e subsample because they have $M_\bullet = 10^5$ M$_\odot$ at both inclinations of the unresolved gaseous disk and we will discuss them in Sect. 3.5.3. So we remained with 14 galaxies with $\sigma_e < 90$ km s^{-1} (Table 3.1). We found almost no variation in $M_\bullet$ by considering the stellar mass contribution in the dynamical model of NGC 4212, NGC 4245, NGC 5194, and NGC 5879 and a small variation of about 4% for NGC 5643 and NGC 6300. For the remaining galaxies, the stellar mass contribution was remarkable: IC 342 (63%), NGC 2685 (13%), NGC 3021 (72%), NGC 3259 (67%), NGC 3982 (54%), NGC 4041 (11%), NGC 4321 (22%), NGC 5427 (23%).

Georgiev & Böker (2014) presented a catalogue of 228 NSCs in spiral galaxies by analysing the HST/WFPC2 archival images. They found a NSC in NGC 3259, NGC 4041 and NGC 5427 but not in IC 342 and NGC 5879. On the contrary, Böker et al. (1999) and Scott & Graham (2013) detected a NSC in IC 342 and NGC 5879, respectively. Scarlata et al. (2004) analyzed the nuclear properties of nearby spiral galaxies from HST/STIS acquisition images. They identified a resolved star cluster from a central excess of light in the surface brightness profiles of NGC 3021, NGC 4041, NGC 4212, and NGC 4321. With the same method B09 also found an excess of light in the nucleus of NGC 4245. On the other hand, NGC 2685 contains a NSD (Ledo et al., 2010) which corresponds to a less concentrated stellar mass with respect to one of a NSC.

Table 3.11: As in Table 3.9 but as a function of the size of the central aperture.

	All	0.1×0.15 arcsec^2	0.2×0.25 arcsec^2	0.2×0.30 arcsec^2
N	80	12	46	22
γ	20.4%	3.5%	24.0%	22.2%
	E	0.1×0.15 arcsec^2	0.2×0.25 arcsec^2	0.2×0.30 arcsec^2
N	29	6	8	15
γ	11.9%	1.9%	8.7%	17.5%
	S0	0.1×0.15 arcsec^2	0.2×0.25 arcsec^2	0.2×0.30 arcsec^2
N	13	2	9	2
γ	15.7%	4.0%	20.0%	27.3%
	S	0.1×0.15 arcsec^2	0.2×0.25 arcsec^2	0.2×0.30 arcsec^2
N	38	4	29	5
γ	25.7%	5.7%	29.4%	34.2%

Notes: The mean decrease and number of galaxies are reported for each sample.

Table 3.12: As in Table 3.9 but as a function of the galaxy distance.

	All	$D < 25$ Mpc	$25 < D < 50$ Mpc	$D > 50$ Mpc
N	80	42	12	26
γ	20.4%	20.9%	19.7%	19.9%
	E	$D < 25$ Mpc	$25 < D < 50$ Mpc	$D > 50$ Mpc
N	38	7	6	16
γ	11.9%	10.0%	4.1%	15.6%
	S0	$D < 25$ Mpc	$25 < D < 50$ Mpc	$D > 50$ Mpc
N	13	8	2	3
γ	15.7%	16.7%	25.4%	19.4%
	S	$D < 25$ Mpc	$25 < D < 50$ Mpc	$D > 50$ Mpc
N	38	27	4	7
γ	25.7%	25.0%	40.1%	29.8%

Notes: The mean decrease and number of galaxies are reported for each sample.

Table 3.13: As in Table 3.9 but as a function of the size of central aperture and galaxy distance.

	0.1×0.15 arcsec^2	0.2×0.25 arcsec^2	0.2×0.30 arcsec^2
$D < 25$ Mpc	5.3%	18.9%	44.0%
$25 < D < 50$ Mpc	2.7%	33.8%	8.1%
$D > 50$ Mpc	3.0%	42.5%	17.4%

Notes: The mean decrease is reported for each sample.

So we can impute the large stellar contribution in the galaxy nucleus to the presence of a NSC for IC 342, NGC 3021, NGC 3259, NGC 4041, NGC 4321, and NGC 5427 and of a NSD for NGC 2685. In the case of IC 342, the MGE analysis could have been hampered by the absence of the a well-defined nucleus, which led to an overestimate of the stellar mass contribution. The distance (41.7 Mpc) played role in enhancing the stellar mass contribution of NGC 5427. Although a NSC could reside in the center of NGC 4212 and NGC 4245, their $M_\bullet$ did not change by including the stellar mass contribution in the dynamical model.

Galaxies with not matched gas velocity dispersion

We found $M_\bullet = 10^5$ $M_\odot$ for 8 galaxies at 81° and for 7 galaxies at both inclinations when considering the stellar mass contribution in the dynamical model (Table 3.3). We were not able to match the low gas velocity dispersion with that predicted by the dynamical model. As a consequence the quoted $M_\bullet$ corresponds to the lowest $M_\bullet$ in the grid of models and represents an upper limit to the actual $M_\bullet$ value. These galaxies were discarded from the previous analysis since they would have strongly biased the results.

This issue arose more frequently for $i = 81°$ because the stellar mass contribution is larger at higher inclination. But, we could have overestimated the stellar mass. This is the case of distant galaxies, of galaxies with an irregular central surface-brightness distribution which results in overestimating the stellar light in the MGE model, and of galaxy nuclei hosting a younger and metal-poorer stellar population which require a smaller $(M/L)_\star$ than that we adopted.

NGC 5347 (37.1 Mpc) and especially UGC 1395 (69.9 Mpc) have a large distance with respect to the median value of the sample (25.7 Mpc) and so their stellar mass contribution could be particularly large. The nuclear region of IC 342 is composed of bright knots rather than a well-defined nucleus, whereas the nucleus of NGC 4507 is heavily obscured by dust. In both cases the stellar light could have been overestimated in the MGE model. For the other galaxies the MGE model reproduced in a proper way the central surface brightness. Certainly in some cases (e.g., IC 342 and NGC 3259 which harbor a NSC) the adopted $(M/L)_\star$ could be larger than the adopted one. This is actually a critical issue since using $(M/L)_\star = 1.1$ $M_\odot/$ $L_\odot$ (i.e., 4 times less than the adopted one), we found $M_\bullet > 10^5$ $M_\odot$ for most of the above galaxies.

Comparison with the literature

We compared the $M_\bullet$ stringent limits of Sample B with the $M_\bullet$ estimates obtained by modelling the resolved kinematics of gas, stars, and water masers available in the literature. We found accurate $M_\bullet$ measurements for 21 galaxies, and $M_\bullet$ upper limits for another 6 galaxies. We rescaled these values accordingly to our distances and reported them in Table 3.3. We considered only the 21 accurate $M_\bullet$ values as shown in Fig. 3.20.

Our $M_\bullet$ stringent limits at $i = 33°$ are smaller than their corresponding accurate $M_\bullet$ estimate for only 7 galaxies, whereas all but 3 of our $M_\bullet$ stringent limits at $i = 81°$ are smaller than accurate $M_\bullet$ measurements. Nevertheless, most of our $M_\bullet$ upper limits are fully

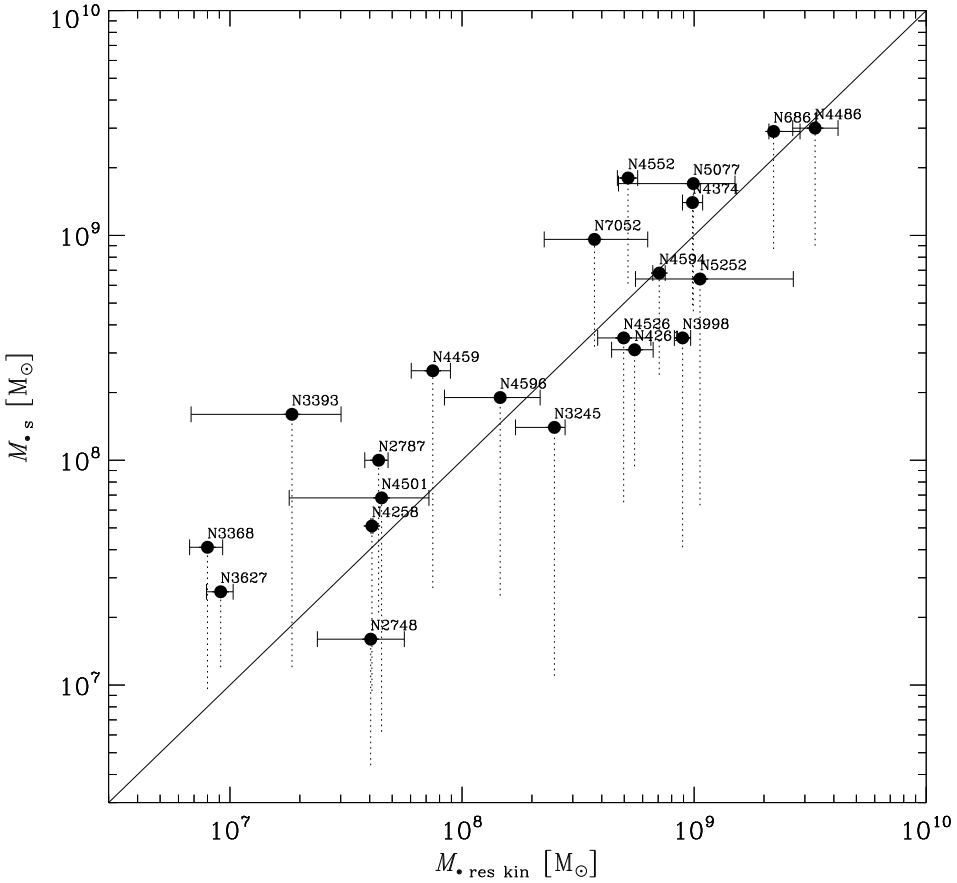

Figure 3.20: Comparison between our $M_\bullet$ stringent limits and accurate measurements of $M_\bullet$ based on the resolved kinematics of gas, stars, and water masers available in the literature. The upper and lower edges of the dotted lines correspond to the $M_\bullet$ values that we estimated assuming an inclination of $i = 33°$ and $81°$ for the unresolved gaseous disk, respectively.

consistent with their corresponding accurate $M_\bullet$ estimates. As expected, the inclination of the gaseous disk is a key information and the agreement is even stronger if we adopt the inclination obtained by modeling the ionized-gas resolved kinematics for NGC 2787 (Sarzi et al., 2001), NGC 4374 (Walsh et al., 2010), NGC 4459 and NGC 4596 (Sarzi et al., 2001), NGC 5077 (de Francesco et al., 2008), and NGC 7052 (van der Marel & van den Bosch, 1998). On the contrary, the inclination of the gas disk is not available for galaxies where the motion of stars or masers where used to derive $M_\bullet$.

Even if they are not actual estimates, our 21 $M_\bullet$ stringent limits at $i = 33°$ exceed only a median factor of 1.3 the accurate $M_\bullet$ measurements. Moreover, with this technique it was possible to collect a sample of 100 objects at a relatively cheap cost in terms of both observation time and modeling and it could be useful to put constraints on scaling relation along with actual $M_\bullet$ measurements, as B12 already did.

Table 3.14: Central value of the Gaussian function fitted to histograms and median and mean value for the ratios between the $M_\bullet$ values at $i = 33°$ and the expected ones from the $M_\bullet - \sigma_e$ relation.

33°	Peak A	Median A	Mean A	Peak B	Median B	Mean B
All	1.8	1.9	3.4	1.6	1.7	2.7
$\sigma_e < 90$ km s^{-1}	3.0	3.3	8.4	1.4	2.2	5.5
$90 < \sigma_e < 220$ km s^{-1}	2.0	2.1	3.0	2.0	1.9	2.6
$\sigma_e > 220$ km s^{-1}	0.9	0.97	1.3	0.92	0.95	1.3

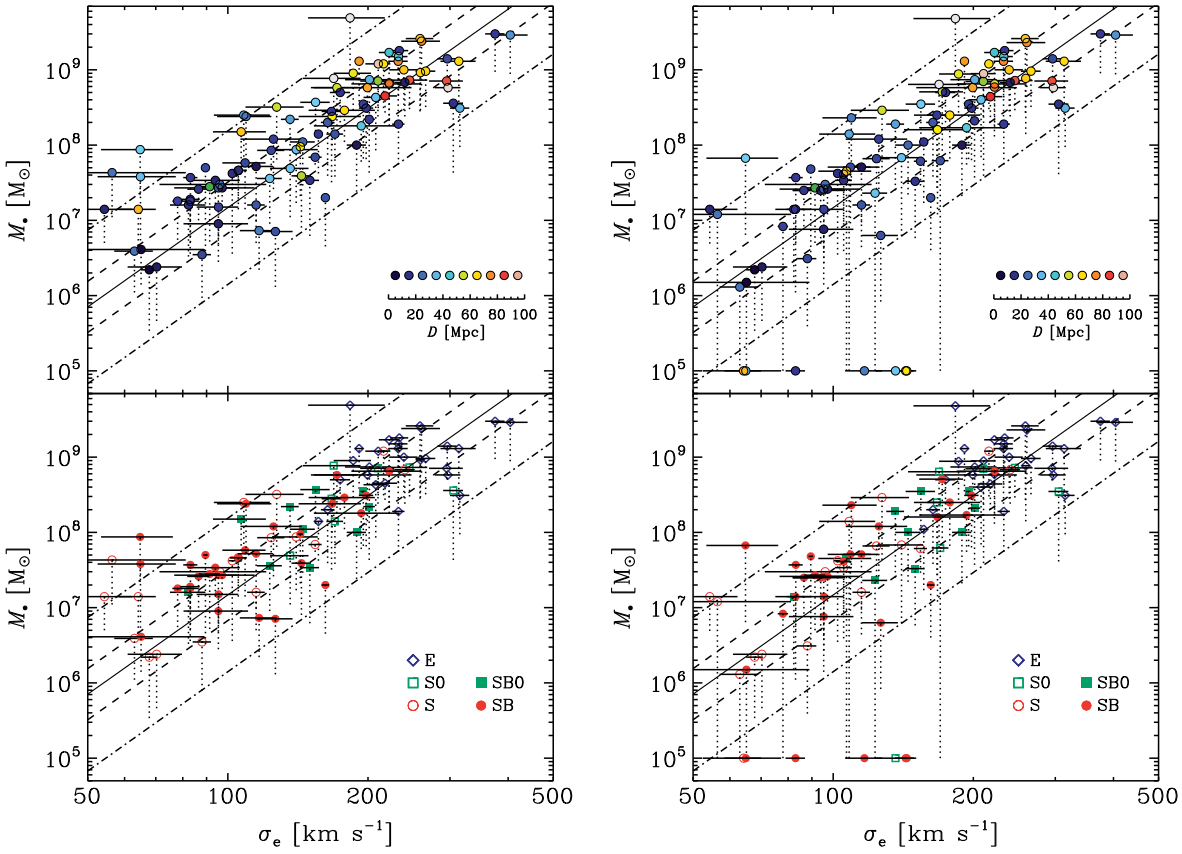

Figure 3.21: Comparison between the $M_\bullet$ stringent limits of Sample A (*left-hand panels*) and Sample B (*right-hand panels*) as a function of galaxy distance (*upper panels*) and morphological type (*lower panels*). The upper and lower edges of the dotted lines correspond to $M_\bullet$ values estimated assuming an inclination of $i = 33°$ and 81° for the unresolved gaseous disk, respectively. The solid line is the $M_\bullet - \sigma_e$ relation by Kormendy & Ho (2013) with the dashed and dotted-dashed lines showing the $\pm 1\sigma$ and $\pm 3\sigma$ scatter in $M_\bullet$, respectively.

3.5.4 Comparison with the $M_\bullet - \sigma_e$ relation

We considered the $M_\bullet$ values of Sample A and Sample B with respect to the $M_\bullet - \sigma_e$ relation (Fig. 3.21). Although more updated versions of the $M_\bullet - \sigma_e$ relation are available in the

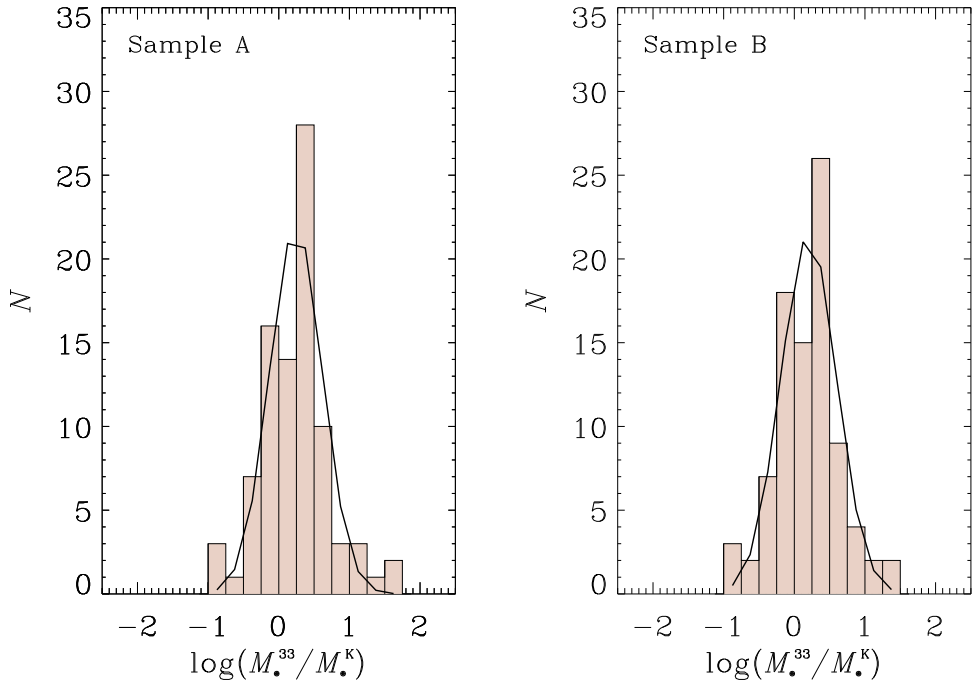

Figure 3.22: Distribution (pink histogram) and corresponding Gaussian fit (black solid line) of the ratios between the measured $M_\bullet$ stringent limits assuming an inclination of $i = 33°$ for the unresolved gaseous disk and the values of $M_\bullet$ expected from the $M_\bullet - \sigma_e$ relation by Kormendy & Ho (2013) for Sample A (*left-hand panel*) and B (*right-hand panel*).

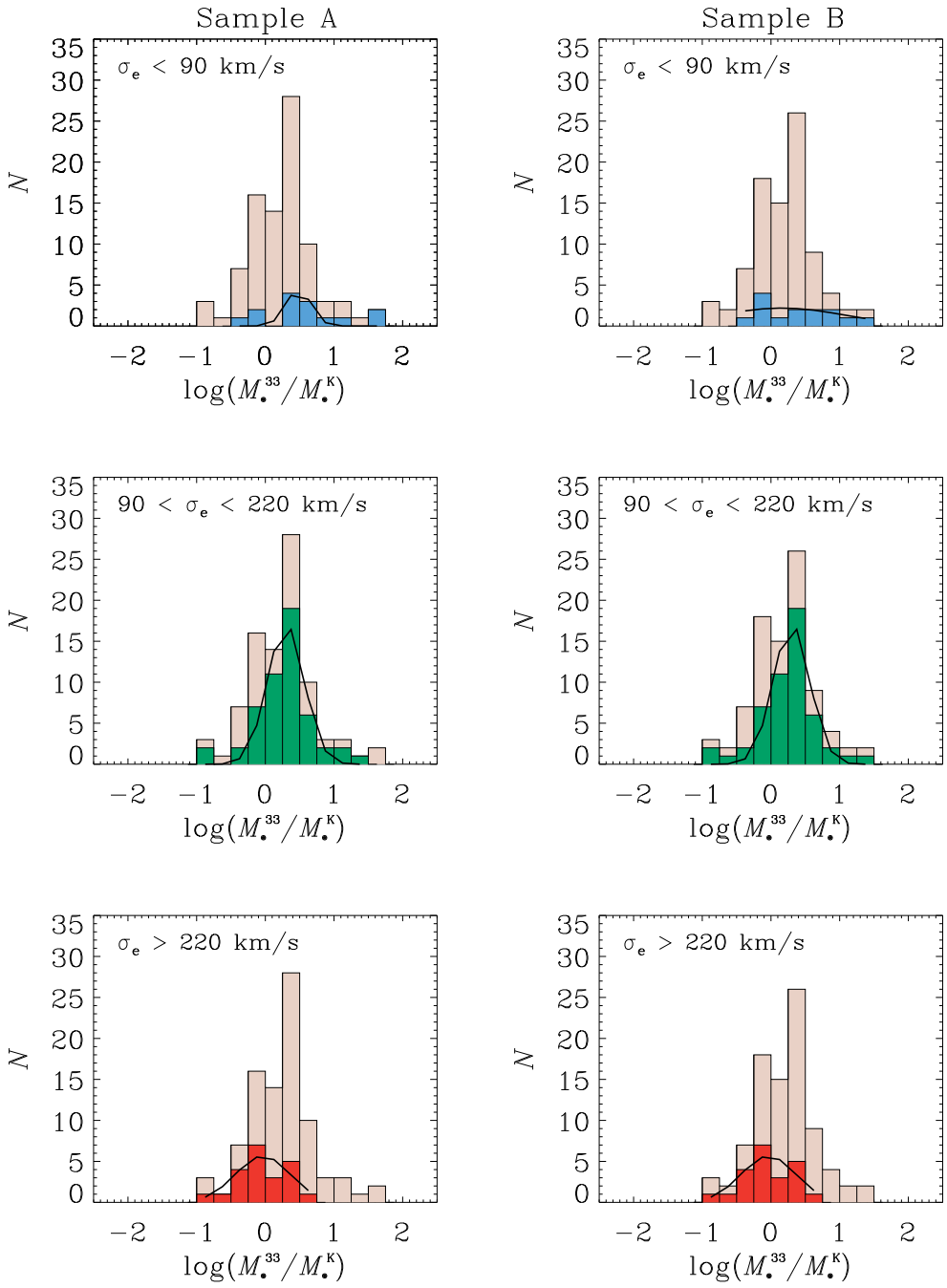

Figure 3.23: As in Fig. 3.22, but also showing the subsamples of galaxies with $\sigma_e < 90$ km s^{-1} (cyan histograms, *top panels*), $90 < \sigma_e < 220$ km s^{-1} (green histograms, *middle panels*), and $\sigma_e > 220$ km s^{-1} (red histograms, *bottom panels*). In each panel, the black solid line is Gaussian fit to the distribution of the subsample galaxies.

literature (e.g., van den Bosch, 2016), we preferred the one by Kormendy & Ho (2013) because of their careful selection of the galaxy sample. In the following analysis, we limited the comparison to the 88 $M_\bullet$ values at $i = 33°$ and 80 $M_\bullet$ values at $i = 81°$ with $M_\bullet > 10^5$ $M_\odot$ from both Sample A and Sample B.

First, we investigated the distribution of the $M_\bullet$ values at $i = 33°$ from Sample B in the $M_\bullet - \sigma_e$ plane by calculating the Spearman rank and the Pearson correlation coefficients. The first coefficient assesses how well the relation between two variables can be described employing a monotonic function, whereas the second one addresses the possible presence of a linear relation (Press et al., 1992). We found a Spearman rank coefficient of 0.88 which suggests a very strong positive correlation and a Pearson correlation coefficient of 0.87 which confirms the presence of a linear relation. This justified our linear fit to the data. We obtained a slope of 3.57 ± 0.22, which is shallower that the value of 4.38 ± 0.29 found by Kormendy & Ho (2013). The two values are not consistent each other within 1σ but it has to be kept in mind that a few outliers could affect this estimate. For Sample A, we found very similar Spearman rank (0.87) and Pearson correlation (0.85) coefficients, whereas the slope of the linear fit was appreciably shallower (3.32 ± 0.22). This is an effect of the decrease of the stellar mass contribution with increasing values of σ_e (see Sect. 3.5.3).

The distributions of the ratios between the $M_\bullet$ stringent limits from Sample A and Sample B and the corresponding $M_\bullet$ predicted from the adopted $M_\bullet - \sigma_e$ relation were fitted with a Gaussian (Fig. 3.23). We found for Sample A and Sample B a peak value of 1.8 and 1.6, respectively and a median value of 1.9 and 1.7, respectively. Both distributions are not symmetric with a long tail towards very high values, as it results from their mean values of 3.4 and 2.7, respectively (Table 3.14). Nevertheless, $M_\bullet$ values of Sample B are systematically closer to the $M_\bullet - \sigma_e$ relation than the ones of Sample A stressing the importance of taking into account for the stellar mass contribution when measuring the $M_\bullet$ upper limits from unresolved ionized-gas kinematics.

The $M_\bullet$ values of four objects of Sample B are well above the 3σ line from the $M_\bullet - \sigma_e$ relation. These are NGC 5427 and NGC 5879 in the low-σ_e range, and NGC 4579 and UGC 7115 in the intermediate-σ_e range. If we reject these outliers, the median ratio of Sample B decreases to 1.6 whereas the peak value of the Gaussian remains the same.

Low-σ_e range

The intermediate-σ_e range includes 14 galaxies, 2 of which are strong outliers with respect the $M_\bullet - \sigma_e$ relation (NGC 5427 and NGC 5879)

In this σ_e range we observed a large dispersion of the $M_\bullet$ values of Sample B. According to the very low Spearman rank (0.36) and Pearson correlation coefficients (0.28), neither a linear nor a monotonic function can be fitted to the data. By disregarding the two outlier galaxies, the two coefficients increases to 0.71 and 0.59, respectively. We performed a linear fit with a slope of 4.90 ± 2.14, but the correlation is weak as shown by the low Pearson correlation coefficient and corresponding large uncertainty on the slope.

Fig. 3.23 shows that the $M_\bullet$ values of Sample A are a factor of 3.0 larger than those expected from the $M_\bullet - \sigma_e$ relation, whereas the $M_\bullet$ values of Sample B are only a factor of

1.4 larger. On the other hand, we derived a median value of 3.3 for the $M_\bullet$ ratios of Sample A and of 2.2 for those of Sample B (Table 3.14). But they are not distributed as a Gaussian and we did not perform any fit.

As already pointed out in Sect. 3.5.3, the stellar mass contribution could be larger in galaxies with a small $M_\bullet$ which is actually the case for this σ_e range. We investigated the position of the $M_\bullet$ of Sample A and Sample B with respect to the $M_\bullet - \sigma_e$ relation. We checked whether the galaxies of Sample A with a NSC or NSD were those farther from the relation and moved closer to it after accounting for the stellar mass contribution in the dynamical model (Fig. 3.21). NGC 3310, NGC 5347 and UGC 1395 were discarded from this subsample because their $M_\bullet = 10^5$ $M_\odot$ at both inclination as discussed in Sect. 3.5.3. The $M_\bullet$ of NGC 3021, NGC 5427, and NGC 5879 are above 3σ from the $M_\bullet - \sigma_e$ relation. After accounting for the stellar mass contribution, the $M_\bullet$ value of NGC 3021 moves under the 3σ line, that of NGC 5427 move a little but remained above the 3σ line and that of NGC 5879 remains in the same position. Whereas the NSC of NGC 3021 and NGC 5427 may have played a role in determining the correct value of $M_\bullet$, in the case of NGC 5879 the presence of a NSC is controversial (see Scott & Graham, 2013; Georgiev & Böker, 2014, for different results). The $M_\bullet$ of NGC 4245 and NGC 5643 are placed between 2 and 3σ from the $M_\bullet - \sigma_e$ and they remain almost in the same position after considering the stellar mass contribution. NGC 4245 does not move from its position even if a NSC could reside in its center (B09). For NGC 5643 there is no information in the literature about the possible presence of a NSC. The $M_\bullet$ of NGC 3982, NGC 2685, NGC 4321, and NGC 6300 are located between 1 and 2σ above the $M_\bullet - \sigma_e$ relation. Taking into account for the stellar mass contribution, they move under (NGC 3982), or overlap (NGC 2685, NGC 4321), or remain above (NGC 6300) the 1σ line. NGC 4321 harbors a NSC and NGC 2685 a NSD, whereas there is no information about NGC 3982 and NGC 6300. The $M_\bullet$ of IC 342 and NGC 3259 are between the $M_\bullet - \sigma_e$ relation and 1σ line and they move downward between the relation and -1σ line. There is a NSC in both galaxies, even if the stellar light contribution of IC 0342 could have been overestimated by the MGE model. The $M_\bullet$ of NGC 4212 and NGC 5194 are located between the $M_\bullet - \sigma_e$ relation and -1σ line and maintain their position, even if NGC 4212 hosts a NSC. Finally, the $M_\bullet$ of NGC 4041 was under the -1σ line and probably decreases a little for the presence of a NSC.

Intermediate-σ_e range

The intermediate-σ_e range counts 52 galaxies, 2 of which are strong outliers with respect the $M_\bullet - \sigma_e$ relation (NGC 4579 and UGC 7115).

We found that 40 and 12 $M_\bullet$ values of Sample B which are positioned above and under the $M_\bullet - \sigma_e$ relation, respectively. Their Spearman rank and Pearson correlation coefficients are 0.81 and 0.77, respectively with a linear-fit slope of 4.05 ± 0.48. This is larger compared to what we obtained for the entire sample. We found similar results also by excluding NGC 4579 and UGC 7115. Indeed, the Spearman rank and Pearson correlation coefficients increase only to 0.83 and 0.80, respectively with a linear-fit slope of 4.01 ± 0.43. Both slopes are consistent within 1σ to the slope of the Kormendy & Ho (2013) relation.

By considering the median of the ratios between the $M_\bullet$ stringent limits of Sample B and their corresponding values from $M_\bullet - \sigma_e$, we derived a median factor of 2.1 and 1.9 for Sample A and Sample B, respectively. We calculated a peak value of 2.0 for Sample A and Sample B by fitting a Gaussian (Fig. 3.22 and Table 3.14). In both cases the median and peak values are quite similar, but smaller than the mean value due also to the presence of a number of outliers in the high end of the $M_\bullet$ ratio distributions.

High-σ_e range

The high-σ_e range includes 22 galaxies.

B09 found a systematic flattening in the distribution of their upper limits with larger σ_e by performing a linear fit to $M_\bullet$ values. They considered progressively larger σ_e ranges and disregarded the $M_\bullet$ values in the low-σ_e range. On the contrary, we did not find clearcut evidence for such a flattening. We considered the Sample B and disregarded galaxies with $\sigma_e < 90$ km s^{-1}. By performing a linear fit to $M_\bullet$ values with σ_e out to 220 km s^{-1}, 260 km s^{-1}, 300 km s^{-1}, and 375 km s^{-1}, we found slopes of 3.87 ± 0.49, 3.99 ± 0.37, 3.79 ± 0.33 and 3.50 ± 0.30, respectively.

The peaks of the Gaussian fit to the distribution of the ratios between the $M_\bullet$ stringent limits of Sample A and Sample B and their corresponding values from $M_\bullet - \sigma_e$ are both centered on 0.92 and their median is 0.97 and 0.92, respectively (Table 3.14). So the $M_\bullet$ masses are well-distributed around the $M_\bullet - \sigma_e$ in this σ_e range (Fig. 3.22). The distribution of the $M_\bullet$ ratios shows shallow flattening with respect to those in the other σ_e ranges. For Sample B and disregarding galaxies with $\sigma_e < 90$ km s^{-1}, we fit with a Gaussian the $M_\bullet$ ratios with σ_e out to 220 km s^{-1}, 260 km s^{-1}, 300 km s^{-1}, and 375 km s^{-1} and found central peak values of 1.9, 1.8, 1.7, and 1.7, and median values of ratios of 1.8, 1.8, 1.7, and 1.7, respectively.

Comparison between the two inclinations

The Sample B at $i = 33°$ contains 8 more galaxies compared to that at $i = 81°$, as we pointed out in Sect. 3.5.3. We discard these galaxies to perform a fair comparison between the results obtained for Sample B on the same 80 $M_\bullet$ values at $i = 33°$ and 81°. To this aim, we repeated the Gaussian fit of the distribution of the $M_\bullet$ ratios at $i = 33°$, we calculated the Spearman rank and the Pearson correlation coefficients and performed again the linear fit. The same was done for the $M_\bullet$ values obtained at $i = 81°$.

For the $M_\bullet$ ratios at $i = 33°$, we found a Gaussian peak value of 1.7 and a median value of 1.8. For $\sigma_e < 90$ km s^{-1}, $90 < \sigma_e < 220$ km s^{-1}, and $\sigma_e > 220$ km s^{-1} we obtained peak values of 2.7, 2.0, and 0.9, respectively and median values of 3.2, 1.9, and 1.0, respectively. Comparing these results with those reported in Table 3.14, we obtained the same values in the intermediate and high-σ_e ranges, whereas they are quite different in the low-σ_e range. For the $M_\bullet$ ratios at $i = 81°$, we found a peak value of 0.3 and a median value of 0.4. For $\sigma_e < 90$ km s^{-1}, $90 < \sigma_e < 220$ km s^{-1}, and $\sigma_e > 220$ km s^{-1} we obtained peak values of 0.2, 0.4, and 0.3, respectively and median values of 0.3, 0.4, and 0.3, respectively. As expected,

the $M_\bullet$ values at 81° lie on average well below the $M_\bullet - \sigma_e$ relation. By considering both inclinations, the $M_\bullet$ values at $i = 81°$ are positioned much farther from the $M_\bullet - \sigma_e$ relation than those at $i = 33°$. We expect that the $M_\bullet$ values at $i = 60°$ will place on average just below the $M_\bullet - \sigma_e$ relation. This could be the consequence of having adopted a very large value for the $(M/L)_\star$ to maximize the stellar mass contribution all over the galaxy sample.

The linear fit of the $M_\bullet$ values of all the sample galaxies has a slope of 3.47 ± 0.24 for $i = 33°$ and 3.86 ± 0.26 for $i = 81°$, whereas the slope for the intermediate-σ_e range is 4.18 ± 0.49 for $i = 33°$ and 4.21 ± 0.55 for $i = 81°$. These two slopes are both consistent within 1σ with the slope of the Kormendy & Ho (2013) relation.

3.6 Conclusions

We obtained $M_\bullet$ stringent limits for 100 nearby galaxies by modeling of the [NII]λ6583 emission-line width measured on sub-arcsecond apertures with STIS using the dynamical model by Sarzi et al. (2002) and B09. In constraining the $M_\bullet$ value, we took into account the stellar mass contribution in the galaxy nucleus. We analyzed the galaxy sample of B09, B12, and Pagotto et al. (2017), who derived the $M_\bullet$ stringent limits by disregarding the stellar mass contribution. We repeated the $M_\bullet$ measurements of B09 and B12 to perform a plain comparison between the $M_\bullet$ values determined with and without including the stellar mass in the dynamical model.

We estimated the stellar mass contribution of the sample galaxies by modeling the surface brightness distribution measured from HST archival images as a sum of a set of Gaussians and by adopting the mass-to-light ratio of an old and metal-rich stellar population ($(M/L)_\star = 4.32$ $M_\odot/ L_\odot$, Vazdekis et al. 2012). We therefore maximized the amount of stellar mass that resides within the aperture size of each galaxy. For some galaxies, this was overestimated since their nucleus host younger and less metal-rich stellar populations with a smaller $(M/L)_\star$.

We found that on average the stellar mass contribution was larger in the low-σ_e range (24% for $\sigma_e < 90$ km s^{-1} at $i = 33°$) and it progressively decreases until it became negligible in the high-σ_e range (2% for $\sigma_e > 220$ km s^{-1} at $i = 33°$). Moreover, it was smaller for elliptical galaxies (3% at $i = 33°$) than for lenticulars (15% at $i = 33°$) and spirals (14% at $i = 33°$). In galaxies with larger $M_\bullet$ and σ_e, the SBH dominates the gravitational potential of nuclear regions. This is case of ellipticals, which are characterized by $M_\bullet > 10^8$ $M_\odot$ at $i = 33°$ which is much larger than the stellar mass contribution. Conversely, most spirals have $M_\bullet < 10^8$ $M_\odot$ at $i = 33°$ which is comparable to the mass contribution of the stars.

We also found that on average the stellar mass contribution is lower for smaller apertures of 0.1×0.15 arcsec^2 (6% at $i = 33°$), whereas there is not a clear correlation with the galaxy distance. This is expected because galaxies with very different σ_e values and morphological types are included in the same distance bins. Moreover, the sample was selected to include only nearby galaxies with a median distance $D = 25.7$ Mpc. So their distances are comparable except for a few cases. We did not observe any correlation between the stellar mass contribution and the physical size of the apertures.

In the low-σ_e range some of the sample galaxies with the larger stellar mass contribution

harbor a NSC or a NSD. Their presence certainly contributes to the stellar mass in the nucleus of 7 galaxies. In a few lenticulars and spirals, we were not able to match the observed [NII]λ6583 width with that predicted by the dynamical model and placed an upper limits of $M_\bullet < 10^5$ $M_\odot$ on the mass of their central SBH. We concluded that this could due to the large value adopted for $(M/L)_\star$. For example, Walcher et al. (2006) derived $(M/L)_\star = 0.08 - 2.06$ $M_\odot$/ $L_\odot$ (a factor 2 to 5 smaller than our value) for a sample of late-type spiral galaxies hosting a NSC by fitting composite population synthesis models to their nuclear spectra. This reduction of the mass-to-light ratio can be hardly considered in the case of ellipticals, since for them it is not common to harbor young stellar populations in the nuclear regions.

Overall it can be noticed that the stellar masses are quite smaller with respect to the $M_\bullet$ values, except for galaxies in the low-σ_e range. We explain this effect to the fact that we restricted our consideration to only nearby galaxies and this choice actually minimizes the amount of the stellar mass within the selected nuclear apertures.

At $i = 33°$, the median of the ratios between the $M_\bullet$ values we obtained and those predicted by the $M_\bullet - \sigma_e$ relation is 1.9, disregarding the stellar mass contribution, and 1.7 taking it into account. Accounting for the stellar mass distribution, the deviation of the $M_\bullet$ stringent limits from the $M_\bullet - \sigma_e$ relation significantly reduces in the low-σ_e large and becomes negligible in the high-σ_e range.

In the range $90 < \sigma_e < 220$ km s^{-1} the $M_\bullet$ values at $i = 33°$ run almost parallel to the $M_\bullet - \sigma_e$ relation with a slope of 4.00 ± 0.48, which is consistent with the findings of Kormendy & Ho (2013, 4.38 ± 0.29). Considering the entire σ_e range, the linear-fit slope is 3.56 ± 0.22 and indicates a shallow flattening for both $\sigma_e > 220$ km s^{-1} and $\sigma_e < 90$ km s^{-1}. The distribution of the $M_\bullet$ at $i = 81°$ was analyzed and compared in a consistent way with the one at $i = 33°$ by limiting the sample at $i = 33°$ to the same objects considered at $i = 81°$. From this analysis, we found that the $M_\bullet$ values at 81° are positioned farther from the $M_\bullet - \sigma_e$ relation with respect to those at $i = 33°$. This could be a consequence of having adopted a very large $(M/L)_\star$ value all throughout the galaxy sample.

On average our $M_\bullet$ stringent limits at $i = 33°$ are a only factor 1.7 larger than $M_\bullet$ predicted by the $M_\bullet - \sigma_e$ relation and a factor 1.3 larger than actual $M_\bullet$ values based on resolved kinematics. This is a striking result if we consider that our dynamical analysis does not rely on spatially-resolved distribution and kinematics of the gaseous tracer within the galaxy nucleus aperture and does not account for the presence of nongravitational forces which could further broaden the width of the emission lines. We concluded that nongravitational forces play a minor role in a vast majority of the sample galaxies by analysing the profile of the [NII]λ6583 emission line of the shape of its flux radial profile.

Chapter 4

A catalogue of nuclear stellar velocity dispersions of nearby galaxies from Hα STIS spectra to constrain supermassive black hole masses

Abstract. We present new measurements for the nuclear stellar velocity dispersion σ_* within sub-arcsecond apertures for a sample of 28 nearby galaxies. Our data consist of Space Telescope Imaging Spectrograph (STIS) long-slit spectra obtained with the G750M grating centered on the Hα spectral range. We fit the spectra using an extensive library of single stellar population models and Gaussian emission lines, while constraining in most cases the stellar-population content from an initial fit to G430L STIS spectra equally present in the Hubble Space Telescope archive. We illustrate how these sub-arcsecond σ_* measurements can be useful for constraining the mass $M_\bullet$ of supermassive black holes (SBHs) by concentrating specifically on the cases of the lenticular galaxies NGC 4435 and NGC 4459. These are characterized by similar ground-based half-light radii stellar velocity dispersion $\sigma_{\rm e}$ values but remarkably different $M_\bullet$ as obtained from modelling their central ionized-gas kinematics. In particular NGC 4435 appears to host a significantly undermassive SBH compared to that expected from the well-known $M_\bullet - \sigma_{\rm e}$ relation. For both galaxies, we build Jeans axisymmetric dynamical models to match the ground-based stellar kinematics obtained with the Spectrographic Areal Unit for Research on Optical Nebulae integral-field spectrograph, including a SBH with $M_\bullet$ value as predicted by the $M_\bullet - \sigma_{\rm e}$ relation and using high-resolution HST images taken with the Advanced Camera for Surveys as a base for constructing the stellar-mass model. By mimicking the HST observing conditions we then use such reference models to make a prediction for the nuclear σ_* value. Whereas this was found to agree with our nuclear σ_* measurement for NGC 4459, for NGC 4435 the observed σ_* is remarkably smaller than that predicted, which further suggests that this galaxy could host an undermassive SBH.

4.1 Introduction

Nowadays, there is a large body of evidence supporting the idea that a supermassive black hole (SBH), with a mass $M_\bullet$ ranging from 10^6 to 10^{10} $M_\odot$, lies in the center of most of galaxies. Over the last two decades, the SBH mass was found to correlate with several properties of their host galaxy and, in particular, of its spheroidal component, which corresponds to the entire galaxy in the case of ellipticals or to the bulge for lenticulars and spirals. These correlations suggest that the SBHs and their host spheroids grew together, and since the slope and scatter of such correlations are thought to relate to the details of the SBH-galaxy coevolution, there is constant demand for collecting $M_\bullet$ measurements across a large number of galaxies encompassing a wide range of host-galaxy masses and morphologies (see Kormendy & Ho, 2013, for a review).

The relationship between $M_\bullet$ and the stellar velocity dispersion σ_* of the spheroidal component is currently the tightest correlation discovered so far (Beifiori et al., 2012; Kormendy & Ho, 2013; van den Bosch, 2016), although there are open issues about its slope (Saglia et al., 2016), whether the SBHs in barred and ordinary galaxies and/or classical and pseudobulges follow the same correlation (Graham, 2016b), and the role of the over and undermassive SBHs with respect to those tracing the correlation (Savorgnan & Graham 2015, Krajnović et al. 2018b). In fact, there is still a need to increase the statistics of $M_\bullet$ in some specific physical ranges. Indeed van den Bosch et al. (2015) and Shankar et al. (2016) showed that the available $M_\bullet$ estimates and their scaling relations suffer from a remarkable bias since less dense galaxies are under represented in the SBH demography. The variety of tracers, dynamical models, and algorithms adopted to recover the mass distribution in the center of galaxies and constrain $M_\bullet$ is a further complication when building an unbiased sample. One significant contribution in this direction was given by the $M_\bullet$ stringent limits obtained for more than one hundred galaxies by Sarzi et al. (2002), Beifiori et al. (2009) and Pagotto et al. (2017), using nuclear line-width measurement for the nebular emission observed at sub-arcsecond resolution with the Hubble Space Telescope (HST).

Outlier galaxies with $M_\bullet$ far from the predictions of scaling relations represent an interesting challenge for understanding the coevolution of galaxies and SBHs. High $M_\bullet$ outliers include NGC 4468b (Kormendy et al., 1997) and NGC 1277 (van den Bosch et al., 2012), which are characterized by a steep inward σ_* gradient with central values not consistent with the Faber-Jackson relation, NGC 4342 (Cretton & van den Bosch, 1999), which is the strongest outlier in the $M_\bullet - M_{k,\mathrm{bulge}}$ correlation, NGC 1271 (Walsh et al., 2015) and MRK 1216 (Walsh et al., 2017), which have too large σ_* with respect to their K-band luminosity. Finding low $M_\bullet$ outliers, or even ruling out the presence of a SBH is a more challenging task given the detection threshold imposed by the angular resolution of present telescopes. Yet, remarkably low $M_\bullet$ outlier examples do exist, such as the radio-loud elliptical NGC 4335 (Verdoes Kleijn et al., 2002) and the barred lenticular NGC 4435 (Coccato et al., 2006), where $M_\bullet$ was constrained from the central ionized-gas kinematics observed with HST, or the lenticular NGC 4474 and elliptical NGC 4551, where $M_\bullet$ stringent limits were derived from stellar dynamical models and ground-based integral-field observations assisted by adaptive optics (Krajnović et al., 2018b). The merging galaxies NGC 1316 (Nowak et al., 2008) and

NGC 4382 (Gültekin et al., 2011) have also quite small $M_\bullet$ for their galaxy luminosities, but in these cases it is not clear if this could be linked to the merger physics and to limitations in search techniques. From a theoretical perspective, models of SBH evolution (e.g., Volonteri et al., 2011) predict that about 20% of galaxies with masses between 10^9 and 10^{10} $M_\odot$ should be characterized by $M_\bullet$ values critically below those predicted from present scaling relations. This is explained by ineffective growth of the SBHs, which also could be ejected or not formed at all from the very beginning. Therefore, assessing the fraction of undermassive black holes in nearby galaxies is crucial to understand how the SBHs increased their mass and settled in galactic nuclei.

In this context, this work provides a catalogue of new measurements of nuclear σ_* that can be useful for the purpose of constraining $M_\bullet$. The chapter is organized as follows. We describe the sample selection in Sect. 4.2. We measure the nuclear σ_* of the sample galaxies from Space Telescope Imaging Spectrograph (STIS) spectra in Sect. 4.3. We study in more detail NGC 4435 and NGC 4459 in Sect. 4.4 to illustrate how combining Advanced Camera for Surveys (ACS) photometry along with Spectrographic Areal Unit for Research on Optical Nebulae (SAURON) integral-field spectroscopy can constrain $M_\bullet$. Finally, we present our conclusions in Sect. 4.5. We adopt $H_0 = 70$ km s^{-1} Mpc^{-1}, $\Omega_{\rm M} = 0.3$, and $\Omega_\Lambda = 0.7$ as cosmological parameters all through the charter.

4.2 Sample selection

In order to measure the nuclear σ_* in nearby galaxies, we looked in the Mikulski Archive for Space Telescopes (MAST) for all the STIS medium-resolution spectra that were obtained with the slit crossing the nucleus.

We first considered the archival spectra of galaxies obtained with the G430M grating, except for those already obtained by Krajnović & Jaffe (2004) who already measured the stellar velocity and velocity dispersion along the major axis of four early-type galaxies. Unfortunately, almost all the other spectra were heavily contaminated by strong and broad [OIII]$\lambda\lambda 4959, 5007$ emission lines due to the presence of an AGN which prevented us to successfully measure the stellar kinematics. We then looked for archival spectra obtained with the G750M grating, excluding also in this case the observations of Batcheldor et al. (2013) who already provided stellar kinematics measurements for 36 galaxies in the wavelength range centered on the CaII absorption triplet at about 8500 Å. This initial pruning left us with the same sample of 177 galaxies compiled by Beifiori et al. (2009) for which the G750M grating was centered on the Hα line, to which we added 9 more galaxies observed with STIS in the same wavelength range after 2009. Among these 186 objects, we excluded those with STIS spectra displaying strong AGN emission and adopted a threshold for the signal-to-noise ratio in the stellar continuum at $S/N = 15$ per resolution element to perform reliable σ_* measurements.

This selection led to a final sample composed of 28 nearby galaxies ($D < 70$ Mpc), covering a wide range of morphological types (from E to Scd) and nuclear activity (Seyfert 2, LINERs, HII nuclei), which are listed in Table 4.1. Almost all them were observed with the 0.2 arcsec-

Table 4.1: Properties of the sample galaxies.

Galaxy	Mor. T.	Sp. Cl.	D [Mpc]	$\sigma_{*,\mathrm{fix}}$ [km s^{-1}]	$\sigma_{*,\mathrm{free}}$ [km s^{-1}]
(1)	(2)	(3)	(4)	(5)	(6)
IC0342	SABcd(rs)	H	4.3	-	$53.9^{+7.8}_{-3.8}$
NGC 2685	(R)SB0$^+$pec	S2/T2:	14.3	$62.7^{+8.8}_{-7.8}$	$51.0^{+9.7}_{-8.3}$
NGC 3245	SA0^0(r):?	T2:	23.2	-	$260.4^{+29.2}_{-23.5}$
NGC 3368	SABab(rs)	L2	17.8	$93.4^{+6.4}_{-6.1}$	$103.9^{+7.9}_{-4.7}$
NGC 3379	E1	L2/T2::	18.0	-	$264.7^{+29.6}_{-42.5}$
NGC 3489	SAB0$^+$(rs)	T2/S2	14.6	$74.1^{+3.9}_{-4.0}$	$78.2^{+2.4}_{-3.5}$
NGC 3627	SABb(s)	T2/S2	15.4	$114.3^{+18.5}_{-13.6}$	-
NGC 3675	SAb(s)	T2	14.4	$110.7^{+13.7}_{-11.1}$	$115.5^{+8.1}_{-17.2}$
NGC 3992	SBbc(rs)	T2:	17.5	$145.9^{+13.1}_{-13.3}$	$146.1^{+14.3}_{-11.9}$
NGC 4030	SAbc(s)	H*	26.1	$82.3^{+27.7}_{-26.8}$	$87.4^{+18.1}_{-16.6}$
NGC 4245	SB0/a(r):	H	16.7	$83.8^{+7.2}_{-7.0}$	$75.6^{+5.3}_{-4.6}$
NGC 4314	SBa(rs)	L2	17.8	$78.2^{+9.3}_{-7.3}$	$69.8^{+9.8}_{-6.5}$
NGC 4321	SABbc(s)	T2	27.1	$56.9^{+12.3}_{-12.2}$	$61.3^{+11.5}_{-12.9}$
NGC 4414	SAc(rs)?	T2:	14.2	$82.4^{+3.9}_{-3.3}$	$85.2^{+3.7}_{-7.8}$
NGC 4429	SA0$^+$(r)	T2	20.5	$213.2^{+22.3}_{-18.3}$	$201.7^{+22.6}_{-21.2}$
NGC 4435	SB0^0(s)	T2/H:	16.0	$87.3^{+10.2}_{-8.8}$	$95.0^{+10.9}_{-9.4}$
NGC 4459	SA0$^+$(r)	T2:	21.7	$214.6^{+11.2}_{-12.0}$	$200.2^{+12.5}_{-10.2}$
NGC 4477	SB0(s):?	S2	23.8	$154.4^{+15.2}_{-11.5}$	$158.4^{+11.2}_{-18.2}$
NGC 4501	SAb(rs)	S2	37.2	$102.4^{+12.3}_{-10.5}$	$91.5^{+13.2}_{-14.8}$
NGC 4548	SBb(rs)	L2	11.5	$79.8^{+11.5}_{-8.9}$	$81.0^{+10.2}_{-11.5}$
NGC 4596	SB0$^+$(r)	L2::	31.7	$219.1^{+20.0}_{-15.5}$	$210.3^{+19.4}_{-14.8}$
NGC 4698	SAab(s)	S2	19.1	$114.9^{+9.9}_{-9.8}$	$109.7^{+10.3}_{-9.8}$
NGC 4736	(R)SAab(r)	L2	7.6	-	$109.9^{+4.8}_{-7.0}$
NGC 4800	SAb(rs)	H	15.5	$89.5^{+7.2}_{-7.6}$	$86.6^{+10.5}_{-7.2}$
NGC 4826	(R)SAab(rs)	T2	10.0	$82.0^{+6.5}_{-5.9}$	$82.7^{+6.1}_{-3.7}$
NGC 5055	SAbc(rs)	T2	9.8	$104.3^{+4.9}_{-5.1}$	$111.1^{+2.0}_{-1.0}$
NGC 7252	(R)SA0^0:	H*	64.1	$74.4^{+13.0}_{-11.4}$	$77.5^{+14.0}_{-11.5}$
NGC 7331	SAb(s)	T2	7.0	$118.9^{+6.7}_{-6.3}$	$115.8^{+10.5}_{-6.3}$

Notes. Col.(1): galaxy name. Col.(2): morphological type from de Vaucouleurs et al. (1991, RC3). Col.(3): nuclear spectral class (Ho et al., 1997), where S = Seyfert, L = LINER, H = HII nucleus, T = transition object (LINER/HII), and 2 = type 2. Classifications evaluated as uncertain or highly uncertain are marked with a single or double colon, respectively. Classifications marked with * are from NASA/IPAC Extragalactic Database (NED). Col.(4): distance from NED. The distances are obtained as $D = V_{3\mathrm{K}}/H_0$, where $V_{3\mathrm{K}}$ is the weighted mean recessional velocity corrected to the reference frame of the microwave background radiation and $H_0 = 70$ km s^{-1} Mpc^{-1}. For IC 0342 we assume the distance reported in Beifiori et al. (2009) and rescaled for $H_0 = 70$ km s^{-1} Mpc^{-1} since $V_{3\mathrm{K}}$ is not provided by NED. Col.(5): nuclear σ_* obtained using the G430L optimal template when fitting the G750M spectra. Col.(6): nuclear σ_* obtained without using the G430L optimal template when fitting the G750M spectra.

Table 4.2: Properties of the G430L STIS spectra.

Galaxy	Prop. Id.	PA	Exp. T.	SP. Range	Bin.	Apert.	
		[°]	[h]	[Å]		[arcsec]	[pc]
(1)	(2)	(3)	(4)	(5)	(6)	(7)	(8)
IC0342	-	-	-	-	-	-	-
NGC 2685	8607	54.4	0.72	3000 – 5700	1×2	0.2×0.30	14×21
NGC 3245	-	-	-	-	-	-	-
NGC 3368	7361	69.5	0.44	3000 – 5700	1×1	0.2×0.25	17×22
NGC 3379	-	-	-	-	-	-	-
NGC 3489	7361	59.1	0.46	3000 – 5700	1×1	0.2×0.25	14×18
NGC 3627	8607	80.1	0.65	3000 – 5700	1×2	0.2×0.30	15×22
NGC 3675	8607	25.9	0.69	3000 – 5700	1×2	0.2×0.30	14×21
NGC 3992	7361	155.3	0.50	3000 – 5700	1×1	0.2×0.25	17×21
NGC 4030	9783	90.7	0.61	3000 – 5700	1×1	0.2×0.25	25×32
NGC 4245	7361	85.7	0.46	3000 – 5700	1×1	0.2×0.25	16×20
NGC 4314	7361	105.3	0.46	3000 – 5700	1×1	0.2×0.25	17×22
NGC 4321	7361	92.9	0.46	3000 – 5700	1×1	0.2×0.25	26×33
NGC 4414	8607	125.1	0.67	3000 – 5700	1×2	0.2×0.30	14×21
NGC 4429	8607	81.1	0.65	3000 – 5700	1×2	0.2×0.30	20×30
NGC 4435	7361	89.6	0.46	3000 – 5700	1×1	0.2×0.25	20×25
NGC 4459	7361	92.9	0.46	3000 – 5700	1×1	0.2×0.25	21×26
NGC 4477	7361	92.8	0.46	3000 – 5700	1×1	0.2×0.25	23×29
NGC 4501	7361	91.9	0.46	3000 – 5700	1×1	0.2×0.25	36×45
NGC 4548	7361	73.2	0.46	3000 – 5700	1×1	0.2×0.25	11×14
NGC 4596	7361	70.3	0.46	3000 – 5700	1×1	0.2×0.25	31×38
NGC 4698	7361	79.0	0.46	3000 – 5700	1×1	0.2×0.25	19×23
NGC 4736	-	-	-	-	-	-	-
NGC 4800	7361	177.5	0.48	3000 – 5700	1×1	0.2×0.25	15×19
NGC 4826	8607	88.1	0.65	3000 – 5700	1×2	0.2×0.30	10×15
NGC 5055	7361	164.5	0.47	3000 – 5700	1×1	0.2×0.25	9×12
NGC 7252	7435	38.1	4.25	3000 – 5700	1×2	0.1×0.10	31×31
NGC 7331	8607	178.9	0.67	3000 – 5700	1×2	0.2×0.30	7×10

Notes. Col.(1): galaxy name. Col(2): HST proposal number for the G430L spectra. Col.(3): position angle of the slit for the G430L spectra. Col.(4): total exposure time for the G430L spectra. Col.(5): spectral range for the G430L spectra. Col.(6): pixel binning for the G430L spectra. Col.(7): size of the nuclear aperture within which the fit was performed for the G430L spectra. Col.(8): physical size of the nuclear aperture within which the fit was performed for the G430L spectra.

Table 4.3: Properties of the G750M STIS spectra.

Galaxy	Prop. Id.	PA	Exp. T.	SP. Range	Bin.	Apert.	
		[°]	[h]	[Å]		[arcsec]	[pc]
(1)	(2)	(3)	(4)	(5)	(6)		
IC0342	8591	13.9	0.80	6300 – 6865	1×1	0.1×0.15	2×3
NGC 2685	8607	54.4	0.86	6300 – 6865	1×2	0.2×0.30	14×21
NGC 3245	7403	2.4	0.75	6300 – 6865	1×1	0.2×0.25	22×28
NGC 3368	7361	69.5	0.75	6300 – 6865	1×1	0.2×0.25	17×22
NGC 3379	8589	75.3	1.78	6300 – 6865	1×1	0.2×0.25	17×22
NGC 3489	7361	59.1	0.71	6300 – 6865	1×1	0.2×0.25	14×18
NGC 3627	8607	80.1	0.79	6300 – 6865	1×2	0.2×0.30	15×22
NGC 3675	8607	25.9	0.83	6300 – 6865	1×2	0.2×0.30	14×21
NGC 3992	7361	155.3	0.82	6300 – 6865	1×1	0.2×0.25	17×21
NGC 4030	8228	42.1	0.24	6490 – 7050	2×2	0.2×0.30	25×38
NGC 4245	7361	85.7	0.75	6300 – 6865	1×1	0.2×0.25	16×20
NGC 4314	7361	105.3	0.75	6300 – 6865	1×1	0.2×0.25	17×22
NGC 4321	7361	92.9	0.74	6300 – 6865	1×1	0.2×0.25	26×33
NGC 4414	8607	125.1	0.81	6300 – 6865	1×2	0.2×0.30	14×21
NGC 4429	8607	81.1	0.79	6300 – 6865	1×2	0.2×0.30	20×30
NGC 4435	7361	89.6	0.74	6300 – 6865	1×1	0.2×0.25	20×25
NGC 4459	7361	92.9	0.74	6300 – 6865	1×1	0.2×0.25	21×26
NGC 4477	7361	92.8	0.73	6300 – 6865	1×1	0.2×0.25	23×29
NGC 4501	7361	91.9	0.74	6300 – 6865	1×1	0.2×0.25	36×45
NGC 4548	7361	73.2	0.74	6300 – 6865	1×1	0.2×0.25	11×14
NGC 4596	7361	70.3	0.75	6300 – 6865	1×1	0.2×0.25	31×38
NGC 4698	7361	79.0	0.74	6300 – 6865	1×1	0.2×0.25	19×23
NGC 4736	8591	50.1	1.09	6300 – 6865	1×1	0.1×0.15	4×6
NGC 4800	7361	177.5	0.80	6300 – 6865	1×1	0.2×0.25	15×19
NGC 4826	8607	88.1	0.80	6300 – 6865	1×2	0.2×0.30	10×15
NGC 5055	7361	164.5	0.79	6300 – 6865	1×1	0.2×0.25	9×12
NGC 7252	8669	126.1	0.19	6490 – 7050	2×2	0.2×0.30	62×93
NGC 7331	8607	178.9	0.81	6300 – 6865	1×2	0.2×0.30	7×10

Notes. Col.(1): galaxy name. Col.(2): HST proposal number for the G750M spectra. Col.(3): position angle of the slit for the G750M spectra. Col.(4): total exposure time for the G750M spectra. Col.(5): spectral range for the G750M spectra. Col.(6): pixel binning for the G750M spectra. Col.(7): size of the nuclear aperture within which the fit was performed for the G750M spectra. Col.(8): physical size of the nuclear aperture within which the fit was performed for the G750M spectra.

wide slit and this yielded a nearly the same spectral resolution of the template spectra we used to measure the stellar kinematics (see Sect. 4.3.2 for details). We considered only two galaxies (IC 0342 and NGC 4736) observed with the 0.1 arcsec-wide slit, owing to the superb S/N of the data. All other archival G750M spectra obtained with the 0.1 arcsec-wide slit have S/N that is too low.

Finally, to help with our stellar kinematics extraction based on the G750M spectra we also looked in the MAST for similarly centered low-resolution G430L spectra for all our sample galaxies, since these spectra can provide useful constraints on the nuclear stellar population composition (see, e.g. Sarzi et al., 2005 and Sect. 4.3.2). G430L spectra were found for 24 objects.

4.3 Nuclear stellar velocity dispersion

4.3.1 Long-slit spectroscopy

We retrieved from the MAST the STIS spectra of the sample galaxies obtained with the G430L and G750M gratings through either the 0.1 arcsec $\times$ 52 arcsec or the 0.2 arcsec $\times$ 52 arcsec slit positioned on the galaxy nucleus. The detector was a SITe CCD with 1024×1024 pixel of 21×21 μm^2. The G430L spectra covered the wavelength range between about 3000 – 5700 Å, whereas the G750M spectra were characterized by a wavelength range of either 6490 – 7050 Å or 6300 – 6865 Å, depending on the tilt angle of the grating. For the G750M spectra, the reciprocal dispersion was 0.554 and 1.108 Å pixel^{-1} for the 1-pixel and 2-pixel binning read-out mode along the dispersion direction, respectively. For an extended source, this setup yielded for the 0.1 arcsec-wide slit an instrumental FWHM of 5.5 and 1.1 Å with the G430L and G750M grating, respectively and it yielded for the 0.2 arcsec-wide slit 10.9 and 2.2 Å with the G430L and G750M grating, respectively (Riley et al., 2017). The spatial scale was 0.0507 and 0.101 arcsec pixel^{-1} for the 1-pixel and 2-pixel binning read-out mode along the spatial direction, respectively. The proposal number, slit width and position angle, pixel binning, wavelength range, and total exposure times of the STIS spectra of the sample galaxies are reported in Table 4.2 and 4.3.

We reduced the spectra following Beifiori et al. (2009) and Pagotto et al. (2017). We used both IRAF[1] tasks and STIS reduction pipeline (Dressel et al., 2007), which we combined in a customized IRAF procedure running the `lacos_spec` task (van Dokkum, 2001) to remove the cosmic rays events or hot pixels. The reduction steps included the subtraction of the overscan, bias and dark contributions, correction for internal flat-field, trimming of the spectra, removal of bad pixels and cosmic rays, wavelength and flux calibration, correction for geometrical distortion, alignment and combination of the spectra obtained for the same galaxy with the same setup. Finally, we averaged the innermost spectral rows of each resulting spectrum for the purpose of analysing a nearly square aperture as prescribed by Beifiori et al. (2009).

[1]Image Reduction and Analysis Facility is distributed by the National Optical Astronomy Observatory (NOAO), which is operated by the AURA, Inc., under cooperative agreement with the National Science Foundation.

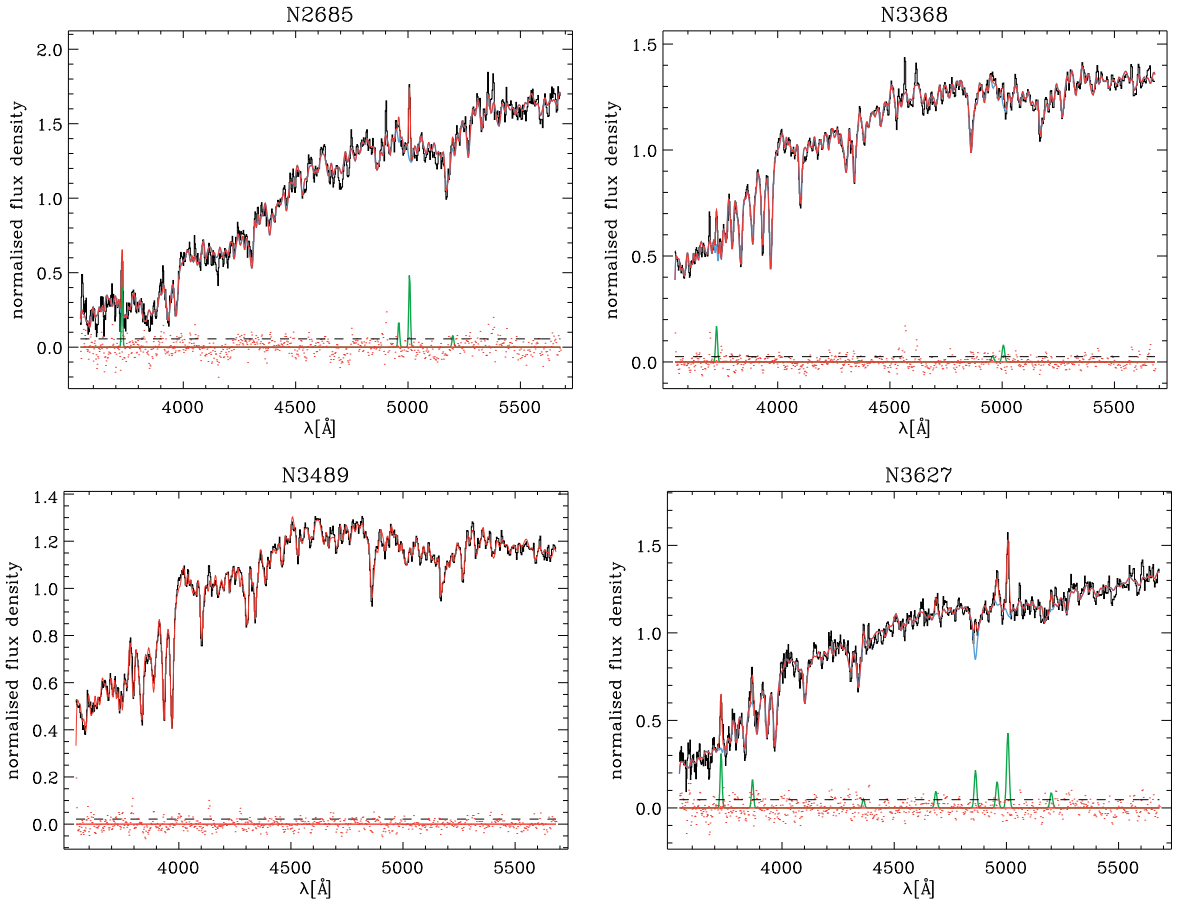

Figure 4.1: Rest-frame G430L spectra of the sample galaxies. The galaxy name is given in each panel and the relative fluxes have false zero points for viewing convenience. The best-fitting model (red line) is the sum of the spectra of the ionized-gas (green line) and stellar component (cyan line). The latter is obtained by convolving the synthetic templates with the best-fitting LOSVD and multiplying them by the best-fitting Legendre polynomials. The residuals (red dots) are obtained by subtracting the model from the spectrum. The dashed line corresponds to the rms of the residuals.

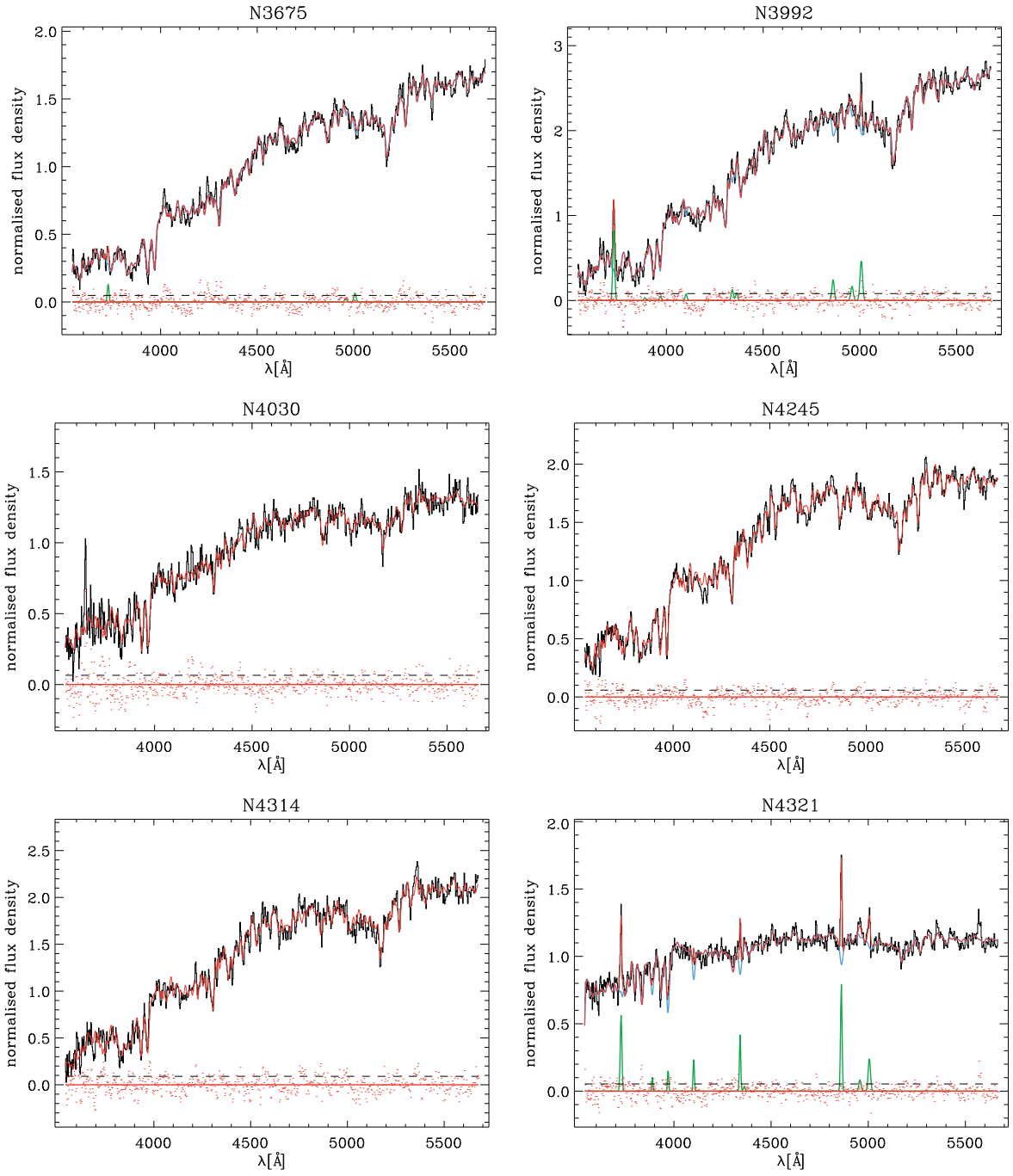

Figure 4.1: Continued.

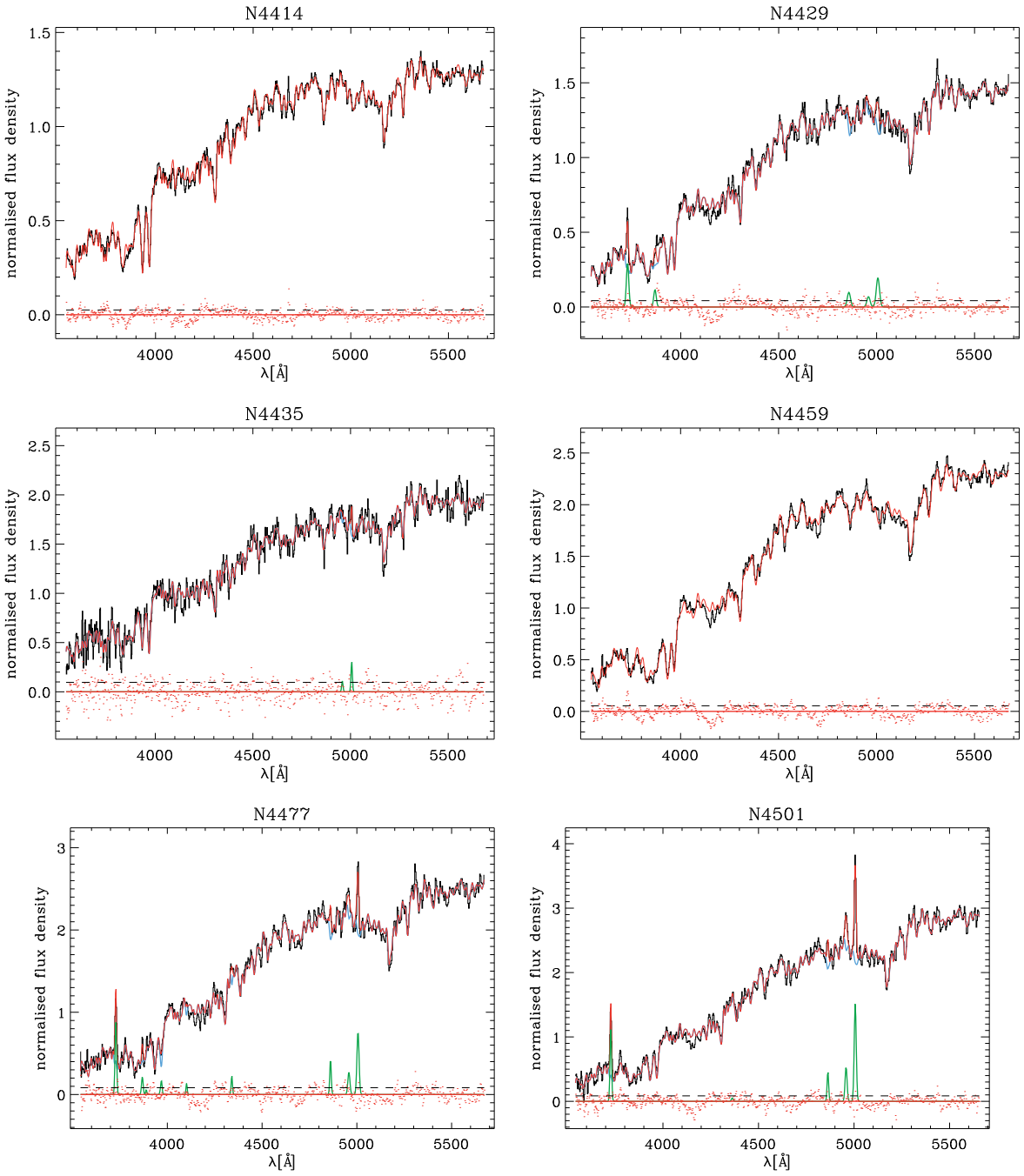

Figure 4.1: Continued.

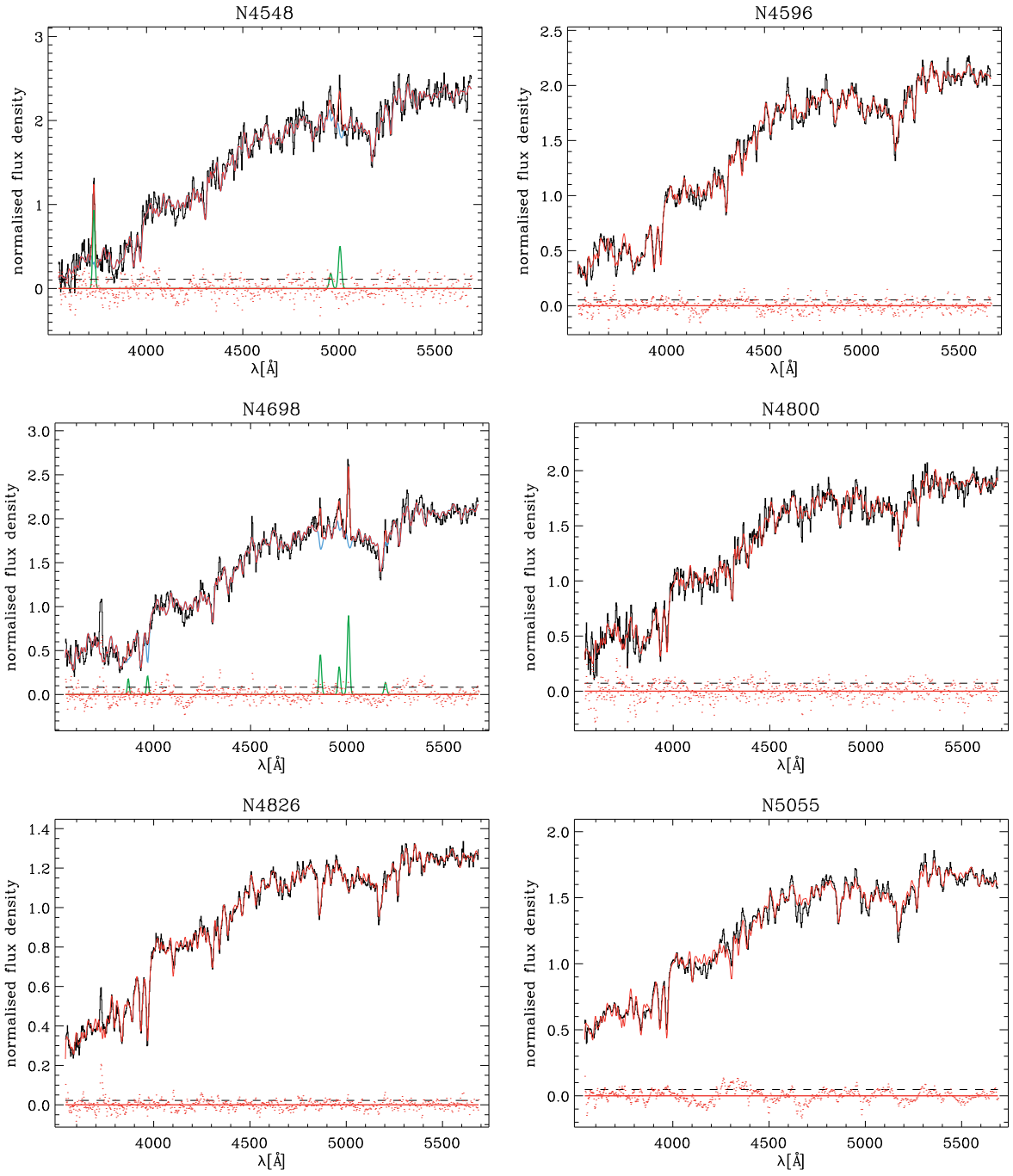

Figure 4.1: Continued.

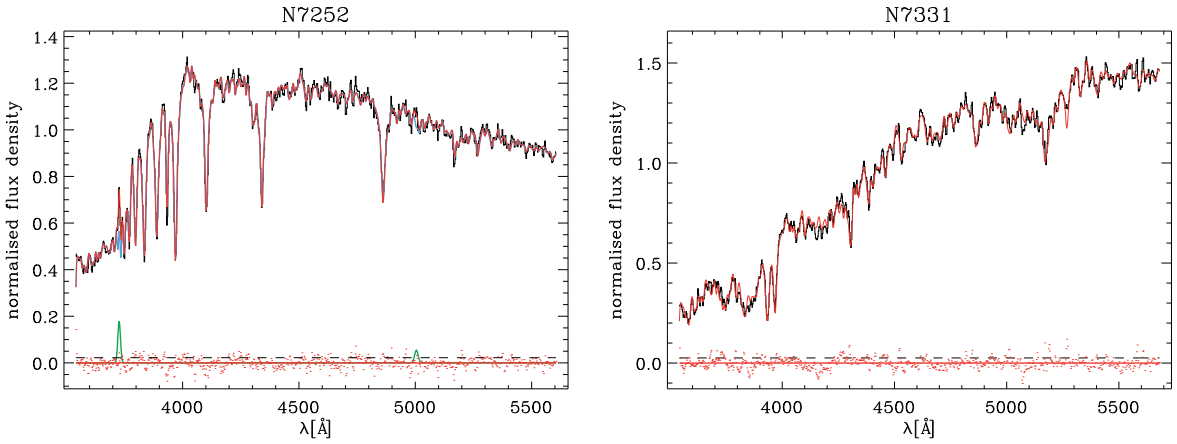

Figure 4.1: Continued.

4.3.2 Stellar kinematics

We measured the nuclear σ_* with the Penalized Pixel Fitting (pPXF, Cappellari & Emsellem, 2004) and the Gas and Absorption Line Fitting (GANDALF, Sarzi et al., 2006) IDL[2] algorithms. Generally speaking, pPXF performs a fit of the spectrum by masking the emission lines. GANDALF provides a complete fit of the whole spectrum by using the result of pPXF as input for the stellar kinematics and fitting the emission lines. To model the stellar continuum we used the library of synthetic spectral energy distributions (SEDs) for single-age, single-metallicity stellar populations provided by Vazdekis et al. (2010), which is based on the Medium Resolution Isaac Newton Telescope Library of Empirical Spectra (MILES, Sánchez-Blázquez et al., 2006) and covers the full optical spectral range of both our G430L and G750M STIS spectra at moderately high resolution ($FWHM = 2.5$ Å, Falcón-Barroso et al., 2011).

The fitting procedure consists of the following steps. We first rebinned each galaxy spectrum and MILES SED template along the dispersion direction to a common logarithmic scale. For each galaxy, we then run a preliminary fit to its STIS G750M spectrum using pPXF while masking the emission lines and assuming a Gaussian LOSVD in order to obtain a starting guess on both velocity and σ_*. We then run a series of GANDALF fits to the nuclear spectrum while optimising the values for the velocity and σ_* that GANDALF takes as input using a downhill simplex method (AMOEBA, Nelder & Mead, 1965). This optimisation yields a final GANDALF fit and best velocity and σ_* values, as well an initial estimate for the errors on these parameters. These error estimates are then refined by means of a grid of GANDALF models based on velocity and σ_* values around the previously found best-fitting results. When necessary we also included a broad-line emission component in our GANDALF fits.

It should be noted that the spectral resolution of the MILES SEDs is somewhat poorer than that of the G750M spectra. Alternatively, we could use the ELODIE stellar library at medium resolution ($\sigma_{\rm inst} = 13$ km s^{-1}, Prugniel & Soubiran, 2001). Indeed, the spectral resolution of the ELODIE stars is higher than those of G430L and G750M spectra and this

[2]Interactive Data Language is distributed by Harris Geospatial Solutions.

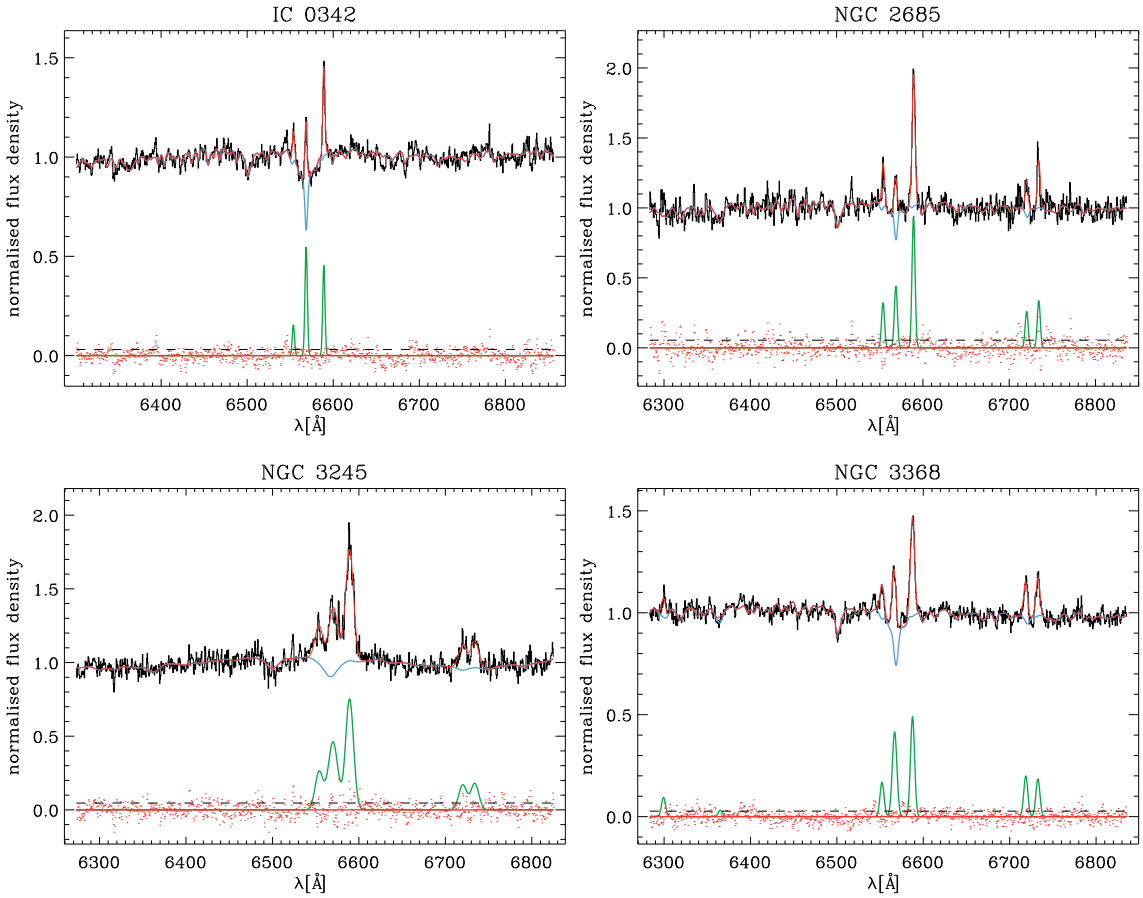

Figure 4.2: Rest-frame G750M spectra of the sample galaxies. The galaxy name is given in each panel and the relative fluxes have false zero points for viewing convenience. The best-fitting model (red line) is the sum of the spectra of the ionized-gas (green line) and stellar component (cyan line). The latter is obtained convolving the optimal template obtained from the fit of the G430L spectrum with the best-fitting LOSVD and multiplying them by the best-fitting Legendre polynomials. The residuals (red dots) are obtained by subtracting the model from the spectrum. The dashed line corresponds to the rms of the residuals.

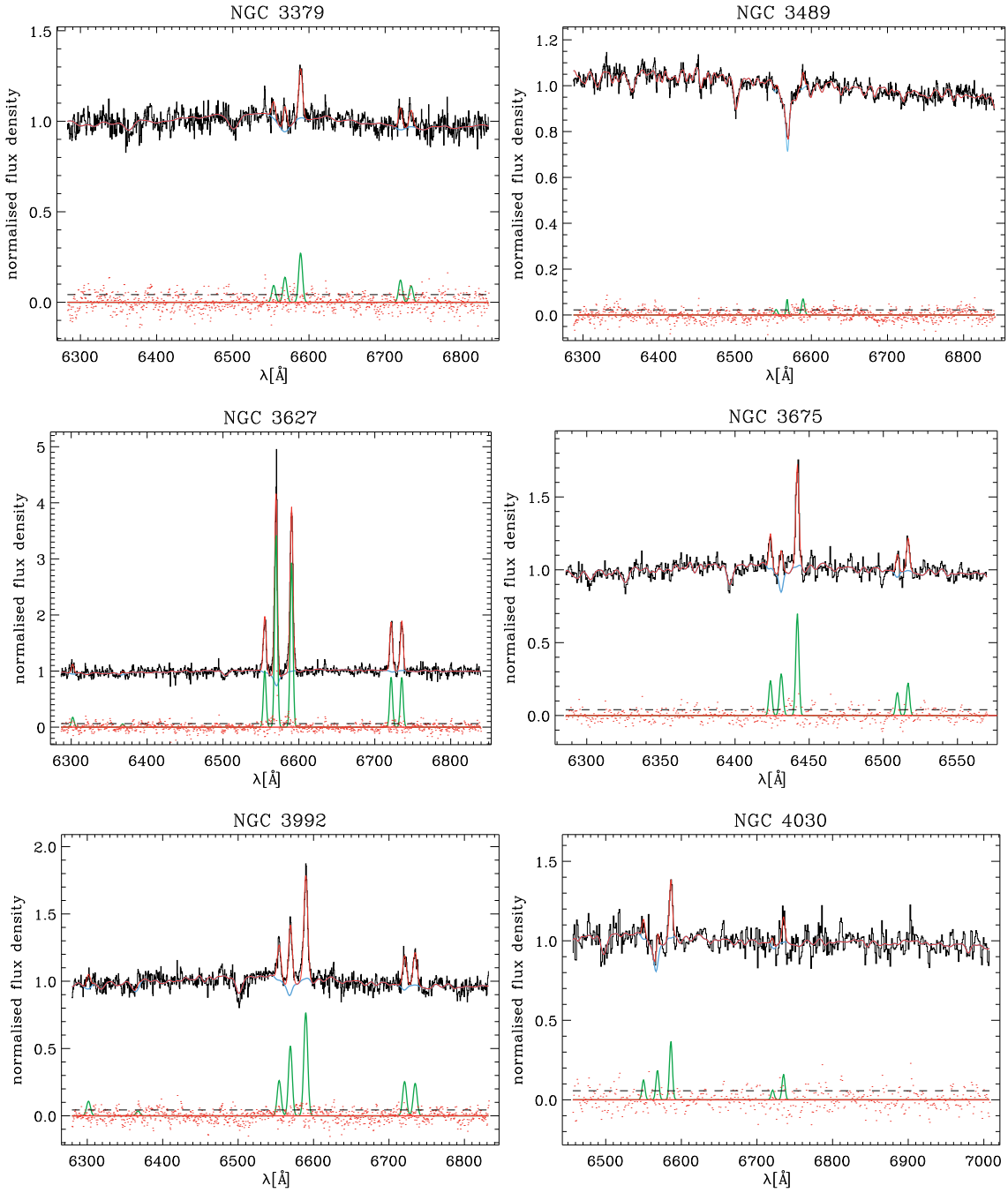

Figure 4.2: Continued.

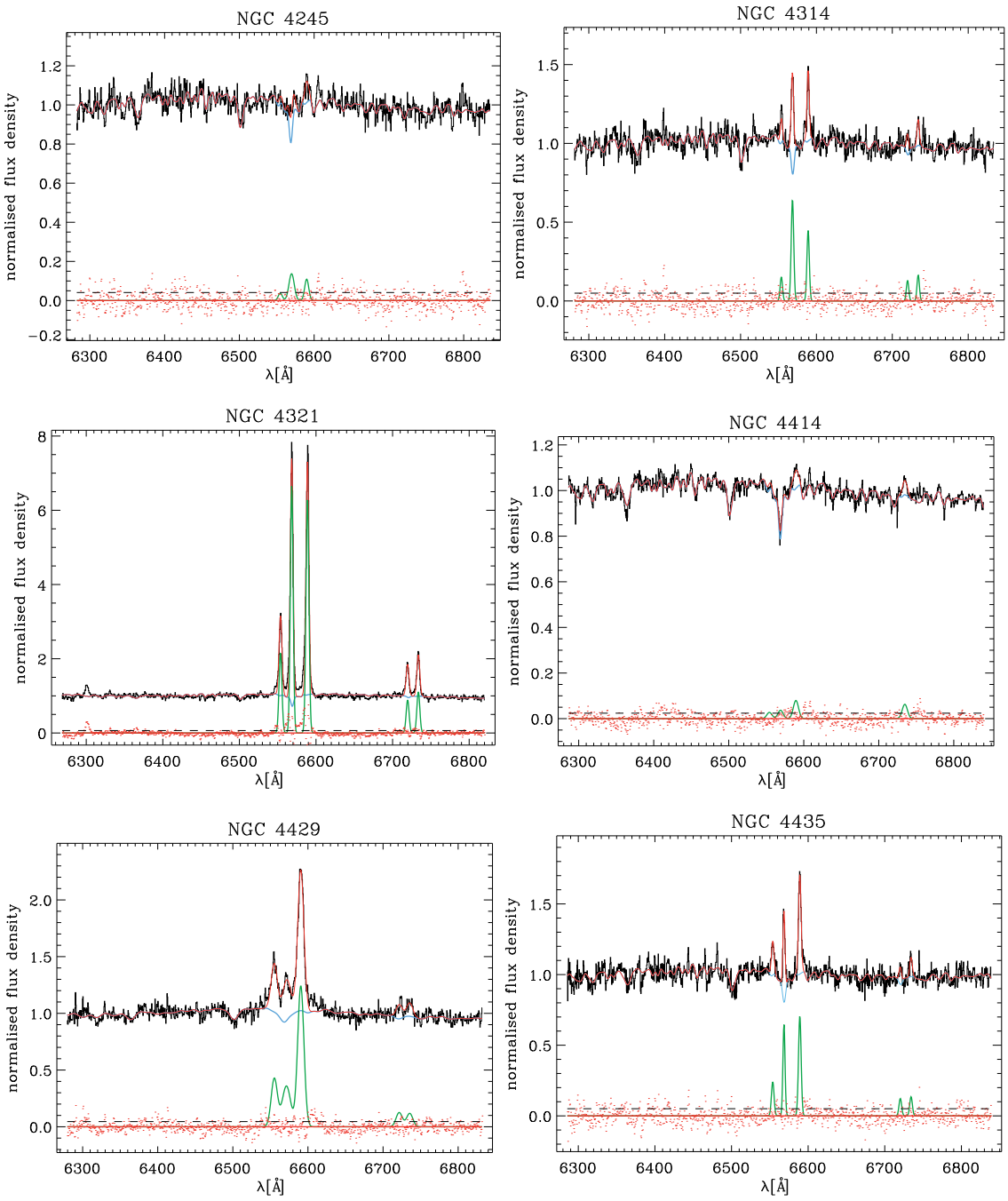

Figure 4.2: Continued.

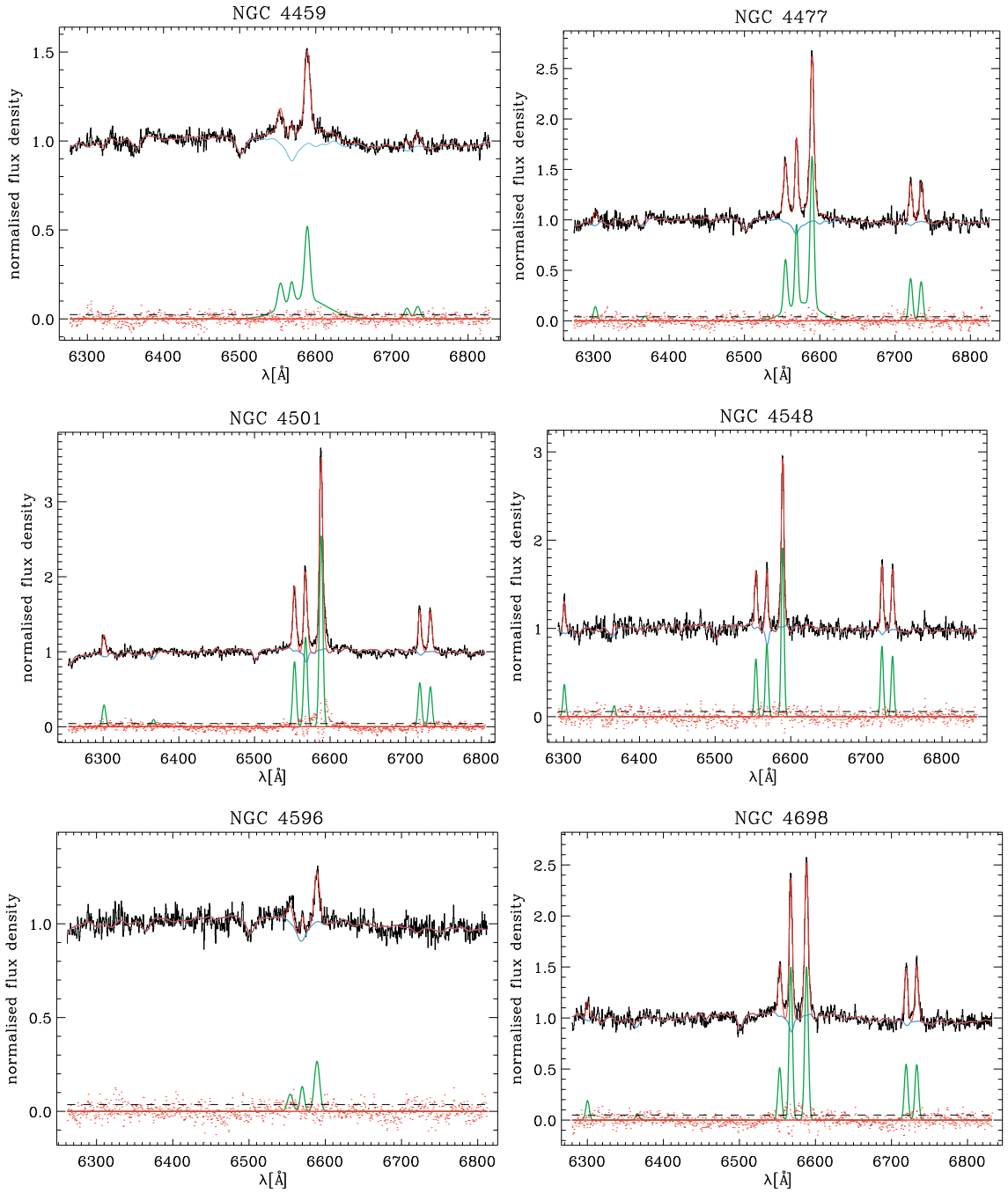

Figure 4.2: Continued.

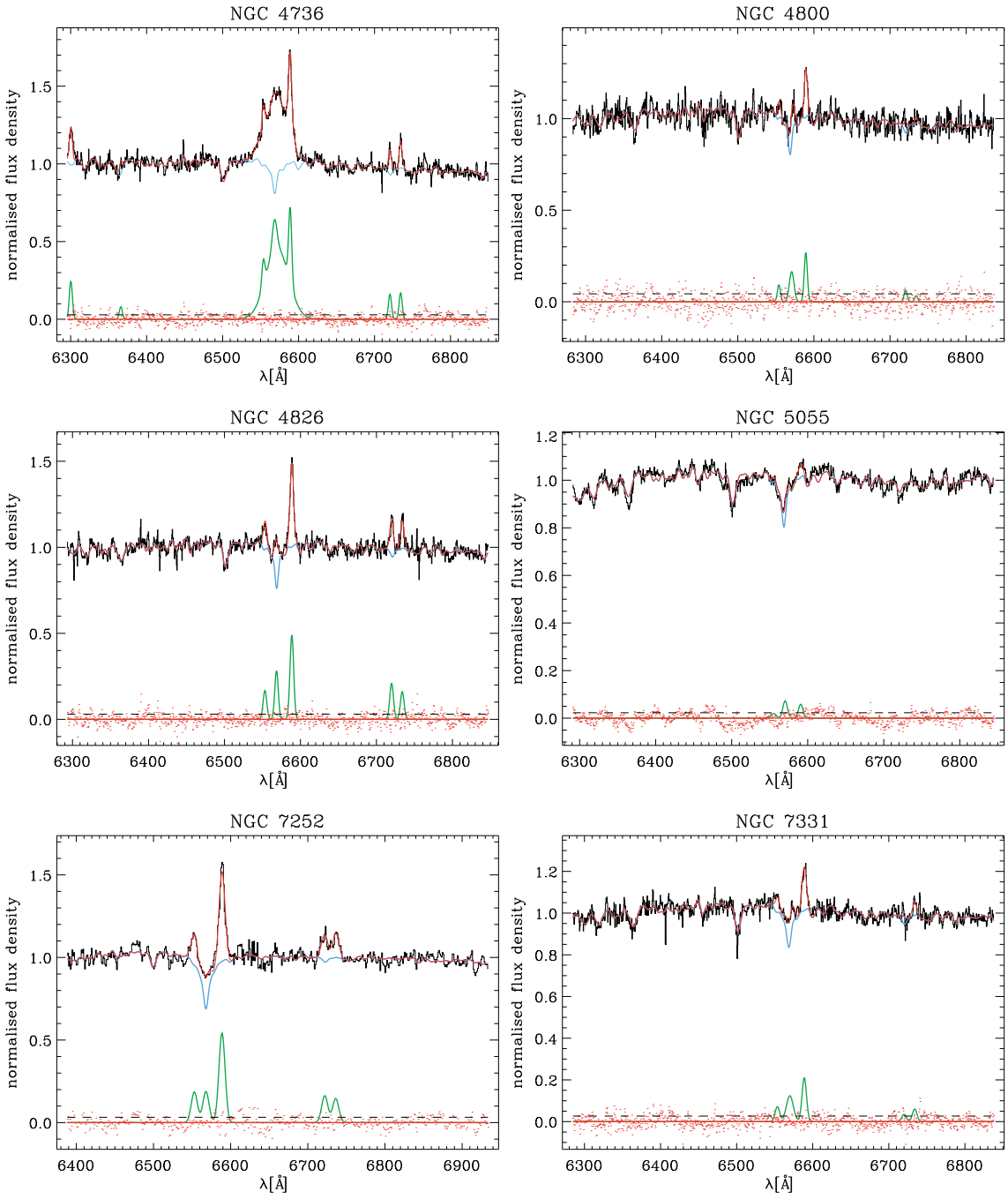

Figure 4.2: Continued.

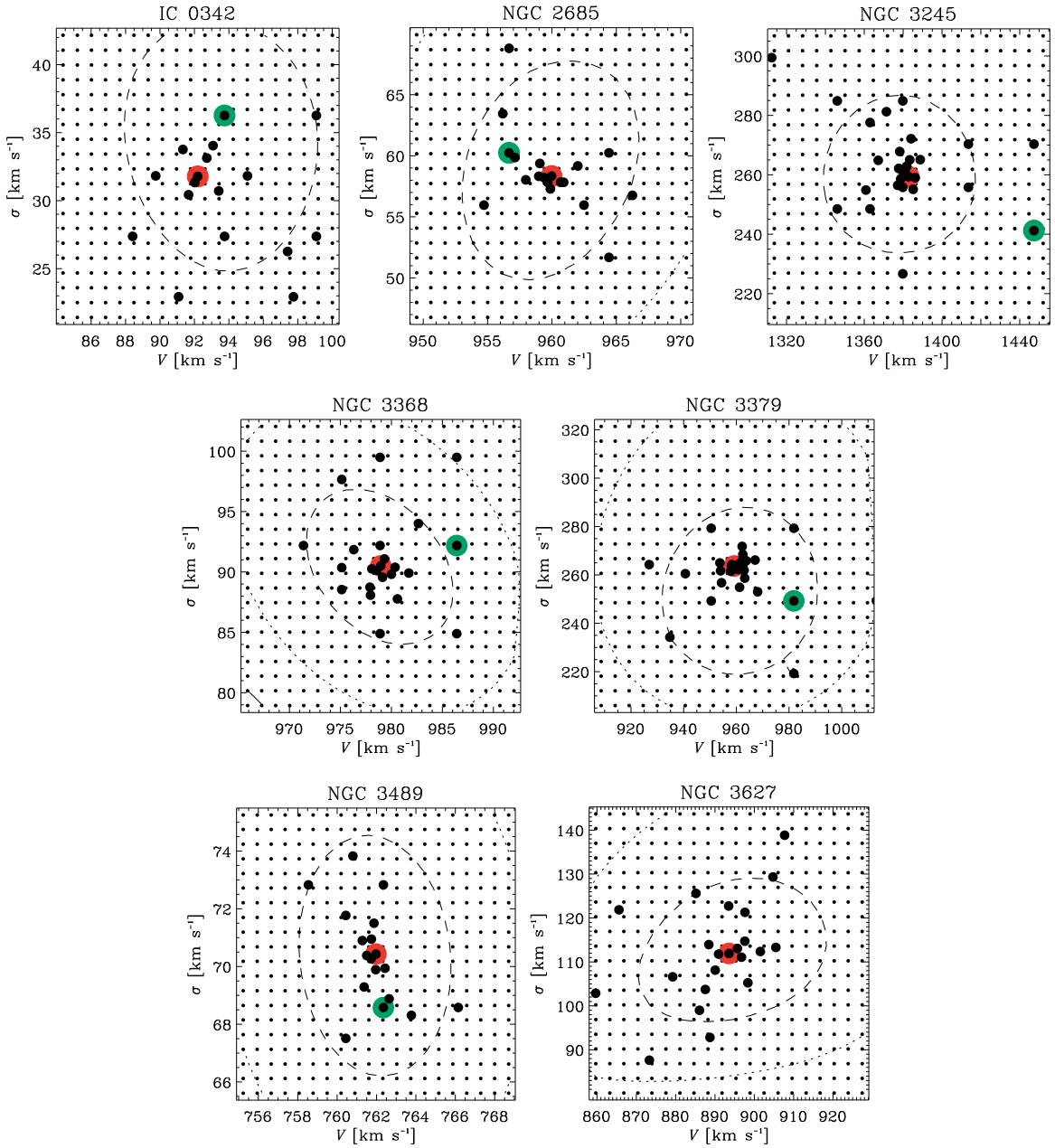

Figure 4.3: Grid of GANDALF models for different velocities and velocity dispersions of the stellar component (black small circles) of the sample galaxies. Velocity dispersions are not corrected for instrumental resolution. The final best-fitting GANDALF model is shown with a big red circle while the starting best-fitting pPXF model is shown with a big green circle. Big black circles correspond to AMOEBA iterations. Contours show the distribution of $\Delta\chi^2 = \chi^2 - \chi^2_{\rm min}$ with the dashed, dotted and solid lines indicating the 1σ, 2σ and 3σ confidence level for two degrees of freedom, respectively.

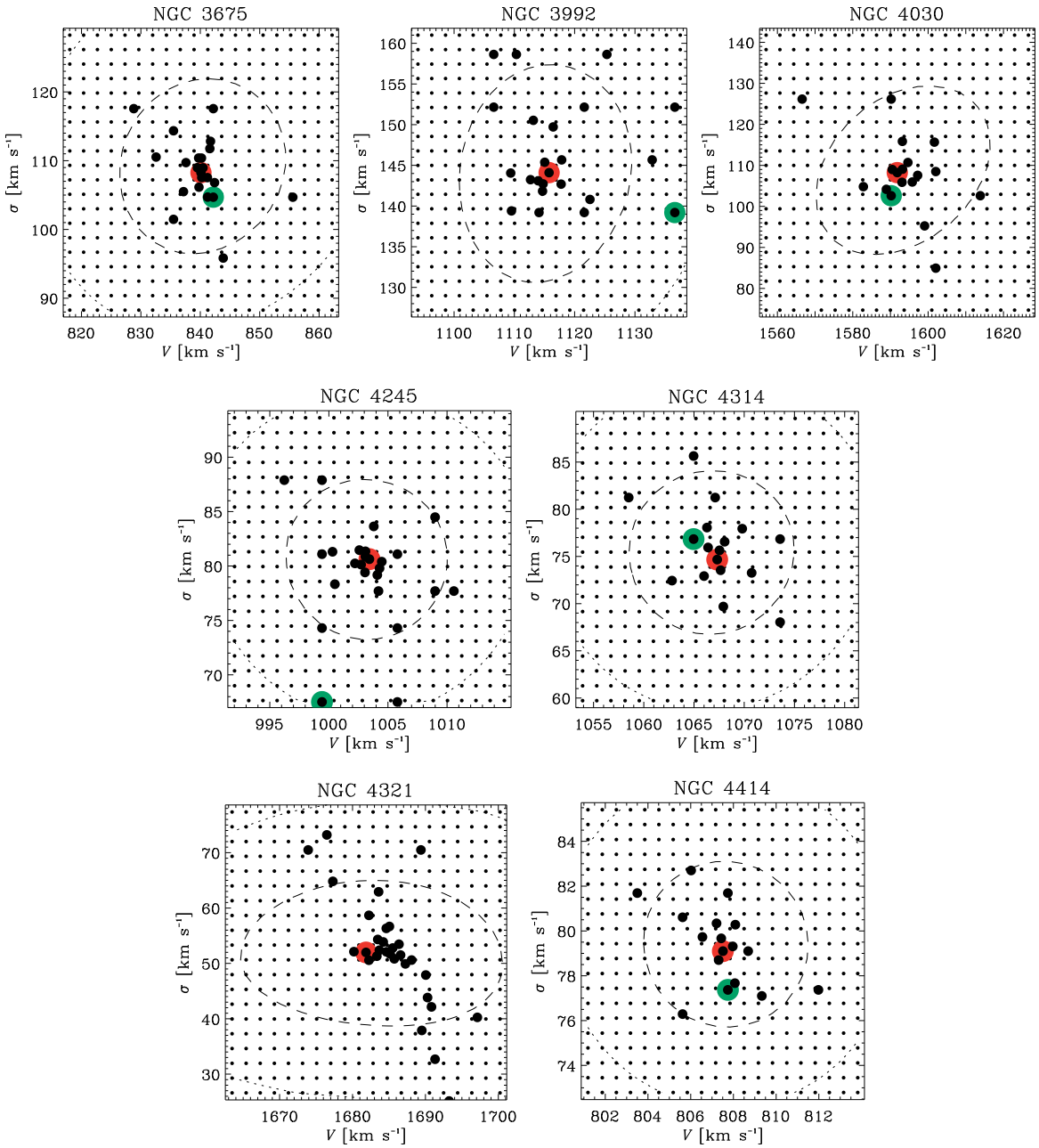

Figure 4.3: Continued.

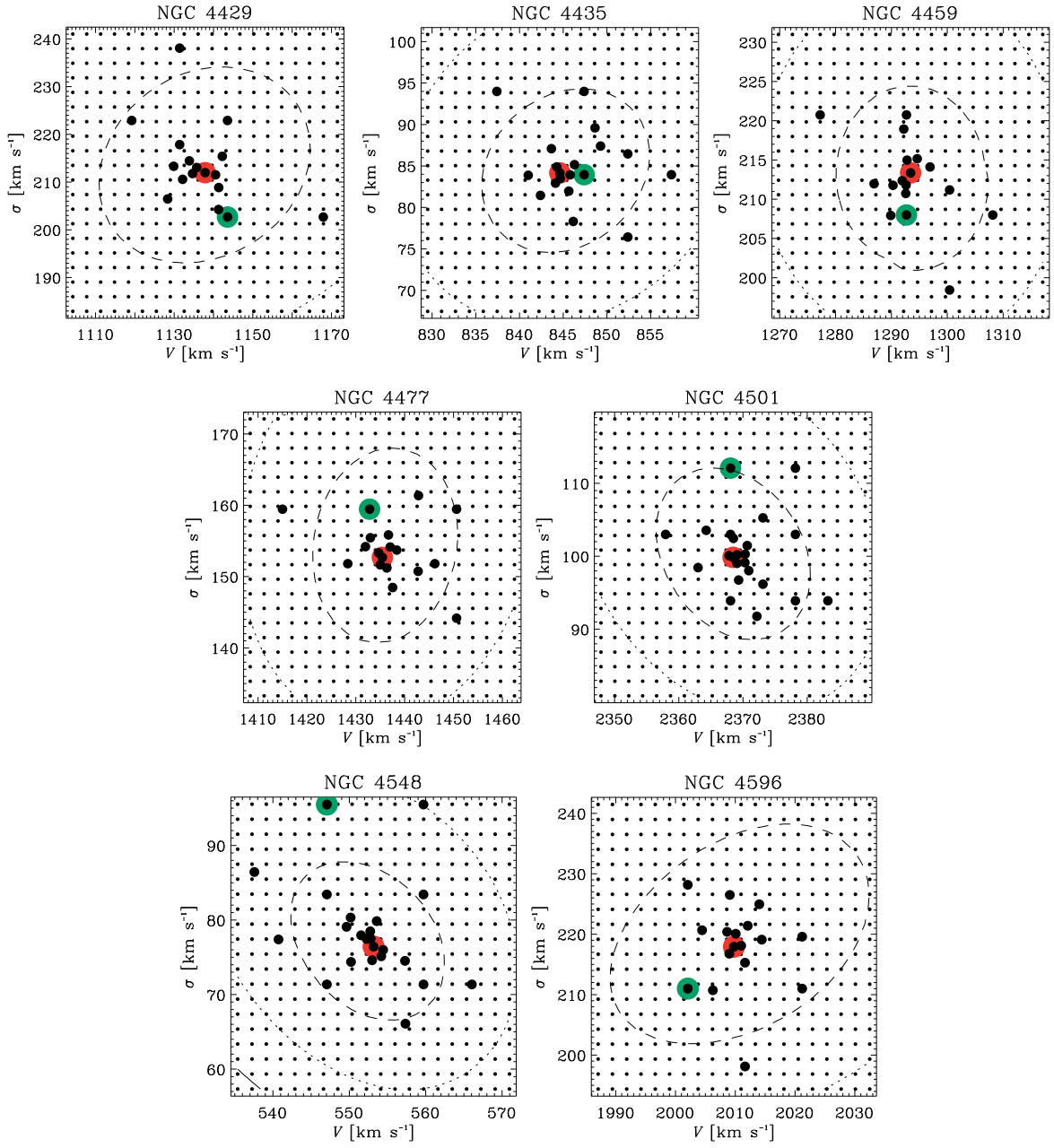

Figure 4.3: Continued.

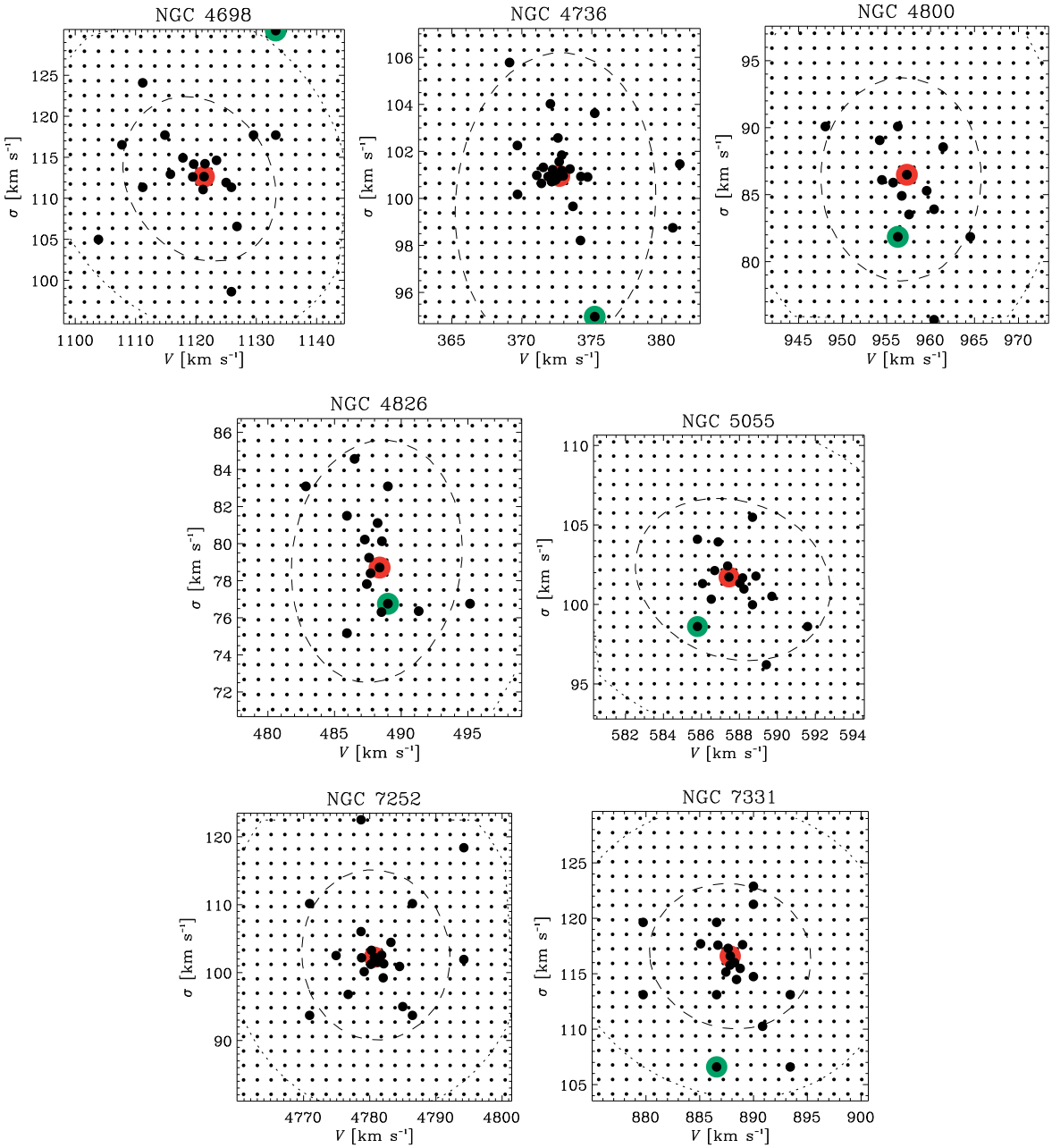

Figure 4.3: Continued.

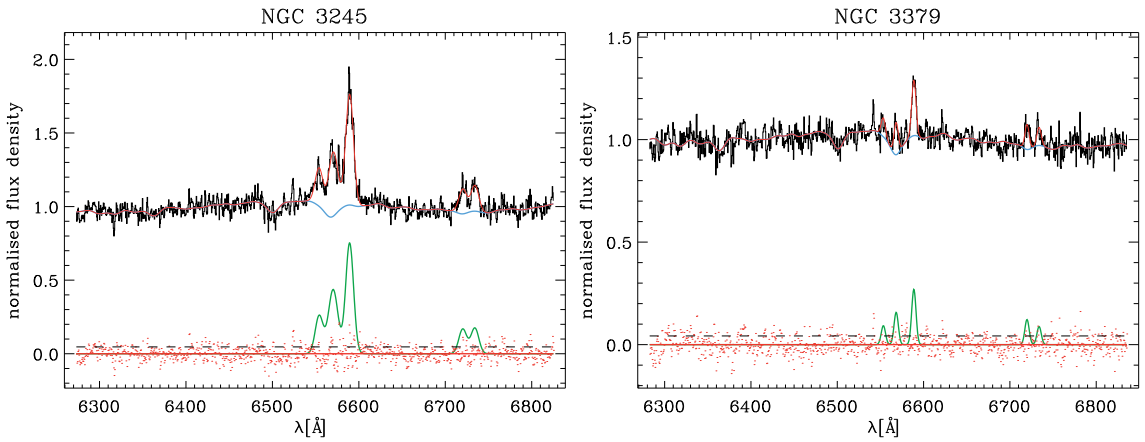

Figure 4.4: Rest-frame G750M spectra of NGC 3245 and NGC 3379. The galaxy name is given in each panel and the relative fluxes have false zero points for viewing convenience. The best-fitting model (red line) is the sum of the spectra of the ionized-gas (green line) and stellar component (cyan line). The latter is obtained convolving the synthetic templates with the best-fitting LOSVD and multiplying them by the best-fitting Legendre polynomials. The residuals (red dots) are obtained by subtracting the model from the spectrum. The dashed line corresponds to the rms of the residuals.

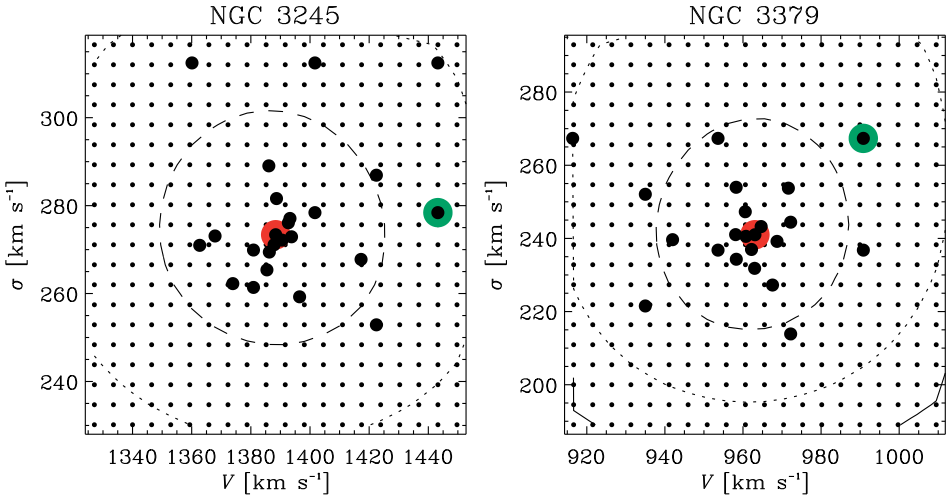

Figure 4.5: Grid of GANDALF models for different velocities and velocity dispersions of the stellar component (black small circles) of NGC 3245 and NGC 3379. Velocity dispersions are not corrected for instrumental resolution. The final best-fitting GANDALF model is shown with a big red circle while the starting best-fitting pPXF model is shown with a big green circle. Big black circles correspond to AMOEBA iterations. Contours show the distribution of $\Delta\chi^2 = \chi^2 - \chi^2_{\rm min}$ with the dashed and dotted lines indicating the 1σ and 2σ confidence level for two degrees of freedom, respectively.

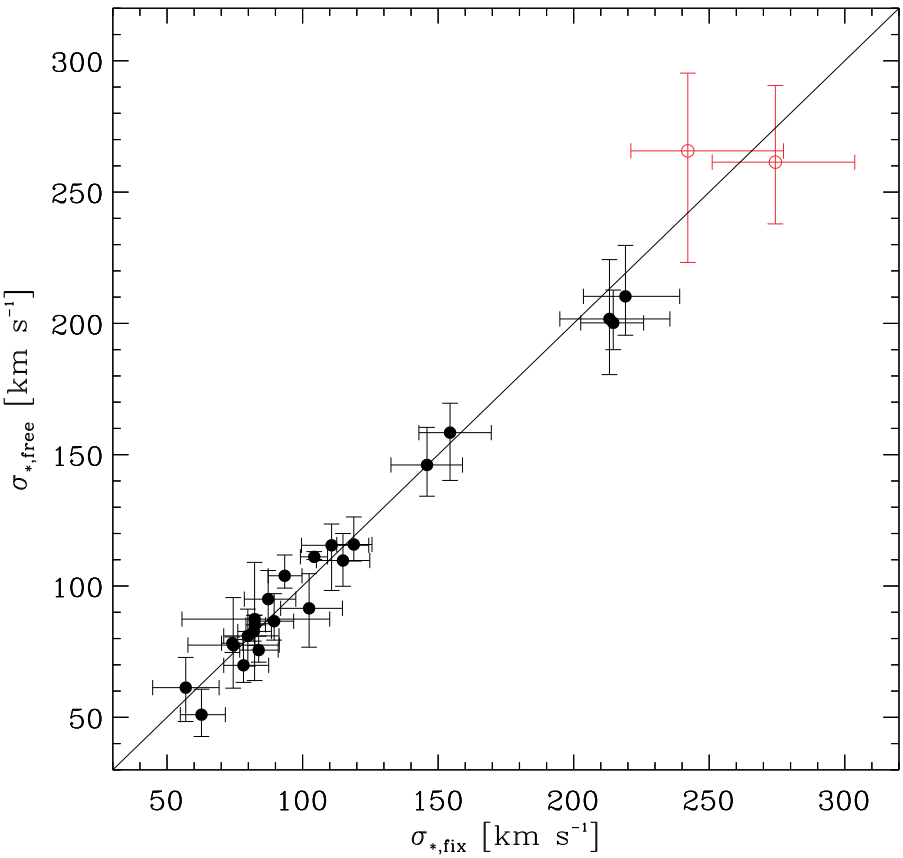

Figure 4.6: Comparison between the values of $\sigma_{*,\mathrm{fix}}$ and $\sigma_{*,\mathrm{free}}$ obtained from the G750M spectra of 23 sample galaxies (black filled circles) with and without adopting the optimal template from the G430L spectra, respectively. The $\sigma_{*,\mathrm{fix}}$ values of NGC 3245 and NGC 3379 (red open circles), for which no G430L spectrum was available, were obtained by averaging the optimal templates of NGC 4429, NGC 4459, and NGC 4596.

would allow us to degrade the resolution of the templates to match those of the galaxy spectra before performing the fit. Nevertheless, we decided to employ the MILES SEDs to obtain results robust against dependences of the fit solution from the initial guesses and template mismatching (see Sect. 4.3.3 for more details).

The MILES resolution, near the Hα line corresponds to an instrumental velocity dispersion σ_{inst} of about 49 km s^{-1} whereas for the G750M spectra $\sigma_{\mathrm{inst}} = 21$ and 43 km s^{-1} for the 0.1 arcsec and 0.2 arcsec-wide slit, respectively. For both pPXF and GANDALF analysis we decided against degrading the resolution of our G750M spectra, since this would artificially smooth our spectra and lead to less reliable error estimates. Instead, we corrected the measured σ_* to account for the mismatch between the instrumental resolution of our G750M data and the MILES templates, by summing such a difference in quadrature to our best-fitting σ_* values. Such a correction is quite significant for 0.1 arcsec-wide slit spectra (ranging from 16 to 8 km s^{-1} for original σ_* estimates of 50 and 100 km s^{-1}, respectively) whereas it remains

Table 4.4: MILES SEDs that constitute the optimal templates of NGC 4429, NGC 4459 and NGC 4596.

	Z	t [Gyr]	weight
NGC 4429			
	0.20	10.00	0.33953
	0.20	17.78	0.66025
	-1.68	00.10	0.00022
NGC 4459			
	0.20	10.00	0.62048
	0.20	17.78	0.37952
NGC 4596			
	0.20	00.28	0.00039
	0.20	00.71	0.00007
	0.20	10.00	0.99935
	-1.68	00.10	0.00018

Notes. For each galaxy we list the templates adopted to fit the G430L spectrum. For each template the metallicity (Z), the age (t) and the corresponding weight are reported.

quite small for the 0.2 arcsec-wide slit ones (ranging from 5 to less than 3 km s^{-1} in the same range).

For the 24 sample galaxies with a G430L spectrum, we further re-fit the G750M spectrum drawing from the results of a previous fit to the G430L spectra in order to better constrain the stellar-population content of the nuclear regions. More specifically, we performed a GANDALF fit to determine the weights of the best-fitting linear combination of MILES SEDs when modelling the G430L spectra and use these to construct an optimal stellar-population template that, in turn, can be used in our GANDALF fit to the G750M spectra. As in the case of the G430L the spectral resolution is significantly worse than that of the MILES SEDs (which is also the reason why the G430L cannot be used to measure σ_* in first place), we proceeded to degrade the resolution of the latter templates to match that of G430L spectra before the fit, as it is common practice in these cases. Fig. 4.1 shows the fit to the G430L spectra.

Figures 4.2 and 4.3 illustrate the quality of our GANDALF fit to the G750M spectra as well as the working of our error estimate for all the sample objects. In this respect, Fig. 4.6 shows the comparison between the values $\sigma_{*,\mathrm{fix}}$ of the nuclear velocity dispersion obtained from the G750M spectra adopting the G430L optimal templates and values $\sigma_{*,\mathrm{free}}$ measured from G750M spectra using the entire MILES SED library, for all but one of the 24 objects with both G430L and G750M spectra (for NGC 3627 only the fit adopting the optimal template was successful). In addition to these, in Fig. 4.6 we also add NGC 3245 and NGC 3379 for

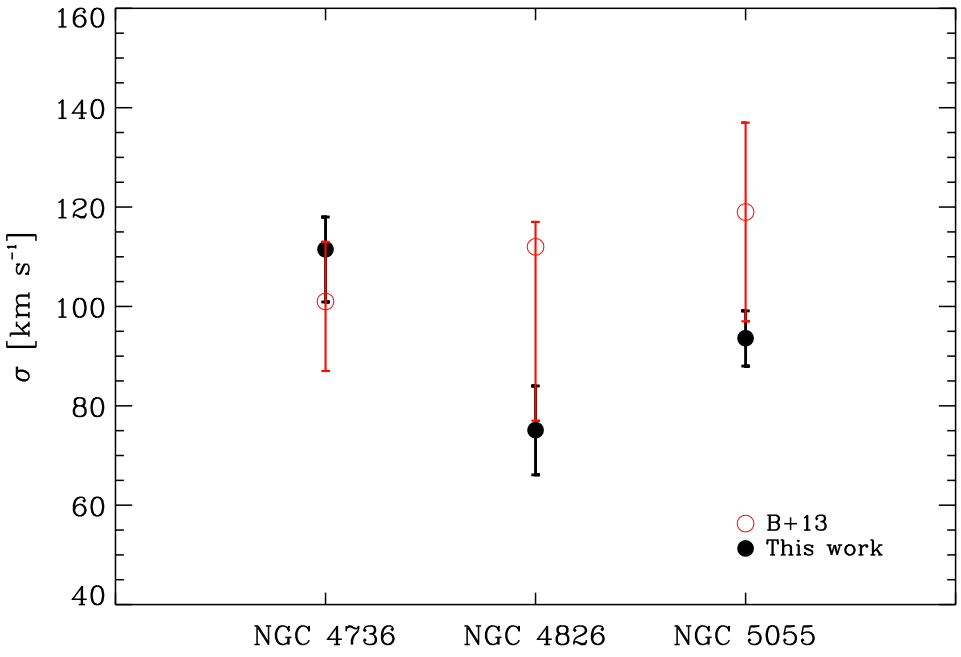

Figure 4.7: Comparison between our sub-arcsecond σ_* measurements of NGC 4736, NGC 4826, and NGC 5055 from G750M spectra in the Hα region (black filled circles) and those by Batcheldor et al. (2013) (red open circles) from G750M spectra centered on the CaII absorption triplet at about 8500 Å.

which we adopted as G430L optimal template the model built by averaging those from the fit to NGC 4429, NGC 4459, and NGC 4596 (see Fig. 4.1 for the corresponding G430L fits). This is appropriate since there are good indications that both NGC 3245 and NGC 3379 host central old stellar population (Kuntschner et al., 2010; McDermid et al., 2015) as indicated by the stellar-population mix returned in the case of the G430L fits to NGC 4429, NGC 4459, and NGC 4596 (see Table 4.4). Indeed, we obtained larger weights for the older and more metal-rich stellar-population templates (for $t \geq 10$ Gyr and $Z = 0.2$), and smaller ones for very young and/or metal poor templates. We found $\sigma_{*,\mathrm{fix}} = 274.4^{+29.3}_{-23.3}$ km s^{-1} for NGC 3245 and $\sigma_{*,\mathrm{fix}} = 242.1^{+35.3}_{-21.0}$ km s^{-1} for NGC 3379, which are consistent with the corresponding values of $\sigma_{*,\mathrm{free}}$ within their 1σ error bars (Table 4.1). The corresponding GANDALF fits to G750M spectra as well as the grid of GANDALF models for error determination for NGC 3245 and NGC 3379 are illustrated in Fig. 4.4 and Fig. 4.5, respectively. Fig. 4.6 shows that the values of $\sigma_{*,\mathrm{fix}}$ and $\sigma_{*,\mathrm{free}}$ are consistent within 1σ errors in almost all cases (see also Table 4.1), which gives us confidence in the $\sigma_{*,\mathrm{free}}$ obtained for those objects (IC 342, NGC 3245, NGC 3379, and NGC 4736) for which G430L spectra are not available.

Batcheldor et al. (2013) already measured the nuclear σ_* of NGC 4736, NGC 4826, and NGC 5055 from G750M spectra and 0.1 arcsec-wide slit in the wavelength range centered on the CaII absorption triplet at about 8500 Å. This allows us to make a comparison between σ_* obtained on sub-arcsecond apertures from G750M spectra in different wavelength ranges and

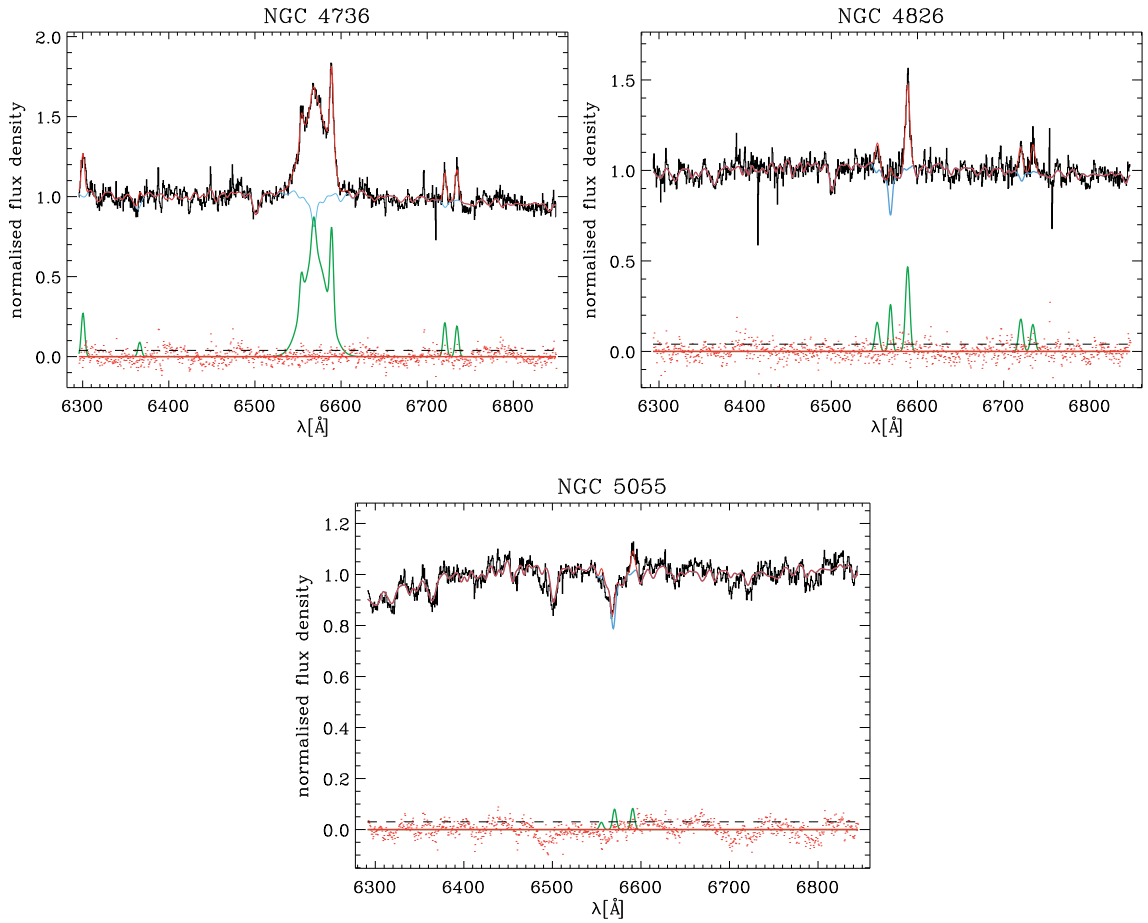

Figure 4.8: Rest-frame G750M spectra of NGC 4736, NGC 4826 and NGC 5055. The galaxy name is given in each panel and the relative fluxes have false zero points for viewing convenience. The best-fitting model (red line) is the sum of the spectra of the ionized-gas (green line) and stellar component (cyan line). The latter is obtained convolving the synthetic templates with the best-fitting LOSVD and multiplying them by the best-fitting Legendre polynomials. The residuals (red dots) are obtained by subtracting the model from the spectrum. The dashed line corresponds to the rms of the residuals.

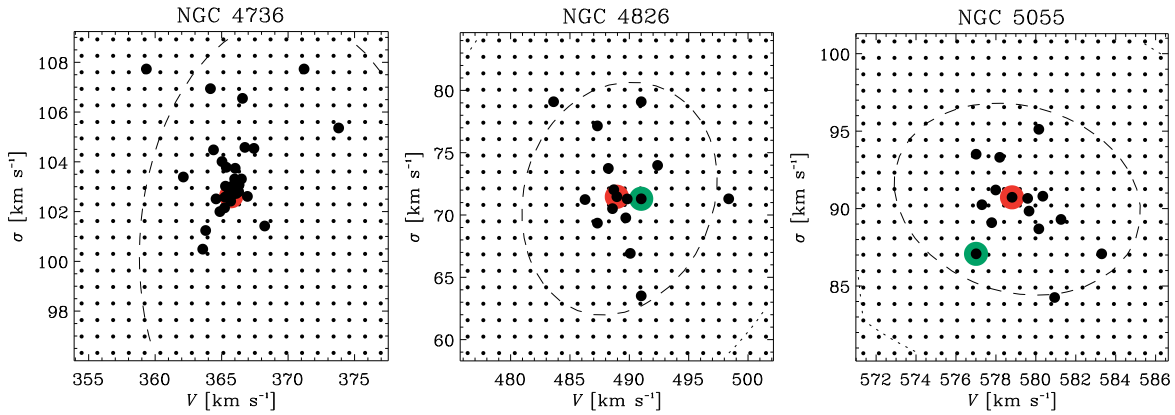

Figure 4.9: Grid of GANDALF models of the G750M spectra for different velocities and velocity dispersions of the stellar component (black small circles) of NGC 4736, NGC 4826 and NGC 5055. Velocity dispersions are not corrected for instrumental resolution. The final best-fitting GANDALF model is shown with a big red circle while the starting best-fitting pPXF model is shown with a big green circle. Big black circles correspond to AMOEBA iterations. Contours show the distribution of $\Delta\chi^2 = \chi^2 - \chi^2_{\rm min}$ with the dashed and dotted lines indicating the 1σ and 2σ confidence level for two degrees of freedom, respectively.

with a different fitting technique. To this aim, we re-extracted the nuclear spectra of these galaxies in apertures matching as much as possible that of Batcheldor et al. (2013, 0.1 arcsec $\times$ 0.05 arcsec) and repeated the fit. For NGC 4736, we were able to match the aperture and found $\sigma_{*,\rm free} = 111.5^{+6.5}_{-10.6}$ km s^{-1}. For NGC 4826 and NGC 5055, we could analyze only a wider aperture since our G750M spectra were taken with the 0.2 arcsec-wide slit. From the spectra extracted from the smallest possible aperture (0.2 arcsec $\times$ 0.1 arcsec for NGC 4826, 0.2 arcsec $\times$ 0.05 arcsec for NGC 5055), we measured $\sigma_{*,\rm fix} = 75.1^{+8.9}_{-9.0}$ km s^{-1} for NGC 4826 and a $\sigma_{*,\rm fix} = 93.6^{+5.5}_{-5.6}$ km s^{-1} for NGC 5055. Our measurements are in agreement with those by Batcheldor et al. (2013) within the 1σ error bars (Fig. 4.7). Our G750M GANDALF fits and grid of GANDALF models employed for the error determination are shown in Fig. 4.8 and Fig. 4.9, respectively.

4.3.3 Fitting issues with the ELODIE stellar library

We attempted to obtain σ_* measurements for the G750M spectra by employing the ELODIE stellar library at medium resolution and the same procedure described in Sect. 4.3.2.

Firstly, we noticed that the final results for the stellar velocity V and σ_* were strongly influenced by the starting guess of velocity $V_{\rm in}$. Here we show this peculiar behavior for the fit of NGC 4435 obtained using the G430L optimal template when fitting the G750M spectrum, as representative example. We tested the dependence of the final results on $V_{\rm in}$ both by employing the ELODIE stellar library and MILES SEDs. We repeated the fit by varying the $V_{\rm in}$ value around that obtained from the MILES SEDs fit ($V \simeq 845$ km s^{-1}). For both libraries, we proceeded with steps of 5, 10 and 50 km s^{-1} by starting from $V_{\rm in}$ values equal

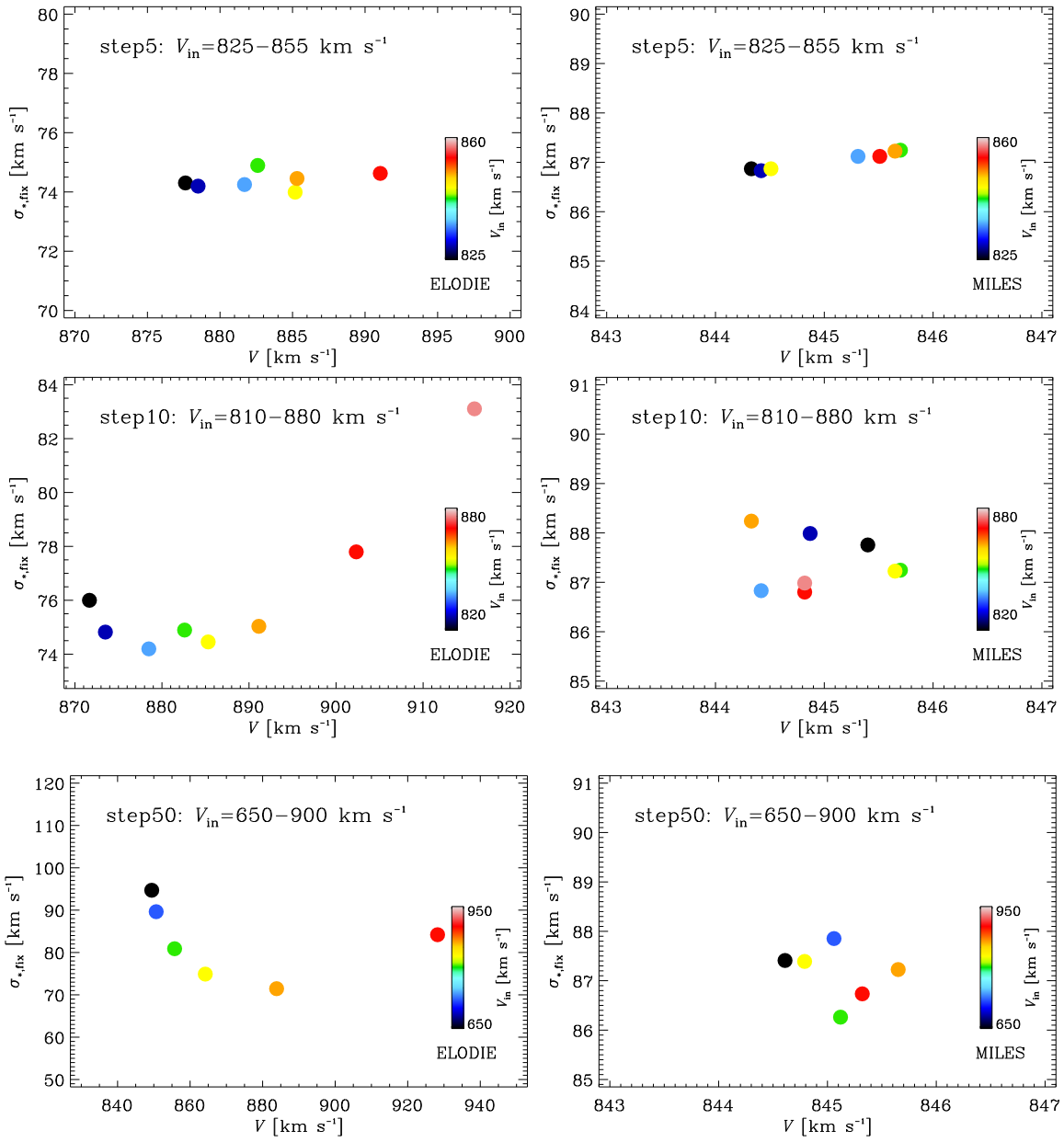

Figure 4.10: GANDALF models for different velocities and velocity dispersions of the stellar component obtained with the ELODIE stellar library (*left panels*) and the MILES SEDs (*right panels*). The range and the step for the $V_{\rm in}$ are reported as well as the $V_{\rm in}$ colorbar.

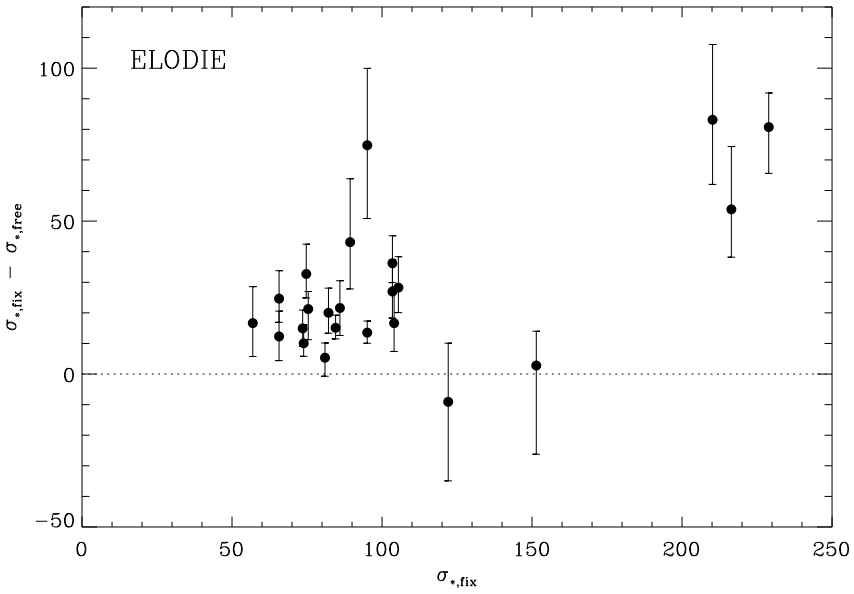

Figure 4.11: Difference between the $\sigma_{*,\rm fix}$ and $\sigma_{*,\rm free}$ as a function of $\sigma_{*,\rm fix}$ obtained with the ELODIE stellar library. The σ_* values are those reported in Tab. 4.5.

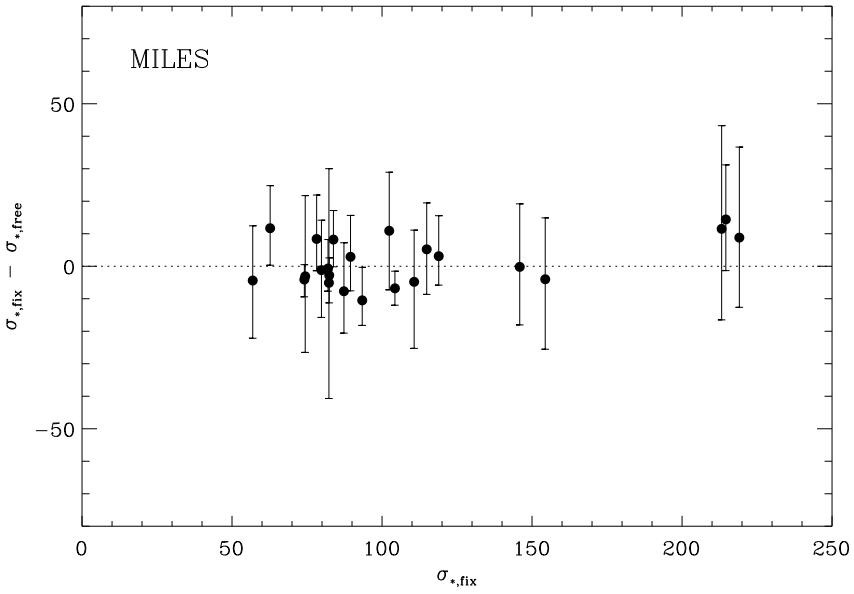

Figure 4.12: Difference between the $\sigma_{*,\rm fix}$ and $\sigma_{*,\rm free}$ as a function of $\sigma_{*,\rm fix}$ obtained with the MILES SEDs. The σ_* values are those reported in Tab. 4.1.

Table 4.5: Values of σ_* for the sample galaxies obtained with the ELODIE stellar library.

Galaxy	$\sigma_{*,\rm fix}$ [km s^{-1}]	$\sigma_{*,\rm free}$ [km s^{-1}]
(1)	(2)	(3)
NGC 2685	$65.7^{+6.6}_{-6.3}$	$41.0^{+6.3}_{-4.5}$
NGC 3368	$81.0^{3.7+}_{-3.8}$	$75.6^{+3.1}_{-4.7}$
NGC 3489	$73.9^{+2.8}_{-2.9}$	$63.8^{+5.3}_{-3.2}$
NGC 3675	$104.0^{+8.2}_{-7.4}$	$87.4^{8.5+}_{-5.5}$
NGC 3992	$122.1^{+18.4}_{-17.1}$	$131.1^{+5.5}_{-19.4}$
NGC 4030	$89.4^{+13.0}_{-12.0}$	$46.3^{+16.1}_{-9.5}$
NGC 4245	$75.4^{+5.5}_{-3.9}$	$54.1^{+1.5}_{-9.2}$
NGC 4314	$86.0^{+6.6}_{-6.1}$	$64.4^{+6.0}_{-6.6}$
NGC 4321	$56.9^{+9.1}_{-6.4}$	$40.3^{+7.7}_{-8.8}$
NGC 4414	$84.5^{3.0+}_{2.7-}$	$69.4^{+2.8}_{-2.5}$
NGC 4429	$210.2^{+21.9}_{-19.2}$	$127.1^{+11.3}_{-8.8}$
NGC 4435	$74.7^{+7.2}_{-6.9}$	$42.0^{+6.5}_{-3.7}$
NGC 4459	$228.9^{+10.5}_{-8.7}$	$148.2^{+3.8}_{-12.4}$
NGC 4477	$151.4^{+10.5}_{-8.7}$	$148.6^{+4.0}_{-27.7}$
NGC 4501	$103.5^{+7.5}_{-5.8}$	$76.5^{+7.2}_{-6.5}$
NGC 4548	$65.7^{+5.3}_{-5.6}$	$53.4^{+6.4}_{-5.6}$
NGC 4596	$216.4^{+7.2}_{-13.8}$	$162.6^{+19.3}_{-7.3}$
NGC 4698	$105.5^{+7.8}_{-5.9}$	$77.2^{+6.5}_{-5.6}$
NGC 4800	$82.2^{+6.2}_{-4.9}$	$62.1^{+5.2}_{-4.6}$
NGC 4826	$73.5^{+4.7}_{-4.3}$	$58.6^{+3.7}_{-4.1}$
NGC 5055	$95.1^{+2.2}_{-2.8}$	$81.5^{+3.1}_{-2.1}$
NGC 7252	$95.1^{+22.7}_{-16.3}$	$20.3^{+10.7}_{-}$
NGC 7331	$103.5^{+5.6}_{-5.5}$	$67.3^{7.0+}_{-3.1}$

Notes. Col.(1): galaxy name. Col.(2): nuclear σ_* obtained using the G430L optimal template when fitting the G750M spectra. Col.(3): nuclear σ_* obtained without using the G430L optimal template when fitting the G750M spectra.

to 825, 810 and 650 km s^{-1} up to 855, 880 and 900 km s^{-1}, respectively. The results are shown in Fig. 4.10. As can be noticed by employing the MILES SEDs, the results for V and $\sigma_{*,\rm fix}$ are very stable against variations on $V_{\rm in}$ and remain almost unchanged also by adopting $V_{\rm in}$ values not so close to the expected ones. Figure 4.10 shows the maximum variations for V and $\sigma_{*,\rm fix}$ ($\Delta V = 1.4$ km s^{-1} and $\Delta\sigma_{*,\rm fix} = 1.4$ km s^{-1} for step5, $\Delta V = 1.4$ km s^{-1} and $\Delta\sigma_{*,\rm fix} = 1.4$ km s^{-1} for step10, $\Delta V = 1.4$ km s^{-1} and $\Delta\sigma_{*,\rm fix} = 1.6$ km s^{-1} for step50). On the contrary, using the ELODIE stars during the fitting procedure led to a visible dependence ($\Delta V = 13.4$ km s^{-1} and $\Delta\sigma_{*,\rm fix} = 0.6$ km s^{-1} for step5, $\Delta V = 44.2$ km s^{-1} and $\Delta\sigma_{*,\rm fix} = 8.9$

km s^{-1} for step10, $\Delta V = 78.8$ km s^{-1} and $\Delta\sigma_{*,\rm fix} = 23.2$ km s^{-1} for step50).

In the case of ELODIE templates, by considering a small range of variation for $V_{\rm in}$ and steps of 5 km s^{-1}, the resulting V and (in particular) $\sigma_{*,\rm fix}$ remain quite constant. Nevertheless, their values are notably different from those obtained from the MILES SEDs (Fig. 4.10, upper panels). By increasing the range of variation for $V_{\rm in}$, the outcomes for V and $\sigma_{*,\rm fix}$ suffer from strong variations (Fig. 4.10, left middle and lower panels). In particular, by increasing $V_{\rm in}$, we measured larger output velocities, whereas the behavior of $\sigma_{*,\rm fix}$ is more complicated. Its value decreases, reaching a minimum close to $V_{\rm in}$ derived from the MILES SEDs fit, and then increases. So depending on which $V_{\rm in}$ is chosen, the output for $\sigma_{*,\rm fix}$ could diverge by a large amount.

Then we restricted the sample of Table 4.1 to the 23 objects for which we measured both $\sigma_{*,\rm fix}$ and $\sigma_{*,\rm free}$ from the G750M spectra by employing the MILES SEDs. We used the same apertures reported in Tables 4.2 and 4.3 for the G430L and G750M spectra, respectively. We employed as $V_{\rm in}$ the ones found from the fits with the MILES SEDs. The results are given in Table 4.5.

We compared these $\sigma_{*,\rm fix}$ and $\sigma_{*,\rm free}$ values in Fig. 4.11 by showing their difference as a function of $\sigma_{*,\rm fix}$. All the galaxies but one are above the dashed line of null difference and on average the values of $\sigma_{*,\rm fix}$ are about 28 km s^{-1} larger than the $\sigma_{*,\rm free}$ values. From this test, we deduced that constraining the stellar populations by using an optimal template could lead to an overestimation of the σ_* value, or conversely and more probably, not using an optimal template could lead to an underestimation of the σ_* value due to difficulties in selecting the proper templates. We repeated this analysis for the MILES SEDs and considering the same sample of galaxies as before. The result is shown in Fig. 4.11, where the galaxies are well-distributed around the dashed line of null difference and the $\sigma_{*,\rm fix}$ values are on average about only 1 km s^{-1} larger than the $\sigma_{*,\rm free}$ ones.

Due to the issues arisen by employing the ELODIE stellar library, we decided to use the MILES SEDs in order to obtain more reliable and stable results.

4.4 Stellar dynamical models for NGC 4435 and NGC 4459

In this section, we focus on the particular cases of NGC 4435 and NGC 4459 since these have very similar ground-based, but quite different STIS measurements of σ_*, which in turn may be indicative of a significantly different $M_\bullet$ at a given, similar bulge mass.

Indeed, whereas the values for $\sigma_{\rm e}$ (the stellar velocity dispersion measured within a circular aperture corresponding to the galaxy effective radius $r_{\rm e}$) obtained by Cappellari et al. (2013) using SAURON integral-field spectroscopy are fairly similar for these two galaxies (amounting to $\sigma_{\rm e}= 152.8 \pm 7.6$ and 158.1 ± 7.9 km s^{-1} for NGC 4435 and NGC 4459, respectively), our STIS measurements return a much smaller $\sigma_{*,\rm fix}$ value for NGC 4435 than for NGC 4459 (amounting to $87.3^{+10.2}_{-8.8}$ and $214.6^{+11.2}_{-12.0}$ km s^{-1}, respectively, see Table 4.1). In fact, the nuclear σ_* value for NGC 4435 is also at odds with what we expect from the aperture velocity dispersion correction for early-type galaxies of Falcón-Barroso et al. (2017), which for a $r_{\rm e} = 23.5$ arcsec would lead to a $\sigma_*= 203.7 \pm 10.1$ km s^{-1}. On the other hand,

for NGC 4459 and a $r_e = 43.1$ arcsec the same aperture correction returns $\sigma_*= 217.9 \pm 10.8$ km s^{-1}, which is entirely consistent with our actual STIS measurement. Although the use of such an aperture correction down to sub-arcsecond scales represents almost an extrapolation given that the work of Falcón-Barroso et al. (2017) is based on ground-based data, the previous comparison further suggests that NGC 4435 and NGC 4459 have very different central stellar kinematics. As to whether this may indicate a different black-hole mass budget, we note that gas-dynamical $M_\bullet$ measurements already point in this direction. Indeed, whereas NGC 4459 shows a $M_\bullet$ value consistent with the $M_\bullet - \sigma_e$ relation (Sarzi et al., 2001), the $M_\bullet$ of NGC 4435 falls significantly below it (Coccato et al., 2006) in spite of their similar σ_e values.

Given these indications, we decided to use the cases of NGC 4435 and NGC 4459 to explore how our STIS sub-arcsecond σ_* measurements can be used to constrain the central mass concentration of galaxies, in particular when large integral-field spectroscopic measurements are available to provide further constraints on the stellar motions. To this goal, in what follows we describe how we proceeded to deproject the stellar surface-brightness distribution to obtain the galaxy luminosity density with the multi Gaussian expansion (MGE) method of Emsellem et al. (1994) and how we built a stellar dynamical model using the Jeans axisymmetric modelling (JAM) algorithm of Cappellari (2008), while assuming the $M_\bullet$ value predicted by the $M_\bullet - \sigma_e$ relation and by matching the SAURON stellar kinematic maps provided by Krajnović et al. (2011).

4.4.1 Properties of NGC 4435

NGC 4435 is a barred lenticular galaxy at a distance $D = 16.0$ Mpc with a central nebular activity of intermediate type between that of LINERs and HII nuclei (Table 4.1). It is a member of the Virgo cluster (Binggeli et al., 1985) and has an absolute total corrected B magnitude $M^0_{B_T} = -19.41$ mag, as obtained from $B_T = 11.74$ mag (RC3).

Although the proximity to the highly disturbed spiral NGC 4438 and the presence of optical plume that appears to connect NGC 4438 to NGC 4435 initially lend to a suggestion that these two galaxies are currently interacting (Vollmer et al., 2005), subsequent works indicate instead that NGC 4435 is relatively undisturbed. Kenney et al. (2008) indeed found that NGC 4438 has in fact collided with the nearby elliptical M86, whereas Cortese et al. (2010) interpreted the optical plume between NGC 4438 and NGC 4435 as Galactic cirrus.

NGC 4435 has boxy isophotes out to about 10 arcsec from the center and disky isophotes outwards. It hosts an inclined dust disk with blue star forming regions in the innermost 4 arcsec from the center (Ferrarese et al., 2006a). Coccato et al. (2006) measured an upper limit of $M_\bullet < 7.5 \times 10^6$ M$_\odot$ from the modelling of resolved, ionized-gas kinematics based on STIS observations along various slit directions and pointed out how this $M_\bullet$ value is far below the prediction of the $M_\bullet - \sigma_e$ relation.

4.4.2 Properties of NGC 4459

NGC 4459 is an unbarred lenticular belonging to the Virgo cluster (Binggeli et al., 1985) at a distance $D = 21.7$ Mpc with central LINER/HII nebular activity (Table 4.1). It has $M^0_{B_\mathrm{T}} = -20.47$ mag from $B_\mathrm{T} = 11.32$ mag (RC3). The early-type morphology of this galaxy was investigated by several authors by performing a photometric decomposition. Kormendy et al. (2009) fitted the V-band surface-brightness radial profile along the major axis of NGC 4459 with a Sérsic law and classified it as an elliptical galaxy. A Sérsic profile was also adopted by Vika et al. (2012) and Beifiori et al. (2012) in their two-dimensional fit of the UKIRT Infrared Deep Sky Survey (UKIDSS) K-band and Sloan Digital Sky Survey (SDSS) i-band images of the galaxy, respectively. On the contrary, Sani et al. (2011) and Savorgnan & Graham (2016) considered an exponential disk in addition to the Sérsic bulge in their photometric decomposition of the Spitzer 3.6-μm image. In their decomposition, Savorgnan & Graham (2016) pointed out that the disk starts to dominate the surface brightness profile for radii larger than 100 arcsec. The galaxy has regular elliptical isophotes although it hosts a dust disk which is extended out to about 8.5 arcsec from the center and characterized by clumps of star formation (Ferrarese et al., 2006a). From the STIS kinematics of the ionized gas, Sarzi et al. (2001) measured a $M_\bullet = 9.4 \times 10^7$ M$_\odot$ by assuming an inclination $i = 47°$ for the gaseous disk. This inclination value was determined by fitting ellipses to the innermost dust lanes, and is consistent with that found by Cappellari et al. (2007) based on stellar-dynamical models.

4.4.3 Broad-band photometry

In order to build a stellar-mass model for NGC 4435 and NGC 4459 and in turn dynamical models capable of constraining $M_\bullet$ using our nuclear σ_* measurements, we need both high-spatial resolution and wide-field images. Therefore, for both galaxies we retrieved Wide Field Camera (WFC) images (Prop. Id. 9401, P.I. Patrick Côté) obtained with the F850LP filter and ACS (Lucas et al., 2016) from the Hubble Legacy Archive (HLA). The available ACS/WFC frames were already reduced and combined with the Python tool `DrizzlePac` (Gonzaga et al., 2012). The final image is characterized by a field of view of 202 arcsec × 202 arcsec and a plate scale of 0.049 arcsec pixel^{-1}. The images were oriented with north at the top and east to the left and given in electrons per second.

We flux calibrated the F850LP images in the AB photometric system as it follows

$$\mu = -2.5 \log \left(\frac{I}{G \cdot s^2} \right) + z_\mathrm{cal} - A_z \tag{4.1}$$

where I is the surface brightness of each pixel in units of electrons per second, G is the gain in electrons per ADU, s is the plate scale in arcsec pixel^{-1}, z_cal is the calibration constant from the header of the images and A_z is the Galactic extinction by Schlafly & Finkbeiner (2011). It is $G = 1$ electrons per ADU and $z_\mathrm{cal} = 24.871$ mag for both galaxies whereas it is $A_z = 0.036$ and 0.057 mag for NGC 4435 and NGC 4459, respectively. We converted the resulting surface brightness into luminosity surface density in solar units using $M_{\odot,z} = 4.52$

mag for the z-band absolute AB magnitude of the Sun.

We subtracted the sky level tabulated by Pavlovsky et al. (2004). For each galaxy, we did a sanity check by comparing the given value with the mean value of the sky level we determined in a large number of 5×5 pixel areas of the image using the `imexamine` task in IRAF. We selected these areas in apparently empty regions far from the galaxy, which we considered free of objects to avoid the contamination of the light of field stars and galaxies, as well as of the target galaxy itself. For the estimated sky value and its error we adopted the average and rms of the mean values, respectively. The estimated sky value of NGC 4435 is consistent with that of Pavlovsky et al. (2004). On the contrary, our estimated sky level of NGC 4459 is significantly higher than that of Pavlovsky et al. (2004), suggesting that the contribution of the galaxy nearly extends out to the edge of the field of view.

4.4.4 Dust masking

As both galaxies display prominent dust lanes in their central regions, we needed to account for their presence when fitting the surface brightness distribution. First, we carefully inspected the distribution of the dust to identify the regions where it may affect the surface brightness analysis. Indeed, NGC 4435 harbors a highly inclined disk of dust near to the center, while NGC 4459 has a more extended dust disk with the outer parts following the surface brightness distribution and the inner ones displaying a more irregular pattern (Fig. 4.14).

We tried to correct the F850LP images for dust absorption by employing the method described by Ferrarese et al. (2006a). To this aim we also retrieved from the HLA archive the ACS images obtained with the F475W filter. We adopted A(F475W)/A(F850LP) = 2.447. The F475W resembles the SDSS-g filter, whereas the F850LP is similar to SDSS-z. We calculated the correction by linearly interpolating the color $(g - z)$ along the major axis of each galaxy in a region immediately beyond where the dust is. We corrected the images by employing the standard Galactic extinction curve given by Cardelli et al. (1989). In this analysis we did not correct the pixels flagged because of noise or cosmic rays.

The observations were carried out in a way that the galaxy centers were in the same pixel position on both F475W and F850LP images and that the position angles were perfectly aligned. We further verified the orientation of the frames by taking advantage of the presence of field stars and employing the task `imexamine`. Then we estimated the sky level with the task `imexamine` and we compared it with the value and tabulated by Pavlovsky et al. (2004). For NGC 4435 we assumed the value measured from the frame since it was compatible with the tabulated one. For NGC 4459 we considered the value from Pavlovsky et al. (2004), since the galaxy was extended on the whole frame and the sky value would be overestimated. Finally we ran the PYRAF task `ellipse` on the F475W and F850LP images after having masked the foreground stars and background galaxies. We employed the sky values along with the results of the routine `ellipse` as guesses to the PYRAF routine `dust.cl` that performed the dust correction. The latter input was used in `dust.cl` to select the regions to be dust-corrected.

The original and the dust corrected images are shown in Fig. 4.13. The dust correction for NGC 4435 is not so effective as for NGC 4459. Indeed, the procedure is based on the assumption that the dust is in the galaxy's foreground (the so-called "screen approximation").

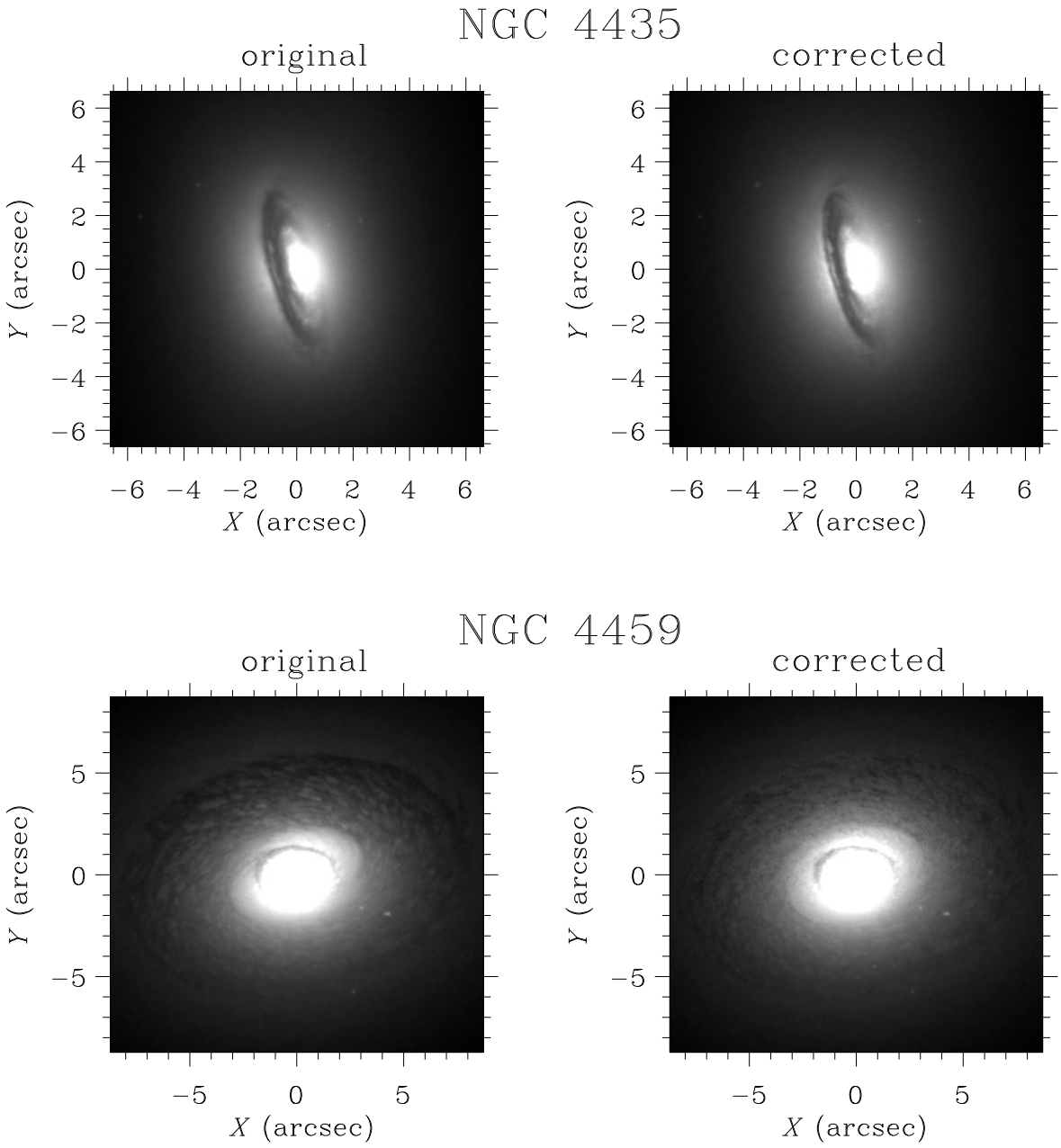

Figure 4.13: *Upper panels*: Central portions of the original (*left panel*) and dust-corrected (*right panel*) F850LP images of NGC 4435. The images are oriented with north at the top and east to the left. *Lower panels*: Same as above, but for NGC 4459.

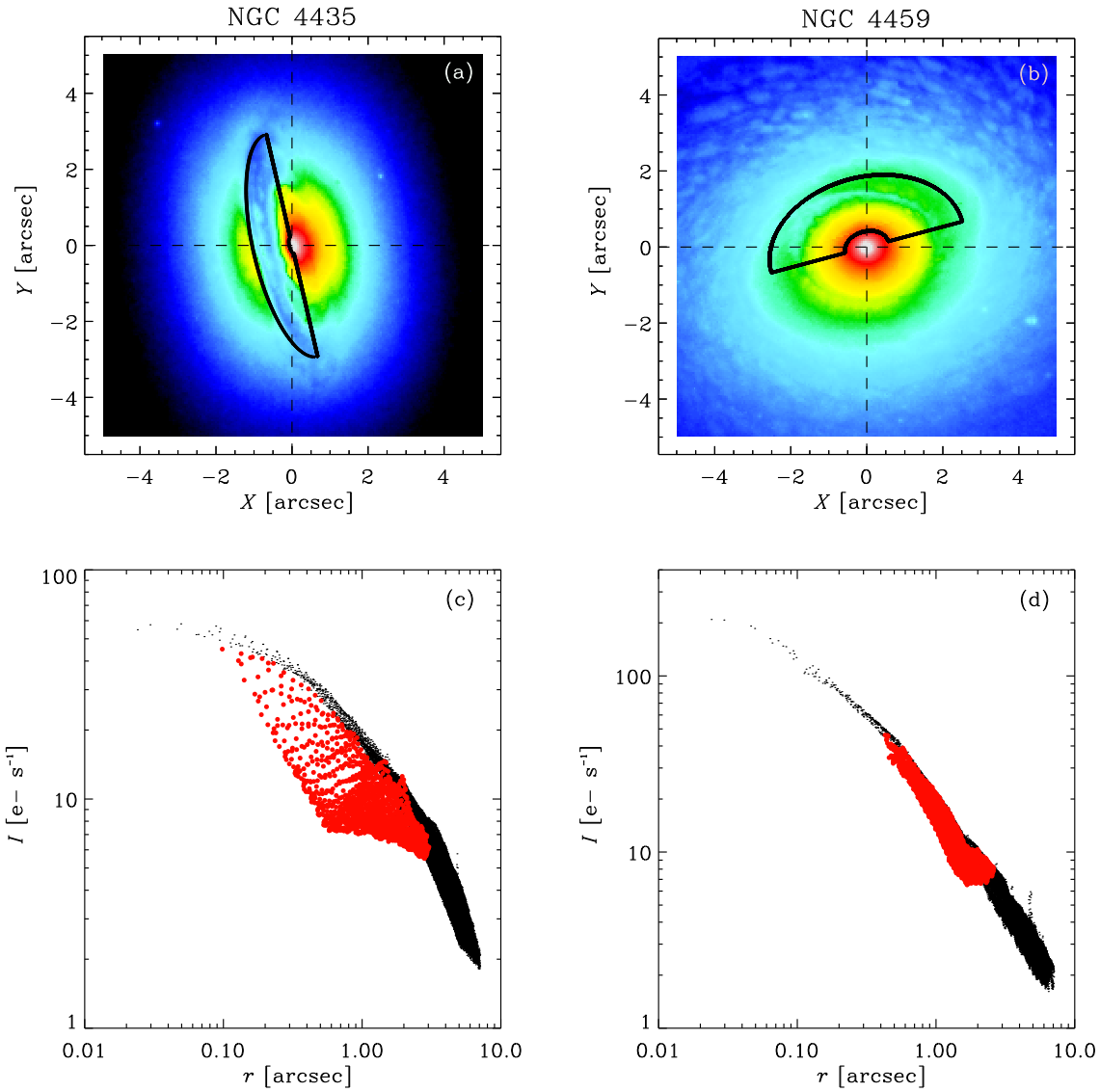

Figure 4.14: *Left-hand panels*: Central portion of the F850LP image of NGC 4435 with the contour (black thick line) of the adopted mask (*top panel*) and surface brightness of the masked (red filled circles) and unmasked pixels (black dots) as a function of their distance from the galaxy center (*bottom panel*). The F850LP image is oriented with north at the top and east to the left and the field of view is 5 arcsec ×5 arcsec. The dashed lines mark the galaxy center. *Right-hand panels*: Same as above, but for NGC 4459.

This is not a good assumption for the edge-on dust disk of NGC 4435, due to the sharp dimming at the disk edge. Nevertheless, it results to be less optically thick than in the original image. On the other hand, the dust lanes of NGC 4459 follow the surface brightness distribution and this allowed us to perform a better correction, even if it was still not so effective in the central region where a second dust disk with a higher inclination than the outer one is present.

We compared our results with those from the literature. Ferrarese et al. (2006a) failed to recover the surface brightness profile within the inner 2.0 arcsec in the case of NGC 4435, while the dust disk can still be seen in the dust-corrected image of Coccato et al. (2006) as well, although it is less optically thick than in the uncorrected image. For NGC 4459, Ferrarese et al. (2006a) did not consider their dust correction to be reliable out to 7.5 arcsec from the center.

Since our result was not so effective and this was confirmed also from the literature, we preferred to mask the dusty regions on the images of galaxies rather than correcting them. In both cases, the mask has the shape of half elliptical annulus with an ellipticity $\epsilon = 1 - \cos i$ given by the inclination of the dust disk. This was measured by Coccato et al. (2006) and Ferrarese et al. (2006a) for NGC 4435 ($i = 70°$) and NGC 4459 ($i = 45°$), respectively (Fig. 4.14). To define the location and size of the masked region and verify whether the galaxy center was obscured, we compared the surface brightness measured in each pixel of the central portion of the image as a function of the distance from the galaxy center.

The mask of NGC 4435 extends between 0.1 arcsec and 4 arcsec along the galaxy major axis. The resulting surface brightness profile reveals a lack of dust in the inner 0.1 arcsec. In fact, the unmasked pixels on the unobscured northwestern side of the galaxy have systematically a brighter surface brightness than those on the dusty southeastern side (Fig. 4.14).

The fact that the outer parts of the dust disk of NGC 4459 follow the surface brightness distribution made it impossible to clearly distinguish obscured and unobscured pixels as we did in the previous case. We chose to mask only the galaxy portion where the dust absorption was stronger and more irregular. Therefore, we masked the northeastern half between 0.4 arcsec and 3 arcsec along the galaxy major axis since there were a few dust-affected pixels in the innermost region (Fig. 4.14).

4.4.5 Multi-Gaussian expansion analysis

In order to obtain a model for the luminosity volume density of both NGC 4435 and NGC 4459, and in turn for their mass density and gravitational potential, we started by parametrizing the surface brightness of the sky-subtracted and dust-masked image of each galaxy as the sum of a set of Gaussian components by using the MGE IDL algorithm by Cappellari (2002). The MGE method indeed allows for a simple reconstruction of the intrinsic surface brightness distribution (provided that the PSF can be approximated as a sum of Gaussian components) and to a straightforward deprojection of the intrinsic surface brightness into the luminosity volume density (which can also be expressed as the sum of a set of Gaussian components too).

Before using the MGE program we performed a photometric analysis in order to estimate

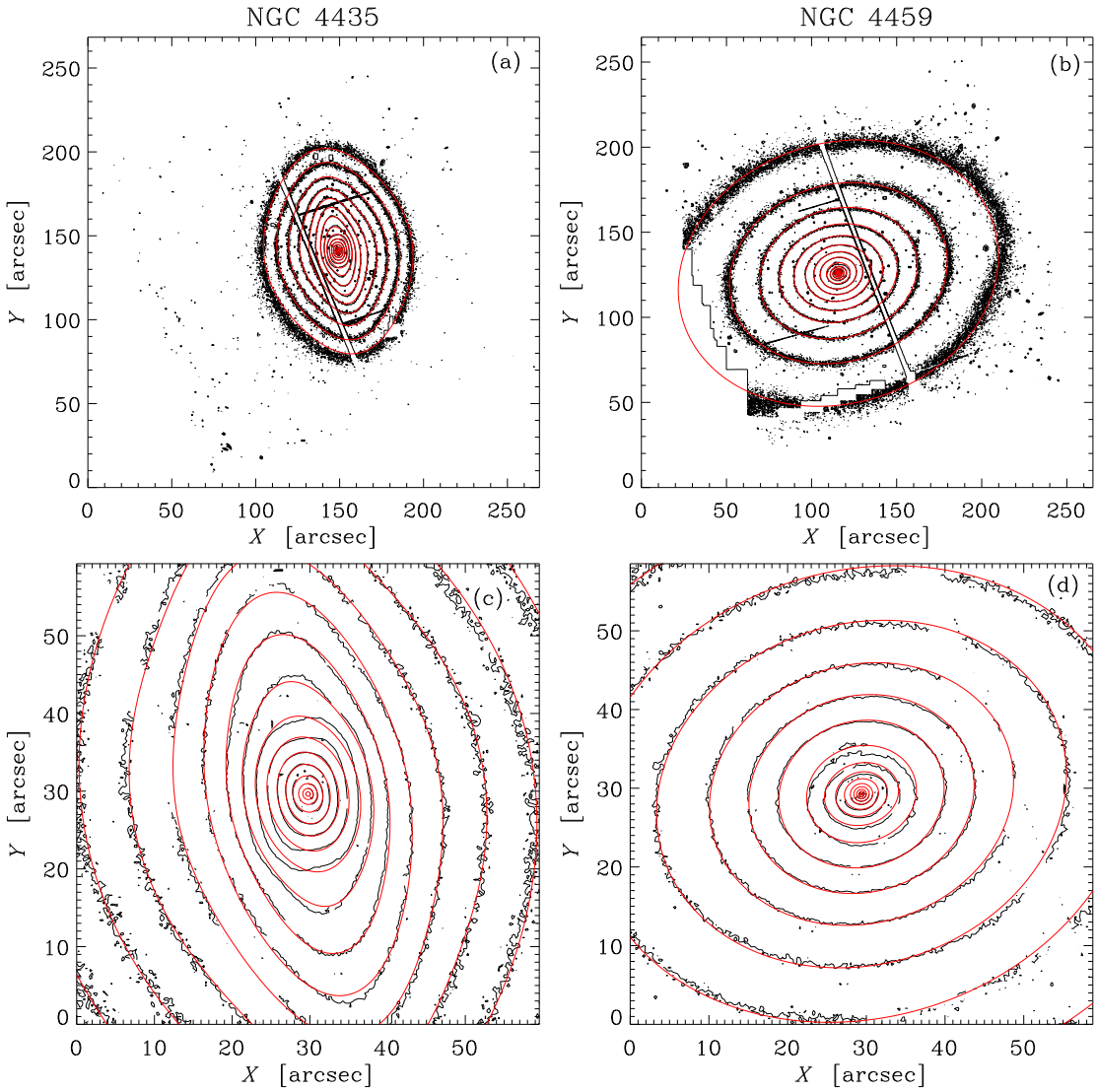

Figure 4.15: *Left-hand panels*: A few reference isophotes for the F850LP image (black lines) and MGE model (red lines) of NGC 4435. The entire field of view (*top panel*) and the central 1 arcmin × 1 arcmin portion (*bottom panel*) of the image are shown. The image is oriented with north at the top and east to the left. Flux levels are normalized to the central surface brightness of the image and the contours are spaced by 0.5 mag arcsec^{-2}. While the MGE model was constrained using the original image, the image shown here is binned by 6×6 pixels to reduce the noise for the comparison purposes only. The gap between the two WFC CCDs and a few bad rows are clearly visible, whereas missing portions of the galaxy isophotes correspond to masked regions. *Right-hand panels*: Same as above, but for NGC 4459.

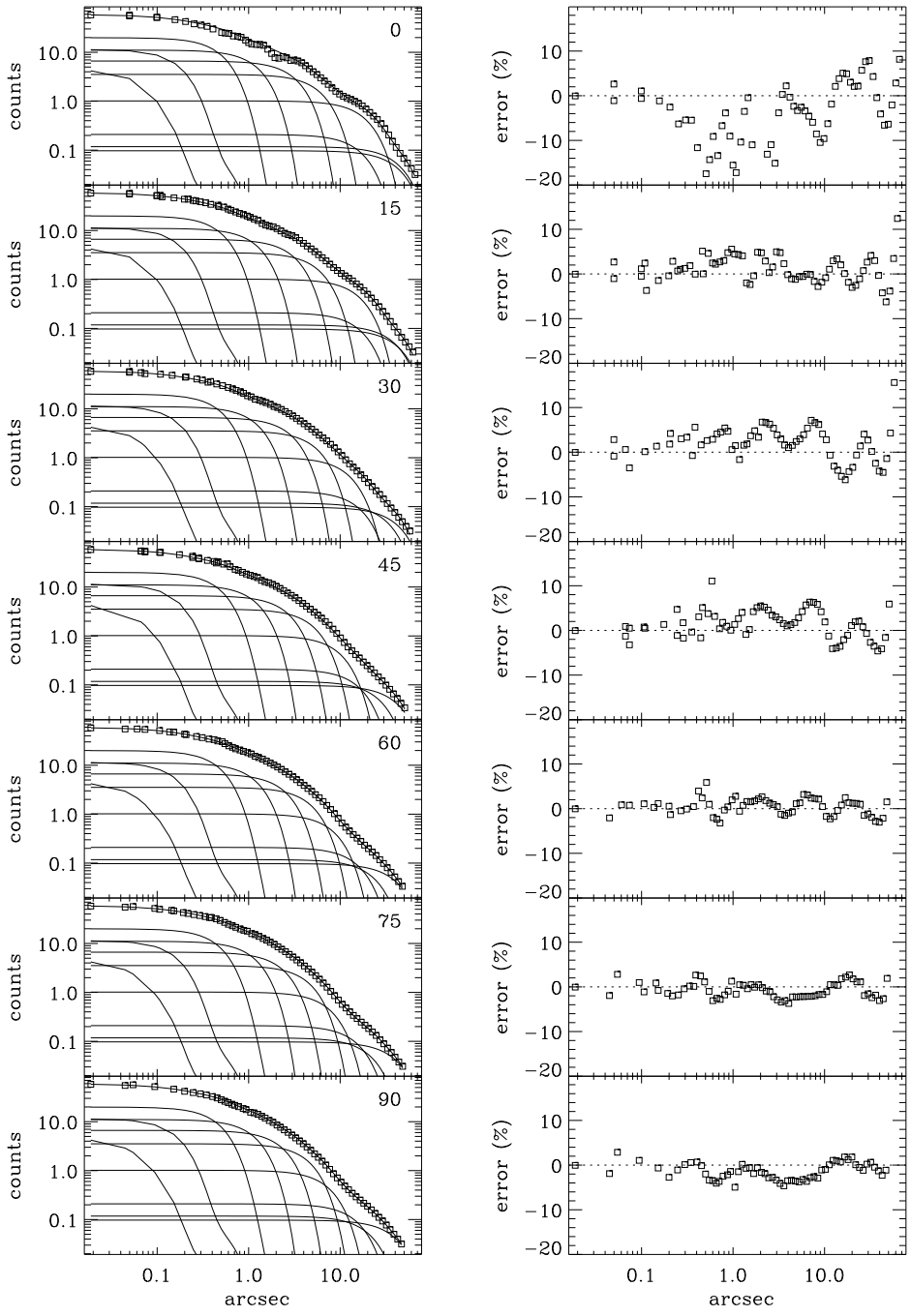

Figure 4.16: *Left panels*: comparison between the ACS/F850LP photometry of NGC 4435 (open squares) and the MGE best-fitting model (solid line). The single convolved Gaussians are illustrated as well. From the top to the bottom the profiles of seven representative sectors within which the photometry was measured are shown spaced in angle between the major (0°) and the minor axis (90°). *Right panels:* radial variation of the relative error along the profiles. The mean absolute deviation between the fitted MGE and the data is of 2.7%.

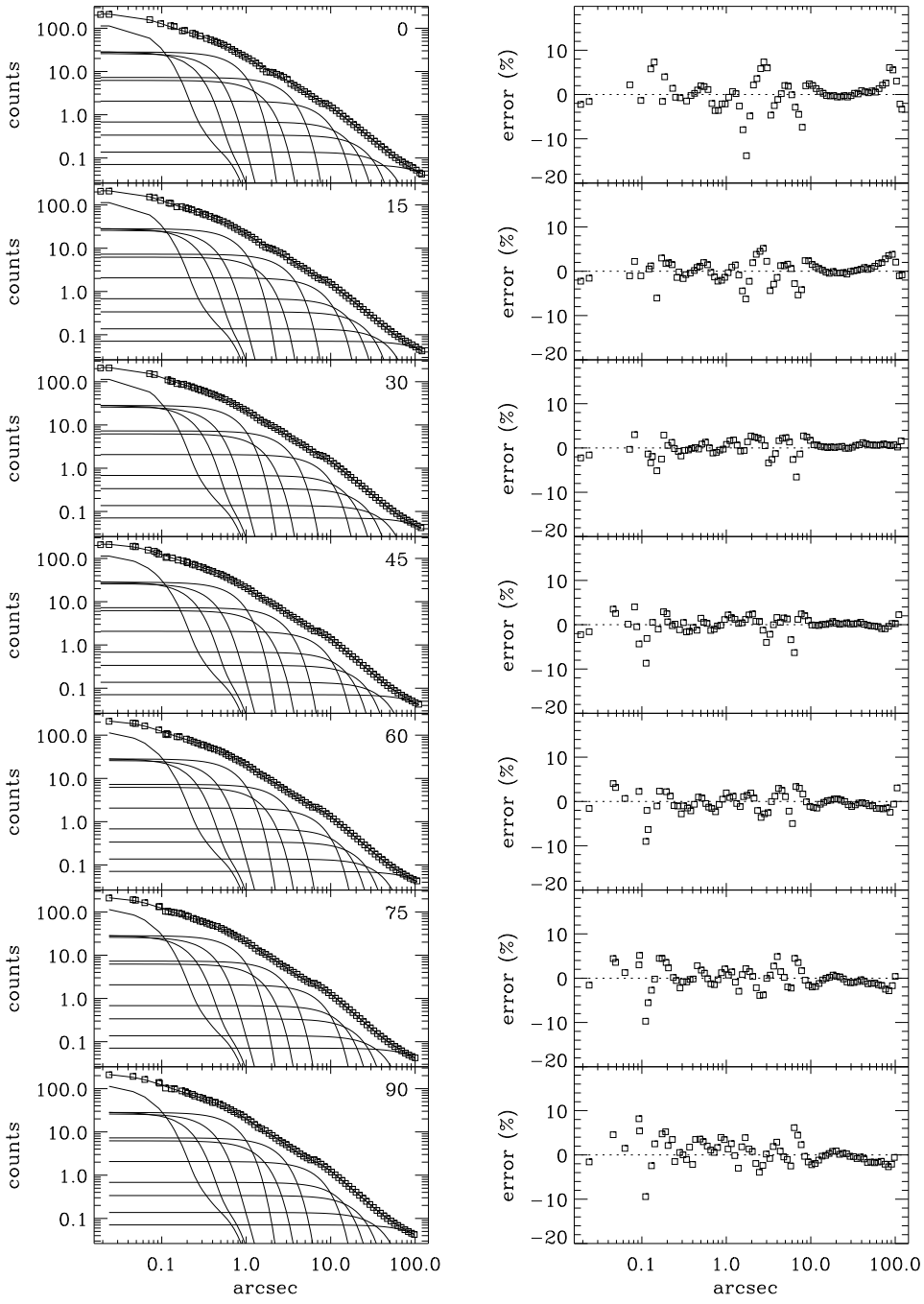

Figure 4.17: The same as in Fig. 4.16 but for NGC 4459. The mean absolute deviation between the fitted MGE and the data is of 1.6%.

the center and position angle of both galaxies. For this we ran the `ellipse` task in IRAF after masking out the remaining foreground stars and background galaxies in the ACS images and inspected the results for the azimuthally-averaged surface brightness, ellipticity, position angle, and center coordinates. In particular, we found no evidence of a varying center within the errors and calculated the mean position angle by averaging the values measured between 3 arcsec and 6 arcsec for NGC 4435 and between 3 arcsec and 5 arcsec for NGC 4459.

We then obtained an MGE best-fitting model to the galaxy surface brightness by keeping constant the center and position angle of the Gaussians and while further restricting the range of the resulting axial ratios of the Gaussian components but keeping the fit acceptable, as described by Scott et al. (2013). This ensured that the permitted galaxy inclinations were not limited to a narrower range than that allowed by the data. We looked for the MGE best-fitting model by using different values of the position angle within 10° from the guess value we obtained from the isophotal fitting. In the fitting process, we used the MGE model of the synthetic F850LP image of the PSF, which we generated with the TINY TIM package (Krist et al., 2011).

In Fig. 4.15, we show the F850LP images of NGC 4435 and NGC 4459 at two different scales with a few representative galaxy isophotes and compare these to their MGE best-fitting models. Figs. 4.16 and 4.17 illustrate the MGE best-fitting models along representative sectors and the corresponding radial variation of the relative error. We modeled the surface brightness radial profile of NGC 4459 as R^{-1} at large radii, where Savorgnan & Graham (2016) reported the presence of an exponential disc.

4.4.6 Jeans axisymmetric dynamical models

With the MGE models at hand, we proceeded to use the JAM IDL algorithm (Cappellari, 2008) to build Jeans axisymmetric dynamical models for NGC 4435 and NGC 4459 in order to test the usefulness of our nuclear σ_* measurements in constraining the $M_\bullet$ of these objects. In particular we aimed to anchor these models by matching the JAM predictions for the stellar $V_{\rm rms} = \sqrt{v_*^2 + \sigma_*^2}$ to the SAURON stellar kinematic measurements of Krajnović et al. (2011) and then to obtain from such best-fitting JAM models a nuclear $V_{\rm rms}(0)$ value at the HST spatial resolution that can be directly compared to our STIS σ_* measurements.

To begin with, we built a set of mass-follows-light models by assuming that the mass volume density follows the luminosity volume density derived from the MGE fit and the deprojection of the galaxy surface brightness. These models have three free parameters that are optimised while matching the observed $V_{\rm rms}$. They are the dynamical mass-to-light ratio $(M/L)_{\rm dyn}$, the galaxy inclination i and the anisotropy parameter $\beta_z = 1 - \sigma_z^2/\sigma_R^2$, where σ_R and σ_z are the radial and vertical components of the velocity dispersion, respectively, in a cylindrical coordinate system with the origin in the center of the galaxy and symmetry axis aligned with its rotation axis. To build such models, we took advantage of the two-dimensional maps of v_* and σ_* provided by the ATLAS$^{\rm 3D}$ survey[3] (see Emsellem et al., 2004; Cappellari et al., 2011; McDermid et al., 2015, for all details). The integral-field spectroscopic data were obtained with SAURON at the William Herschel Telescope (Bacon et al., 2001) in

[3]The ATLAS$^{\rm 3D}$ data are available at `http://www-astro.physics.ox.ac.uk/atlas3d/`.

low resolution mode with a field of view of about 30 arcsec × 40 arcsec. The spatial scale per spaxel was 0.8 arcsec × 0.8 arcsec and the wavelength range between about 4800 and 5380 Å was covered with spectral resolution of $FWHM = 4.2$ Å corresponding to $\sigma_{\rm inst} = 108$ km s^{-1}. The observations were characterized by a typical seeing of $FWHM = 1.5$ arcsec. The data reduction and extraction of the stellar kinematics is presented by Cappellari et al. (2011), while the v_* and σ_* maps of NGC 4435 and NGC 4459 are shown by Krajnović et al. (2011, but see also Emsellem et al., 2004 for NGC 4459). We derived $V_{\rm rms}$ and corresponding errors from the available SAURON kinematics with no further modification.

For NGC 4435, the MGE results allowed only for inclination angles in excess of $i = 67^\circ$ when deprojecting the surface brightness, which is a limit that corresponds well with inclination $i = 70^\circ$ for the central ionized-gas disk as inferred by Coccato et al. (2006) from the dust lane morphology. For NGC 4459 we fixed the inclination by adopting the value of $i = 48^\circ$ from Cappellari et al. (2013), which also agrees with the $i = 47^\circ$ value for the central ionized-gas and dust disk measured by Sarzi et al. (2001). For both galaxies, we then adopt radially constant values for both $(M/L)_{\rm dyn}$ and β_z, which were optimised by χ^2-minimisation based on the $V_{\rm rms}$ measurements and associated errors. For NGC 4459, $\beta_z < 0$ would imply a lower χ^2/DOF, but for the fast rotators the assumption that $\beta_z \geq 0$ is observationally motivated (Cappellari, 2008).

The best-fitting parameters of the mass-follows-light models of NGC 4435 are $(M/L)_{\rm dyn} = 2.18$ M$_\odot$/L$_\odot$, $\beta_z = 0.22$ and $i = 67^\circ$, while for NGC 4459 we find $(M/L)_{\rm dyn} = 1.66$ M$_\odot$/L$_\odot$ and $\beta_z = 0.00$ best-fitting values with $i = 48^\circ$. By construction, these mass-follows-light dynamical models do not include a SBH, so we also constructed a second set of models including a SBH with $M_\bullet$ as predicted by the $M_\bullet - \sigma_{\rm e}$ relation of Kormendy & Ho (2013) and adopting the $\sigma_{\rm e}$ values given by Cappellari et al. (2013), that is, $M_\bullet = 9.5 \cdot 10^7$ and $1.1 \cdot 10^8$ M$_\odot$ for NGC 4435 and NGC 4459, respectively. With these $M_\bullet$ values, the JAM best-fitting parameters for NGC 4435 are $(M/L)_{\rm dyn} = 2.15$ M$_\odot$/L$_\odot$, $\beta_z = 0.21$ and $i = 67^\circ$, while for NGC 4459 we find $(M/L)_{\rm dyn} = 1.65$ M$_\odot$/L$_\odot$ and $\beta_z = 0.00$ with $i = 48^\circ$. Unsurprisingly, these are very similar to the $M_\bullet$=0 models, given that ground-based data generally do not provide much leverage on $M_\bullet$ measurements at the distance of these galaxies.

The comparison between the SAURON $V_{\rm rms}$ maps of NGC 4435 and NGC 4459 and JAM prediction including a SBH are shown in Fig. 4.18. Although the models broadly compare well with the data in these maps, formally the JAM models are not good since they lead to reduced-χ^2 values around 2.8 and 2.5, for NGC 4435 and NGC 4459 respectively. As typical errors for the JAM best-fitting parameters, we therefore adopted the estimates that Lablanche et al. (2012) obtained on the basis of simulations for early-type barred and unbarred galaxies, which correspond to errors smaller than 5° for the inclination, smaller than 0.15 for $(M/L)_{\rm dyn}$ and smaller than 0.3 for β_z. A comparison between our best-fitting values and those of the models of Cappellari et al. (2013) is not possible as the latter do not provide their β_z values.

Fig. 4.19 further illustrates how the JAM models compare to the SAURON measurements by showing major-axis $V_{\rm rms}$ profiles for both data and models within a 0.8 arcsec-wide slit. Fig. 4.19 shows both models with $M_\bullet = 0$ M$_\odot$ and $M_\bullet$ from the $M_\bullet - \sigma_{\rm e}$ relation, which allows us to better appreciate how these models differ by less than 10 km s^{-1} in the central

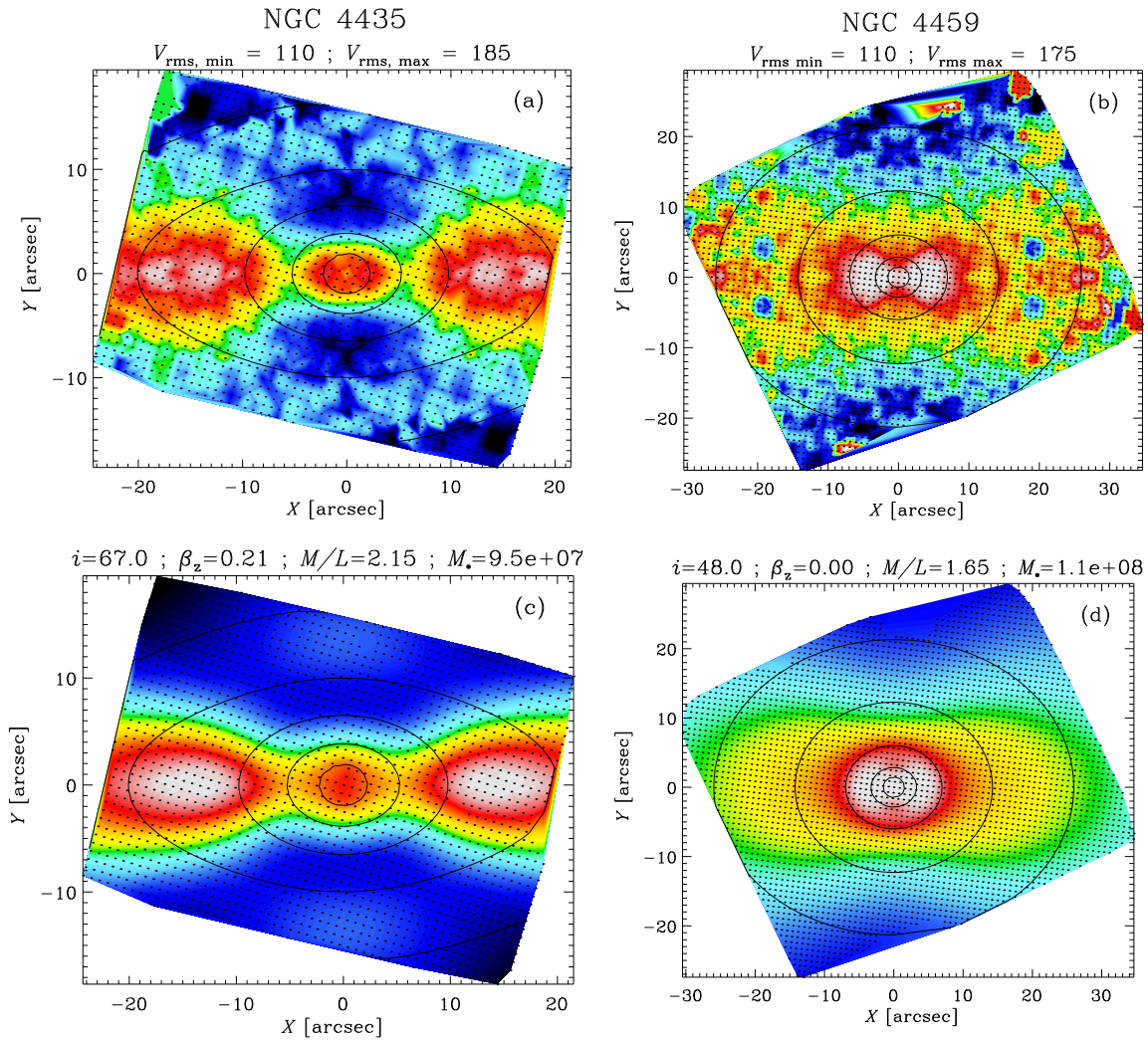

Figure 4.18: *Left-hand panels*: Comparison between $V_{\rm rms}$ from the SAURON stellar kinematics (*top panel*) and second velocity moment from JAM model (*bottom panel*) of NGC 4435. While the models were constrained using the original kinematics, the symmetrized $V_{\rm rms}$ map and bisymmetric JAM map are shown here for the comparison purposes only. The minimum and maximum values of $V_{\rm rms}$ corresponding to black and white levels in the color table are given on top of the SAURON map. The best-fitting parameters of the stellar dynamical model are shown on top of the JAM map. A few reference isophotes for the MGE model of F850LP image are also plotted with the galaxy major axis parallel to the horizontal axis. *Right-hand panels*: Same as above, but for NGC 4459.

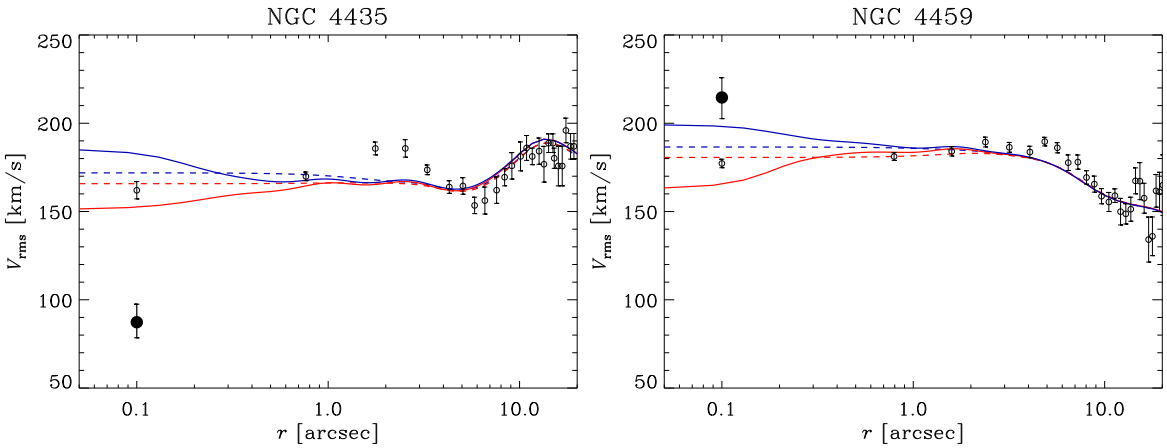

Figure 4.19: *Left-hand panels*: Comparison between the SAURON $V_{\rm rms}$ (black open circles) and second velocity moment from JAM best-fitting models with $M_\bullet = 0$ $M_\odot$(red lines) and $M_\bullet = 9.5 \cdot 10^7$ $M_\odot$ (blue lines) along the major axis of NGC 4435. The dashed and continuous lines correspond to the JAM predictions for the SAURON and HST spatial resolution and sampling, respectively. The black filled circle corresponds to the sub-arcsecond $\sigma_{*,\rm fix}$ measured from the G750M spectrum. The central SAURON $V_{\rm rms}$ and G750M $\sigma_{*,\rm fix}$ are shifted to 0.1 arcsec for the comparison purposes only. *Right-hand panels*: Same as above, but for NGC 4459 with $M_\bullet = 0$ $M_\odot$(red lines) and $M_\bullet = 1.1 \cdot 10^8$ $M_\odot$ (blue lines).

regions, as expected for models tailored to match ground-based observations of limited spatial resolution. The large discrepancy between data and models seen between about 1 arcsec and 3 arcsec for NGC 4435 is due to the two-lobes structure of the SAURON $V_{\rm rms}$ map, which is quite difficult to reproduce (Fig. 4.18).

Having anchored the JAM models to match the SAURON data, we finally obtained the radial profiles of $V_{\rm rms}$ along the major axis of both galaxies by simply changing the spatial resolution and spatial sampling of the JAM models with $M_\bullet = 0$ $M_\odot$ and $M_\bullet$ from the $M_\bullet - \sigma_{\rm e}$ relation to match that of the HST/STIS observations (Fig. 4.19). As expected, the profiles at ground-based and HST resolution begin to differ only in the inner 1 arcsec, with a maximum difference of about 35 km s^{-1} in the center in both NGC 4435 and NGC 4459. This allowed a direct comparison with values of $\sigma_{*,\rm fix}$ we measured from STIS spectra, which are also shown in Fig. 4.19.

For NGC 4435 the STIS $\sigma_{*,\rm fix} = 87.3^{+10.2}_{-8.8}$ km s^{-1} is much smaller than the model prediction, at the HST resolution, of $V_{\rm rms}(0) = 185.3$ km s^{-1} for $M_\bullet = 9.5 \cdot 10^7$ $M_\odot$. In fact, our nuclear σ_* value is even much smaller than the JAM prediction for $M_\bullet = 0$ $M_\odot$. On the other hand, the STIS $\sigma_{*,\rm fix} = 214.6^{+11.2}_{-12.0}$ km s^{-1} of NGC 4459 is consistent within the 1σ errors with the model prediction $V_{\rm rms}(0) = 199.1$ km s^{-1} for $M_\bullet = 1.1 \cdot 10^8$ $M_\odot$.

Even though our reference JAM models are clearly somehow simplistic, in particular since they are based on the common assumption of constant vertical anisotropy profile and also in light of their limited ability to match the SAURON data in detail, we consider it unlikely that more sophisticated models for NGC 4435 will be able to predict a nuclear σ_* values as low as

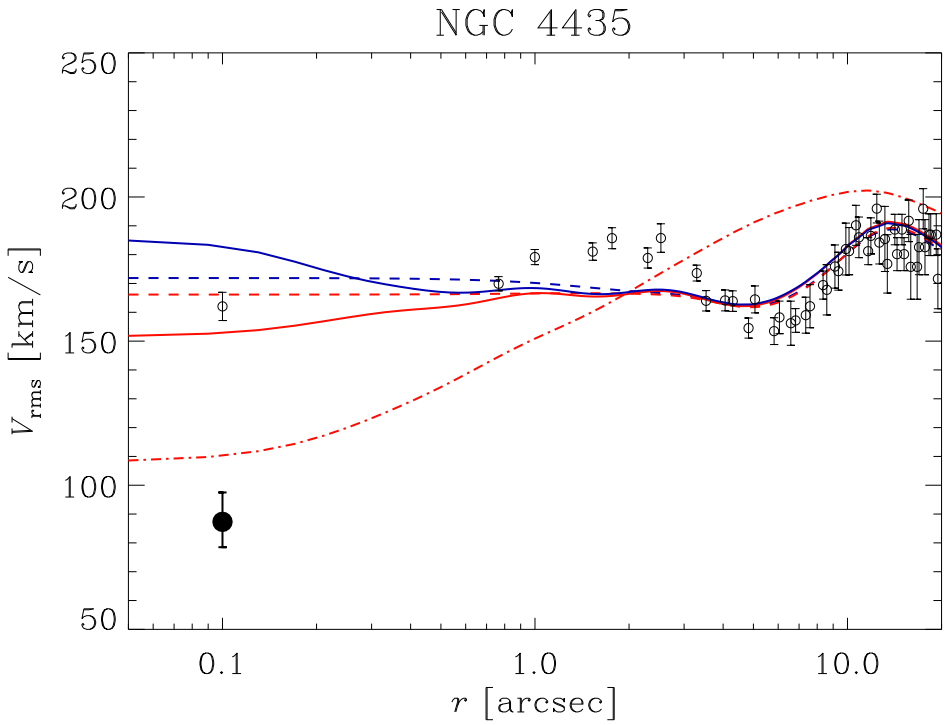

Figure 4.20: The same as in Fig. 4.19 for NGC 4435. The dotted-dashed line corresponds to the prediction for the HST spatial resolution and sampling considering $\beta_z = -0.9$ and $M_\bullet = 0$ $M_\odot$.

those that we observe. For instance, to match the STIS $\sigma_{*,\rm fix}$ alone, we would currently need rather extreme vertical anisotropy β_z values of about -0.9 (Fig. 4.20). Milder β_z variations, on the other hand, may help bridge the gap between the STIS measurements and the JAM model predictions in the case of NGC 4459.

We further analysed the reliability of the σ_* measured for NGC 4435 by building an extended grid of GANDALF models. We adopted σ_* values beyond 185.3 km s^{-1}, that is the central value predicted from HST model of Fig. 4.19. Fig. 4.21 shows a clear single χ^2 minimum and a regular χ^2 distribution with the 3σ contour well below the value of 185.3 km s^{-1}.

In order to further investigate this issue and to verify that HST $\sigma_*(0)$ value of Fig. 4.19 can not be derived from the G750M spectrum of NGC 4435, we broadened the model spectrum of the stellar component to a velocity dispersion of 185.3 km s^{-1}(Fig. 4.21, right panel). We immediately noticed that such a σ_* value is too large to properly fit the G750M spectrum, contrary to the best-fitting value we adopted.

4.5 Conclusions

We considered all the STIS spectra obtained with the G750M grating and bracketing the Hα line available in the MAST and which were placed on the nucleus of a galaxy, in order to

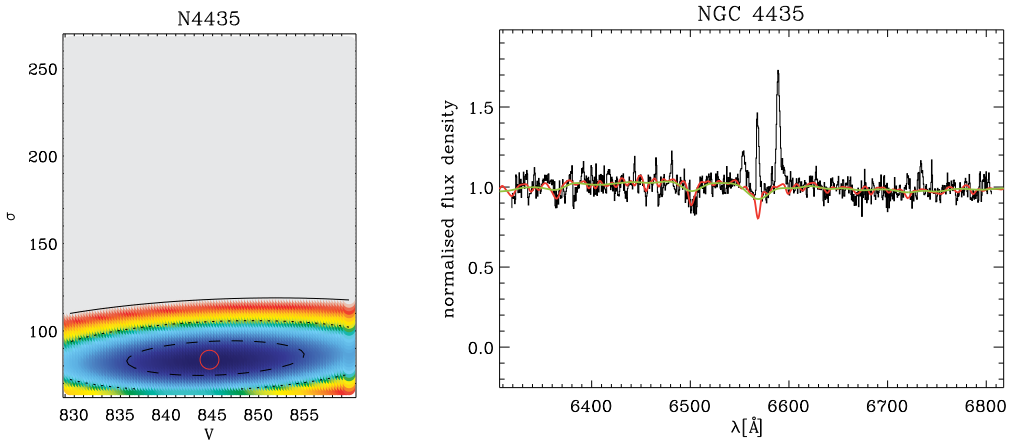

Figure 4.21: *Left panel*: Grid of GANDALF models for different velocities and velocity dispersions for the stellar component of NGC 4435. Velocity dispersions are not corrected for instrumental resolution. The final best-fitting GANDALF model is shown with a big red circle. Contours show the distribution of $\Delta\chi^2 = \chi^2 - \chi^2_{\rm min}$ with the dashed, dotted and solid lines indicating the 1σ, 2σ and 3σ confidence level for two degrees of freedom, respectively. *Right panel*: Spectra of the stellar component for $\sigma_{*,\rm fix} = 87.3$ km s^{-1} (red line) and $\sigma_{*,\rm fix} = 185.3$ km s^{-1} (green line).

obtain stellar velocity dispersion measurements within sub-arcsecond apertures. In this way, we arrived at a sample of 28 relatively nearby galaxies ($D < 70$ Mpc, see Table 4.1), spanning a wide range of morphological types (from E to Scd), central nuclear activity (Seyfert 2, LINERs, HII nuclei) and nuclear stellar velocity dispersion measurements ($50 < \sigma_* < 270$ km s^{-1}). For these objects, we extracted the stellar kinematics by matching the nuclear STIS spectra using the single-age, single-metallicity stellar population models of Vazdekis et al. (2010) and both narrow and broad Gaussian emission lines. For 24 objects we further constrained such a fit by using the optimal template from a similar fit to the G430L low-resolution STIS spectra that were also available for these galaxies, thus effectively fixing the stellar population mix while matching the G750M spectra. The good agreement between the nuclear σ_* values obtained with and without using such additional information, and additionally with the G750M σ_* measurements of Batcheldor et al. (2013) in the CaII triplet near-infrared wavelength region, gave us further confidence in the σ_* measurements for the 4 galaxies for which we could only rely on the G750M spectra.

To start investigating the usefulness of such nuclear σ_* measurements in constraining $M_\bullet$ in nearby galaxies we then considered the case of NGC 4435 and NGC 4459, since these indeed appear to have quite different values of $M_\bullet$ from ionized-gas kinematical measurements despite showing similar ground-based $\sigma_{\rm e}$ values. Indeed, while NGC 4459 shows a $M_\bullet$ value consistent with the $M_\bullet - \sigma_{\rm e}$ relation (Sarzi et al., 2001), the $M_\bullet$ of NGC 4435 falls significantly below it (Coccato et al., 2006). Furthermore, these two galaxies feature quite different nuclear σ_* values in our catalogue, with NGC 4435 displaying a particularly low σ_* value compared to NGC 4459 that could support the finding of Coccato et al. (2006).

We looked into this puzzle by building Jeans axisymmetric stellar dynamical models for

NGC 4435 and NGC 4459 starting from archival ACS images while matching the available integral-field SAURON stellar kinematics. In addition, in these models we adopted either $M_\bullet = 0$ $M_\odot$ or the $M_\bullet$ value from the $M_\bullet - \sigma_e$ relation, which allowed us to predict the central $V_{rms}(0) \simeq \sigma_*$ by mimicking the HST spatial resolution and sampling, while essentially holding to JAM the values for stellar mass-to-light ratio, inclination, and anisotropy parameter that best matched the ground-based kinematics (see Sect. 4.4.6). In the case of NGC 4459 our nuclear σ_* value ($\sigma_{*,fix} = 214.6^{+11.2}_{-12.0}$ km s^{-1}) was nearly consistent with the high-spatial resolution prediction for $V_{rms}(0)$ at the $M_\bullet$ value given by the $M_\bullet - \sigma_e$ relation ($V_{rms}(0) = 199.1$ km s^{-1}), whereas for NGC 4435 the nuclear σ_* value ($\sigma_{*,fix} = 87.3^{+10.2}_{-8.8}$ km s^{-1}) falls significantly below the model predictions even for $M_\bullet = 0$ $M_\odot$ ($V_{rms}(0) = 151.6$ km s^{-1}).

Although our models are relatively simplistic, these results lend further support to the idea that the SBH of NGC 4435 is a genuine low outlier in the $M_\bullet - \sigma_e$ relation, which deserves further investigation. For instance NGC 4435 would be an ideal target for future near-infrared observations from either space (e.g. with JWST) or from the ground using adaptive optics, such as those presented by Krajnović et al. (2018b), who indeed also found evidence for undermassive SBHs in two nearby early-type galaxies. Near-infrared observations could be useful also to confirm that the center is dust free, as we found. Since we are dealing with σ_* measurements within a nuclear aperture, the presence of an unresolved nuclear stellar disk could influence the results, even if a proper dynamical model would be required in order to evaluate the respective contributions of the nuclear stellar disk, bulge, and SBH. Adaptive-optics assisted integral-field observations would also allow us to establish if our nuclear σ_* dip can be explained by the presence of a central dynamically cold component such as a nuclear disk, although we note that in that case the presence of a SBH would be betrayed by an increased central stellar rotation (as also discussed by Krajnović et al., 2018b). Theoretical works indicate that assessing the fraction of undermassive black holes in nearby galaxies would be quite important to constrain the processes driving the mass growth of SBHs and how they settled in galactic nuclei (Volonteri et al., 2011).

Chapter 5

Conclusions and future perspectives

In this thesis, we aimed to increase the demography of nearby galaxies ($D < 103$ Mpc) with stringent limits for the mass $M_\bullet$ of their supermassive black hole (SBH). On one hand, large samples of stringent limits and accurate $M_\bullet$ values are needed to analyze the scaling relations between the mass of SBHs and the properties of their host galaxies. In particular, $M_\bullet$ stringent limits are quite cheap from both an observational and computational point of view and can be easily computed for a large number of galaxies. On the other hand, putting constraints on $M_\bullet$ is especially useful to identify the low and high-$M_\bullet$ outliers from the scaling relations. In the following, we collect the main conclusions and future perspectives for each Chapter of the thesis.

Chapter 2: We aimed to increase the galaxy sample with $M_\bullet$ stringent limits already obtained by Beifiori et al. (2009, 2012) by selecting from the objects excluded by Beifiori et al. (2009) 9 galaxies with detected emission lines in Space Telescope Imaging Spectrograph (STIS) spectra taken with the G750M grating. We discarded NGC 3003 since the [NII]λ6583 flux profile was characterized by a strongly irregular shape not consistent with a Gaussian function and NGC 4420 since we were not totally convinced of the presence of ionized gas. We derived the central stellar velocity dispersion from new long-slit spectra obtained at the Asiago Astrophysical observatory and we calculated the stellar velocity dispersion σ_c within 1/8 the effective radius r_e. r_e was estimated either from a two-dimensional photometric decomposition of the i-band images of the Sloan Digital Sky Survey or from the literature. We successfully obtained new $M_\bullet$ stringent limits for a sample of 7 nearby galaxies, which cover different morphological types (1 elliptical, 3 unbarred and 3 barred spirals according to the photometric decomposition) and span a wide range of central stellar velocity dispersion ($71 < \sigma_c < 248$ km s^{-1}) and $M_\bullet$ ($3.6 \cdot 10^6 < M_\bullet < 1.1 \cdot 10^9$ M$_\odot$ assuming $i = 33°$ for the unresolved gaseous disk and $1.0 \cdot 10^6 < M_\bullet < 2.9 \cdot 10^8$ M$_\odot$ for $i = 81°$). We compared these $M_\bullet$ stringent limits with those of Beifiori et al. (2009, 2012) and found them to be consistent with each other. On average, our $M_\bullet$ values run parallel to and above the $M_\bullet - \sigma_c$ relation of Ferrarese & Ford (2005) with no systematic trend depending on the galaxy distance or presence of a bar. With our investigation, the number of galaxies with $M_\bullet$ stringent limits obtained from nebular-line width increases to 114. Most of our $M_\bullet$ limits actually are positioned in the poorly populated

low-σ_c end of the $M_\bullet - \sigma_c$ relation.

Concerning future perspectives, it could be possible to search for archival G750M emission-line spectra observed after 2012 or obtain new spectra with the Hubble Space Telescope (HST) or large ground-based telescopes assisted with adaptive optics for objects which are under-respresented in the current sample, in particular those in the low-σ_c regime. Recently, Shankar et al. (2016) have pointed out that the SBHs studied in the literature are harbored by host galaxies that are not representative of the bulk of the local galaxies. This issue is mainly related to the need of resolving the SBH sphere of influence to obtain reliable $M_\bullet$ measurements and to the fact that low $M_\bullet$ are more challenging to measure. From this, follows that all the scaling relations could be biased. By considering the optical/NIR spectral range, it could be interesting to address this issue by selecting and observing galaxies chosen expressly to correct this bias. HST could be sufficient in some cases, but the new generation of ground (e.g., the European Extremely Large Telescope) and space-based (e.g., the James Webb Space Telescope) telescopes will be suitable for this task.

Chapter 3: We considered the sample of 114 galaxies previously collected and we aimed at obtaining more stringent limits for the $M_\bullet$ by modeling of the [NII]λ6583 emission-line width measured on sub-arcsecond apertures with STIS taking into account the stellar mass contribution, which was previously disregarded. We estimated the stellar mass contribution of the sample galaxies by modeling the surface brightness distribution measured from HST archival images as a sum of a set of Gaussians and by adopting the mass-to-light ratio ($(M/L)_\star = 4.32$ $M_\odot/$ $L_\odot$) of an old and metal-rich stellar population (Vazdekis et al., 2012). For each galaxy we therefore maximized the amount of stellar mass that resides within the aperture size of the nuclear spectrum. Some galaxies host younger and less metal-rich stellar populations in their nucleus with a smaller $(M/L)_\star$. We successfully conducted this analysis for 100 galaxies. We repeated the $M_\bullet$ measurements of Beifiori et al. (2009, 2012) to perform a plain comparison between the $M_\bullet$ values determined with and without including the stellar mass in the dynamical model.

We found that on average the stellar mass contribution is larger in the low effective stellar velocity dispersion (σ_e) range (24% for $\sigma_e <$ 90 km s^{-1} at $i = 33°$) and it progressively decreases until it became negligible in the high-σ_e range (2% for $\sigma_e >$ 220 km s^{-1} at $i = 33°$). Moreover, it is smaller for elliptical galaxies (3% at $i = 33°$) than for lenticulars (15% at $i = 33°$) and spirals (14% at $i = 33°$). In galaxies with larger $M_\bullet$ and σ_e, the SBH dominates the gravitational potential of nuclear regions. This is case of ellipticals, which are characterized by $M_\bullet > 10^8$ $M_\odot$ at $i = 33°$ which is much larger than the stellar mass contribution. Conversely, most of spirals have $M_\bullet < 10^8$ $M_\odot$ at $i = 33°$ which is comparable to the mass contribution of the stars.

We also found that on average the stellar mass contribution is smaller for narrower apertures of 0.1×0.15 arcsec^2 (6% at $i = 33°$), whereas there is not a clear correlation with the galaxy distance. This is expected because galaxies with very different σ_e values and morphological types are included in the same distance bins. Moreover, the sample was selected to include only nearby galaxies with a median distance $D = 25.7$ Mpc, so their distances are all comparable except for a few cases. We did not observe any correlation between the stellar

mass contribution and the physical size of the apertures.

In the low-σ_e range some of the sample galaxies with the larger stellar mass contribution harbor a nuclear stellar cluster/disk, and these certainly contribute to the stellar mass in the nucleus of 7 galaxies. In a few lenticulars and spirals, we were not able to match the observed [NII]λ6583 width with that predicted by the dynamical model and placed an upper limits of $M_\bullet < 10^5$ $M_\odot$ on the mass of their central SBH. We concluded that this could due to the large value adopted for $(M/L)_\star$. For example, Walcher et al. (2006) derived $(M/L)_\star = 0.08 - 2.06$ $M_\odot$/ $L_\odot$ (a factor 2 to 5 smaller than ours) for a sample of late-type spiral galaxies hosting a nuclear stellar cluster by fitting composite population synthesis models to their nuclear spectra. This decrease of $(M/L)_\star$ can be hardly considered in the case of ellipticals, since they rarely harbor young stellar populations in the nuclear regions.

At $i = 33°$, the median of the ratios between the $M_\bullet$ values we obtained and those predicted by the $M_\bullet - \sigma_e$ relation is 1.9 disregarding the stellar mass contribution and 1.7 accounting for it. Accounting for the stellar mass distribution, the deviation of the $M_\bullet$ stringent limits from the $M_\bullet - \sigma_e$ relation significantly reduces in the low-σ_e range and becomes negligible in the high-σ_e range.

In the range $90 < \sigma_e < 220$ km s^{-1} the $M_\bullet$ values at $i = 33°$ run almost parallel to the $M_\bullet - \sigma_e$ relation with a slope of 4.00 ± 0.48, which is consistent with the findings of Kormendy & Ho (2013). Considering the entire σ_e range, the linear-fit slope is 3.56 ± 0.22 and it is indicative of a shallow flattening for both $\sigma_e > 220$ km s^{-1} and $\sigma_e < 90$ km s^{-1}. The distribution of the $M_\bullet$ at $i = 81°$ was analyzed and compared in a consistent way with the one at $i = 33°$ by limiting the sample at $i = 33°$ to the same objects considered at $i = 81°$. From this analysis we conclude that the $M_\bullet$ values at 81° are positioned farther from the $M_\bullet - \sigma_e$ relation than those at $i = 33°$. This could be a consequence of having adopted a very large $(M/L)_\star$ value all throughout the galaxy sample.

On average our $M_\bullet$ stringent limits at $i = 33°$ are only a factor of 1.7 larger than $M_\bullet$ predicted by the $M_\bullet - \sigma_e$ relation and a factor of 1.3 larger than actual $M_\bullet$ values based on resolved kinematics. This is a striking result if we consider that our dynamical analysis does not rely on spatially-resolved distribution and kinematics of the gaseous tracer within the galaxy nucleus aperture and does not account for the presence of nongravitational forces which could further broaden the width of the emission lines. We concluded that nongravitational forces play a minor role in the majority of the sample galaxies by analysing the profile of the [NII]λ6583 emission line of the shape of its flux radial profile.

Concerning the future, firstly the whole analysis should be repeated by discarding those objects affected by dust in the central region, to compare our results to those obtained with a dust-free sample. Secondly, it could be interesting to estimate the actual $(M/L)_\star$, even if this could not be done for the whole galaxy sample and in a homogeneous way (e.g., by using the same filters in the case it is derived with images or using the same spectral range in the case of spectra). But in principle this analysis could be performed with a subsample in order to assess the impact of our hypothesis on the final $M_\bullet$ values, in particular in the cases in which a young and/or metal-poor population is present in the galaxy nucleus. After obtaining the $(M/L)_\star$ and the new $M_\bullet$ stringent limits for the largest possible sample, the $M_\bullet$ values

obtained for those galaxies without matched gas velocity dispersion should be inspected. In our analysis those objects were characterized by $M_\bullet < 10^5$ $M_\odot$ and it could be intriguing to verify if the new $M_\bullet$ still remain far from the $M_\bullet - \sigma_e$ relation. This allows us to identify potential low-mass outliers from the $M_\bullet - \sigma_e$, for which further study would be required.

Chapter 4: We considered all the archival STIS spectra obtained with the G750M grating targeting the nucleus of a galaxy in order to measure the nuclear stellar velocity dispersion σ_* within a sub-arcsecond aperture. We collected a sample of 28 nearby galaxies, spanning a wide range of morphological types (from E to Scd) and central nuclear activity (Seyfert 2, LINERs, HII nuclei). We fitted the STIS spectra to obtain the stellar kinematics by using the single-age, single-metallicity stellar population models of Vazdekis et al. (2010) and both narrow and broad Gaussian emission lines. For 24 objects we further constrained such a fit by using the optimal template from a similar fit to the low-resolution G430L STIS spectra, thus fixing the stellar population mix while matching the G750M spectra. We obtained good agreement between the nuclear σ_* values obtained with and without constraining the stellar populations and this gave us further confidence in the σ_* measurements for the 4 galaxies for which we could only rely on the G750M spectra. Moreover, for three galaxies in the sample we found a good agreement by comparing their σ_* measurements with those of Batcheldor et al. (2013) which were obtained with the G750M grating but using the CaII triplet near-infrared wavelength region.

To investigate the importance of such nuclear σ_* measurements in constraining $M_\bullet$ in nearby galaxies, we then considered NGC 4435 and NGC 4459. These lenticular galaxies appear to have quite different values of $M_\bullet$ from ionized-gas kinematic measurements, despite showing similar ground-based σ_e values. Indeed, while NGC 4459 shows a $M_\bullet$ value consistent with the $M_\bullet - \sigma_e$ relation (Sarzi et al., 2001), the $M_\bullet$ of NGC 4435 significantly falls below it (Coccato et al., 2006).

To solve this puzzle, we built Jeans axisymmetric stellar dynamical models for both NGC 4435 and NGC 4459 starting from archival images obtained with the Advanced Camera for Surveys and matching the available integral-field SAURON stellar kinematics. In addition, in these models we adopted either $M_\bullet = 0$ $M_\odot$ or the $M_\bullet$ value from the $M_\bullet - \sigma_e$ relation, which allowed us to predict the central σ_* by mimicking the HST spatial resolution and sampling, while essentially holding the values for stellar mass-to-light ratio, inclination, and anisotropy parameter that best matched the ground-based kinematics. In the case of NGC 4459, our nuclear σ_* value is nearly consistent with the high-spatial resolution prediction for σ_* at the $M_\bullet$ value given by the $M_\bullet - \sigma_e$ relation, whereas for NGC 4435 the nuclear σ_* value falls significantly below the model predictions even for $M_\bullet = 0$ $M_\odot$. Although our models are somehow simplistic, these results lend further support to the idea that the SBH of NGC 4435 is a genuine low outlier in the $M_\bullet - \sigma_e$ relation, which deserves further investigation.

NGC 4435 would be an ideal target for future near-infrared observations from either space (e.g., with JWST) or ground assisted by adaptive optics, such as those presented by Krajnović et al. (2018b), who indeed also found evidence for undermassive SBHs in two nearby early-type galaxies. Integral-field observations would also allow us to establish whether the nuclear σ_* dip we observed can be explained by the presence of a central dynamically cold component

like a nuclear disk, although we note that in that case the presence of a SBH would be betrayed by an increased central stellar rotation. Theoretical works indicate that assessing the fraction of undermassive black holes in nearby galaxies would be quite important to constrain the processes driving the mass growth of SBHs and how they settled in galactic nuclei (Volonteri et al., 2011).

Bibliography

Aguerri J. A. L., González-García A. C., 2009, A&A, 494, 891

Alam S., et al., 2015, ApJS, 219, 12

Atkinson J. W., et al., 2005, MNRAS, 359, 504

Baade W., Minkowski R., 1954, ApJ, 119, 206

Bacon R., et al., 2001, MNRAS, 326, 23

Barth A. J., Sarzi M., Rix H.-W., Ho L. C., Filippenko A. V., Sargent W. L. W., 2001, ApJ, 555, 685

Barth A. J., Greene J. E., Ho L. C., 2005, ApJ, 619, L151

Batcheldor D., Axon D., Valluri M., Mandalou J., Merritt D., 2013, AJ, 146, 67

Beifiori A., Sarzi M., Corsini E. M., Dalla Bontà E., Pizzella A., Coccato L., Bertola F., 2009, ApJ, 692, 856

Beifiori A., Courteau S., Corsini E. M., Zhu Y., 2012, MNRAS, 419, 2497

Bernardi M., Sheth R. K., Tundo E., Hyde J. B., 2007, ApJ, 660, 267

Binggeli B., Sandage A., Tammann G. A., 1985, AJ, 90, 1681

Binney J., Mamon G. A., 1982, MNRAS, 200, 361

Böker T., van der Marel R. P., Vacca W. D., 1999, AJ, 118, 831

Bower G. A., et al., 1998, ApJ, 492, L111

Bower G. A., Wilson A. S., Heckman T. M., Magorrian J., Gebhardt K., Richstone D. O., Peterson B. M., Green R. F., 2000, in American Astronomical Society Meeting Abstracts. p. 1566

Burbidge G. R., Burbidge E. M., Sandage A. R., 1963, Reviews of Modern Physics, 35, 947

Calzetti D., Kinney A. L., Storchi-Bergmann T., 1994, ApJ, 429, 582

Caon N., Capaccioli M., D'Onofrio M., 1993, MNRAS, 265, 1013

Capetti A., Marconi A., Macchetto D., Axon D., 2005, A&A, 431, 465

Cappellari M., 2002, MNRAS, 333, 400

Cappellari M., 2008, MNRAS, 390, 71

Cappellari M., Emsellem E., 2004, PASP, 116, 138

Cappellari M., Verolme E. K., van der Marel R. P., Verdoes Kleijn G. A., Illingworth G. D., Franx M., Carollo C. M., de Zeeuw P. T., 2002, ApJ, 578, 787

Cappellari M., et al., 2007, MNRAS, 379, 418

Cappellari M., Neumayer N., Reunanen J., van der Werf P. P., de Zeeuw P. T., Rix H.-W., 2009, MNRAS, 394, 660

Cappellari M., et al., 2011, MNRAS, 413, 813

Cappellari M., et al., 2013, MNRAS, 432, 1709

Cardelli J. A., Clayton G. C., Mathis J. S., 1989, ApJ, 345, 245

Coccato L., Sarzi M., Pizzella A., Corsini E. M., Dalla Bontà E., Bertola F., 2006, MNRAS, 366, 1050

Corsini E. M., Morelli L., Pastorello N., Dalla Bontà E., Pizzella A., Portaluri E., 2016, MNRAS, 457, 1198

Corsini E. M., Wegner G. A., Thomas J., Saglia R. P., Bender R., 2017, MNRAS, 466, 974

Cortese L., Bendo G. J., Isaak K. G., Davies J. I., Kent B. R., 2010, MNRAS, 403, L26

Costantin L., Méndez-Abreu J., Corsini E. M., Morelli L., Aguerri J. A. L., Dalla Bontà E., Pizzella A., 2017, A&A, 601, A84

Cretton N., van den Bosch F. C., 1999, ApJ, 514, 704

Dalla Bontà E., Ferrarese L., Corsini E. M., Miralda-Escudé J., Coccato L., Sarzi M., Pizzella A., Beifiori A., 2009, ApJ, 690, 537

Davis T. A., Bureau M., Cappellari M., Sarzi M., Blitz L., 2013, Nature, 494, 328

Devereux N., Ford H., Tsvetanov Z., Jacoby G., 2003, AJ, 125, 1226

Dressel L., Holfeltz S., Quijano J. K., 2007, STIS Data Handbook, Version 5.0 (Baltimore, MD: STScI)

Emsellem E., Monnet G., Bacon R., 1994, A&A, 285, 723

Emsellem E., et al., 2004, MNRAS, 352, 721

Fabian A. C., 1999, MNRAS, 308, L39

Falcón-Barroso J., Sánchez-Blázquez P., Vazdekis A., Ricciardelli E., Cardiel N., Cenarro A. J., Gorgas J., Peletier R. F., 2011, A&A, 532, A95

Falcón-Barroso J., et al., 2017, A&A, 597, A48

Ferrarese L., Ford H., 2005, Space Sci. Rev., 116, 523

Ferrarese L., Merritt D., 2000, ApJ, 539, L9

Ferrarese L., Ford H. C., Jaffe W., 1996, ApJ, 470, 444

Ferrarese L., et al., 2006a, ApJS, 164, 334

Ferrarese L., et al., 2006b, ApJ, 644, L21

Ferrers N. M., 1877, Quart. J. Pure and Appl. Math, 14, 1

Fisher D. B., Drory N., 2016, in Laurikainen E., Peletier R., Gadotti D., eds, Astrophysics and Space Science Library Vol. 418, Galactic Bulges. p. 41

Freeman K. C., 1970, ApJ, 160, 811

Gebhardt K., et al., 2000, ApJ, 539, L13

Gebhardt K., et al., 2003, ApJ, 583, 92

Gebhardt K., Adams J., Richstone D., Lauer T. R., Faber S. M., Gültekin K., Murphy J., Tremaine S., 2011, ApJ, 729, 119

Genzel R., Townes C. H., 1987, ARA&A, 25, 377

Genzel R., Eisenhauer F., Gillessen S., 2010, Reviews of Modern Physics, 82, 3121

Georgiev I. Y., Böker T., 2014, MNRAS, 441, 3570

Gerhard O. E., 1993, MNRAS, 265, 213

Ghez A. M., Salim S., Hornstein S. D., Tanner A., Lu J. R., Morris M., Becklin E. E., Duchêne G., 2005, ApJ, 620, 744

Ghez A. M., et al., 2008, ApJ, 689, 1044

Gillessen S., Eisenhauer F., Fritz T. K., Bartko H., Dodds-Eden K., Pfuhl O., Ott T., Genzel R., 2009, ApJ, 707, L114

Girardi L., Bressan A., Bertelli G., Chiosi C., 2000, A&AS, 141, 371

Gonzaga S., et al., 2012, The DrizzlePac Handbook, (Baltimore, MD: STScI)

Graham A. W., 2016a, in Meiron Y., Li S., Liu F.-K., Spurzem R., eds, IAU Symposium Vol. 312, Star Clusters and Black Holes in Galaxies across Cosmic Time. p. 269

Graham A. W., 2016b, in Laurikainen E., Peletier R., Gadotti D., eds, Astrophysics and Space Science Library Vol. 418, Galactic Bulges. p. 263

Graham A. W., Spitler L. R., 2009, MNRAS, 397, 2148

Greene J. E., Ho L. C., 2007, ApJ, 670, 92

Gültekin K., et al., 2009, ApJ, 698, 198

Gültekin K., Richstone D. O., Gebhardt K., Faber S. M., Lauer T. R., Bender R., Kormendy J., Pinkney J., 2011, ApJ, 741, 38

Hamuy M., Walker A. R., Suntzeff N. B., Gigoux P., Heathcote S. R., Phillips M. M., 1992, PASP, 104, 533

Hamuy M., Suntzeff N. B., Heathcote S. R., Walker A. R., Gigoux P., Phillips M. M., 1994, PASP, 106, 566

Häring N., Rix H.-W., 2004, ApJ, 604, L89

Herrnstein J. R., Moran J. M., Greenhill L. J., Trotter A. S., 2005, ApJ, 629, 719

Ho L. C., Filippenko A. V., Sargent W. L. W., 1997, ApJS, 112, 315

Ho L. C., Sarzi M., Rix H.-W., Shields J. C., Rudnick G., Filippenko A. V., Barth A. J., 2002, PASP, 114, 137

Hopkins P. F., Hernquist L., Cox T. J., Robertson B., Krause E., 2007, ApJ, 669, 67

Hu J., 2008, MNRAS, 386, 2242

Huré J.-M., Hersant F., Surville C., Nakai N., Jacq T., 2011, A&A, 530, A145

Jardel J. R., et al., 2011, ApJ, 739, 21

Jørgensen I., Franx M., Kjaergaard P., 1995, MNRAS, 276, 1341

Kenney J. D. P., Tal T., Crowl H. H., Feldmeier J., Jacoby G. H., 2008, ApJ, 687, L69

Kinney A. L., Calzetti D., Bohlin R. C., McQuade K., Storchi-Bergmann T., Schmitt H. R., 1996, ApJ, 467, 38

Kormendy J., Ho L. C., 2013, ARA&A, 51, 511

Kormendy J., Richstone D., 1995, ARA&A, 33, 581

Kormendy J., et al., 1997, ApJ, 482, L139

Kormendy J., Fisher D. B., Cornell M. E., Bender R., 2009, ApJS, 182, 216

Kormendy J., Bender R., Cornell M. E., 2011, Nature, 469, 374

Krajnović D., Jaffe W., 2004, A&A, 428, 877

Krajnović D., et al., 2011, MNRAS, 414, 2923

Krajnović D., Cappellari M., McDermid R. M., 2018a, MNRAS, 473, 5237

Krajnović D., et al., 2018b, MNRAS, 477, 3030

Krist J. E., Hook R. N., Stoehr F., 2011, in Optical Modeling and Performance Predictions V. p. 81270J

Kroupa P., 2001, MNRAS, 322, 231

Kuntschner H., et al., 2010, MNRAS, 408, 97

Kuo C. Y., et al., 2011, ApJ, 727, 20

Lablanche P.-Y., et al., 2012, MNRAS, 424, 1495

Lauer T. R., et al., 2007, ApJ, 662, 808

Ledo H. R., Sarzi M., Dotti M., Khochfar S., Morelli L., 2010, MNRAS, 407, 969

Lucas R. A., et al., 2016, ACS Instrument Handbook, Version 8.0, (Baltimore, MD: STScI)

Lynden-Bell D., 1969, Nature, 223, 690

Lynds C. R., Sandage A. R., 1963, ApJ, 137, 1005

Macchetto F., Marconi A., Axon D. J., Capetti A., Sparks W., Crane P., 1997, ApJ, 489, 579

Magorrian J., et al., 1998, AJ, 115, 2285

Marconi A., Hunt L. K., 2003, ApJ, 589, L21

Marconi A., et al., 2003, ApJ, 586, 868

Markwardt C. B., 2009, in Bohlender D. A., Durand D., Dowler P., eds, Astronomical Society of the Pacific Conference Series Vol. 411, Astronomical Data Analysis Software and Systems XVIII. p. 251

Martín-Navarro I., Mezcua M., 2018, ApJ, 855, L20

McConnell N. J., Ma C.-P., 2013, ApJ, 764, 184

McDermid R. M., et al., 2015, MNRAS, 448, 3484

McMaster M., et al., 2008, Wide Field and Planetary Camera 2 Instrument Handbook v. 10.0

Méndez-Abreu J., Aguerri J. A. L., Corsini E. M., Simonneau E., 2008, A&A, 478, 353

Méndez-Abreu J., Debattista V. P., Corsini E. M., Aguerri J. A. L., 2014, A&A, 572, A25

Méndez-Abreu J., et al., 2017, A&A, 598, A32

Méndez-Abreu J., et al., 2018, MNRAS, 474, 1307

Mezcua M., 2017, International Journal of Modern Physics D, 26, 1730021

Mezcua M., Hlavacek-Larrondo J., Lucey J. R., Hogan M. T., Edge A. C., McNamara B. R., 2018, MNRAS, 474, 1342

Miyoshi M., Moran J., Herrnstein J., Greenhill L., Nakai N., Diamond P., Inoue M., 1995, Nature, 373, 127

Moffat A. F. J., 1969, A&A, 3, 455

Morelli L., Parmiggiani M., Corsini E. M., Costantin L., Dalla Bontà E., Méndez-Abreu J., Pizzella A., 2016, MNRAS, 463, 4396

Nelder J. A., Mead R., 1965, Computer Journal, 7, 308

Neumayer N., Cappellari M., Reunanen J., Rix H.-W., van der Werf P. P., de Zeeuw P. T., Davies R. I., 2007, ApJ, 671, 1329

Nowak N., Saglia R. P., Thomas J., Bender R., Davies R. I., Gebhardt K., 2008, MNRAS, 391, 1629

Pagotto I., et al., 2017, Astronomische Nachrichten, 338, 841

Parsa M., Eckart A., Shahzamanian B., Karas V., Zajaček M., Zensus J. A., Straubmeier C., 2017, ApJ, 845, 22

Pastorini G., et al., 2007, A&A, 469, 405

Pavlovsky C., et al., 2004, ACS Instrument Handbook, Version 5.0, (Baltimore, MD: STScI)

Peterson B. M., 2014, Space Sci. Rev., 183, 253

Pizzella A., Corsini E. M., Morelli L., Sarzi M., Scarlata C., Stiavelli M., Bertola F., 2002, ApJ, 573, 131

Press W. H., Teukolsky S. A., Vetterling W. T., Flannery B. P., 1992, Numerical recipes in C. The art of scientific computing, (Cambridge: University Press)

Prugniel P., Soubiran C., 2001, A&A, 369, 1048

Rees M. J., 1984, ARA&A, 22, 471

Riley A., et al., 2017, STIS Instrument Handbook, Version 16.0. (Baltimore, MD: STScI)

Rossa J., van der Marel R. P., Böker T., Gerssen J., Ho L. C., Rix H.-W., Shields J. C., Walcher C.-J., 2006, AJ, 132, 1074

Rusli S. P., et al., 2013a, AJ, 146, 45

Rusli S. P., Erwin P., Saglia R. P., Thomas J., Fabricius M., Bender R., Nowak N., 2013b, AJ, 146, 160

Saglia R. P., et al., 2016, ApJ, 818, 47

Salo H., et al., 2015, ApJS, 219, 4

Salpeter E. E., 1964, ApJ, 140, 796

Sánchez-Blázquez P., et al., 2006, MNRAS, 371, 703

Sani E., Marconi A., Hunt L. K., Risaliti G., 2011, MNRAS, 413, 1479

Sargent W. L. W., Young P. J., Boksenberg A., Shortridge K., Lynds C. R., Hartwick F. D. A., 1978, ApJ, 221, 731

Sarzi M., Rix H.-W., Shields J. C., Rudnick G., Ho L. C., McIntosh D. H., Filippenko A. V., Sargent W. L. W., 2001, ApJ, 550, 65

Sarzi M., et al., 2002, ApJ, 567, 237

Sarzi M., Rix H.-W., Shields J. C., Ho L. C., Barth A. J., Rudnick G., Filippenko A. V., Sargent W. L. W., 2005, ApJ, 628, 169

Sarzi M., et al., 2006, MNRAS, 366, 1151

Sarzi M., Ledo H. R., Dotti M., 2015, MNRAS, 453, 1070

Savorgnan G. A. D., 2016, ApJ, 821, 88

Savorgnan G. A. D., Graham A. W., 2015, MNRAS, 446, 2330

Savorgnan G. A. D., Graham A. W., 2016, ApJS, 222, 10

Scarlata C., et al., 2004, AJ, 128, 1124

Schlafly E. F., Finkbeiner D. P., 2011, ApJ, 737, 103

Schmidt M., 1963, Nature, 197, 1040

Schödel R., et al., 2002, Nature, 419, 694

Schwarz G., 1978, Ann. Stat., 6, 461

Schwarzschild M., 1979, ApJ, 232, 236

Schwarzschild M., 1993, ApJ, 409, 563

Scott N., Graham A. W., 2013, ApJ, 763, 76

Scott N., et al., 2013, MNRAS, 432, 1894

Sérsic J. L., 1968, Atlas de Galaxias Australes, (Cordoba: Observatorio Astronomico)

Seth A. C., Dalcanton J. J., Hodge P. W., Debattista V. P., 2006, AJ, 132, 2539

Seth A., Agüeros M., Lee D., Basu-Zych A., 2008, ApJ, 678, 116

Shankar F., et al., 2016, MNRAS, 460, 3119

Shankar F., Bernardi M., Sheth R. K., 2017, MNRAS, 466, 4029

Shapiro K. L., Cappellari M., de Zeeuw T., McDermid R. M., Gebhardt K., van den Bosch R. C. E., Statler T. S., 2006, MNRAS, 370, 559

Sheth K., et al., 2010, PASP, 122, 1397

Silk J., Rees M. J., 1998, A&A, 331, L1

Siopis C., et al., 2009, ApJ, 693, 946

Tanaka Y., et al., 1995, Nature, 375, 659

Thomas J., Saglia R. P., Bender R., Thomas D., Gebhardt K., Magorrian J., Richstone D., 2004, MNRAS, 353, 391

Thomas J., Ma C.-P., McConnell N. J., Greene J. E., Blakeslee J. P., Janish R., 2016, Nature, 532, 340

Vazdekis A., Sánchez-Blázquez P., Falcón-Barroso J., Cenarro A. J., Beasley M. A., Cardiel N., Gorgas J., Peletier R. F., 2010, MNRAS, 404, 1639

Vazdekis A., Ricciardelli E., Cenarro A. J., Rivero-González J. G., Díaz-García L. A., Falcón-Barroso J., 2012, MNRAS, 424, 157

Verdoes Kleijn G. A., van der Marel R. P., de Zeeuw P. T., Noel-Storr J., Baum S. A., 2002, AJ, 124, 2524

Vika M., Driver S. P., Cameron E., Kelvin L., Robotham A., 2012, MNRAS, 419, 2264

Vollmer B., Braine J., Combes F., Sofue Y., 2005, A&A, 441, 473

Volonteri M., Natarajan P., Gültekin K., 2011, ApJ, 737, 50

Walcher C. J., et al., 2005, ApJ, 618, 237

Walcher C. J., Böker T., Charlot S., Ho L. C., Rix H.-W., Rossa J., Shields J. C., van der Marel R. P., 2006, ApJ, 649, 692

Walsh J. L., Barth A. J., Ho L. C., Filippenko A. V., Rix H.-W., Shields J. C., Sarzi M., Sargent W. L. W., 2008, AJ, 136, 1677

Walsh J. L., Barth A. J., Sarzi M., 2010, ApJ, 721, 762

Walsh J. L., van den Bosch R. C. E., Barth A. J., Sarzi M., 2012, ApJ, 753, 79

Walsh J. L., Barth A. J., Ho L. C., Sarzi M., 2013, ApJ, 770, 86

Walsh J. L., van den Bosch R. C. E., Gebhardt K., Yildirim A., Gültekin K., Husemann B., Richstone D. O., 2015, ApJ, 808, 183

Walsh J. L., van den Bosch R. C. E., Gebhardt K., Yıldırım A., Gültekin K., Husemann B., Richstone D. O., 2017, ApJ, 835, 208

Woltjer L., 1959, ApJ, 130, 38

Woo J.-H., Yoon Y., Park S., Park D., Kim S. C., 2015, ApJ, 801, 38

Xiao T., Barth A. J., Greene J. E., Ho L. C., Bentz M. C., Ludwig R. R., Jiang Y., 2011, ApJ, 739, 28

de Francesco G., Capetti A., Marconi A., 2006, A&A, 460, 439

de Francesco G., Capetti A., Marconi A., 2008, A&A, 479, 355

de Vaucouleurs G., de Vaucouleurs A., Corwin Jr. H. G., Buta R. J., Paturel G., Fouque P., 1991, Third Reference Catalogue of Bright Galaxies, (Berlin: Springer) (RC3)

van Dokkum P. G., 2001, PASP, 113, 1420

van den Bosch R. C. E., 2016, ApJ, 831, 134

van den Bosch R. C. E., de Zeeuw P. T., 2010, MNRAS, 401, 1770

van den Bosch R. C. E., Gebhardt K., Gültekin K., van de Ven G., van der Wel A., Walsh J. L., 2012, Nature, 491, 729

van den Bosch R. C. E., Gebhardt K., Gültekin K., Yıldırım A., Walsh J. L., 2015, ApJS, 218, 10

van der Kruit P. C., 1979, A&AS, 38, 15

van der Marel R. P., 1994, MNRAS, 270, 271

van der Marel R. P., Franx M., 1993, ApJ, 407, 525

van der Marel R. P., van den Bosch F. C., 1998, AJ, 116, 2220